



HAL
open science

Theoretical developments and experimental evaluation of a novel collaborative multi-drones grasping and manipulation system of large objects.

Zhongmou Li

► **To cite this version:**

Zhongmou Li. Theoretical developments and experimental evaluation of a novel collaborative multi-drones grasping and manipulation system of large objects.. Automatic. École centrale de Nantes, 2021. English. NNT : 2021ECDN0019 . tel-03284256

HAL Id: tel-03284256

<https://theses.hal.science/tel-03284256>

Submitted on 12 Jul 2021

HAL is a multi-disciplinary open access archive for the deposit and dissemination of scientific research documents, whether they are published or not. The documents may come from teaching and research institutions in France or abroad, or from public or private research centers.

L'archive ouverte pluridisciplinaire **HAL**, est destinée au dépôt et à la diffusion de documents scientifiques de niveau recherche, publiés ou non, émanant des établissements d'enseignement et de recherche français ou étrangers, des laboratoires publics ou privés.

THÈSE DE DOCTORAT DE

L'ÉCOLE CENTRALE DE NANTES

ÉCOLE DOCTORALE N° 601
*Mathématiques et Sciences et Technologies
de l'Information et de la Communication*
Spécialité : *Automatique, productique et robotique*

Par

Zhongmou LI

Theoretical developments and experimental evaluation of a novel collaborative multi-drones grasping and manipulation system of large objects

Thèse présentée et soutenue à Nantes, le 31 Mars 2021

Unité de recherche : UMR 6004, Laboratoire des Sciences du Numérique de Nantes (LS2N)

Rapporteurs avant soutenance :

Marc GOUTTEFARDE Directeur de recherche, Université de Montpellier
Pascal MORIN Professeur des universités, Sorbonne université, Paris

Composition du Jury :

Président :	Franck PLESTAN	Professeur des universités, École Centrale de Nantes
Examineurs :	Tobias BRUCKMANN	Enseignant chercheur, University of Duisburg-Essen (Allemagne)
	Rogelio LOZANO	Directeur de recherche, Université de technologie de Compiègne
Directrice de thèse :	Isabelle FANTONI	Directrice de recherche, École Centrale de Nantes
Co-encadrants de thèse :	Abdelhamid CHRIETTE	Maître de conférences, École Centrale de Nantes
	Vincent BÉGOC	Enseignant chercheur, ICAM site de Vendée

ACKNOWLEDGEMENT

It has been one month since I finished my defense on 31 March 2021. Life, after the defense, is still new or unreal to me. I could not have imagined one day might come when I do not need to do anything. Now, it comes to me finally. It finishes, yes, it has really and finally finished.

According to my three-year experience, no one can do his thesis alone. Here, I mean a Ph.D. candidate has to or must cooperate with others in order to correct research directions, get inspired for new ideas, work together to accelerate projects, etc. I am lucky and I am proud of saying thank you to my directors, my colleagues in the ARMEN team at LS2N, my friends at Centrale Nantes in France, and ones in China.

Robotics is an interdisciplinary research area. My three directors are all from different domains: Isabelle Fantoni is a researcher in control, Abdelhamid Chriette is an expert in UAV, Vincent Bégoc has a lot of research experience in mechanics. Because my thesis project involves knowledge of three different domains, it took quite a lot of time for me to understand the project and achieve agreements. During those time, we succeeded in setting the project on wheels thanks to their endless patience. Also, I want to say thanks to the three children of Vincent: Louise, Juliette et Malo. Playing with these three angels gives me a really nice memory. At the same time, I would like to thank the jury members for showing interest in my work and attending my defense.

Colleagues in the ARMEN team at LS2N are friendly guys and provide enormous help to my thesis. Thanks go to Julian, who helps me a lot with drone experiments and control, Guillaume helping me on underactuated fingers, and my dear marpione Franco who is my C++ and Latex slave. Minglei, Rafael, David, and Damien give me suggestions about how to conduct research work as well as how to make choices for the future career. The advice is as essential as those professional ones, which is helpful for thinking and planning.

A thesis is a major part of the life of each Ph.D. student. Therefore, the tension caused by the research progress and failure leads to pressure or even depression. I learn this point from my six months' writing of the thesis alone in my 24 m² apartment in the national confinement. The loneliness is hard to deal with. That is why I must say thank you to

my friends who keep my accompany: Haixin, Chunxiao, Shiyu, and Zhangyu. A special thanks go to Peidong at Centrale Nantes. I cannot remember how many times we walked from Centrale to Commerce, how many bottles we have drunk together. It has been a wonderful experience to be your friend here.

Thanks to my friends Shuo in England, Bobo, and Xiang in China for their kind help when I struggled to find a direction in my thesis. That should go to Wei and Mingyang in France for creating a Centrale group and keeping me accompany even in the confinement.

Finally, I must say thank you to my parents and my sister. Without your support, I could never continue and finish my thesis.

Comment devrais-je appeler ce livre? Un livre permet de consigner ce qu'une personne pense, fait et sent. Est-ce un journal, un autoportrait, ou une biographie?

Au moment où vous lisez ce livre ouvert dans votre main, il me décrit sans que je n'ai rien tu de mauvais, rien ajouté de bon. C'est mon travail, je le connais bien. Tous les mots, les équations et les phrases dans ce livre, ont bien été rédigés de mes mains et basé sur mon travail réalisé pendant les trois ans de Novembre 2017 à Mars 2021.

Ma thèse a permis de développer un nouveau robot, depuis son concept jusqu'au prototype, qui peut saisir et manipuler des objets. Mais, ce n'est pas juste une note de travail comme une recette. Elle explique la méthodologie que j'ai développée pour réaliser un robot. Durant le développement du robot, j'ai dû choisir la direction à donner à ma thèse parmi une multitude de possibilités. Après de nombreux essais, j'ai finalement trouvé une méthode qui est expliquée dans ma thèse permettant la réalisation du robot. D'autres solutions sont bien sûr possible, j'en suis bien conscient.

Si quelqu'un trouve ma thèse et décide d'utiliser quelque chose, j'espère, qu'il fera attention au lien entre la partie à laquelle il s'intéresse et les autres, parce que aucune partie n'est seule dans la perspective globale de la thèse. Il est vrai que ma thèse a fait part à de l'ingénierie répondant à un besoin pratique. Le plus difficile problème dans ma thèse, a été de savoir comment proposer une problématique scientifique et de trouver une contribution originale? Il faut produire une contribution scientifique pour obtenir un diplôme doctorat, c'est différent qu'un travail d'ingénieur ou de master. C'est pourquoi cela a été très dur pour moi lorsque je me suis débattu dans le travail d'ingénierie et je ne trouvais pas de méthode. Avec l'aide de ma directrice et de mes directeurs, nous avons réussi à extraire des problématiques concrètes et les avons résolues grâce à l'abstraction. Nous avons ainsi pu contribuer à l'avancement scientifique. Le robot étant nouveau, les solutions abstraites sont originales, et bien sûr, nouvelles.

Pour finir, pour celui qui est en train de lire ma thèse, je vous dirais merci pour votre confiance sur mon travail et je vous assure tout ce que vous trouverez dans cette thèse est basé sur un travail solide et des données réelles. Je finis ici par les phrases de Rousseau :

"Volià ce que j'ai fait, ce que j'ai pensé, ce que je fus."

—Les Confessions, Jean-Jacques Rousseau

吾生于梓州乡间，年少之时，驰骋山间以游乐，呼朋陋室以娱情。虽处红尘之外，然多得自然之趣。家严豁达不拘小节，常贵素业而轻钱财。每有闲暇，捧清茶一杯，持古卷两册，怡然自得。于章句之间，偶有所得则捻须微笑。吾幼时好奇多问，家父学识渊博，必能解吾所疑。吾由此以好文，心向博学之士，诚效家父之风也。

后离家远游，求学长安。若滑泥扬波，苟得荣华，进可博名利于世，退可保无穷困之苦。然经世致用之术，吾亦求之以近吾性。故志无倾夺，远离故乡，以孑立之身，问道海外。惟愿白发之时回顾平生，不曾因患得失而惧抉择，未尝以畏前程而改夙愿。至今，已历五年也。于此之时，有所感念，试为数言，请诸君一听：

夫天地如逆旅，光阴似过客。神龟虽寿，亦有尽时，金谷盛宴，徒遗痕迹。而人生百年，少有能至，老壮之间，相去几何。文帝云年寿有时而尽，荣乐止乎其身，此之谓也。若少小蹉跎，则白首奈何，冯唐之叹，壮士扼腕。是以君子于学，修身治业，以慕圣贤之道。丈夫立世，砥志砺节，以成栋梁之才。

今四夷未服，九州图裂。外有虎狼之徒，狼视周围，祸乱华夏社稷。内有东南宵小，牝鸡司晨，覬觐中华神器。故海内忧患，匹夫愤惋。此正英雄用武，志士效命之际。若明君待以国士之礼，则报以漆身之节，肝脑涂地而不悔。若贤主施以五穀之恩，则效以犬马之劳，肌肤横分而无旋踵。入庙堂之上，则运筹帷幄，匡扶社稷，为黎民开万世太平。出疆场之外，则登锋履刃，刻石勒功，驱胡虏于黄沙之外。

且天下汹汹，欺上瞒下之徒逢君之恶，于江山抱火屠薪；陶朱之家侈靡相竞，弃礼仪而捐廉耻；左道之人鼓吹邪说，尚帷薄偷香之事。至此四维不张，天道难安。故世人延颈以待君子，拨乱反正修仁行义。而吾辈所以焚膏继晷，昼夜长吟，若学问未成，忧之甚矣。何也？其功业未成是小，而失天下之望为大；全果腹之需是轻，为他人衣食为重；寻章摘句是末，而立身为正为先。今日，诸君与我，皆有求索之志，习中正之学，负一技之长，兼士子之心，应戮力同心，为汉家除残去秽，解天下之忧。

勿忘吾辈入世所为者，苍生耳。

TABLE OF CONTENTS

Introduction	19
1 State of the art	23
1.1 Background of aerial manipulation	24
1.1.1 Manipulation from ground robots	24
1.1.2 Aerial robots	26
1.1.3 Single quadrotor embedding a gripper or a manipulator	30
1.1.4 Manipulation with multiple quadrotors	32
1.2 Background of self-adaptive grippers	38
1.2.1 Introduction to self-adaptive grippers	39
1.2.2 Stability of a self-adaptive grasp	41
1.3 Conclusions	43
2 Static and dynamic modeling of Flying Gripper	45
2.1 Flying Gripper: a novel concept of aerial manipulator	46
2.1.1 Description of the architecture of Flying Gripper with Fixed-Attitude Quadrotors (FG-FAQ)	46
2.1.2 Description of the architecture of Flying Gripper with Mobile-Attitude Quadrotors (FG-MAQ)	50
2.2 Static modeling of Flying Gripper	53
2.3 Dynamic modeling of Flying Gripper	61
2.3.1 Dynamic modeling of FG-FAQ	62
2.3.2 Dynamic modeling of FG-MAQ	65
2.4 Conclusions	72
3 Wrench capability analysis of Flying Gripper	75
3.1 Introduction to wrench capability analysis	76
3.1.1 Connections between grasping, cable robots and aerial robots	76
3.1.2 Introduction to polytope's notations	78

TABLE OF CONTENTS

3.1.3	Overview of the proposed method to obtain the available body wrench set	79
3.2	Wrench capability analysis of a Planar Aerial Manipulator (PAM)	82
3.2.1	Available body wrench set of PAM-FAB	82
3.2.2	Available body wrench set of PAM-MAB	89
3.2.3	Available body wrench set of PAM-MAB for all admissible configurations	93
3.2.4	Discussion on results	96
3.3	Wrench capability analysis of FG-FAQ and FG-MAQ	100
3.3.1	Available body wrench sets of FG-FAQ and FG-MAQ	100
3.3.2	Discussion on results	102
3.4	Conclusions	106
4	Model Predictive Control of Flying Gripper with Fixed-Attitude Quadrotors (FG-FAQ)	109
4.1	Control scheme of FG-FAQ	110
4.1.1	High-level motion controller	111
4.1.2	Control allocation	112
4.2	Model Predictive Control of FG-FAQ	114
4.2.1	Introduction to Model Predictive Control	114
4.2.2	Application of Model Predictive Control for FG-FAQ	115
4.3	Co-simulation of FG-FAQ robot	118
4.3.1	Case study: FG-FAQ robot grasping a 1kg object with disturbances	118
4.3.2	Case study: FG-FAQ robot grasping, transporting and placing a 1kg object	125
4.3.3	Discussion on co-simulation results of FG-FAQ robot	126
4.4	Conclusions	131
5	Dynamic Control Allocation and experimentation of Flying Gripper with Mobile-Attitude Quadrotors (FG-MAQ)	133
5.1	Control scheme of FG-MAQ	134
5.1.1	High-level motion controller	135
5.1.2	Control allocation	137
5.1.3	Quadrotor controller	137
5.2	Dynamic Control Allocation of FG-MAQ	139

5.2.1	Introduction to Dynamic Control Allocation	140
5.2.2	Constraints in Dynamic Control Allocation of FG-MAQ	143
5.2.3	Continuity of control in Dynamic Control Allocation of FG-MAQ	145
5.3	Co-simulation of a Rigid Platform with Mobile-Attitude Quadrotors (RP-MAQ)	146
5.3.1	Introduction to RP-MAQ	146
5.3.2	Discussion on co-simulation results of RP-MAQ robot	148
5.4	Experimentations with RP-MAQ robot	150
5.4.1	Experimental setup	154
5.4.2	Sensors and communication protocol	156
5.4.3	Discussion on experimental results of RP-MAQ robot	159
5.5	Experimentations with FG-MAQ robot	161
5.5.1	Prototype of FG-MAQ	162
5.5.2	Case study: FG-MAQ robot hovering under disturbances	165
5.5.3	Case study: FG-MAQ robot approaching and grasping a large size object	169
5.5.4	Discussion on experimental results of FG-MAQ robot	172
5.6	Conclusions	174
	Conclusions	177
	Appendices	183
	A Operations on polytopes	184
A.1	Convex set and polytope	184
A.1.1	Polytope	184
A.1.2	\mathcal{H} -representation and \mathcal{V} -representation of polytope	186
A.1.3	Maximal inscribed sphere in a polytope	187
A.2	Operations on polytopes	188
A.2.1	Linear mapping of a polytope	188
A.2.2	Minkowski sum	190
A.2.3	Intersection	190
A.2.4	Remarks on the complexity of operations on polytopes	191

B Wrench capability analysis of a Planar Flying Gripper actuated by two quadrotors (PFG)	193
B.1 Wrench capability analysis of a Planar Flying Gripper actuated by two quadrotors (PFG)	193
B.1.1 Available body wrench set of PFG-FAQ	193
B.1.2 Available body wrench set of PFG-MAQ	198
B.1.3 Available body wrench set of PFG-MAQ for all admissible configurations	201
B.1.4 Discussion on results	203
Bibliography	207

NOTATIONS

General symbols

x variable

\dot{x}, \ddot{x} first and second time derivatives of variable x

\mathbf{x} vector

\mathbf{X} matrix

\mathbf{x}^T transpose of the vector \mathbf{x}

\mathbf{e}_k unit vector with the k^{th} element being 1

\mathbf{X}^T transpose of the matrix \mathbf{X}

\mathbf{X}^+ Pseudo-Inverse of the matrix \mathbf{X}

$\mathcal{F}_0(O_0, \mathbf{x}_0, \mathbf{y}_0, \mathbf{z}_0)$ world frame

$\mathcal{F}_b(O_b, \mathbf{x}_b, \mathbf{y}_b, \mathbf{z}_b)$ frame of the body structure of the robot

$\mathcal{F}_i(O_i, \mathbf{x}_i, \mathbf{y}_i, \mathbf{z}_i)$ local frame of the i^{th} UAV, $i = 1, 2, 3, 4$

$\mathcal{F}_{s_i}(O_{s_i}, \mathbf{x}_{s_i}, \mathbf{y}_{s_i}, \mathbf{z}_{s_i})$ frame attached to the worm screw linked to the i^{th} UAV, $i = 1, 2, 3, 4$

${}^b\mathbf{R}_i$ rotation matrix of \mathcal{F}_i w.r.t \mathcal{F}_b

${}^0\mathbf{R}_i$ rotation matrix of \mathcal{F}_i w.r.t \mathcal{F}_0

${}^0\mathbf{R}_b$ rotation matrix of \mathcal{F}_b w.r.t \mathcal{F}_0

${}^0\mathbf{R}_{s_i}$ rotation matrix of \mathcal{F}_{s_i} w.r.t \mathcal{F}_0

${}^b\mathbf{R}_{s_i}$ rotation matrix of \mathcal{F}_{s_i} w.r.t \mathcal{F}_b

${}^s\mathbf{R}_i$ rotation matrix of \mathcal{F}_i w.r.t \mathcal{F}_{s_i}

\mathbf{q}^f vector of generalized coordinates of FG-FAQ robot

\mathbf{q}^m	vector of generalized coordinates of FG-MAQ robot
\mathbf{p}_b	pose vector of the body structure expressed in \mathcal{F}_0
${}^0\mathbf{x}_b$	position vector of the body structure expressed in \mathcal{F}_0
$\boldsymbol{\eta}_b$	Euler angle vector of the body structure \mathcal{F}_b w.r.t \mathcal{F}_0 : the roll/pitch/yaw angles ϕ_b, θ_b, ψ_b and $\boldsymbol{\eta}_b = [\phi_b \ \theta_b \ \psi_b]^T$
\mathbf{q}_a^f	vector regrouping UAVs' attitude vectors of FG-FAQ robot
\mathbf{q}_a^m	vector regrouping UAVs' attitude vectors of FG-MAQ robot
${}^b\mathbf{r}_i$	position vector of the i^{th} UAV's centroid (origin of \mathcal{F}_i) w.r.t to \mathcal{F}_b expressed in \mathcal{F}_b
${}^b\boldsymbol{\omega}_b$	vector of angular velocity of \mathcal{F}_b expressed in \mathcal{F}_b
${}^b\mathbf{f}_{ext}({}^0\mathbf{f}_{ext})$	external force vector acting on the body structure applied by the environment expressed in \mathcal{F}_b (\mathcal{F}_0)
${}^b\boldsymbol{\tau}_{ext}$	external torque vector acting on the body structure applied by the environment expressed in \mathcal{F}_b
${}^b\mathbf{w}_{ext}$	external wrench vector acting on the body structure applied by the environment composed of a force and a torque expressed in \mathcal{F}_b that ${}^b\mathbf{w}_{ext} = [{}^b\mathbf{f}_{ext}^T \quad {}^b\boldsymbol{\tau}_{ext}^T]^T$
\mathbf{w}_{ext}	external wrench vector acting on the body structure applied by the environment composed of a force expressed in \mathcal{F}_0 and a torque expressed in \mathcal{F}_b that $\mathbf{w}_{ext} = [{}^0\mathbf{f}_{ext}^T \quad {}^b\boldsymbol{\tau}_{ext}^T]^T$
${}^b\mathbf{f}_b$	force vector exerted on the body structure by UAVs expressed in \mathcal{F}_b
${}^0\mathbf{f}_b$	force vector exerted on the body structure by UAVs expressed in \mathcal{F}_0
${}^b\boldsymbol{\tau}_b$	torque vector exerted on the body structure by UAVs expressed in \mathcal{F}_b
${}^b\mathbf{w}_b$	wrench vector exerted on the body structure by UAVs composed of a force and a torque expressed in \mathcal{F}_b that ${}^b\mathbf{w}_b = [{}^b\mathbf{f}_b^T \quad {}^b\boldsymbol{\tau}_b^T]^T$
\mathbf{w}_b	wrench vector exerted on the body structure by UAVs composed of a force expressed in \mathcal{F}_0 and a torque expressed in \mathcal{F}_b that $\mathbf{w}_b = [{}^0\mathbf{f}_b^T \quad {}^b\boldsymbol{\tau}_b^T]^T$
d_q	distance between the centroid of UAV and propeller's axes of rotation
$\omega_{i,j}$	speed of the j^{th} motor of UAV i

NOTATIONS

ω_{\min}	minimal motor speed
ω_{\max}	maximal motor speed
Ω_i	vector of motor speed squares of the i^{th} UAV
$\underline{\Omega}$	lower boundry of Ω_i : $\underline{\Omega} = [\omega_{\min} \ \omega_{\min} \ \omega_{\min} \ \omega_{\min}]^T$
$\overline{\Omega}$	upper boundry of Ω_i : $\overline{\Omega} = [\omega_{\max} \ \omega_{\max} \ \omega_{\max} \ \omega_{\max}]^T$
Ω	vector regrouping motor speed squares Ω_i of all UAVs
${}^i\omega_i$	angular velocity vector of \mathcal{F}_i expressed in \mathcal{F}_i
$\boldsymbol{\eta}_i$	Euler angle vector of \mathcal{F}_i w.r.t \mathcal{F}_0 with roll/pitch/yaw angle ϕ_i, θ_i, ψ_i that $\boldsymbol{\eta}_i = [\phi_i \ \theta_i \ \psi_i]^T$
$\boldsymbol{\psi}$	vector regrouping all UAVs' yaw angles: $\boldsymbol{\psi} = [\psi_1 \ \psi_2 \ \psi_3 \ \psi_4]^T$
${}^0\mathbf{f}_i$	thrust force vector produced by the i^{th} UAV expressed in \mathcal{F}_0
${}^i\mathbf{f}_i$	thrust force vector produced by the i^{th} UAV expressed in \mathcal{F}_i
${}^s\mathbf{f}_i$	thrust force vector produced by the i^{th} UAV expressed in \mathcal{F}_{s_i}
$f_{i,x}$	thrust force produced by the i^{th} UAV along \mathbf{x}_i axis in \mathcal{F}_i
$f_{i,y}$	thrust force produced by the i^{th} UAV along \mathbf{y}_i axis in \mathcal{F}_i
$f_{i,z}$	thrust force produced by the i^{th} UAV along \mathbf{z}_i axis in \mathcal{F}_i
\mathbf{f}_z	vector regrouping all UAVs' thrust forces along \mathbf{z}_i axis of \mathcal{F}_i that $\mathbf{f}_z = [f_{1,z} \ f_{2,z} \ f_{3,z} \ f_{4,z}]^T$
${}^i\boldsymbol{\tau}_i$	torque vector produced by the i^{th} UAV expressed in \mathcal{F}_i
$\tau_{i,x}$	torque produced by the i^{th} UAV along \mathbf{x}_i axis in \mathcal{F}_i
$\tau_{i,y}$	torque produced by the i^{th} UAV along \mathbf{y}_i axis in \mathcal{F}_i
$\tau_{i,z}$	torque produced by the i^{th} UAV along \mathbf{z}_i axis in \mathcal{F}_i
$\boldsymbol{\tau}_z$	vector regrouping all UAVs' torques along \mathbf{z}_i axis in \mathcal{F}_i that $\boldsymbol{\tau}_z = [\tau_{1,z} \ \tau_{2,z} \ \tau_{3,z} \ \tau_{4,z}]^T$
${}^0\mathbf{f}_q$	vector regrouping all UAVs' thrust force vectors expressed in \mathcal{F}_0 that ${}^0\mathbf{f}_q = [{}^0\mathbf{f}_1^T \ {}^0\mathbf{f}_2^T \ {}^0\mathbf{f}_3^T \ {}^0\mathbf{f}_4^T]^T$
${}^q\boldsymbol{\tau}_q$	vector regrouping all UAVs' torques: ${}^q\boldsymbol{\tau}_q = [{}^1\boldsymbol{\tau}_1^T \ {}^2\boldsymbol{\tau}_2^T \ {}^3\boldsymbol{\tau}_3^T \ {}^4\boldsymbol{\tau}_4^T]^T$

-
- ${}^i\mathbf{w}_i^r$ reduced wrench vector generated by the i^{th} UAV expressed in \mathcal{F}_i (${}^i\mathbf{w}_i^r \in \mathbb{R}^{4 \times 1}$ for a quadrotor)
- ${}^i\mathbf{w}_i$ wrench vector generated by the i^{th} UAV expressed in \mathcal{F}_i (${}^i\mathbf{w}_i \in \mathbb{R}^{6 \times 1}$ in $SE(3)$)
- ${}^q\mathbf{w}_q$ vector regrouping wrenches ${}^i\mathbf{w}_i$ of all UAVs: ${}^q\mathbf{w}_q = [{}^1\mathbf{w}_1^T \quad {}^2\mathbf{w}_2^T \quad {}^3\mathbf{w}_3^T \quad {}^4\mathbf{w}_4^T]^T$
- ${}^q\mathbf{w}_q^r$ vector regrouping reduced wrenches ${}^i\mathbf{w}_i^r$ of all UAVs: ${}^q\mathbf{w}_q^r = [{}^1\mathbf{w}_1^{rT} \quad {}^2\mathbf{w}_2^{rT} \quad {}^3\mathbf{w}_3^{rT} \quad {}^4\mathbf{w}_4^{rT}]^T$
- ${}^b\mathbf{W}_i^r$ mapping matrix for i^{th} UAV's reduced wrench ${}^i\mathbf{w}_i^r$ from \mathcal{F}_i to \mathcal{F}_b
- ${}^b\mathbf{W}_i$ mapping matrix for i^{th} UAV's wrench ${}^i\mathbf{w}_i$ from \mathcal{F}_i to \mathcal{F}_b
- ${}^s\mathbf{W}_i$ mapping matrix for i^{th} UAV's wrench ${}^i\mathbf{w}_i$ from \mathcal{F}_i to \mathcal{F}_{s_i}
- ${}^b\mathbf{W}_q$ mapping matrix for all UAVs that maps ${}^q\mathbf{w}_q$ to ${}^b\mathbf{w}_b$
- ${}^b\mathbf{W}_q^r$ mapping matrix for all UAVs that maps ${}^q\mathbf{w}_q^r$ to ${}^b\mathbf{w}_b$
- ${}^b\mathbf{W}_\Omega$ mapping matrix for all UAVs that maps Ω to ${}^b\mathbf{w}_b$
- \mathbf{W}_Ω mapping matrix for all UAVs that maps Ω to \mathbf{w}_b
- \mathbf{W}_f mapping matrix for all UAVs that maps ${}^0\mathbf{f}_q$ to \mathbf{w}_b

ACRONYMS

ACTR Aerial Cable-Towed Robot.

CDPR Cable-Driven Parallel Robot.

CoM Center of Mass.

DCA Dynamic Control Allocation.

DOF Degrees of Freedom.

ESC Electronic Speed Controllers.

FCU Flight Control Unit.

FG Flying Gripper.

FG-MAQ Flying Gripper with Mobile-Attitude Quadrotors.

FG-FAQ Flying Gripper with Fixed-Attitude Quadrotors.

MAV Micro Aerial Vehicle.

MOCAP Motion Capture System.

MPC Model Predictive Control.

PAM Planar Aerial Manipulator.

PAM-MAB Planar Aerial Manipulator with Mobile-Attitude Birotors.

PAM-FAB Planar Aerial Manipulator with Fixed-Attitude Birotors.

PFG Planar Flying Gripper actuated by Two Quadrotors.

PFG-MAQ Planar Flying Gripper with Mobile-Attitude Quadrotors.

PFG-FAQ Planar Flying Gripper with Fixed-Attitude Quadrotors.

PI Pseudo-Inverse.

PWM Pulse Width Modulation.

ROS Robot Operating System.

RPi Raspberry PI.

RP-MAQ Rigid Platform with Mobile-Attitude Quadrotors.

UAV Unmanned Aerial Vehicle.

INTRODUCTION

Context of the thesis

Unmanned Aerial Vehicles (UAVs) are being widely used in both military and civilian applications including surveillance of indoor and outdoor environments, remote inspection, monitoring of hostile environments, etc. Due to their flying capability and larger workspace compared with other robots, the use of UAVs when interacting with the environment is becoming more and more popular. In this context, aerial manipulation is a new research area, in which UAVs are equipped with mechanical devices like grippers and manipulators to grasp and manipulate objects in $SE(3)$. As a consequence, compared to robots fixed to the ground, aerial manipulators extend robots' workspace from the ground to the air and provide flying platforms for various devices.

Lots of works use quadrotors in the domain of aerial manipulation, because they are off the shelf components, efficient and low-cost. The most basic approach is simply to attach a gripper to a single quadrotor to perform grasping tasks. Other strategies consist in attaching manipulators to a quadrotor so that the aerial manipulator gains an enhanced manipulability. However, there are also drawbacks. As an example, a quadrotor is under-actuated, which limits its manipulability. The payload of one quadrotor is another key limit. In order to increase the payload, emerging works investigate multi-quadrotor robots for increased manipulability. Using multiple quadrotors with cables can largely increase the payload of the robot. Other works use multiple quadrotors in aerial manipulation where each quadrotor exerts contact and friction forces to grasp an object.

Even though the aforementioned approaches have proven effective in grasping and manipulating an object, they cannot perform all of the following phases: grasping, manipulating, and transporting a large size object autonomously. For quadrotors embedding a gripper and/or a manipulator, it is difficult to deal with large objects, as a larger object often requires a larger gripper/manipulator, which in return reduces the payload. Quadrotors using cables are not designed to grasp an object, which instead needs to be manually attached to cables before performing tasks. For grasps depending on the contact and friction forces between quadrotors and the object, the stability of the obtained grasp

highly relies on contact friction that is hard to estimate and measure, which makes the grasp insecure in real conditions.

For the above reasons, aerial manipulation of large size objects is still an open problem. In order to address this problem, this thesis proposes a novel concept of aerial manipulator called Flying Gripper that can grasp, manipulate, and transport a large size object.

Contributions of the thesis

A novel concept of aerial manipulator called Flying Gripper is proposed in this thesis. This concept combines self-adaptive fingers and multiple quadrotors, and uses the quadrotors' yaw rotations to control closing/opening self-adaptive fingers. Compared to other robots, the Flying Gripper has four key advantages (see page 46):

1. It obtains full manipulability in $SE(3)$ relying on the use of multiple quadrotors.
2. It can produce an enveloping grasp thanks to self-adaptive fingers while adjusting the fingers' configurations to the grasped object's size and shape.
3. It can produce a secured grasp because of the introduction of non-backdrivable mechanisms for transmitting the closing motion of fingers. Once an object is grasped, the robot does not need energy to seize the object when manipulating.
4. It uses the quadrotors' yaw rotations instead of introducing additional motors to actuate the fingers. To the best of our knowledge, it is the first attempt to use multiple quadrotors' yaw rotations contributing to an aerial manipulation task.

The main contributions of the thesis are listed as follows:

1. **Two robot designs based on the concept of Flying Gripper: one with Fixed-Attitude Quadrotors (FG-FAQ), and one with Mobile-Attitude Quadrotors (FG-MAQ).**

In chapter 2, we present the concept of Flying Gripper that is composed of four quadrotors, four self-adaptive fingers and a body structure. The closing/opening motion of each finger is actuated by one quadrotor's yaw rotation. Two different architectures of Flying Gripper are proposed: one with Fixed-Attitude Quadrotors (FG-FAQ) where each quadrotor has only one degree of freedom (its yaw rotation angle) w.r.t the body structure, and a modified one with Mobile-Attitude Quadrotors (FG-MAQ) where each quadrotor has three degrees of freedom (its roll, pitch and yaw rotation angles) w.r.t the body structure using passive universal joints.

Therefore, compared to FG-FAQ, the FG-MAQ robot allows each quadrotor to modify its attitude w.r.t the body structure while generating a yaw rotation to close/open one finger. We then derive the static and dynamic models for the FG-FAQ and FG-MAQ robots respectively.

2. **A wrench capability analysis method for FG-FAQ and FG-MAQ.**

We build the available wrench set that can be applied to the robot by quadrotors, which is called available body wrench set, to analyze the robot's manipulability. In chapter 3, we propose a geometric method to analyze the manipulability of the FG-FAQ and FG-MAQ robots. This method begins with modeling the actuators capabilities of each quadrotor as a polytope, based on which we compute the available body wrench set considering the actuators capabilities, the mobility of quadrotors imposed by passive universal joints and actuating fingers by quadrotors. Results at each step can be visualized in a 3D space and the final results show that FG-MAQ has a better manipulability than FG-FAQ does.

3. **Application of Model Predictive Control for FG-FAQ.**

For the FG-FAQ robot, we propose a controller design method to control the robot's motion while closing/opening the robot's fingers in chapter 4. As an aerial manipulator, the FG-FAQ robot needs to perform grasping and to deal with variation of dynamic parameters due to the grasped object and unknown configuration of the fingers. Therefore, we design a controller scheme consisting of two modules: *i*) a high motion controller module to enable the robot to move from an initial pose to a final one, following a reference trajectory dealing with variable dynamic parameters; *ii*) a control allocation module not only to distribute control efforts, but also to ensure closing and opening fingers during the trajectory tracking. A model predictive controller is used in the high motion controller module. The effectiveness of the designed controller and its robustness against noise and disturbances are validated in co-simulations.

4. **Experimental validation of a Dynamic Control Allocation algorithm on FG-MAQ.**

Chapter 5 presents a strategy to control the robot's pose and the quadrotors' yaw rotations for driving fingers. In the controller design, we assume that each quadrotor can change its attitude instantly, then the body structure is considered to be fully controllable and there exists a redundancy of actuation. The developed controller for the FG-MAQ robot includes three modules: a high motion controller

module, a control allocation module and a quadrotor controller module. In order to enable the robot to track reference trajectories, control efforts are computed by the high motion controller module, which are distributed by the control allocation module to the quadrotor controllers. Then, the quadrotor controller embedded in each quadrotor computes the control input based on two signals: *i*) the output of the control allocation module for tracking the reference trajectory; *ii*) the reference yaw angle for closing/opening the finger. A Dynamic Control Allocation algorithm is applied in the control allocation module for distributing control efforts, while reducing energy consumption and managing the control input continuity, considering the constraints of the robot's mechanical limits and actuators' capabilities. We first test the designed controller on a simplified prototype of the FG-MAQ robot in both co-simulations and experiments. Finally, we build a prototype of FG-MAQ and test the controller's performance in experiments. The experimental results validate that FG-MAQ is able to follow a reference trajectory under disturbances while closing fingers on a large size object.

As mentioned above, the aim of this thesis is to propose a new concept in the field of aerial manipulation robotics. We thus propose a complete study of a new architecture composed of four quadrotors acting as actuators of a hand with four self-adaptive fingers. This concept is called Flying Gripper and is able to perform all of the following phases: grasping, manipulating, and transporting a large size object autonomously. For developing this new concept, a systematic method is presented: introduce the mechanical design, develop the static and dynamic models, analyze manipulability, design and test a controller in co-simulations, build a prototype and test the designed controller in experiments (only for FG-MAQ). Thus, we realize this Flying Gripper concept from a sketch design to a validated prototype.

Publication

Zhongmou Li, Xiaoxiao Song, Vincent Bégoc, Abdelhamid Chriette, and Isabelle Fantoni. *"Dynamic Modeling and Controller Design of a novel aerial grasping robot"*. In: 23rd CISM IFToMM Symposium on Robot Design, Dynamics and Control (RoManSy2020). Sapporo, Japan, Sept. 2020.

STATE OF THE ART

1.1	Background of aerial manipulation	24
1.2	Background of self-adaptive grippers	38
1.3	Conclusions	43

Unmanned Aerial Vehicles (UAVs) are becoming more and more popular in interacting physically with the environment due to their flying capacity and greater workspace compared with other robots. In this context, UAVs are equipped with mechanical devices like grippers and manipulators to grasp and manipulate objects in $SE(3)$. Thus, they extend robots' workspace from the ground to the air and provide flying platforms for various devices. This new areas is called aerial manipulation.

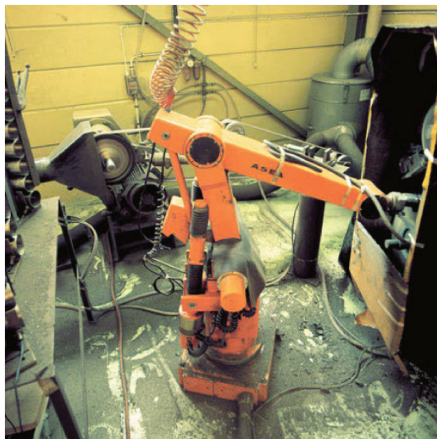
Section 1.1 presents a review of aerial manipulation. Under the background of the robot manipulation, aerial robots are applied in this domain because of their flight capability and greater workspace. Among different existing UAVs, this thesis mainly focuses on approaches using quadrotors. In the domain of aerial manipulation, we introduce current approaches using a single quadrotor and approaches using multiple quadrotors.

Compared to parallel-jaw grippers that are used in most of the existing aerial manipulators, self-adaptive grippers have three main advantages: *i*) produce an enveloping grasp dealing with positioning uncertainty, *ii*) generate a secured grasp using non-backdrivable mechanisms, *iii*) provide a lightweight and sensor-free solution. Thus, self-adaptive grippers are used as key components in the Flying Gripper robot. Section 1.2 introduces the concept of self-adaptive grippers and how they mechanically adapt to the shape of the grasped object in order to produce an enveloping grasp.

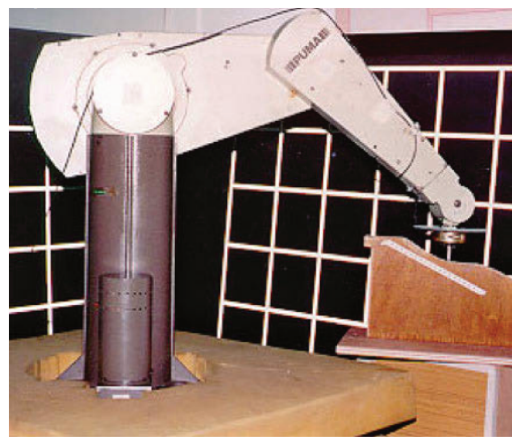
1.1 Background of aerial manipulation

1.1.1 Manipulation from ground robots

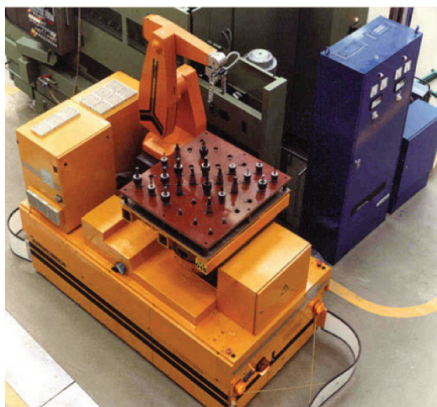
Robotics has been a popular research area for decades that attracts a lot of attention from researchers in industries and academic laboratories. Due to their autonomy, robots can help or replace human for some tasks, and they can have even better performances in areas where it was not possible before. Thus, many different robots are designed for various purposes. One of the most common applications in industry and in laboratories is to perform tasks involving grasping, transporting, packaging, palletizing, and picking [Hägele et al., 2016].



(a) IRB-6



(b) PUMA



(c) MORO developed at Fraunhofer IPA



(d) KUKA omniRob

Figure 1.1 – Manipulation performed by robots in industry [Hägele et al., 2016]

Indeed, robots are developed and employed to grasp and manipulate objects partic-

ularly in both industry and academic areas (see Fig. 1.1). First of all, robots can grasp and manipulate both small and large objects, which is difficult for humans. Furthermore, robots can be controlled remotely by a human operator, so that other workers can work at a safe distance and avoid potential danger during tasks.

In most of scenarios, these robot possess a fixed base, and are thus named ground robots. Early, examples of such robots are IRB-6 and PUMA robots, see Fig. 1.1a and Fig. 1.1b. Their workspace is largely limited by their fixed base and modifying this workspace requires disassembly and assembly, which is time consuming and expensive. In this context, robots are combined with mobile platforms or vehicles in order to improve their mobility and flexibility (see Fig. 1.1c and Fig. 1.1d). Thanks to mobile platforms, robots are not fixed to a given place and gain a mobile workspace for manipulation. However, despite the mobility of such robots, they are still constrained to the ground.



Figure 1.2 – Aerial robots: a Bell 206 helicopter of the Los Angeles Police Department [Wikipedia contributors, 2020b] in (a), a DJI Mavic Mini quadrotor [DJI, 2021b] in (b).

On the other hand, aerial robots, such as helicopters, quadrotors (see Fig. 1.2), can fly freely in unlimited space and have greater workspace compared with ground and mobile robots. However, these aerial robots have limited manipulation capabilities and are more intended to surveillance operations. Thus, by combining manipulators with aerial vehicles, the robot’s workspace is extended from the ground to the air (see Fig. 1.3). Such robots are therefore widely used in the field of manipulation due to their flying ability and unlimited workspace.

As a consequence, there has been an increased interest for investigating UAVs and their applications. UAVs, because of their versatility, are expected to accomplish increasingly complex tasks including physical interaction with the environment. In this context,

aerial manipulators are intended to use UAVs to perform tasks such as grasping, transporting, positioning, assembly and disassembly of mechanical parts, which is referred to as aerial manipulation (detailed surveys can be found in [Khamseh et al., 2018, Meng et al., 2020, Ruggiero et al., 2018]). This new research area proposes challenges in the mechanical design of aerial vehicles and in the control of their dynamics due to the physical interactions with their environment. This thesis focuses on utilizing UAVs for grasping and manipulation tasks.

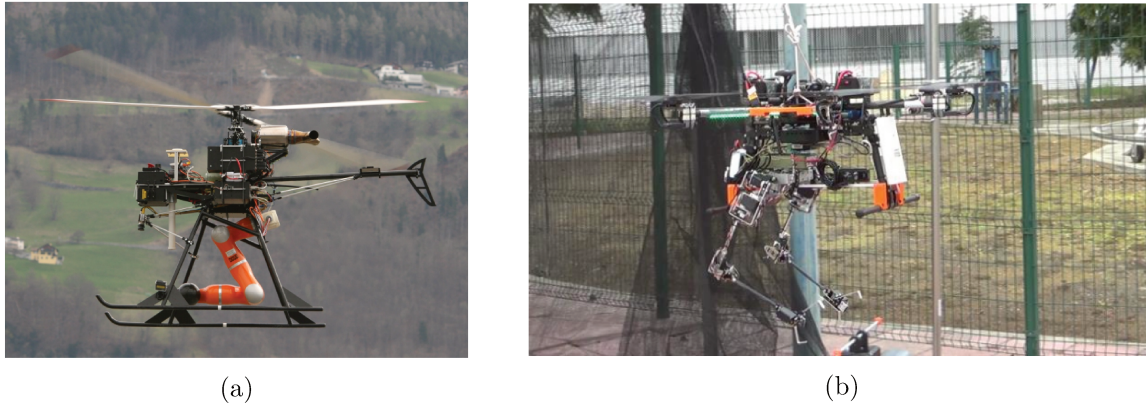


Figure 1.3 – Manipulation performed by aerial manipulators [Laiacker et al., 2016, Suarez et al., 2017b].

1.1.2 Aerial robots

Since the last decade, the number of aerial robot applications has increased significantly. UAVs can be classified into three main categories based on their working principle: fixed-wing UAVs, helicopters, multi-rotor UAVs (see Fig. 1.4).

Fixed-wing UAVs can fly for long periods of time and over long distances, but they require relatively high cruise velocity for a stable flight and they cannot perform hovering during a flight (see Fig. 1.4a). Thanks to rotating propellers, helicopters (see Fig. 1.4b) are capable of achieving hovering and stable flight. Nevertheless their applications are often limited to transporting operations due to their large size, highly detailed and non-linear dynamics [Padfield, 2008]. On the contrary, smaller flying robots, e.g. Micro Aerial Vehicles (MAVs), have reliable mathematical models and advanced nonlinear controllers are implementable into real systems.

A multi-rotor UAV is a rotorcraft with more than two rotors and named accordingly to its specific number of rotors. Indeed, quadrotors with 4 rotors and hexarotors with 6



(a) fixed-wing UAV [Staub, 2018]



(b) helicopter [Staub, 2018]



(c) quadrotor from DJI [DJI, 2021c]



(d) hexarotor from DJI [DJI, 2021a]

Figure 1.4 – Collections of Unmanned Aerial Vehicle (UAV): (a) fixed-wing UAV, (b) helicopter, (c) quadrotor, (d) hexarotor.

rotors are two most common multi-rotor UAVs (see Fig. 1.4c and Fig. 1.4d). Particularly, quadrotors have been widely used in the field of robotics because they provide vertical take off and landing, agile maneuverability, low-cost manufacturability with reduced mechanical complexity, and especially stable hovering ability [Özbek et al., 2016, Nonami et al., 2010]. A quadrotor consists of 4 symmetrically aligned individual rotors attached to a rigid cross airframe [Mahony et al., 2012] and a hexarotor has 6 rotors (see Fig. 1.5a and Fig. 1.5b). For a quadrotor, one couple of opposite rotors spin in the clockwise direction, while the other two in the counterclockwise direction (see Fig. 1.5a). Each propeller generates a vertical thrust force w.r.t to the propeller plane and a drag torque (see Fig. 1.5c). In most cases, rotors are placed in a common plane and have parallel directions to collectively counteract gravity effects. As a consequence, conventional quadrotors and hexarotors have underactuated dynamics which implies a couplings between the rotational dynamics and horizontal translational dynamics.

It is essential to note that quadrotors cannot achieve 6 DOF because of their underactuation. Only the altitude and 3 DOF attitude can be independently controlled. As

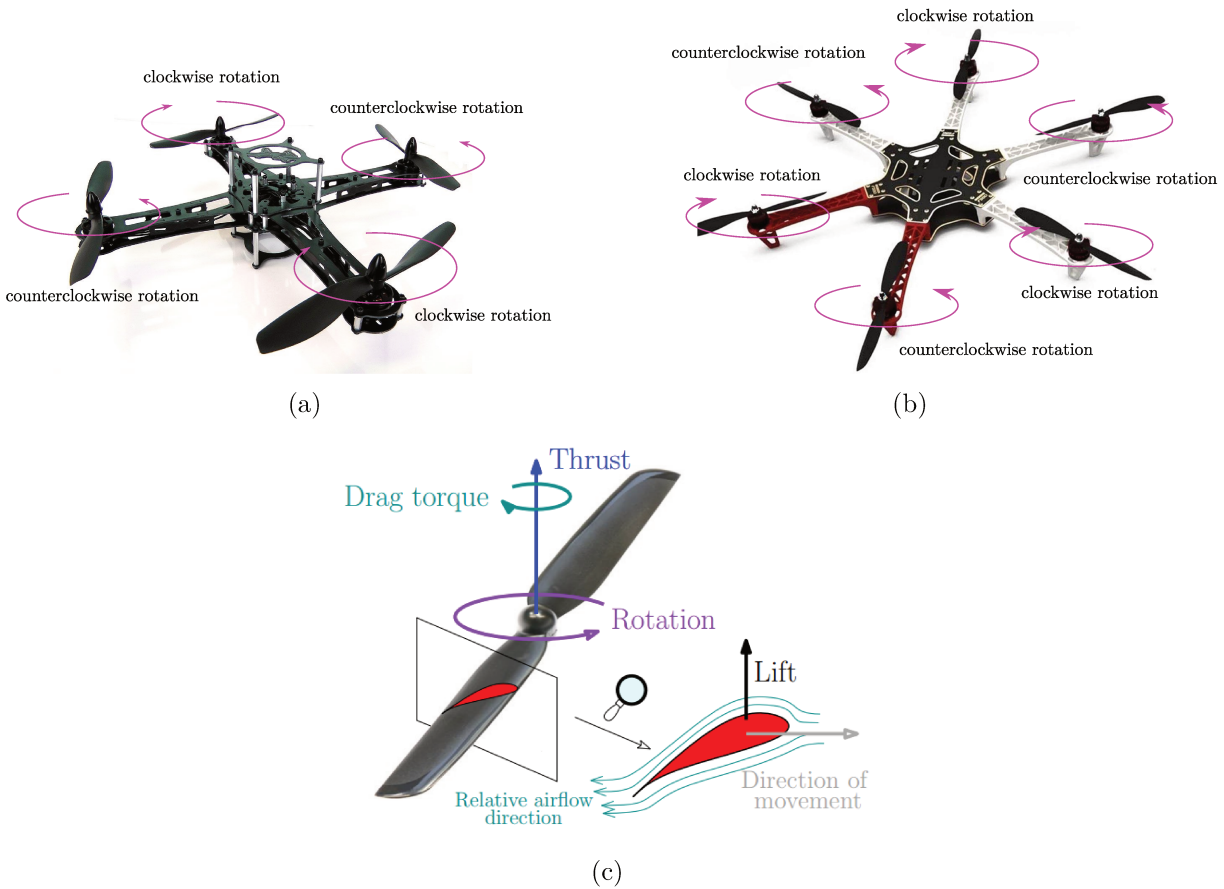


Figure 1.5 – Multi-rotor UAV: a quadrotor consists of 4 symmetrically aligned individual rotors attached to a rigid cross airframe in (a), a hexarotor consists of 6 symmetrically aligned individual rotors attached to a rigid airframe in (b), each propeller generates a thrust force and a drag torque [Bicego, 2019] in (c).

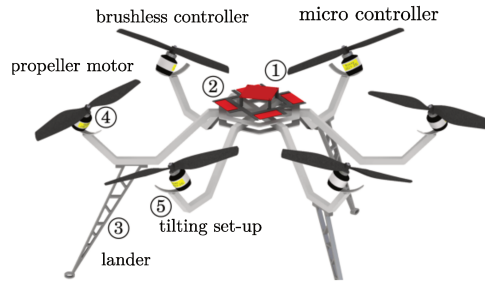
a result, a quadrotor has to change its attitude in order to translate horizontally. From a control perspective, a quadrotor is an underactuated system with 6 DOF (3 DOF in translation and 3 DOF in rotation) and 4 driven rotors (see Fig. 1.5).

There are two approaches to obtain full manipulability in $SE(3)$ [Rashad et al., 2020]: *i)* using fixed propellers with dissimilar orientations, which researchers refer to as fixed-tilt concepts, *ii)* actively tilting the propellers using extra actuators, which researchers refer to as variable-tilt concepts. For the fixed-tilt concepts, orientations of propellers can be optimized to increase manipulability, while for the variable-tilt concepts, orientations of propellers must be controlled by extra actuators in real time to gain full manipulability. For hexarotors, both approaches are tested by researchers (see Fig. 1.6). For the first one, see examples in [Jiang and Voyles, 2013] and [Oosedo et al., 2015], while for the second

one, see examples in [Ryll et al., 2016] and [Kamel et al., 2018]. Different from hexarotors, quadrotors have only 4 rotors and extra actuators are used to rotate propellers to obtain full manipulability (see Fig. 1.7). Interesting works in this direction can be found in [Ryll et al., 2012, Oosedo et al., 2015, Abiko and Harada, 2021, Magariyama and Abiko, 2020]. Drawbacks of these two approaches should also be noted. Both of them decrease the payload and increase the energy consumption for vehicles. Furthermore, even though a rotating propeller can change its attitude in order to generate a 3 dimensional force and expand the agility and manipulability, such robots require complex controllers and it is difficult to achieve stable flight [Oosedo et al., 2015].



(a) [Jiang and Voyles, 2013]



(b) [Rajappa et al., 2015]



(c) [Ryll et al., 2016]



(d) [Kamel et al., 2018]

Figure 1.6 – Hexarotors achieve full manipulability in $SE(3)$: using fixed propellers in (a) and (b), and using rotating propellers in (c) and (d).

As explained before, we choose quadrotors as the UAVs to be studied and used in this thesis, because of their capabilities of taking off and landing vertically, agile maneuverability, low-cost manufacturability with reduced mechanical complexity, and especially stable hovering ability. Therefore, in what follows, we mainly focus on applications of quadrotors for manipulation and grasping tasks in aerial manipulation.

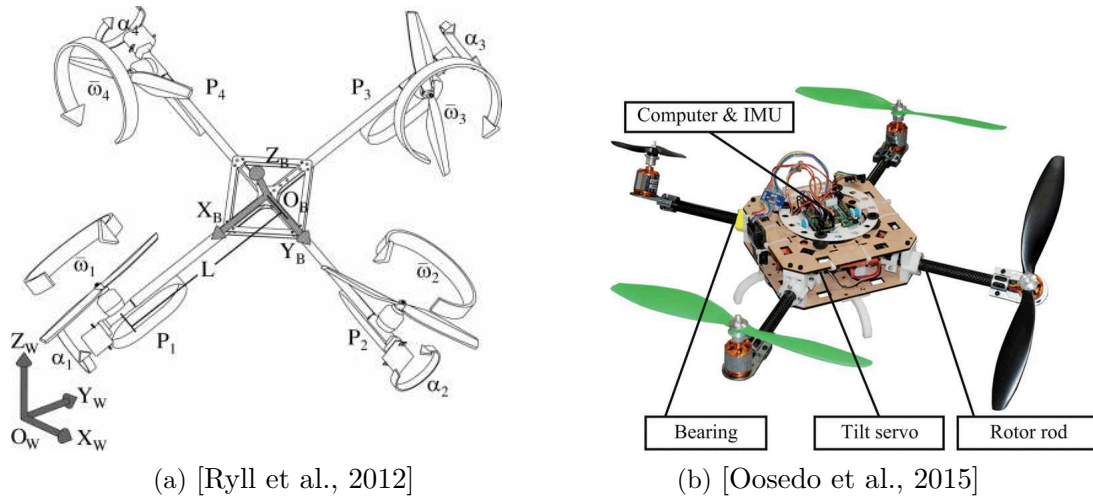


Figure 1.7 – Quadrotors with rotating propellers achieve full manipulability in $SE(3)$.

1.1.3 Single quadrotor embedding a gripper or a manipulator

In aerial manipulation, UAVs work as flying bases in most common scenarios, and one or multiple mechanisms, like a gripper or a serial manipulator, are attached to the aerial vehicle in order to improve the dexterity during the task accomplishment. The UAV itself works as an aerial platform and the mechanism attached to this platform is responsible for grasping and manipulating an object. Indeed, this design approach has been popular among researchers, because it combines both advantages of the UAV i.e. a vast workspace and the dexterity of a serial manipulator.

Gripper

The most simple approach is to attach a gripper to a quadrotor to grasp and place an object (see Fig. 1.8). Authors in [Mellinger et al., 2011] attach a gripper to a quadrotor to pick up and transport payloads. Researchers in [Thomas et al., 2013] present a quadrotor equipped with a gripper that is designed for performing grasping at high speeds. A compliant bistable gripper is attached to a palm-size quadrotor to perch on cylindrical objects [Zhang et al., 2019]. There are interesting works to mention: a gripper with a self-sealing suction cup can apply pulling forces to grasp objects with varying sizes in [Kessens et al., 2016]; an underactuated gripper attached to a helicopter that allows for large positioning errors between the helicopter and the target object in [Pounds et al., 2011]. However, grippers in these approaches cannot deal with large size objects as a single quadrotor's payload cannot afford large size grippers.



(a) [Mellinger et al., 2011]



(b) [Mellinger et al., 2011]



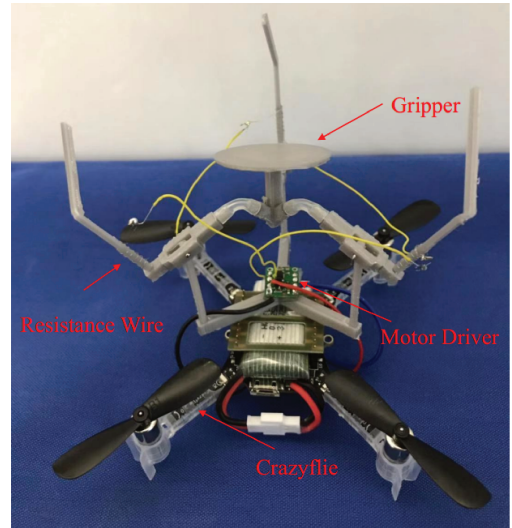
(c) [Pounds et al., 2011]



(d) [Kessens et al., 2016]



(e) [Thomas et al., 2013]



(f) [Zhang et al., 2019]

Figure 1.8 – Aerial manipulation robots: quadrotor equipped with a gripper.

Serial manipulator

One can also endow a quadrotor with one serial manipulator to obtain high levels of dexterity (see Fig. 1.9). Thanks to the embedded manipulator, the robot can manipulate the object independently from the motion of the quadrotor and better compensate external disturbances. So, researchers attach manipulators with a different number of DOF to quadrotor, see [Kim et al., 2013, Heredia et al., 2014, Bellicoso et al., 2015, Ruggiero

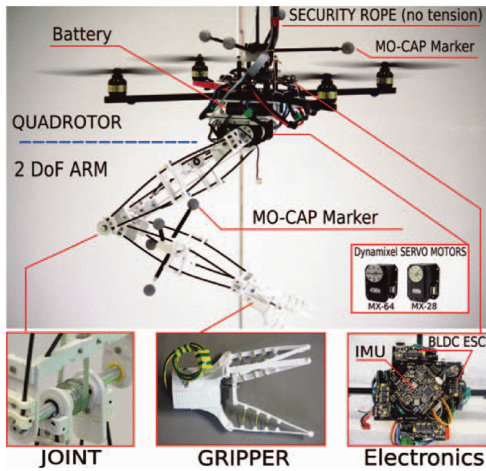
et al., 2015, Garimella and Kobilarov, 2015, Tognon et al., 2017] and Fig. 1.9. It is interesting to note that a parallel manipulator is also attached to a quadrotor in [Danko et al., 2015, Kamel et al., 2016] (see Fig. 1.10). However, dexterity comes with a strong mechanical coupling between the quadrotor and the manipulator’s dynamics. The robot system results to be very complex and the underactuation of quadrotor causes great challenges for the design of controllers. Furthermore, payload is still a key limit when embedding a manipulator.

Dual-arm manipulator

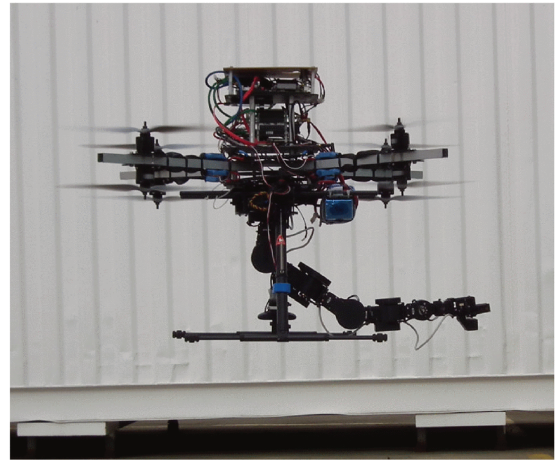
Most of researchers use only one manipulator, but quadrotors with dual-arm are also studied (see Fig. 1.11). Authors use a quadrotor equipped with two manipulators and the quadrotor’s yaw rotation is used for valve turning in [Korpela et al., 2014]. Lightweight manipulators are designed in order to mitigate constraints of the payload in [Suarez et al., 2015, Suarez et al., 2016], then they are used to build an aerial manipulation robot with two lightweight manipulators in [Suarez et al., 2017b, Suarez et al., 2017a, Suarez et al., 2019]. There are some quite interesting works to note: a dual-arm compliant manipulator is attached to a micro quadrotor to mimic bird perching and grasping in [Yu et al., 2019]; a long-bar extension that incorporates a lightweight dual arm in the tip is proposed to obtain a safety distance between rotors and the manipulated object in [Caballero et al., 2017, Caballero et al., 2018]. Still, those manipulators with more dexterity always lead to more complex designs and increased weight, which decreases the payload further and increases the energy consumption because of embedded motors.

1.1.4 Manipulation with multiple quadrotors

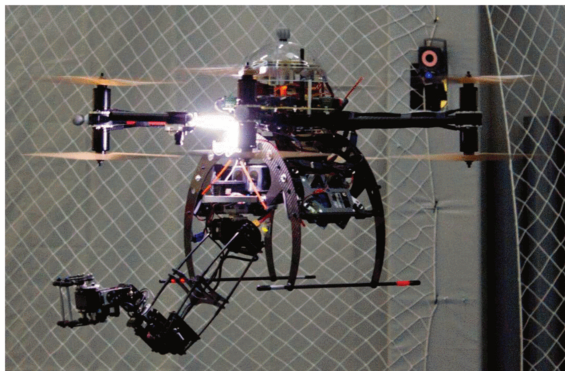
In order to increase the payload, multiple quadrotors can be used cooperatively in aerial manipulation. One useful interaction tool is the use of one or more cables (see Fig. 1.12). A payload is attached to cables that are fixed to the UAVs and cables must be kept in tension during the operation. Researchers have adopted this approach in transporting objects with multiple UAVs, see, e.g. [Michael et al., 2011, Sreenath and Kumar, 2013, Manubens et al., 2013, Lim et al., 2017, Rossi et al., 2019, Sanalidro et al., 2020]. Due to the use of multiple UAVs, these approaches allow the transportation of larger objects compared with a single UAV and allow longer flight time. However, the connection between cables and the object must be done before the manipulation task, thus requiring



(a) [Tognon et al., 2017]



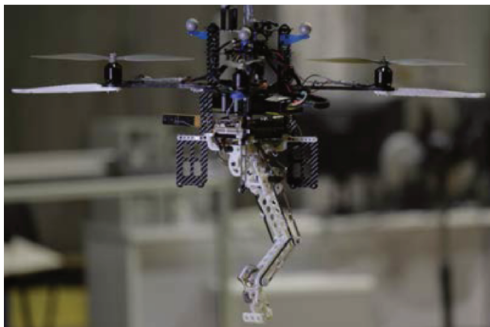
(b) [Heredia et al., 2014]



(c) [Ruggiero et al., 2015]



(d) [Kim et al., 2013]



(e) [Bellicoso et al., 2015]

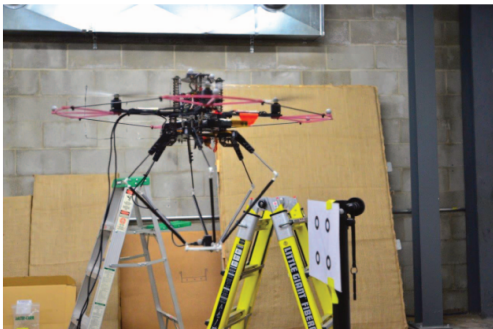


(f) [Garimella and Kobilarov, 2015]

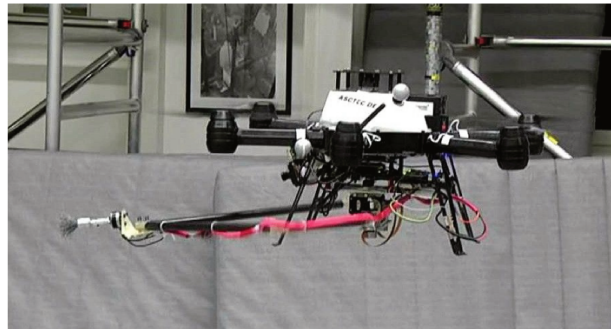
Figure 1.9 – Aerial manipulation robots: quadrotor equipped with a serial manipulator.

the object to be attached manually to the cables and reducing the robot’s autonomy.

Another approach uses multiple UAVs to exert multiple contacts on the object in order to grasp and manipulate it (see Fig. 1.13). In [Gioioso et al., 2014], a team of quadrotors is used to grasp a large object in co-simulations and each quadrotor contributes



(a) [Danko et al., 2015]

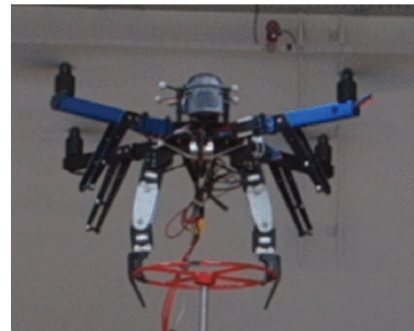


(b) [Kamel et al., 2016]

Figure 1.10 – Aerial manipulation robots: quadrotor equipped with a parallel manipulator.



(a) [Suarez et al., 2017b]



(b) [Korpela et al., 2014]



(c) [Yu et al., 2019]



(d) [Caballero et al., 2018]

Figure 1.11 – Aerial manipulation robots: quadrotor equipped with a dual-arm manipulator.

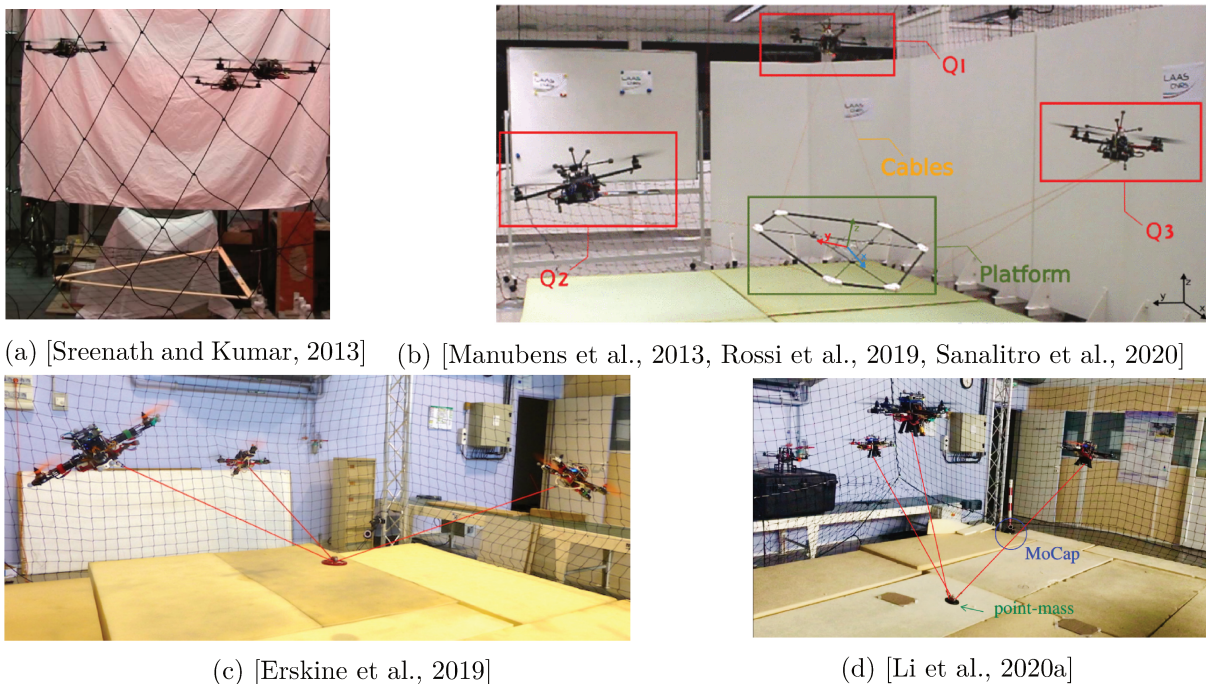
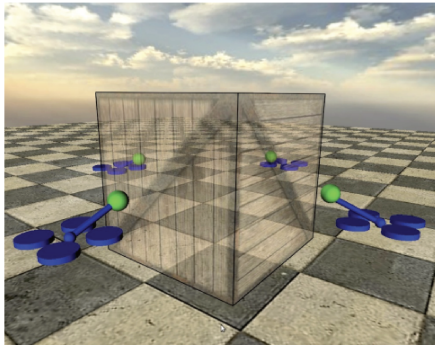


Figure 1.12 – Aerial manipulation robots: multiple quadrotors equipped with cables.

to the grasping task with a single contact point at the tooltip. However this is only validated in co-simulations, the grasp’s security highly relies on friction and could hardly be guaranteed in real conditions. A novel flying platform based on modular robots capable of grasping and transporting objects is proposed in [Saldana et al., 2017]. In [Zhao et al., 2016, Zhao et al., 2017, Zhao et al., 2018], a multi-rotor with two-dimensional multiple links is proposed to perform aerial transporting operations and aerial manipulation. In this approach, The whole robot works as an entire gripper and performs whole-body grasping. However, the stability of the obtained grasp depends on friction which is difficult to estimate in practice and makes the grasp insecure. There are also interesting robots that are composed of multiple quadrotors (see Fig. 1.14). In [Nguyen et al., 2018], authors use multiple quadrotors connected to single platform through spherical joints and the quadrotors are used as rotating thrust generators. Authors in [Six et al., 2017, Six et al., 2018] introduce the concept of parallel flying manipulators, where quadrotors are used as actuators, connected to a platform through rigid articulated passive legs.

To the best of our knowledge, current manipulation robots using a single or multiple quadrotor still have the following drawbacks (see Table 1.1):

1. Grasping capability of aerial manipulation robots mostly depends on their embed-



(a) [Gioioso et al., 2014]

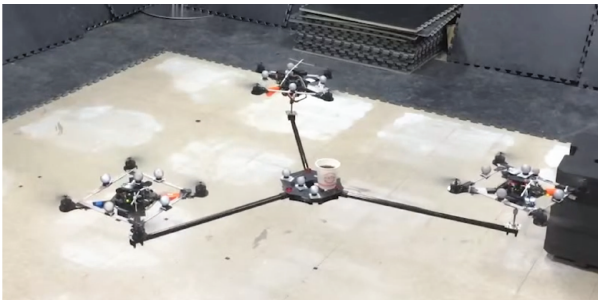


(b) [Gabrich et al., 2018]

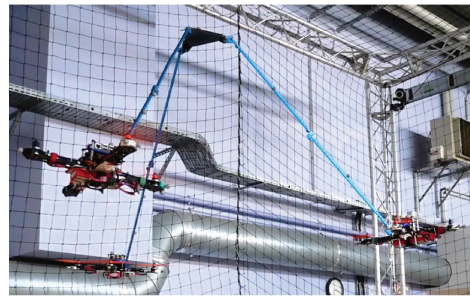


(c) [Zhao et al., 2017]

Figure 1.13 – Aerial manipulation robots: multiple quadrotors, in (a) and (b), and multiple rotors, in (c), exert contacts to grasp and manipulate objects



(a) [Nguyen et al., 2018]



(b) prototype of flying parallel robot at LS2N [Six et al., 2018]

Figure 1.14 – New aerial manipulation robots built with multiple quadrotors.

ded grippers and manipulators. Due to the payload limit, the existing grippers and manipulators can only grasp, manipulate and transport small objects, but have difficulties for large ones.

2. Most multi-quadrotor systems are dedicated to manipulation, not grasping, which reduces the system autonomy. Quadrotors with cables are able to transport and

Table 1.1 – Main characteristics of aerial manipulation robots

reference	prototype	grasp	manipulation	$SE(3)$	large objects
[Mellinger et al., 2011]	quadrotor with a gripper	X	X	X	
[Kessens et al., 2016]	quadrotor with a gripper using a self-sealing suction cup	X	X	X	
[Zhang et al., 2019]	quadrotor with a miniature bistable gripper	X	X	X	
[Thomas et al., 2013]	quadrotor with a gripper for high speed grasping	X	X	X	
[Tognon et al., 2017]	quadrotor with a 2 DOF manipulator	X	X	X	
[Heredia et al., 2014]	AMUSE with a 7 DOF manipulator arm	X	X	X	
[Ruggiero et al., 2015]	ARCAS with a 6 DOF manipulator	X	X	X	
[Kim et al., 2013]	quadrotor with a 2 DOF manipulator	X	X	X	
[Bellicoso et al., 2015]	PUL5AR with a 5 DOF manipulator	X	X	X	
[Garimella and Kobilarov, 2015]	quadrotor with a 2 DOF manipulator	X	X	X	
[Danko et al., 2015]	quadrotor with a 6 DOF parallel manipulator			X	
[Kamel et al., 2016]	quadrotor with a 3 DOF parallel manipulator			X	
[Suarez et al., 2017b]	quadrotor with dual 4 DOF manipulators	X	X	X	
[Korpela et al., 2014]	quadrotor with dual 2 DOF manipulators	X	X	X	
[Yu et al., 2019]	quadrotor with dual 2 DOF manipulators	X	X	X	
[Caballero et al., 2018]	quadrotor with dual 4 DOF manipulators	X	X	X	
[Sreenath and Kumar, 2013]	3 quadrotors with cables		X	X	X
[Manubens et al., 2013, Rossi et al., 2019, Sanalidro et al., 2020]	FlyCrane		X	X	X
[Erskine et al., 2019]	ACTSs		X	X	X
[Li et al., 2020a]	VACTSs		X	X	X
[Gioioso et al., 2014]	Flying hand	X	X	X	
[Gabrich et al., 2018]	Flying Gripper based on cuboid modular robots	X	X	X	
[Zhao et al., 2017]	two-dimensional multilinks	X	X	X	
[Anzai et al., 2018]	HALO	X	X	X	
[Nguyen et al., 2018]	S3Q			X	
[Six et al., 2017, Six et al., 2018]	flying parallel robot			X	

manipulate large objects, but they need manual help to attach the cables to the object and cannot perform grasping operations, which therefore reduces the autonomy of robots. Regarding existing multi-quadrotor robots dedicated to grasping, such as the Flying Hand, they provide a grasp whose quality is subject to friction between the robot and the object, which is insecure in aerial manipulation.

3. In most cases using multiple quadrotors, the yaw motion of each quadrotor does not contribute to the manipulation task, making this DOF useless.

1.2 Background of self-adaptive grippers

As we explained previously, for most aerial manipulators, a UAV merely works as a flying platform, while execution of tasks like grasping and manipulation is performed by mechanical devices attached to the vehicle, such as grippers and manipulators.

Indeed, most of the existing aerial manipulators attach basic parallel-jaw gripper to a single quadrotor or to a platform actuated by multiple quadrotors. However, this type of gripper cannot adapt to the shape of the grasped object, or perform enveloping grasps. Neither can it deal with large objects which require large grippers and dramatically limit the payload. However, it is worthy to notice that some researchers propose new aerial manipulators that are equipped with self-adaptive fingers in [Thomas et al., 2013, Tognon et al., 2017, Pounds et al., 2011].

In this thesis, we develop a concept of flying hand actuated by multiple quadrotors that is called Flying Gripper. This concept was presented in an earlier paper [Saint-Sevin et al., 2019] (see Fig. 1.15). This hand is designed to be self-adaptive in order to

1. grasp a large size object adapting to its shape and size;
2. produce an enveloping and secured grasps.

A guideline is given in [Saint-Sevin et al., 2019] to optimize the geometric parameters of a planar version of Flying Gripper in order to maximize the robot’s manipulability and capability to produce form-closed grasps.

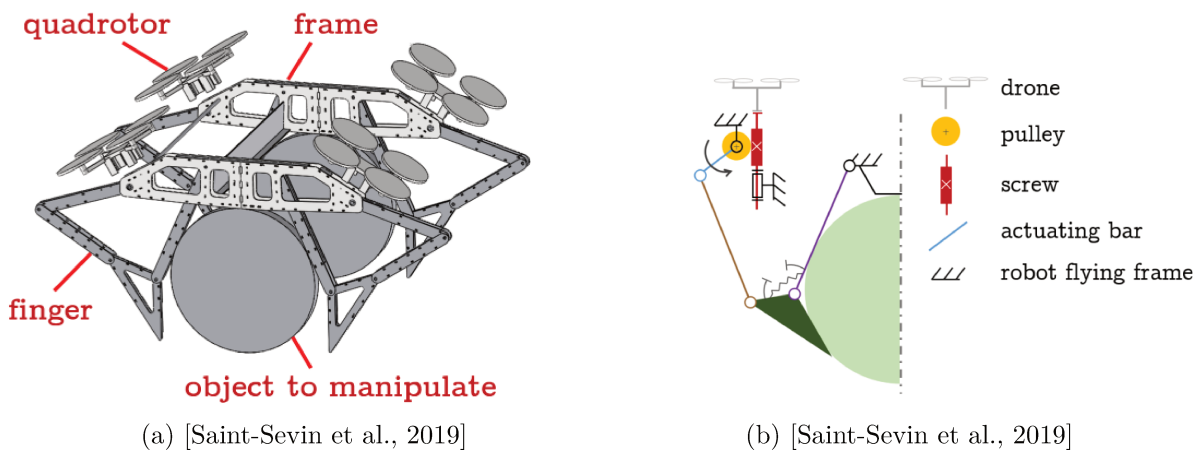


Figure 1.15 – CAD view of Flying Gripper in [Saint-Sevin et al., 2019]

Note that a robot or gripper is said to be underactuated when it has fewer actuators than DOF. However, it should be emphasized that most of underactuated grippers make

use of elastic elements and mechanical stops to constrain the configuration of the hand in a static mode. This makes this type of underactuation different from that of a quadrotor. In order to avoid confusion on the concept of underactuation between quadrotors and grippers, we use the term self-adaptive for an underactuated gripper in this thesis.

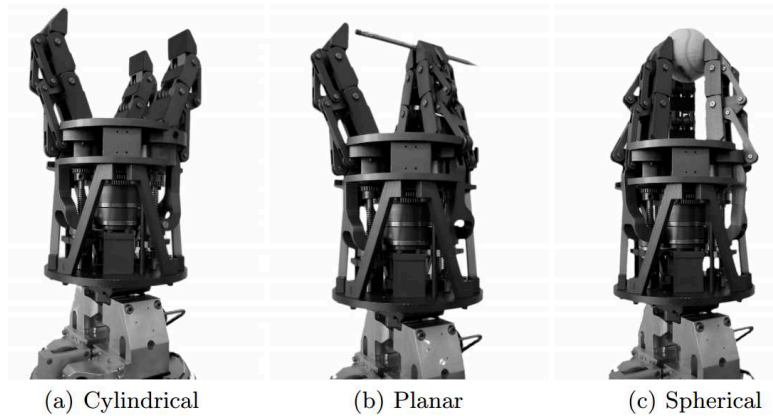
1.2.1 Introduction to self-adaptive grippers

Self-adaptive grippers permit to obtain an enveloping grasp without requiring multiple actuators or sensors. Particularly, self-adaptive grippers are able to deal with positioning uncertainty and size variation of the object to be grasped. Examples of self-adaptive grippers are given in Fig. 1.16. Application of self-adaptation enables grippers to adapt to the geometry of the grasped object [Krut and Begoc, 2011], where this shape adaptation when grasping is due to the mechanical intelligence [Gosselin, 2005] embedded into the design of self-adaptive grippers. Also, it reduces the number of required actuators such that complex control strategies are no longer needed.

Indeed, a large diversity of mechanical devices are able to realize self-adaptation. Self-adaptive grippers can be classified depending on the type of mechanism they use to transmit the input torque to phalanxes [Krut et al., 2010] and more details can be found in [Krut, 2005]:

1. A differential mechanism is a two-DOF mechanism that may distribute a single input into two outputs, such as movable pulleys, seesaw mechanisms, fluidic T-pipes, planetary and bevel gear differentials [Birglen and Gosselin, 2006]. One example gripper using differential mechanisms is the SARAH Hand [Birglen et al., 2008b] (see Fig. 1.16a).
2. A compliant mechanism uses non-rigid, elastic or flexible materials [Deimel and Brock, 2016]. For instance, RBO Hand 2 (see Fig. 1.16b) is a compliant and self-adaptive robotic hand designed for dexterous grasping [Wall et al., 2017];
3. A self-locking mechanism prevents all return motion of the finger phalanxes no matter what disturbances are exerted on the grasped object. Particularly, non-backdrivable or anti-return mechanisms are implemented in the transmission of the fingers' closing motion, because they have a strong impact on the grasp quality. One good example is BarrettHand (see Fig. 1.16c).

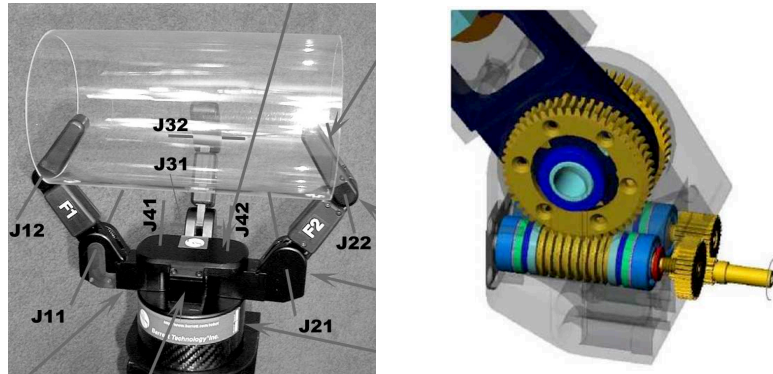
Based on the analysis above, this thesis chooses to focus on differential mechanisms. When associated to non-backdrivable mechanisms, they can perform stable grasps that do



(a) SARAH Hand [Birglen et al., 2008b]



(b) RBO hand 2 [Wall et al., 2017]



(c) BarrettHand gripper [Townsend, 2000]

Figure 1.16 – Self-adaptive grippers with different mechanical devices: Robot hand SARAH using differential mechanism in (a), RBO hand 2 using compliant mechanism in (b), BarrettHand gripper using self-locking mechanism in (c).

not rely on actuator’s capabilities nor on friction [Krut et al., 2010]. As a good example of differential mechanisms, a four-bar mechanism is able to produce grasps adapting to the geometry of the grasped object. The closing sequence shown in Fig. 1.17 illustrates that a four-bar mechanism adapts its shape to the grasped object and finally produces

an enveloping and rigid grasp. Due to these properties, we choose four-bar mechanisms to develop the fingers for Flying Gripper [Saint-Sevin et al., 2019].

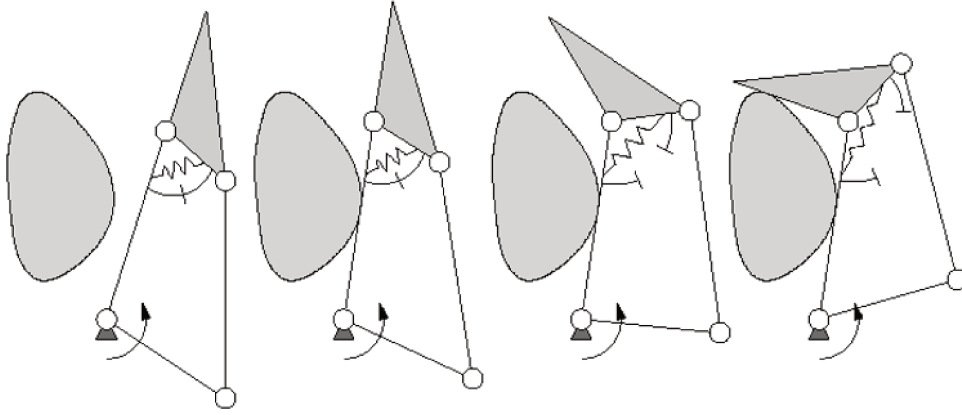


Figure 1.17 – Closing sequence of a four-bar self-adaptive gripper [Birglen and Gosselin, 2004]

1.2.2 Stability of a self-adaptive grasp

When using a self-adaptive gripper, even if it distributes actuation to each phalanx of the gripper, it is not possible to control independently each contact force to obtain a stable grasp. Indeed, the grasp stability of a self-adaptive gripper depends on its mechanical design which should be optimized, otherwise it is possible to produce the so-called "ejection phenomenon" [Birglen and Gosselin, 2004, Birglen et al., 2008c] (one example is shown in Fig. 1.18). Indeed, for a four-bar mechanism, the actuation torque is distributed to both phalanxes of the finger (see Fig 1.17). However, if negative contact forces are required to obtain the static equilibrium of the finger, due to the unilaterality of contact forces, it results in a backward motion of the corresponding phalanx, which is the "ejection phenomenon".

Form-closure and force-closure are two main concepts for studying the static stability of a grasp. Form-closure describes the capability of a hand to prevent any motion of a grasped object, while force-closure describes the ability of a hand to counterbalance any external disturbance exerted on a grasped object [Krut et al., 2010]. The former one depends on the geometric property and the latter one relies on friction, gravity and capacity of actuators. One example of form-closure is illustrated in Fig. 1.19.

Then, the concept of form-closure has been extended to self-adaptive grippers in [Krut et al., 2010]: a self-adaptive grasp is form-closed if and only if for any motion of the grasp,

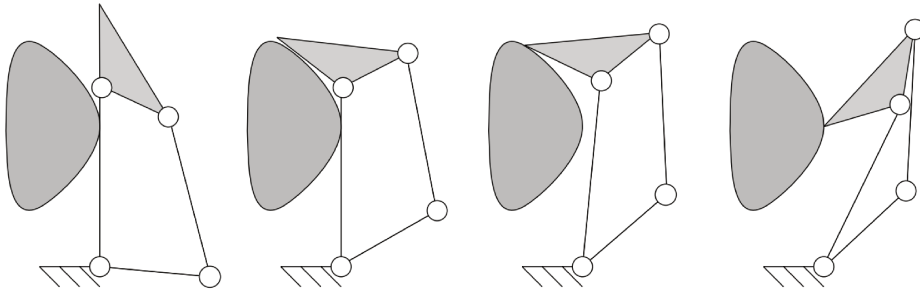


Figure 1.18 – Ejection phenomenon with a four-bar self-adaptive gripper [Birglen et al., 2008a]

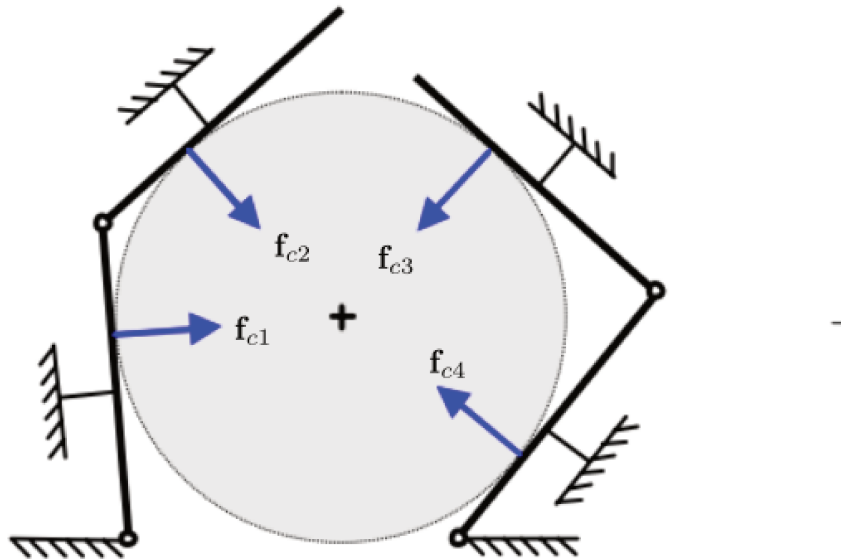


Figure 1.19 – A 1st-order form-closure grasp [Begoc et al., 2006]: f_{ci} , $i = 1, 2, 3, 4$, are contact forces between the gripper and the object.

i.e. motion of the system "object + hand", at least one of the unilateral kinematic constraints (contact constraints and non-backdrivable constraints) is violated. This concept of form-closure is a merely geometrical and qualitative property which does not rely on actuators capability, on friction forces, nor on the magnitude of external disturbances. Because of safety reasons, we decide to choose form-closure as the criterion for our gripper design in [Saint-Sevin et al., 2019]. Achieving form-closure grasps using a self-adaptive gripper requires the introduction of non-backdrivable mechanisms in the transmission of the closing motion of the gripper (see Fig. 1.15b).

Non-backdrivable mechanisms merely allow the transmission from the input to the

output and they are incapable of transmitting motion and power from the output to the input. Examples of non-backdrivable mechanisms are given in Fig. 1.20: a "wheel and worm drive" mechanism (or worm-gear mechanism), a lead screw and nut mechanism and a freewheel mechanism. In this thesis, non-backdrivable worm-gear mechanisms are used to contribute a form-closure capability and more details can be found in [Krut et al., 2010].

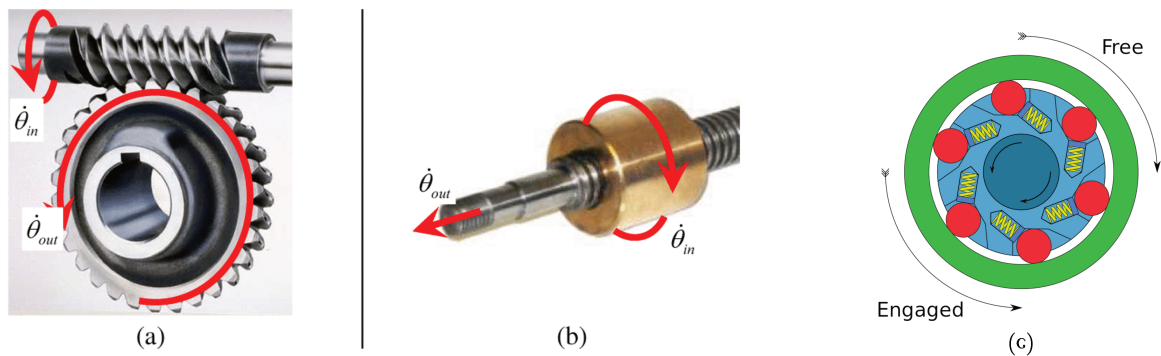


Figure 1.20 – Examples of non-backdrivable mechanisms: (a) "wheel and worm drive"[Krut et al., 2010], (b) lead screw and nut mechanism [Krut et al., 2010], (c) freewheel mechanism [Wikipedia contributors, 2020a].

Indeed, worm-gear mechanisms are used to transmit actuation to the four-bar mechanism fingers for the Flying Gripper robot and those worm-gear mechanisms are chosen to be non-backdrivable to produce form-closure grasps [Saint-Sevin et al., 2019]. Therefore, once an enveloping grasp is performed by the four-bar mechanism fingers, the non-backdrivable worm-gear mechanisms produce a secured grasps preventing the fingers from opening itself.

1.3 Conclusions

This chapter has presented the state of the art of aerial manipulation robots and introduced self-adaptive grippers.

In the first section, we have presented a short review of manipulation from ground robots to manipulation by aerial robots. Different aerial manipulators using a single quadrotor and multiple quadrotors were introduced and analyzed. The analysis showed that existing current aerial manipulation robots mainly use quadrotors as simple flying platforms and manipulation is performed by embedded grippers and manipulators. However, those grippers and manipulators reduce the payload and cannot deal with large size

objects. This leads to the motivation of this thesis: develop the concept Flying Gripper that is able to grasp, manipulate and transport large size objects.

It was shown that most of the existing aerial manipulators use basic parallel-jaw grippers and this type of gripper cannot adapt to the shape of the grasped object to perform enveloping grasps nor to deal with positioning uncertainty of the object to grasp. Thus, in the second section, we introduced the concept of underactuated grippers or self-adaptive grippers that is one key component of Flying Gripper. Among different self-adaptive grippers, four-bar mechanisms that are able to adapt to the shape and size of the grasped object were used in the concept for Flying Gripper. It was shown that such grippers are able to produce form-closure grasps if non-backdrivable mechanism are used to transmit closing motion. Finally, it showed that thanks to self-adaptive grippers and non-backdrivable mechanisms, the Flying Gripper robot is able to produce an enveloping and secured grasp.

STATIC AND DYNAMIC MODELING OF FLYING GRIPPER

2.1	Flying Gripper: a novel concept of aerial manipulator	46
2.2	Static modeling of Flying Gripper	53
2.3	Dynamic modeling of Flying Gripper	61
2.4	Conclusions	72

This chapter presents a new concept of aerial manipulation robot named "Flying Gripper". This robot is an aerial manipulator that is intended to perform grasping, manipulating and transporting of large objects autonomously in $SE(3)$. The robot Flying Gripper is composed of four quadrotors, four self-adaptive fingers and a body structure. Each finger has two phalanges and is self-adaptive so that it can produce an enveloping grasps adapting to the size and shape of the object and deal with positioning uncertainty. The closing/opening motion of each finger is actuated by one quadrotor's yaw rotation. This rotation is transmitted through a non-backdrivable mechanism so that the finger cannot move back once it is in contact with the object, in order to produce a safe grasp.

Section 2.1 mainly introduces the architecture of the novel aerial manipulation robot concept. It presents two different architectures of Flying Gripper: one with Fixed-Attitude Quadrotors (FG-FAQ), and one with Mobile-Attitude Quadrotors (FG-MAQ). This is followed by the presentation of the working principles permitting the robot to grasp and manipulate a large size object. Section 2.2 proposes a general form for developing the static model for both robots. Section 2.3 is devoted to developing the dynamic models for the two different robot concepts respectively.

2.1 Flying Gripper: a novel concept of aerial manipulator

The concept of the Flying Gripper (FG) robot comes from the practical limitations of aerial manipulation robots actuated by a single UAV or multiple UAVs that cannot perform grasping, manipulating and transporting large size objects autonomously.

Compared to existing aerial manipulation robots, the main advantages of our robot are:

1. The robot is a 6 DOF aerial manipulator and it achieves full manipulability in $SE(3)$. In theory, the robot is able to manipulate objects with 3 DOF in translation and 3 DOF in rotation, however its roll and pitch rotations are limited due to the design.
2. Compared to existing solutions, our robot, thanks to the use of self-adaptive fingers, can adapt to the shape and size of a large object and is robust to uncertainty in the positioning of the robot w.r.t the object.
3. Worm-gear mechanisms are introduced in the transmission of opening/closing motion of the fingers in order to perform a secured grasp.
4. As far as we know about aerial manipulation robots, only few robots take advantages the yaw motion of a quadrotor to contribute to manipulation tasks, see [Korpela et al., 2014, Car et al., 2018]. In most cases using multiple quadrotors, the yaw motion of each quadrotor does not contribute to the manipulation task, making this DOF useless. In our robot, the quadrotors' yaw rotations are used to open or close the fingers during grasping: no additional actuators nor sensors are needed to drive the fingers.

In the following, we present the architectures of two versions of the Flying Gripper, one with Fixed-Attitude Quadrotors (FG-FAQ) and one with Mobile-Attitude Quadrotors (FG-MAQ).

2.1.1 Description of the architecture of Flying Gripper with Fixed-Attitude Quadrotors (FG-FAQ)

Here, we describe a first version of Flying Gripper that is composed of a body structure, four self-adaptive fingers and four fixed-attitude quadrotors. We name this robot Flying

Gripper with Fixed-Attitude Quadrotors (FG-FAQ). Its CAD view is given in Fig. 2.1. The four quadrotors are linked to the body structure such that the robot is able to exert forces and torques in any direction independently. Each finger is actuated by the yaw torque of the corresponding quadrotor through a worm-gear mechanism. It has two phalanges in order to produce an enveloping grasp of the object. A differential four-bar mechanism permits to share the input yaw torque to both phalanges so that the finger can adapt its configuration to the size and shape of the object. It also permits to deal with positioning uncertainty in the position of the object w.r.t the robot.

All quadrotors are linked to the body structure with a tilting angle w.r.t the vertical (see Fig. 2.1a), such that the robot can exert forces and torques on the body structure in any direction: it allows full manipulability of the grasped object in $SE(3)$. Each quadrotor is attached to a worm screw of the body structure through a passive revolute joint (R-joint) (see Fig. 2.1c) to authorize the yaw rotation of each quadrotor w.r.t the body structure. This yaw motion is transmitted to the finger through a worm-gear mechanism (see Fig. 2.1c). Usually, in most applications, the four propellers of a quadrotor are driven in order to cancel the resultant yaw torque and keep yaw rotation fixed. To the best of our knowledge, this is a first attempt to use the yaw rotations of multiple quadrotors to contribute to a task.

Indeed, a worm screw is attached to each quadrotor and a gear is attached to an actuation bar (see Fig. 2.1b), such that a rotation of the quadrotor about its yaw axis is transmitted to an actuation bar making the finger open or close. Worm screws of quadrotors 1 and 3 and those of quadrotors 2 and 4 are chosen with opposite hand (left and right) such that the resultant quadrotors yaw torques acting on the body structure can be canceled while fingers open or close all together.

The grasping sequence of self-adaptive fingers is illustrated in Fig. 2.2. Bar (1) is the actuation bar of a four-bar mechanism that is used to introduce self-adaptation between both phalanxes of each finger. In their open configuration (see Fig. 2.2(a)), fingers behave as rigid bodies thanks to a spring and a mechanical stop between the proximal (3) and the distal (4) phalanxes. The yaw torque of each quadrotor is transmitted to the actuation bar (1) through a worm-gear mechanism. When the proximal phalanx (3) contacts the object in Fig. 2.2(b), each quadrotor keeps turning so that the distal phalanx (4) rotates with respect to the proximal one, until it produces an enveloping grasp in Fig. 2.2(c). When grasping, self-adaptive fingers automatically adapt their configuration to the geometry of the grasped object. It is worthy to mention that this adaption does not require a large

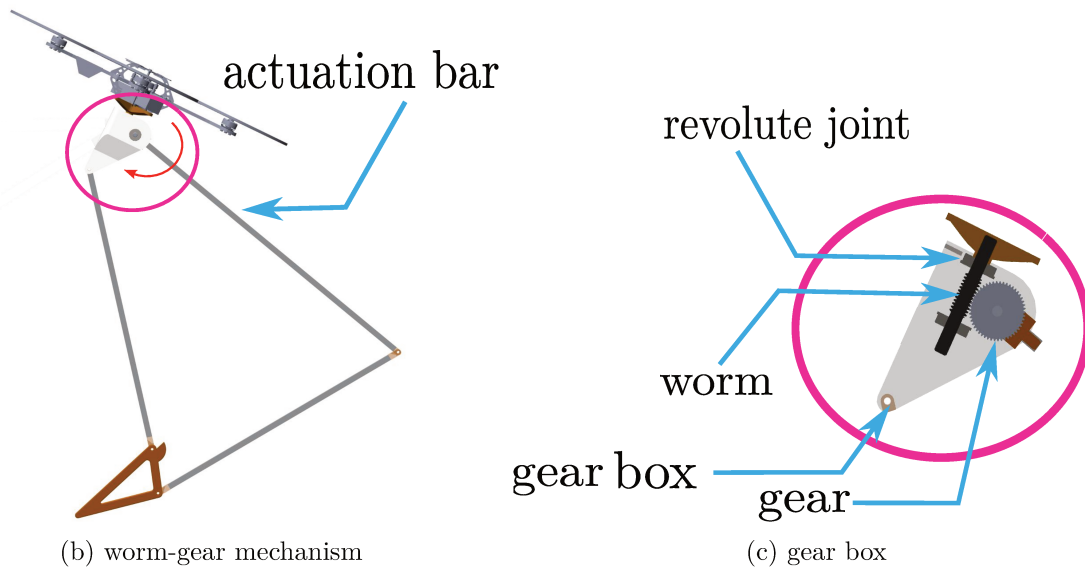
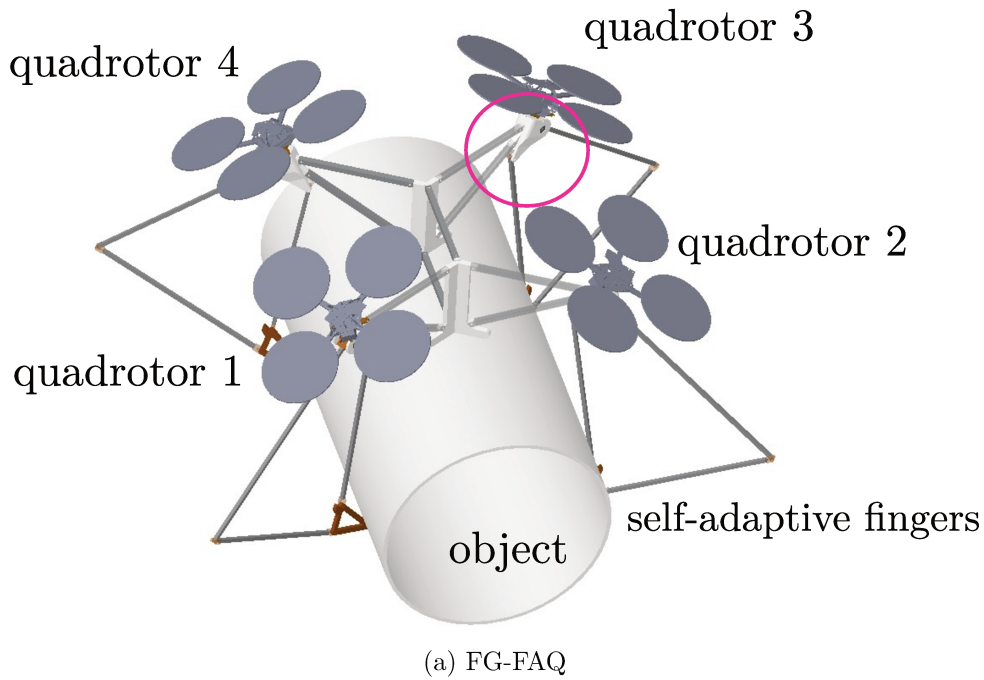


Figure 2.1 – (a) CAD view of Flying Gripper with Fixed-Attitude Quadrotors (FG-FAQ) that is composed of a body structure, four self-adaptive fingers and four quadrotors. (b) Each quadrotor is linked to a worm screw and this worm screw is linked to the body structure through a passive revolute joint, which allows each quadrotor’s yaw rotation w.r.t the body structure. (c) The quadrotor’s yaw rotation is transmitted through a worm-gear mechanism to the finger’s actuation bar in order to drive the opening/closing motion of the finger. The gear box is rigidly attached to the body structure.

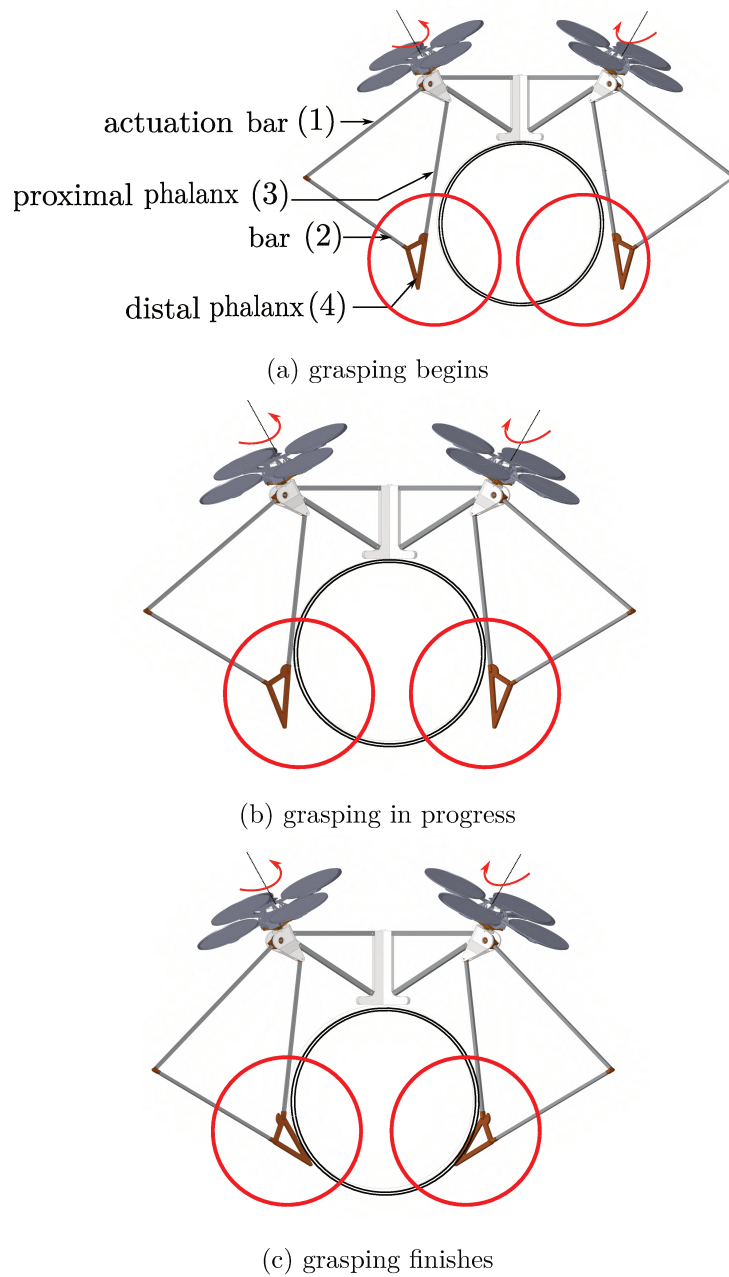


Figure 2.2 – Grasping sequence of FG-FAQ robot: (a) when grasping begins, the quadrotors produce yaw rotations to close fingers; (b) then the proximal phalanxes (3) come in contact with the object, the quadrotors keep turning until distal phalanxes come in contact too; (c) once the object is grasped, the fingers are kept closed and cannot move backwards until the quadrotors rotate in opposite directions.

number of sensors or actuators, nor a complex control strategy.

Worm-gears introduced in the transmission of the opening/closing motion of fingers are

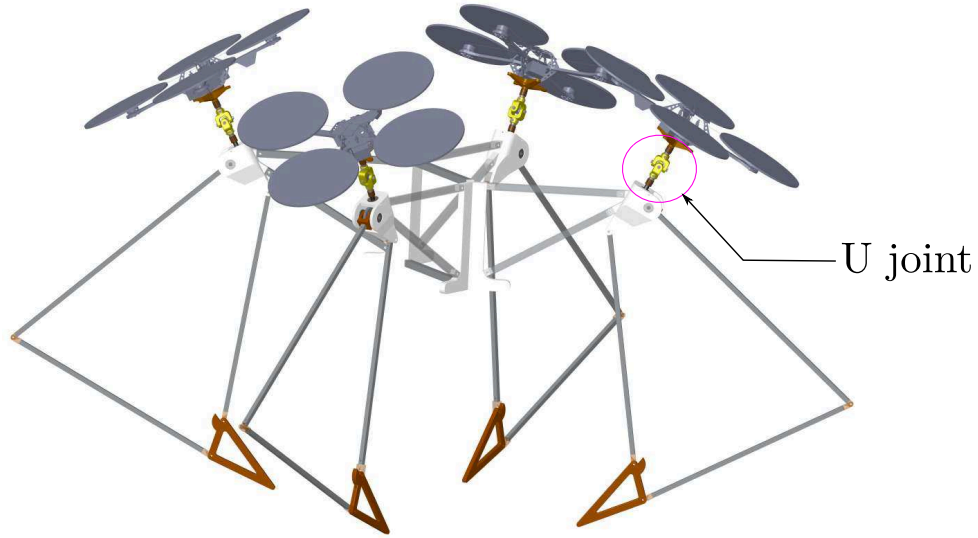
chosen to be non-backdrivable in order to produce form-closed grasps [Krut et al., 2010]. This type of grasp stability criteria is particularly interesting in the case of an aerial manipulation robot. Indeed, this criteria relies on a purely geometric analysis of the grasp and thus does not rely on the capability of actuators neither on friction. Basically, once all phalanxes contact the object, the non-backdrivable worm-gear mechanisms prevent fingers from opening itself. To open the fingers, it is necessary to rotate quadrotors in the reverse direction. The lengths of phalanxes and the lengths of bars of the four-bar mechanism are derived from the optimization proposed in [Saint-Sevin et al., 2019] in order to maximize the capability of the gripper to produce form-closed grasps despite positioning uncertainty.

The robot has four different operating modes:

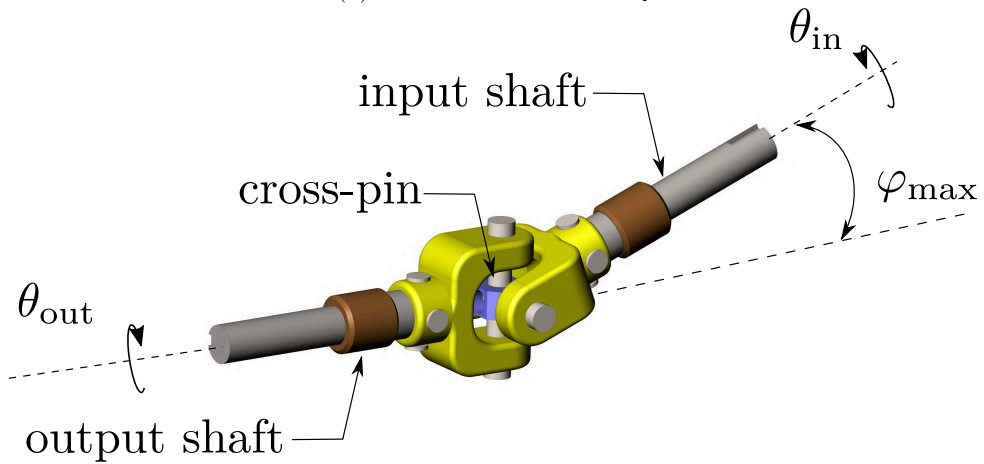
1. Free flight: fingers are open and the robot flies without any object. The yaw rotation of each quadrotor should be kept fixed during this mode.
2. Grasping: the robot is above the object and maintains its position and orientation compensating its own gravity. All quadrotors rotate along their yaw axis in order to close fingers until the object is grasped and all phalanxes are in contact with the object.
3. Manipulation: the robot flies and manipulates the object as specified by the task. The yaw rotation of each quadrotor will be kept fixed during this mode in order to keep the object inside the fingers.
4. Placing: once arrived at its final destination, the robot opens its fingers using yaw motion of each quadrotor while maintaining its position and orientation.

2.1.2 Description of the architecture of Flying Gripper with Mobile-Attitude Quadrotors (FG-MAQ)

Here, we present a modified version of Flying Gripper robot that uses universal joints (U-joints) to link each quadrotor with the corresponding worm screw (see Fig. 2.3). Each U-joint allows two supplementary DOF (roll and pitch rotations) to each quadrotor w.r.t the body structure. Introducing a U-joint between the quadrotor and the worm screw allows the quadrotor to modify its attitude w.r.t the body structure while transmitting its yaw rotation to the worm screw to open/close the finger even if axes are not coincident. This new design is in the sequel Flying Gripper with Mobile-Attitude Quadrotors (FG-MAQ).



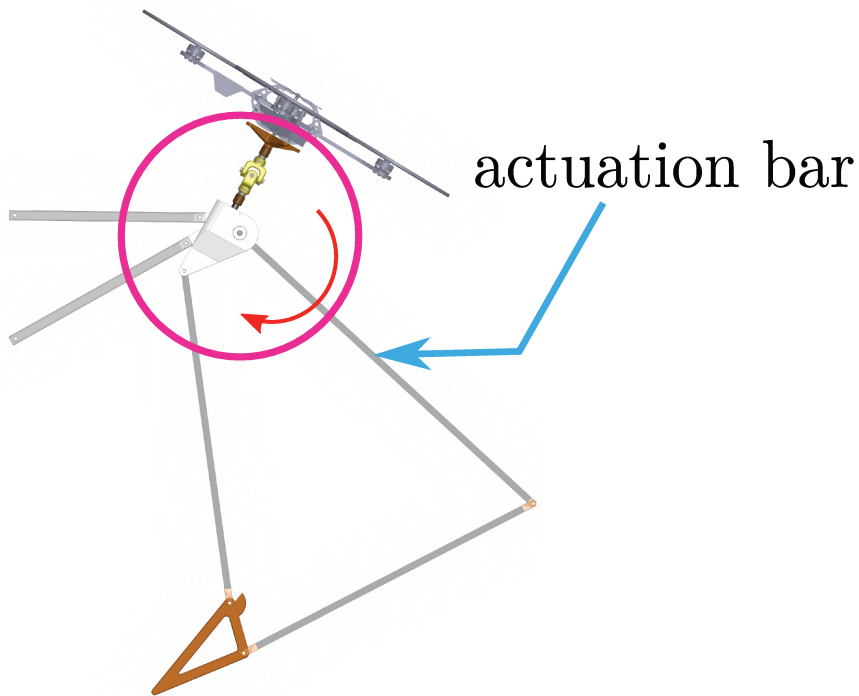
(a) CAD view of FG-MAQ



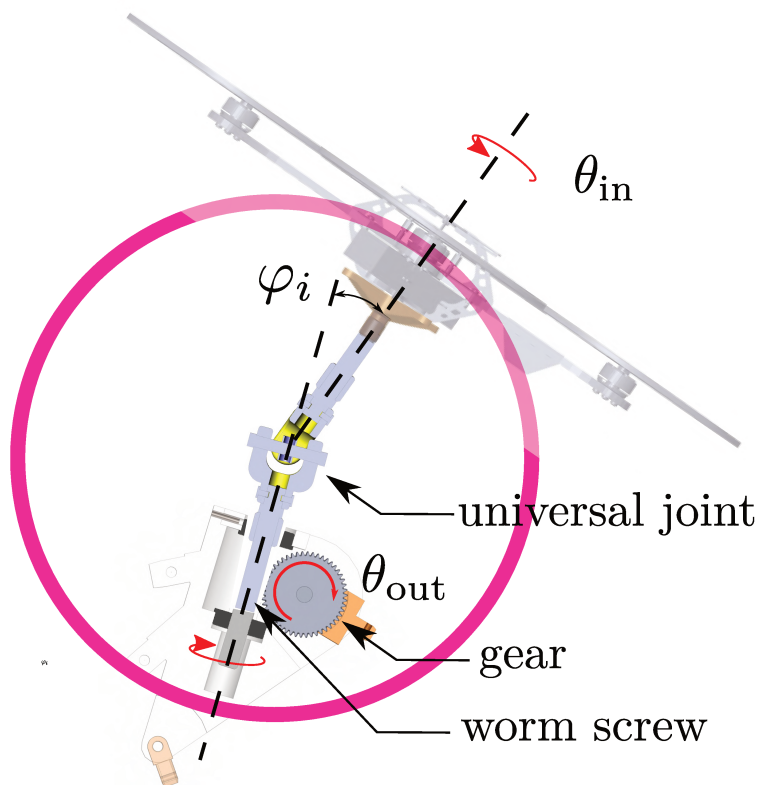
(b) U-joint with the maximal shaft alignment angle φ_{\max}

Figure 2.3 – CAD view of Flying Gripper with Mobile-Attitude Quadrotors (FG-MAQ) that is composed of a body structure, four self-adaptive fingers and four quadrotors. Each quadrotor is linked to a worm screw through a U-joint.

A U-joint connects two non-parallel rotating shafts allowing the transmission of torque and rotary motion from one shaft to another at fixed or varying angles of intersection (see Fig. 2.3b). It transmits the rotation θ_{in} of the input shaft (linked to a quadrotor) to the rotation θ_{out} of the output shaft (linked to a worm screw) for driving the actuation bar (see Fig. 2.4). For the FG-MAQ architecture, the rotation of the worm screw w.r.t the body structure is achieved through the use of ball bearings.



(a) actuation bar driven by quadrotor's yaw rotation



(b) worm screw is linked to U-joint and worm gear is linked to actuation bar

Figure 2.4 – U-joint of FG-MAQ robot links a quadrotor to a worm screw and a worm gear is linked to an actuation bar. The quadrotor's yaw rotation is transmitted to the worm screw in order to drive the actuation bar.

Compared to the architecture FG-FAQ initially presented in the previous section, the FG-MAQ robot using U-joints enables each quadrotor to adapt its attitude w.r.t the robot's body. The quadrotors' attitudes can be modified according to the task. For instance, while grasping, quadrotors can be maintained tilted to achieve full manipulability and, thus, be able to compensate external perturbations to achieve precise positioning of the robot (see Fig. 2.5a). While taking off, quadrotors can be kept horizontal in order to reduce energy consumption, since, in this configuration, the resultant thrust force of each quadrotor is vertical and completely contributes to gravity compensation (see Fig. 2.5b). It should be noticed that each quadrotor's rotation is constrained by the mechanical stop of U-joint. Indeed, a maximal angle φ_{\max} between the input axis and output axis must not be overpassed (see Fig. 2.3b).

On a control point of view, the control input of the FG-FAQ robot is chosen to be the motor speed of all quadrotors, which is used in the controller design in chapter 4. However, for the FG-MAQ robot, thanks to the 2 supplementary DOF of each quadrotor, it is possible to control the attitude and the resultant absolute thrust force of each quadrotor. The transformation between the attitude and the thrust force and the motor speed is achieved by autopilots, such as Pixhawk¹. This approach is used in experiments and the results are presented in chapter 5.

2.2 Static modeling of Flying Gripper

As an aerial manipulation robot, our robot can generate wrenches in order to manipulate a grasped object. A general formulation of the static model is proposed for the robot in order to study how the wrench applied to the body structure is produced.

Parameterization

As the first step of the static modeling, we will denote the frames by the following notations in Fig. 2.6. The term \mathcal{F}_0 stands for the world frame with its origin O_0 and axes $\mathbf{x}_0, \mathbf{y}_0, \mathbf{z}_0$. The frame \mathcal{F}_b is a coordinate system with origin O_b attached at CoM of the body structure and axes $\mathbf{x}_b, \mathbf{y}_b, \mathbf{z}_b$. For each quadrotor, \mathcal{F}_i is a coordinate system attached to the i^{th} quadrotor with its origin O_i at the CoM and axes $\mathbf{x}_i, \mathbf{y}_i, \mathbf{z}_i$ (the axis \mathbf{z}_i represents the local frame thrust direction of the quadrotor).

1. <https://pixhawk.org/>

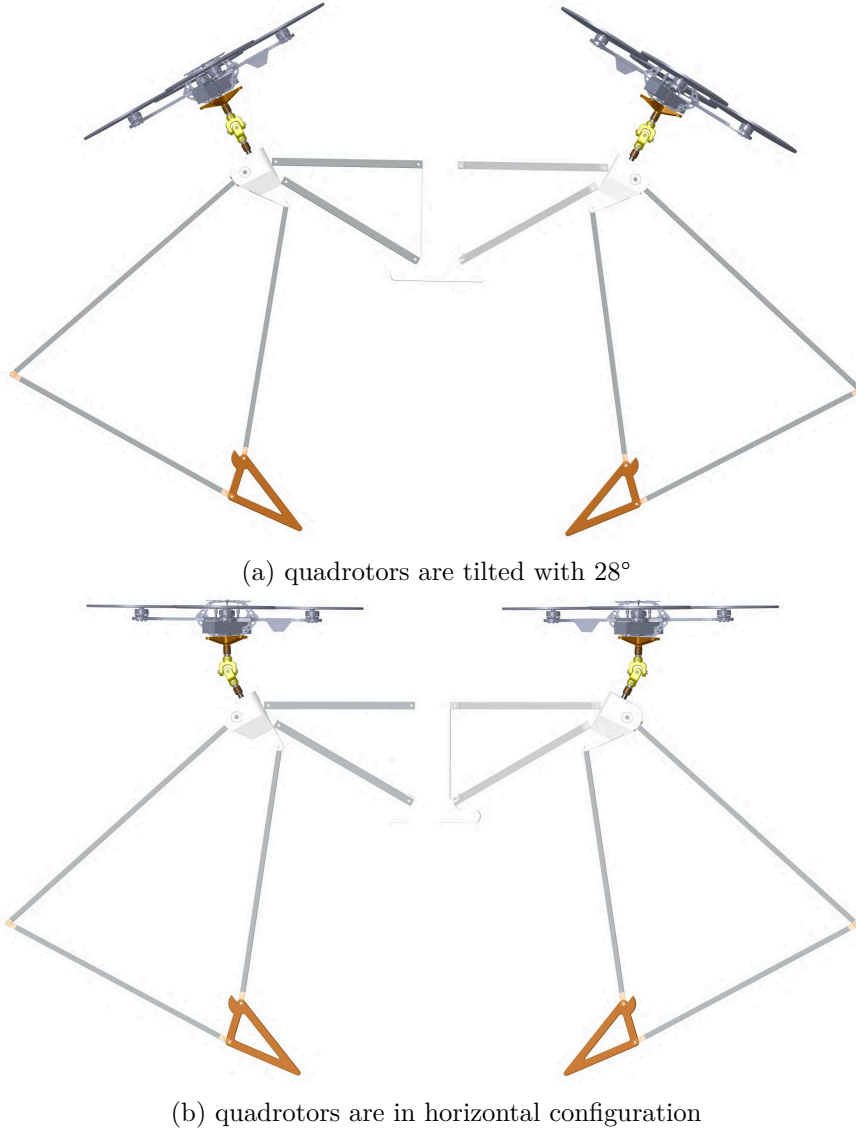


Figure 2.5 – Two different configurations of FG-MAQ: one with quadrotors tilted with 28° and the other one with quadrotors kept horizontal

Figure 2.7 shows the main geometrical parameters of the robot: the length L_x , the width L_y and the height L_z of the robot. Those three parameters decide the dimension of the robot. Let us give the attitude of quadrotor i w.r.t the body structure by the rotation matrix ${}^b\mathbf{R}_i \in \mathbb{R}^{3 \times 3}$ which can be determined by an Euler angle vector $[{}^b\phi_i \quad {}^b\theta_i \quad {}^b\psi_i]$ (with XYZ sequence) such that

$${}^b\mathbf{R}_i = \mathbf{R}_x({}^b\phi_i)\mathbf{R}_y({}^b\theta_i)\mathbf{R}_z({}^b\psi_i). \quad (2.1)$$

Table 2.1 – Main symbols used in the static modeling

Symbol	Definition
${}^b\mathbf{r}_i$	Position vector of the i^{th} quadrotor's centroid (origin of \mathcal{F}_i) in \mathcal{F}_b
m_b	Mass of the body structure
m_i	Mass of the i^{th} quadrotor
m_t	Total mass of the robot
${}^b\mathbf{R}_i$	Rotation matrix of \mathcal{F}_i w.r.t \mathcal{F}_b
${}^0\mathbf{R}_i$	Rotation matrix of \mathcal{F}_i w.r.t \mathcal{F}_0
${}^i\mathbf{f}_i$	Thrust force vector produced by the i^{th} quadrotor expressed in \mathcal{F}_i
${}^i\boldsymbol{\tau}_i$	Torque vector produced by the i^{th} quadrotor expressed in \mathcal{F}_i
${}^b\mathbf{f}_{ext}$ (${}^0\mathbf{f}_{ext}$)	External force vector acting on the robot body applied by the environment expressed in \mathcal{F}_b (\mathcal{F}_0)
${}^b\boldsymbol{\tau}_{ext}$	External torque vector acting on the robot body applied by the environment expressed in \mathcal{F}_b
${}^i\mathbf{w}_i$	Wrench vector generated by i^{th} quadrotor expressed in \mathcal{F}_i
$\boldsymbol{\Omega}_i$	Vector of motor speeds square of the i^{th} quadrotor
$[\mathbf{x}]_{\times}$	Skew-symmetric matrix of vector \mathbf{x}

For the FG-FAQ architecture, each quadrotor has only one DOF: its yaw rotation around z_i because of the revolute joint between the worm screw and the body structure. Thus, among the three angles ${}^b\phi_i, {}^b\theta_i, {}^b\psi_i$, the terms ${}^b\phi_i, {}^b\theta_i$ are two constant parameters, while ${}^b\psi_i$ is a variable used to open or close the finger. Roll and pitch orientations of the quadrotors w.r.t the body structure are defined in a symmetric way:

- ${}^b\mathbf{R}_1 = \mathbf{R}_x(\alpha) \cdot \mathbf{R}_y(\beta) \cdot \mathbf{R}_z({}^b\psi_1)$,
- ${}^b\mathbf{R}_2 = \mathbf{R}_x(-\alpha) \cdot \mathbf{R}_y(\beta) \cdot \mathbf{R}_z({}^b\psi_2)$,
- ${}^b\mathbf{R}_3 = \mathbf{R}_x(-\alpha) \cdot \mathbf{R}_y(-\beta) \cdot \mathbf{R}_z({}^b\psi_3)$,
- ${}^b\mathbf{R}_4 = \mathbf{R}_x(\alpha) \cdot \mathbf{R}_y(-\beta) \cdot \mathbf{R}_z({}^b\psi_4)$.

Parameters α and β are two supplementary design parameters of the FG-FAQ architecture. However, for the FG-MAQ robot, α and β do not determine the attitudes of the quadrotors because of the U-joints, but they determine attitudes of the worm screws w.r.t body structure and thus the range of rotation of each quadrotor.

Then, we define the generalized coordinates that fully describe configurations for the two designs FG-FAQ and FG-MAQ respectively $\mathbf{q}^f = [\mathbf{p}_b^T \quad \mathbf{q}_a^{fT}]^T \in \mathbb{R}^{10 \times 1}$ for FG-FAQ and $\mathbf{q}^m = [\mathbf{p}_b^T \quad \mathbf{q}_a^{mT}]^T \in \mathbb{R}^{18 \times 1}$ for FG-MAQ:

- $\mathbf{p}_b = [{}^0\mathbf{x}_b^T \quad \boldsymbol{\eta}_b^T]^T \in \mathbb{R}^{6 \times 1}$ describes the pose of the body structure. The position vector is ${}^0\mathbf{x}_b = [x_b \quad y_b \quad z_b]^T \in \mathbb{R}^{3 \times 1}$ expressed in the world frame \mathcal{F}_0 and $\boldsymbol{\eta}_b = [\phi_b \quad \theta_b \quad \psi_b]^T \in \mathbb{R}^{3 \times 1}$ is the vector of Euler angles (with ZYX sequence) of the body structure frame \mathcal{F}_b w.r.t the world frame \mathcal{F}_0 ;
- $\mathbf{q}_a^f = [{}^b\psi_1 \quad {}^b\psi_2 \quad {}^b\psi_3 \quad {}^b\psi_4] \in \mathbb{R}^{4 \times 1}$ is the vector of quadrotors' yaw angles defined for FG-FAQ;

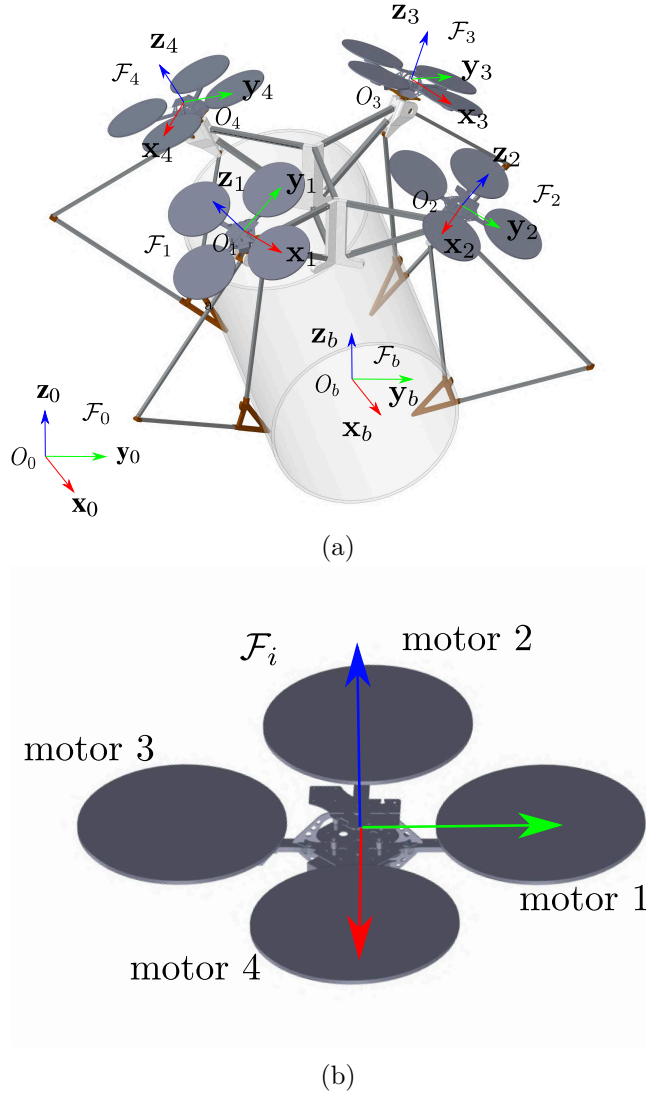
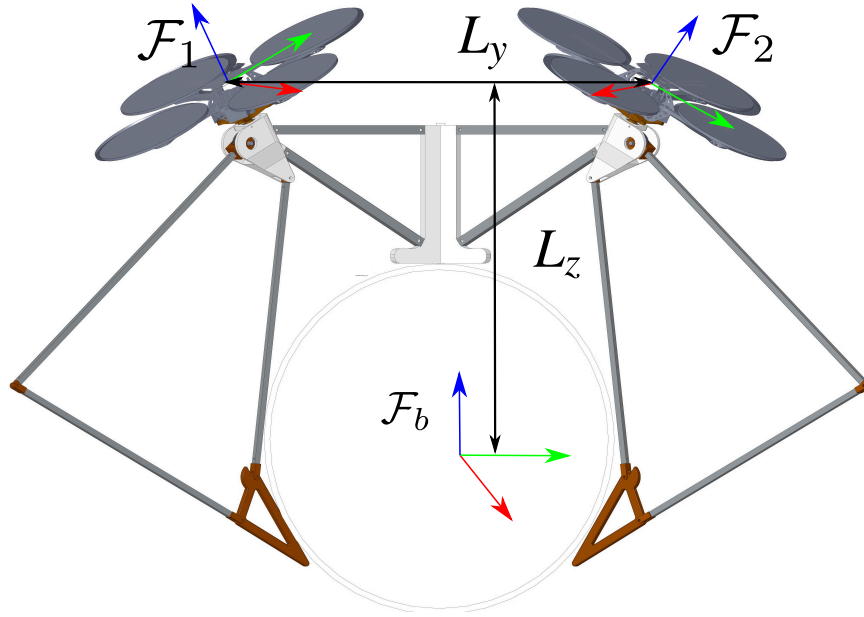


Figure 2.6 – Representation of FG-FAQ robot and its main coordinates: (a) world frame \mathcal{F}_0 , body frame \mathcal{F}_b ; (b) quadrotor's local frame \mathcal{F}_i ($i = 1, \dots, 4$).

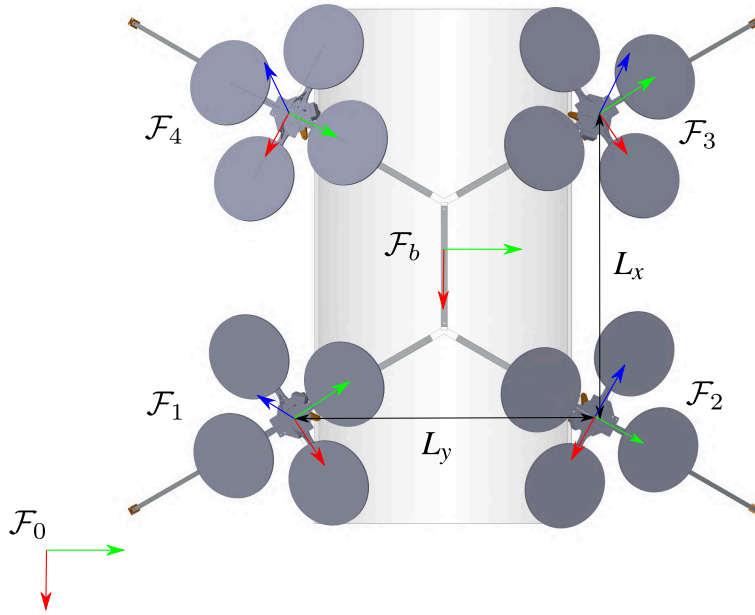
— $\mathbf{q}_a^m = [\boldsymbol{\eta}_1^T \quad \boldsymbol{\eta}_2^T \quad \boldsymbol{\eta}_3^T \quad \boldsymbol{\eta}_4^T]^T \in \mathbb{R}^{12 \times 1}$ is defined for FG-FAQ, where $\boldsymbol{\eta}_i = [\phi_i \quad \theta_i \quad \psi_i]^T \in \mathbb{R}^{3 \times 1}$ is the vector of Euler angles (with ZYX sequence) representing the attitude of frame \mathcal{F}_i w.r.t the world frame \mathcal{F}_0 .

Static modeling - a general formulation

The four quadrotors generate wrenches to drive the robot and manipulate objects. The resultant wrench applied to the body structure decides the robot's manipulability. In this thesis, we call this resultant wrench applied to the body structure as the "body



(a) front view of the robot



(b) top view of the robot

Figure 2.7 – Parameters presentation of FG-FAQ robot: L_x, L_y, L_z are the length, width and height of the robot.

wrench". In the following, we build the static model of the robot studying the relation between the wrenches produced by quadrotors ${}^i\mathbf{w}_i$ in \mathcal{F}_i and the body wrench ${}^b\mathbf{w}_b$ in \mathcal{F}_b .

First of all, each quadrotor produces a thrust force vector ${}^i\mathbf{f}_i \in \mathbb{R}^{3 \times 1}$ and a torque vector ${}^i\boldsymbol{\tau}_i \in \mathbb{R}^{3 \times 1}$ expressed in the local frame \mathcal{F}_i .

Applying the Newton's first law on the body structure, the total net force must be zero at static equilibrium. This is modeled in the body frame \mathcal{F}_b that

$$\sum_{i=1}^4 {}^b\mathbf{R}_i {}^i\mathbf{f}_i + {}^b\mathbf{f}_{ext} - {}^b\mathbf{R}_0 m_t \mathbf{g} = \mathbf{0} \quad (2.2)$$

where ${}^b\mathbf{f}_{ext} \in \mathbb{R}^{3 \times 1}$ is the external force exerted on the body structure expressed in \mathcal{F}_b . The terms $m_t = m_b + \sum_{i=1}^4 m_i$ is the mass of the whole robot as m_b and m_i are the mass of the body structure and the i^{th} quadrotor, and \mathbf{g} is a vector representing the gravity acceleration.

The total net torque must also be zero in the body frame \mathcal{F}_b to satisfy static conditions:

$$\sum_{i=1}^4 \left([{}^b\mathbf{r}_i]_{\times} {}^b\mathbf{R}_i {}^i\mathbf{f}_i + {}^b\mathbf{R}_i {}^i\boldsymbol{\tau}_i \right) + {}^b\boldsymbol{\tau}_{ext} = \mathbf{0} \quad (2.3)$$

where ${}^b\mathbf{r}_i \in \mathbb{R}^{3 \times 1}$ is the coordinate vector of O_i expressed in \mathcal{F}_b , $[{}^b\mathbf{r}_i]_{\times} \in \mathbb{R}^{3 \times 3}$ is the skew-symmetric matrix representing the cross product with ${}^b\mathbf{r}_i$ under a matrix form, and ${}^b\boldsymbol{\tau}_{ext} \in \mathbb{R}^{3 \times 1}$ stands for the external torque vector exerted on the body structure expressed in \mathcal{F}_b .

Thus, we can write the static model of the FG robot expressed in \mathcal{F}_b in a compact form

$$\begin{cases} \sum_{i=1}^4 {}^b\mathbf{R}_i {}^i\mathbf{f}_i + {}^b\mathbf{f}_{ext} - {}^b\mathbf{R}_0 m_t \mathbf{g} = \mathbf{0} \\ \sum_{i=1}^4 \left([{}^b\mathbf{r}_i]_{\times} {}^b\mathbf{R}_i {}^i\mathbf{f}_i + {}^b\mathbf{R}_i {}^i\boldsymbol{\tau}_i \right) + {}^b\boldsymbol{\tau}_{ext} = \mathbf{0} \end{cases} \quad (2.4)$$

In order to obtain a more general form for the static model expressed in Eq.(2.4), we use the term ${}^b\mathbf{w}_{ext} = [{}^b\mathbf{f}_{ext}^T \quad {}^b\boldsymbol{\tau}_{ext}^T]^T \in \mathbb{R}^{6 \times 1}$ to represent the external wrench applied on the body structure. As a consequence, the static model of the robot in Eq. (2.4) can be written in a new form as

$${}^b\mathbf{w}_{ext} + \sum_{i=1}^4 {}^b\mathbf{W}_i {}^i\mathbf{w}_i - \begin{bmatrix} {}^b\mathbf{R}_0 m_t \mathbf{g} \\ 0 \end{bmatrix} = \mathbf{0}, \quad (2.5)$$

reduced wrench ${}^i\mathbf{w}_i^r = [f_{i,z} \quad {}^i\boldsymbol{\tau}_i^T]^T \in \mathbb{R}^{4 \times 1}$, which is modeled by the equation

$${}^i\mathbf{w}_i^r = \boldsymbol{\Gamma}_i \boldsymbol{\Omega}_i. \quad (2.9)$$

2. Quadrotor i can only generate a thrust force along \mathbf{z}_i axis in local frame \mathcal{F}_i which leads to

$${}^i\mathbf{f}_i = [0 \quad 0 \quad f_{i,z}]^T. \quad (2.10)$$

In Eq.(2.9), $\boldsymbol{\Gamma}_i$ and $\boldsymbol{\Omega}_i$ are defined as

- $\boldsymbol{\Gamma}_i \in \mathbb{R}^{4 \times 4}$ is an invertible and constant matrix, depending on the quadrotor's frame and aerodynamic coefficients (see Fig. 2.6), that is defined as

$$\boldsymbol{\Gamma}_i = \begin{bmatrix} c_t & c_t & c_t & c_t \\ d_q c_t & 0 & -d_q c_t & 0 \\ 0 & d_q c_t & 0 & -d_q c_t \\ -c_a & c_a & -c_a & c_a \end{bmatrix} \quad (2.11)$$

where c_t, c_a are aerodynamic coefficients and d_q is the distance between the CoM of the quadrotor and one motor;

- $\boldsymbol{\Omega}_i = [\omega_{i,1}^2 \quad \omega_{i,2}^2 \quad \omega_{i,3}^2 \quad \omega_{i,4}^2]^T \in \mathbb{R}^{4 \times 1}$ is the vector of motor speed squares of the i^{th} quadrotor with $\omega_{i,j}$ being the speed of the j^{th} motor of the i^{th} quadrotor ($j = 1, \dots, 4$).

Since $\boldsymbol{\Gamma}_i$ is always invertible, the input of the i^{th} quadrotor can either be the motor speed square $\boldsymbol{\Omega}_i$ or, directly, the reduced wrench ${}^i\mathbf{w}_i^r$. Thus, we can rewrite the static model in Eq.(2.5) and Eq.(2.7) using the quadrotors' reduced wrenches:

$${}^b\mathbf{w}_{ext} + \sum_{i=1}^4 {}^b\mathbf{W}_i^r {}^i\mathbf{w}_i^r - \begin{bmatrix} {}^b\mathbf{R}_0(m_t \mathbf{g}) \\ \mathbf{0} \end{bmatrix} = \mathbf{0}, \quad (2.12)$$

or

$${}^b\mathbf{w}_{ext} + {}^b\mathbf{W}_q^r {}^q\mathbf{w}_q^r - \begin{bmatrix} {}^b\mathbf{R}_0(m_t \mathbf{g}) \\ \mathbf{0} \end{bmatrix} = \mathbf{0}. \quad (2.13)$$

where

1. ${}^q\mathbf{w}_q^r = [{}^1\mathbf{w}_1^r \quad {}^2\mathbf{w}_2^r \quad {}^3\mathbf{w}_3^r \quad {}^4\mathbf{w}_4^r]^T \in \mathbb{R}^{16 \times 1}$;
2. ${}^b\mathbf{W}_q^r = [{}^b\mathbf{W}_1^r \quad {}^b\mathbf{W}_2^r \quad {}^b\mathbf{W}_3^r \quad {}^b\mathbf{W}_4^r] \in \mathbb{R}^{6 \times 16}$, where ${}^b\mathbf{W}_i^r \in \mathbb{R}^{6 \times 4}$ is a matrix map-

ping the i^{th} quadrotor's reduced wrench to the body frame \mathcal{F}_b

$${}^b\mathbf{W}_i^r = \left[\begin{array}{c|c} {}^b\mathbf{R}_i\mathbf{e}_3 & \mathbf{0} \\ \hline \begin{bmatrix} b\mathbf{r}_i \end{bmatrix}_\times {}^b\mathbf{R}_i\mathbf{e}_3 & {}^b\mathbf{R}_i \end{array} \right] \quad (2.14)$$

where $\mathbf{e}_3 = [0 \ 0 \ 1]^T$.

Also, we can write the static model in Eq.(2.12) and Eq.(2.13) w.r.t the quadrotors' motor speed squares as

$${}^b\mathbf{w}_{ext} + \sum_{i=1}^4 {}^b\mathbf{W}_i^r \Gamma_i \Omega_i - \begin{bmatrix} {}^b\mathbf{R}_0(m_t\mathbf{g}) \\ \mathbf{0} \end{bmatrix} = \mathbf{0}, \quad (2.15)$$

or

$${}^b\mathbf{w}_{ext} + {}^b\mathbf{W}_\Omega \Omega - \begin{bmatrix} {}^b\mathbf{R}_0(m_t\mathbf{g}) \\ \mathbf{0} \end{bmatrix} = \mathbf{0} \quad (2.16)$$

where

- $\Omega = [\Omega_1^T \ \Omega_2^T \ \Omega_3^T \ \Omega_4^T]^T \in \mathbb{R}^{16 \times 1}$ is the vector grouping motor speed squares of all quadrotors,
- ${}^b\mathbf{W}_\Omega = {}^b\mathbf{W}_q^r \Gamma \in \mathbb{R}^{6 \times 16}$ and $\Gamma = \text{diag}(\Gamma_1, \Gamma_2, \Gamma_3, \Gamma_4) \in \mathbb{R}^{16 \times 16}$.

2.3 Dynamic modeling of Flying Gripper

In previous section, we develop a general form for the static model of both robots in Eq.(2.12), Eq.(2.13), Eq.(2.15) and Eq.(2.16). In this section, we are going to build dynamic models that will be used for designing a controller in chapter 4 and 5.

We introduce the following assumptions with the aim of simplifying dynamic modeling:

1. Each part of the robot is considered as one rigid body;
2. For the FG-MAQ robot, each quadrotor's CoM coincides with the center of rotation of the corresponding U-joint;
3. We consider the fingers to close or open slowly, thus we neglect the dynamics of the fingers, of the worm gear mechanisms and the quadrotors' yaw velocities. In such a case, we can consider each finger as one single rigid body: the robot is thus simplified to a body structure and four quadrotors;

Table 2.2 – Main symbols used in the dynamic modeling

Symbol	Definition
\mathbf{I}_i	Inertia matrix of the i^{th} quadrotor expressed in \mathcal{F}_i
\mathbf{I}_b	Inertia matrix of the body structure expressed in \mathcal{F}_b
${}^b\mathbf{I}_i$	Inertia matrix of the i^{th} quadrotor expressed in \mathcal{F}_b
\mathbf{I}_t	Inertia matrix of the whole robot expressed in \mathcal{F}_b
${}^b\boldsymbol{\omega}_b$ (${}^0\boldsymbol{\omega}_b$)	Vector of angular velocity of \mathcal{F}_b expressed in \mathcal{F}_b (\mathcal{F}_0)
${}^i\boldsymbol{\omega}_i$	Vector of angular velocity of \mathcal{F}_i expressed in \mathcal{F}_i
${}^0\mathbf{f}_{i,b}$	Force vector acting on the robot body applied structure by the i^{th} quadrotor expressed in \mathcal{F}_0
${}^0\mathbf{f}_b$	Force vector acting on the robot body structure applied by quadrotors expressed in \mathcal{F}_0

- The object once grasped, has no motion w.r.t the fingers and the robot. The body structure and the object are assumed to be one single rigid body after grasping.

2.3.1 Dynamic modeling of FG-FAQ

For the FG-FAQ architecture, we recall the generalized coordinate vector $\mathbf{q}^f = [\mathbf{p}_b^T \quad \mathbf{q}_a^{fT}]^T \in \mathbb{R}^{10 \times 1}$ where $\mathbf{p}_b \in \mathbb{R}^{6 \times 1}$ represents the body structure pose (position and attitude) and $\mathbf{q}_a^f \in \mathbb{R}^{4 \times 1}$ represents quadrotors' yaw angles.

Each quadrotor is linked to the robot structure through a worm gear mechanism such that the position of the quadrotor's CoM w.r.t the body structure is fixed and constant. Therefore, translations of all quadrotors are coupled with that of the body structure, while the rotational dynamic of each quadrotor is not considered, since the yaw velocity is neglected and pitch and roll rotations are not authorized by the FG-FAQ architecture. Therefore, the whole robot (the body structure, the fingers and the quadrotors) will be considered as one rigid and single body.

We derive the dynamic model of the robot using the Newton-Euler formalism in order to relate its motion to the forces and torques acting on the body structure.

The translational dynamic model is developed in the world frame \mathcal{F}_0

$$m_t {}^0\ddot{\mathbf{x}}_b = \sum_{i=1}^4 {}^0\mathbf{f}_i - m_t \mathbf{g} + {}^0\mathbf{f}_{ext} \quad (2.17)$$

where m_t stands for the total mass of the robot

$$m_t = m_b + \sum_{i=1}^4 m_i. \quad (2.18)$$

Before we build the rotational dynamic model, we compute the total inertia of the robot

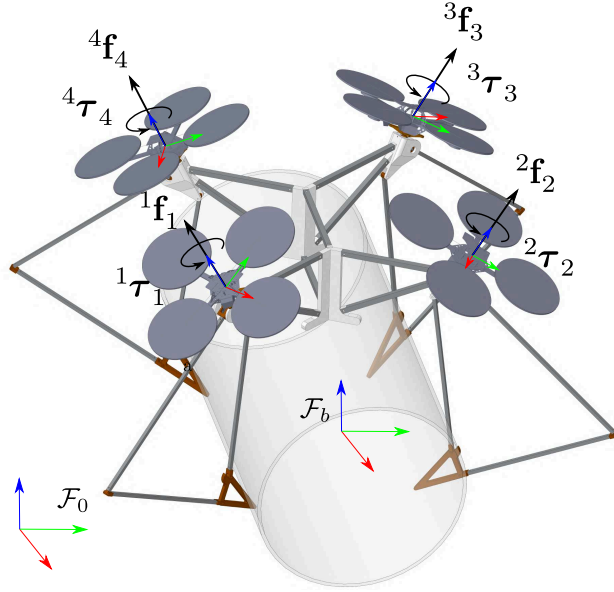


Figure 2.8 – Representation of FG-FAQ robot and its main variables: each quadrotor produces a thrust force ${}^i\mathbf{f}_i \in \mathbb{R}^{3 \times 1}$ and a torque ${}^i\boldsymbol{\tau}_i \in \mathbb{R}^{3 \times 1}$ expressed in frame \mathcal{F}_i .

expressed in the body frame \mathcal{F}_b that

$$\mathbf{I}_t = \sum_{i=1}^4 {}^b\mathbf{I}_i + \mathbf{I}_b \quad (2.19)$$

where \mathbf{I}_b is the inertia matrix of the body structure expressed in \mathcal{F}_b , and ${}^b\mathbf{I}_i$ is the inertia matrix of quadrotor i expressed in \mathcal{F}_b that is obtained by applying the Steiner's theorem [Lynch and Park, 2017]

$${}^b\mathbf{I}_i = {}^b\mathbf{R}_i \mathbf{I}_i {}^b\mathbf{R}_i^T - m_i [{}^b\mathbf{r}_i]_{\times} [{}^b\mathbf{r}_i]_{\times}. \quad (2.20)$$

Note that we compute \mathbf{I}_b considering the body structure with a fixed configuration of fingers and we consider it as a constant. It is worthy to mention that the fingers' configurations evolve during grasping, which causes a variation of \mathbf{I}_b . In this thesis, we will consider this variation of \mathbf{I}_b as a modeling error, which is treated as noise and disturbances in the controller design.

Therefore, the rotational dynamic model in the body frame \mathcal{F}_b is developed by the

equation

$$\mathbf{I}_t {}^b \dot{\boldsymbol{\omega}}_b + [{}^b \boldsymbol{\omega}_b]_{\times} \mathbf{I}_t {}^b \boldsymbol{\omega}_b = \sum_{i=1}^4 \left([{}^b \mathbf{r}_i]_{\times} {}^b \mathbf{R}_i {}^i \mathbf{f}_i + {}^b \mathbf{R}_i {}^i \boldsymbol{\tau}_i \right) + {}^b \boldsymbol{\tau}_{ext} \quad (2.21)$$

where the angular velocity ${}^b \boldsymbol{\omega}_b$ can be obtained from the derivative of the Euler angle $\boldsymbol{\eta}_b$ using the formula [Carrillo et al., 2013]

$${}^b \boldsymbol{\omega}_b = \mathbf{T}_b \dot{\boldsymbol{\eta}}_b \quad (2.22)$$

in which

$$\mathbf{T}_b = \begin{bmatrix} 1 & 0 & -\sin \theta_b \\ 0 & \cos \phi_b & \cos \theta_b \sin \phi_b \\ 0 & -\sin \phi_b & \cos \theta_b \cos \phi_b \end{bmatrix}. \quad (2.23)$$

Then, we are able to rewrite the rotational dynamic model in \mathcal{F}_b as

$$\mathbf{I}_t \mathbf{T}_b \ddot{\boldsymbol{\eta}}_b + \mathbf{I}_t \dot{\mathbf{T}}_b \dot{\boldsymbol{\eta}}_b + [\mathbf{T}_b \dot{\boldsymbol{\eta}}_b]_{\times} \mathbf{I}_t \mathbf{T}_b \dot{\boldsymbol{\eta}}_b = \sum_{i=1}^4 \left([{}^b \mathbf{r}_i]_{\times} {}^b \mathbf{R}_i {}^i \mathbf{f}_i + {}^b \mathbf{R}_i {}^i \boldsymbol{\tau}_i \right) + {}^b \boldsymbol{\tau}_{ext}. \quad (2.24)$$

Finally, we can write the translational and rotational dynamic models into a compact form as

$$\mathbf{M}_t \ddot{\mathbf{p}}_b + \mathbf{c}_t = \mathbf{w}_b + \mathbf{w}_{ext} \quad (2.25)$$

where

- $\mathbf{M}_t = \begin{bmatrix} m_t \mathbf{I}_3 & \mathbf{0}_3 \\ \mathbf{0}_3 & \mathbf{I}_t \mathbf{T}_b \end{bmatrix}$;
- $\mathbf{c}_t = \begin{bmatrix} -m_t \mathbf{g} \\ \mathbf{I}_t \dot{\mathbf{T}}_b \dot{\boldsymbol{\eta}}_b + [\mathbf{T}_b \dot{\boldsymbol{\eta}}_b]_{\times} \mathbf{I}_t \mathbf{T}_b \dot{\boldsymbol{\eta}}_b \end{bmatrix}$;
- $\mathbf{w}_b = [{}^0 \mathbf{f}_b^T \quad {}^b \boldsymbol{\tau}_b^T]^T \in \mathbb{R}^{6 \times 1}$ is the wrench vector exerted on the robot body by quadrotors composed of a force ${}^0 \mathbf{f}_b$ in \mathcal{F}_0 and a torque ${}^b \boldsymbol{\tau}_b$ expressed in \mathcal{F}_b ;
- $\mathbf{w}_{ext} = [{}^0 \mathbf{f}_{ext}^T \quad {}^b \boldsymbol{\tau}_{ext}^T]^T \in \mathbb{R}^{6 \times 1}$ accounts for the external wrench acting on the robot by the environment.

We can rewrite the dynamic model of the robot as

$$\mathbf{M}_t \ddot{\mathbf{p}}_b + \mathbf{c}_t = \mathbf{w}_b + \cancel{\mathbf{w}_{ext}} \overset{0}{}, \quad (2.26)$$

$$\mathbf{w}_b = \mathbf{W}_{\Omega} \boldsymbol{\Omega}. \quad (2.27)$$

where ${}^b \mathbf{w}_{ext}$ is put to be zero for contact-less operations and we only consider contact-less

operations in this thesis. The matrix $\mathbf{W}_\Omega = \begin{bmatrix} {}^0\mathbf{R}_b & \mathbf{0} \\ \mathbf{0} & \mathbf{I}_3 \end{bmatrix} {}^b\mathbf{W}_\Omega \in \mathbb{R}^{6 \times 16}$ and ${}^b\mathbf{W}_\Omega$ is defined in Eq.(2.16). Note that the above dynamic model is developed for the FG-FAQ robot, however Eq.(2.26) is a general dynamic model for an aerial manipulation robot, whereas Eq.(2.27) depends on the UAVs that compose this aerial manipulation robot.

Remarks and discussion

1. We consider the whole robot as a rigid single body aiming to simplify the dynamic model. We assume fingers to open and close slowly, thus permitting to neglect the dynamics of fingers and the yaw velocities of quadrotors. Modeling error due to this simplification will be compensated by control techniques, which must be validated in simulations.
2. The simplified dynamic model of FG-FAQ robot shows it is overactuated, as $\dim(\mathbf{q}^f) < \dim(\boldsymbol{\Omega})$ (see Table 2.3). This actuation redundancy property implies that there exists an infinity of solutions for a given task. This will be further treated in chapter 4.

2.3.2 Dynamic modeling of FG-MAQ

In this section, the dynamic model of the FG-MAQ robot is developed. The main idea is to calculate the dynamic model in three steps: *i*) simplify dynamics of U-joints; *ii*) build the dynamic models for the body structure and the quadrotors respectively; *iii*) discuss underactuation of the whole robot.

We remind the generalized coordinate vector $\mathbf{q}^m = [\mathbf{p}_b^T \quad \mathbf{q}_a^{mT}]^T \in \mathbb{R}^{18 \times 1}$ where vector $\mathbf{p}_b = [{}^0\mathbf{x}_b^T \quad \boldsymbol{\eta}_b^T]^T \in \mathbb{R}^{6 \times 1}$ describes the pose of body structure and vector $\mathbf{q}_a^m = [\boldsymbol{\eta}_1^T \quad \boldsymbol{\eta}_2^T \quad \boldsymbol{\eta}_3^T \quad \boldsymbol{\eta}_4^T]^T \in \mathbb{R}^{12 \times 1}$ with $\boldsymbol{\eta}_i = [\phi_i \quad \theta_i \quad \psi_i]^T \in \mathbb{R}^{3 \times 1}$ being a vector of Euler angles (roll/pitch/yaw) of frame \mathcal{F}_i with respect to \mathcal{F}_0 .

Simplification of universal joints

U-joints link each quadrotor to its corresponding worm screw (Fig.2.4) and they transform quadrotors' yaw torques to the worm screws for actuating the fingers. In what follows, universal joints will be modeled as spherical joints (S-joints) such that the rotational dynamics of quadrotors is decoupled from the rotational dynamics of the robot's body. To do this, the yaw torque produced by a quadrotor and the yaw velocities are neglected. Moreover, the full dynamic model of one U-joint involves parameters that are not easy

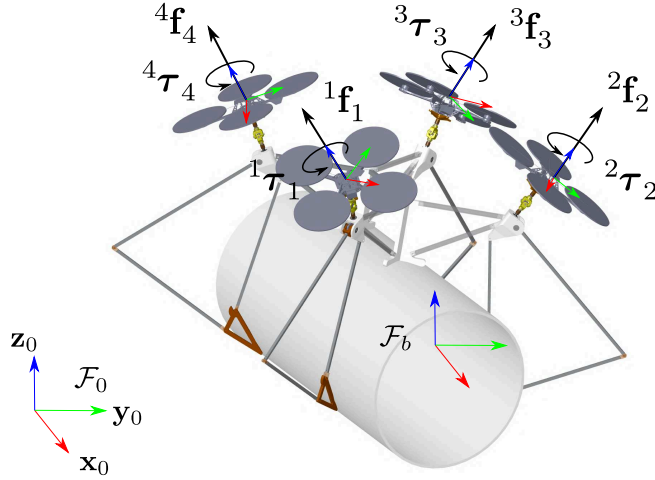


Figure 2.9 – Representation of FG-MAQ robot and its main variables: each quadrotor i generates a thrust force ${}^i\mathbf{f}_i \in \mathbb{R}^{3 \times 1}$ and a torque ${}^i\boldsymbol{\tau}_i \in \mathbb{R}^{3 \times 1}$ expressed in frame \mathcal{F}_i .

to be measured, such as the angular velocity and acceleration of the quadrotor, inertial characteristic of cross, output shaft and the quadrotor, the yaw torque applied by the quadrotor, the shaft alignment angle etc [Šalinić et al., 2017].

Due to these simplifications, the FG-MAQ robot can be viewed as four quadrotors linked to the body structure through passive S-joints in the dynamic modeling.

Dynamic modeling of the body structure

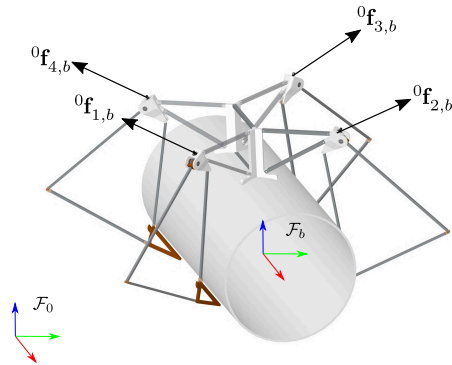


Figure 2.10 – Representation of body structure of FG-MAQ robot and its main variables: ${}^0\mathbf{f}_{i,b} \in \mathbb{R}^{3 \times 1}$ is the interaction force between the i^{th} quadrotor and the body structure expressed in frame \mathcal{F}_0 .

As we model the link between each quadrotor and the body structure as a passive S-

joint, there exists only an interaction force between each quadrotor and the body structure. The interaction force between the i^{th} quadrotor and the body structure is defined as ${}^0\mathbf{f}_{i,b} \in \mathbb{R}^{3 \times 1}$, as shown in Fig. 2.10. Then, applying Newton-Euler method to the body structure gives the translational dynamic equation of the body structure in the world frame \mathcal{F}_0

$$m_b {}^0\ddot{\mathbf{x}}_b = m_b \mathbf{g} + \sum_{i=1}^n {}^0\mathbf{f}_{i,b} + {}^0\mathbf{f}_{ext}, \quad (2.28)$$

Following the same method for the FG-FAQ robot in the previous section, we derive the rotational dynamic model of the body structure in the body frame \mathcal{F}_b

$$\mathbf{I}_b \mathbf{T}_b \ddot{\boldsymbol{\eta}}_b + \mathbf{I}_b \dot{\mathbf{T}}_b \dot{\boldsymbol{\eta}}_b + [\mathbf{T}_b \dot{\boldsymbol{\eta}}_b]_{\times} \mathbf{I}_b \mathbf{T}_b \dot{\boldsymbol{\eta}}_b = \sum_{i=1}^n [{}^b\mathbf{r}_i]_{\times} {}^b\mathbf{R}_0 {}^0\mathbf{f}_{i,b} + {}^b\boldsymbol{\tau}_{ext}. \quad (2.29)$$

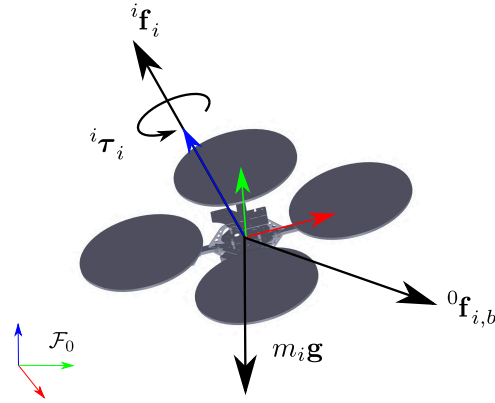


Figure 2.11 – Representation of the i^{th} quadrotor of FG-MAQ robot and its main variables: ${}^i\mathbf{f}_i, {}^i\boldsymbol{\tau}_i$ are the force and torque produced by the quadrotor (expressed in frame \mathcal{F}_i), $m_i \mathbf{g}$ is the gravity force, and ${}^0\mathbf{f}_{i,b}$ is the interaction force between the quadrotor and the body structure (expressed in frame \mathcal{F}_0).

The quadrotors and the body structure are coupled in terms of their translations. We recall one assumption in section 2.3 that each quadrotor's CoM coincides with the center of rotation of the corresponding U-joint. Then, this coupling is modeled by equation

$${}^0\mathbf{x}_i = {}^0\mathbf{x}_b + {}^0\mathbf{R}_b {}^b\mathbf{r}_i. \quad (2.30)$$

Therefore, the translational dynamic model of the i^{th} quadrotor in the world frame \mathcal{F}_0 is

developed as

$$m_i {}^0\ddot{\mathbf{x}}_i = m_i \mathbf{g} - {}^0\mathbf{f}_{i,b} + {}^0\mathbf{f}_i. \quad (2.31)$$

We emulate the interaction forces ${}^0\mathbf{f}_{i,b}$ by combining Eq.(2.28), Eq.(2.29), Eq.(2.30), and Eq.(2.31), which results into a compact form of the dynamic model

$$\mathbf{M}_b \ddot{\mathbf{p}}_b + \mathbf{c}_b = \mathbf{w}_b + \mathbf{w}_{ext} \quad (2.32)$$

where

$$\begin{aligned} \text{— } \mathbf{M}_b &= \begin{bmatrix} m_t \mathbf{I}_3 & -\sum_{i=1}^4 m_i {}^0\mathbf{R}_b [\mathbf{r}_i]_{\times} \mathbf{T}_b \\ \sum_{i=1}^4 m_i [\mathbf{r}_i]_{\times} {}^b\mathbf{R}_0 & \mathbf{I}_t \mathbf{T}_b \end{bmatrix}; \\ \text{— } \mathbf{c}_b &= \begin{bmatrix} \sum_{i=1}^4 m_i {}^0\mathbf{R}_b \left([\mathbf{T}_b \dot{\boldsymbol{\eta}}_b]_{\times} [\mathbf{r}_i]_{\times} \mathbf{T}_b \dot{\boldsymbol{\eta}}_b - [\mathbf{r}_i]_{\times} \dot{\mathbf{T}}_b \dot{\boldsymbol{\eta}}_b \right) - m_t \mathbf{g} \\ -\sum_{i=1}^4 m_i \left([\mathbf{r}_i]_{\times} [\mathbf{T}_b \dot{\boldsymbol{\eta}}_b]_{\times} [\mathbf{r}_i]_{\times} \mathbf{T}_b \dot{\boldsymbol{\eta}}_b + [\mathbf{r}_i]_{\times} {}^b\mathbf{R}_0 \mathbf{g} \right) + [\mathbf{T}_b \dot{\boldsymbol{\eta}}_b]_{\times} \mathbf{I}_b \mathbf{T}_b \dot{\boldsymbol{\eta}}_b + \mathbf{I}_t \dot{\mathbf{T}}_b \dot{\boldsymbol{\eta}}_b \end{bmatrix}; \end{aligned}$$

Indeed, \mathbf{w}_b is the resultant wrench of the four quadrotors thrust forces, which is modeled as

$$\mathbf{w}_b = \mathbf{W}_f {}^0\mathbf{f}_q \quad (2.33)$$

where

$$\begin{aligned} \text{— } {}^0\mathbf{f}_q &= \begin{bmatrix} {}^0\mathbf{f}_1^T & {}^0\mathbf{f}_2^T & {}^0\mathbf{f}_3^T & {}^0\mathbf{f}_4^T \end{bmatrix}^T \in \mathbb{R}^{12 \times 1} \text{ is a vector regrouping thrust forces generated by four quadrotors expressed in } \mathcal{F}_0; \\ \text{— } \mathbf{W}_f &= \begin{bmatrix} \mathbf{I}_3 & \mathbf{I}_3 & \mathbf{I}_3 & \mathbf{I}_3 \\ [{}^b\mathbf{r}_1]_{\times} {}^b\mathbf{R}_0 & [{}^b\mathbf{r}_2]_{\times} {}^b\mathbf{R}_0 & [{}^b\mathbf{r}_3]_{\times} {}^b\mathbf{R}_0 & [{}^b\mathbf{r}_4]_{\times} {}^b\mathbf{R}_0 \end{bmatrix} \in \mathbb{R}^{6 \times 12} \text{ is a matrix that maps } {}^0\mathbf{f}_q \text{ to } \mathbf{w}_b. \end{aligned}$$

Rotational dynamic modeling of the quadrotors

The rotational dynamic models of the quadrotors are computed as the next step. The i^{th} quadrotor's rotational dynamics is given in its local frame \mathcal{F}_i

$$\mathbf{I}_i {}^i\dot{\boldsymbol{\omega}}_i + [{}^i\boldsymbol{\omega}_i]_{\times} \mathbf{I}_i {}^i\boldsymbol{\omega}_i = {}^i\boldsymbol{\tau}_i, \quad (2.34)$$

The angular velocity ${}^i\boldsymbol{\omega}_i$ can be computed from $\dot{\boldsymbol{\eta}}_i$ as the formula [Carrillo et al., 2013]

$${}^i\boldsymbol{\omega}_i = \mathbf{T}_i \dot{\boldsymbol{\eta}}_i \quad (2.35)$$

in which

$$\mathbf{T}_i = \begin{bmatrix} 1 & 0 & -\sin \theta_i \\ 0 & \cos \phi_i & \cos \theta_i \sin \phi_i \\ 0 & -\sin \phi_i & \cos \theta_i \cos \phi_i \end{bmatrix}. \quad (2.36)$$

Thus, we can obtain the rotational dynamic model of quadrotor i in the form

$$\mathbf{I}_i \mathbf{T}_i \ddot{\boldsymbol{\eta}}_i + \mathbf{I}_i \dot{\mathbf{T}}_i \dot{\boldsymbol{\eta}}_i + \left[\mathbf{T}_i \dot{\boldsymbol{\eta}}_i \right]_{\times} \mathbf{I}_i \mathbf{T}_i \dot{\boldsymbol{\eta}}_i = {}^i \boldsymbol{\tau}_i \quad (2.37)$$

that is rewritten as

$$\mathbf{M}_i \ddot{\boldsymbol{\eta}}_i + \mathbf{c}_i = {}^i \boldsymbol{\tau}_i \quad (2.38)$$

where

1. $\mathbf{M}_i = \mathbf{I}_i \mathbf{T}_i \in \mathbb{R}^{3 \times 3}$ is the inertia matrix;
2. $\mathbf{c}_i = \mathbf{I}_i \dot{\mathbf{T}}_i \dot{\boldsymbol{\eta}}_i + \left[\mathbf{T}_i \dot{\boldsymbol{\eta}}_i \right]_{\times} \mathbf{I}_i \mathbf{T}_i \dot{\boldsymbol{\eta}}_i \in \mathbb{R}^{3 \times 1}$ represents the Coriolis/centripetal terms.

For the rotational dynamics of all quadrotors, we write the dynamic equations in a compact form

$$\mathbf{M}_a \ddot{\mathbf{q}}_a^m + \mathbf{c}_a = {}^q \boldsymbol{\tau}_q \quad (2.39)$$

with

- $\mathbf{q}_a^m = \left[\boldsymbol{\eta}_1^T \quad \boldsymbol{\eta}_2^T \quad \boldsymbol{\eta}_3^T \quad \boldsymbol{\eta}_4^T \right]^T$ represents the attitude of all the four drones;
- $\mathbf{M}_a = \text{diag}(\mathbf{M}_1, \mathbf{M}_2, \mathbf{M}_3, \mathbf{M}_4) \in \mathbb{R}^{12 \times 12}$;
- $\mathbf{c}_a = \left[\mathbf{c}_1^T \quad \mathbf{c}_2^T \quad \mathbf{c}_3^T \quad \mathbf{c}_4^T \right]^T \in \mathbb{R}^{12 \times 1}$;
- ${}^q \boldsymbol{\tau}_q = \left[{}^1 \boldsymbol{\tau}_1^T \quad {}^2 \boldsymbol{\tau}_2^T \quad {}^3 \boldsymbol{\tau}_3^T \quad {}^4 \boldsymbol{\tau}_4^T \right]^T \in \mathbb{R}^{12 \times 1}$ is the vector regrouping all quadrotors' torques.

Full dynamic model of FG-MAQ with quadrotors

The full dynamic model of the robot is obtained based on Eq.(2.32), Eq.(2.33) and Eq.(2.39) as

$$\mathbf{M}_b \ddot{\mathbf{p}}_b + \mathbf{c}_b = \mathbf{w}_b + \mathbf{w}_{ext} \xrightarrow{0} \quad (2.40)$$

$$\mathbf{M}_a \ddot{\mathbf{q}}_a^m + \mathbf{c}_a = {}^q \boldsymbol{\tau}_q, \quad (2.41)$$

$$\mathbf{w}_b = \mathbf{W}_f {}^0 \mathbf{f}_q \quad (2.42)$$

where ${}^b \mathbf{w}_{ext}$ is put to be zero for contact-less operations and we only consider contact-less operations for the robot in this thesis. It can be seen from equations (2.40) and (2.41)

that \mathbf{p}_b and its derivatives do not appear in the rotational dynamic equation Eq.(2.41), and \mathbf{q}_a^m and its derivatives do not appear in the translational dynamic equation Eq.(2.40) either. This reveals that the quadrotors' rotational dynamics are independent of the body structure's translational and rotational dynamics.

In Eq.(2.40), Eq.(2.41) and Eq.(2.42), the inputs of the quadrotors are ${}^0\mathbf{f}_q$ and ${}^q\boldsymbol{\tau}_q$. Indeed, couplings exist between the thrust forces ${}^0\mathbf{f}_q$ and the quadrotors' attitudes \mathbf{q}_a^m . The coupling can be demonstrated by the relation between ${}^0\mathbf{f}_i$ and ${}^i\mathbf{f}_i$ for quadrotor i by equation

$${}^0\mathbf{f}_i = {}^0\mathbf{R}_i {}^i\mathbf{f}_i. \quad (2.43)$$

Since ${}^i\mathbf{f}_i = [0 \ 0 \ f_{i,z}]^T$, we rewrite Eq.(2.43) to be

$${}^0\mathbf{f}_i = {}^0\mathbf{R}_i \begin{bmatrix} 0 \\ 0 \\ f_{i,z} \end{bmatrix} \quad (2.44)$$

$$= {}^0\mathbf{R}_i \mathbf{e}_3 f_{i,z} \quad (2.45)$$

$$= \begin{bmatrix} \cos \phi_i \sin \theta_i \\ -\sin \phi_i \\ \cos \phi_i \cos \theta_i \end{bmatrix} f_{i,z}. \quad (2.46)$$

We can see from the relation in Eq.(2.46) that, for each quadrotor i , ${}^0\mathbf{f}_i$ depends on $f_{i,z}$, ϕ_i , θ_i , but it is independent from ψ_i .

In the interest of simplifying our dynamic model, we define a vector \mathbf{f}_z regrouping $f_{i,z}$ of all quadrotors that is

$$\mathbf{f}_z = [f_{1,z} \ f_{2,z} \ f_{3,z} \ f_{4,z}]^T \in \mathbb{R}^{4 \times 1}. \quad (2.47)$$

Consequently, the term ${}^0\mathbf{f}_q$ is expressed as

$${}^0\mathbf{f}_q = \mathbf{R}_r \mathbf{f}_z \quad (2.48)$$

where $\mathbf{R}_r \in \mathbb{R}^{12 \times 4}$ is a matrix depending on \mathbf{q}_a^m as

$$\mathbf{R}_r = \begin{bmatrix} \cos \phi_1 \sin \theta_1 & 0 & 0 & 0 \\ -\sin \phi_1 & 0 & 0 & 0 \\ \cos \phi_1 \cos \theta_1 & 0 & 0 & 0 \\ 0 & \cos \phi_2 \sin \theta_2 & 0 & 0 \\ 0 & -\sin \phi_2 & 0 & 0 \\ 0 & \cos \phi_2 \cos \theta_2 & 0 & 0 \\ 0 & 0 & \cos \phi_3 \sin \theta_3 & 0 \\ 0 & 0 & -\sin \phi_3 & 0 \\ 0 & 0 & \cos \phi_3 \cos \theta_3 & 0 \\ 0 & 0 & 0 & \cos \phi_4 \sin \theta_4 \\ 0 & 0 & 0 & -\sin \phi_4 \\ 0 & 0 & 0 & \cos \phi_4 \cos \theta_4 \end{bmatrix} \quad (2.49)$$

Finally, we obtain the dynamic model for the robot FG-MAQ as

$$\mathbf{M}_b \ddot{\mathbf{p}}_b + \mathbf{c}_b = \mathbf{w}_b \quad (2.50)$$

$$\mathbf{M}_a \ddot{\mathbf{q}}_a^m + \mathbf{c}_a = {}^a \boldsymbol{\tau}_q \quad (2.51)$$

$$\mathbf{w}_b = \mathbf{W}_f {}^0 \mathbf{f}_q \quad (2.52)$$

$${}^0 \mathbf{f}_q = \mathbf{R}_r \mathbf{f}_z \quad (2.53)$$

Till now, this full dynamic model is developed for the FG-MAQ robot with quadrotors being actuators: \mathbf{f}_z regroups all quadrotors' thrust forces along the \mathbf{z}_i direction of \mathcal{F}_i and ${}^a \boldsymbol{\tau}_q$ regroups all quadrotors' torques.

Remarks

1. This dynamic model is developed based on two important assumptions: (1) the slow grasping motion of fingers and the slow yaw rotations of quadrotors. (2) modeling universal joints as spherical joints by neglecting the effect of quadrotors' yaw torques on the body structure.
2. Influences caused by the simplifications of the model will be viewed as model uncertainties and disturbances to be compensated by control techniques, which will be validated in simulations and experiments in chapter 5.
3. The developed dynamic model shows that the FG-MAQ robot is underactuated

Table 2.3 – Comparison between FG-FAQ and FG-MAQ

/	FG-FAQ	FG-MAQ
Generalized coordinates	$\mathbf{q}^f = [\mathbf{p}_b^T \quad \mathbf{q}_a^{fT}]^T$	$\mathbf{q}^m = [\mathbf{p}_b^T \quad \mathbf{q}_a^{mT}]^T$
No. of DOF	10	18
Control input	${}^i\mathbf{w}_i^r \in \mathbb{R}^{4 \times 1}, i = 1, \dots, 4$	${}^i\mathbf{w}_i^r \in \mathbb{R}^{4 \times 1}, i = 1, \dots, 4$
No. of Degrees of actuation	16	16
Underactuated/Overactuated	overactuated	underactuated

as it has the $\dim(\mathbf{q}^m) > (\dim(\mathbf{f}_z) + \dim({}^q\boldsymbol{\tau}_q))$ where $\dim(\mathbf{q}^m) = 18, \dim(\mathbf{f}_z) = 4, \dim({}^q\boldsymbol{\tau}_q) = 12$, while the quadrotors' rotations are fully actuated as $\dim(\mathbf{q}_a^m) = \dim({}^q\boldsymbol{\tau}_q) = 12$ (see Table 2.3).

4. Analysis show that FG-FAQ is overactuated since the number of actuators (16) is greater than the number of DOF (10 generalized coordinates), while FG-MAQ is underactuated, since it exhibits 2 more DOF per quadrotor (pitch and roll rotations) and has a total of 18 generalized coordinates actuated by 16 motors. However, pitch and roll angles of each quadrotor are not imposed by the task and can be freely set in order to chose the direction of the thrust vector. They will be used to control each quadrotor' thrust force vector in chapter 5.

2.4 Conclusions

This chapter presented a new concept of aerial manipulation robot Flying Gripper that is intended to perform grasping, manipulating and transporting large objects autonomously. It is composed of four quadrotors, two self-adaptive fingers and a body structure. The robot manipulates in $SE(3)$ and produces enveloping and secured grasps using self-adaptive fingers. Each finger is actuated by a quadrotor' yaw rotation.

Two original and novel architectures of Flying Gripper were introduced: one with Fixed-Attitude Quadrotors (FG-FAQ), and a modified one with Mobile-Attitude Quadrotors (FG-MAQ). For the FG-MAQ robot, we introduce universal joints to link quadrotors with the body structure such that each quadrotor gains 2 additional DOF in roll and pitch rotations.

We built a general static model for the FG-FAQ and FG-MAQ robots to analyze their body wrench generation at static equilibrium. This static model lays a foundation for analyzing the robot manipulability in chapter 3.

Then, we developed the dynamic models for both robots with the Newton-Euler for-

mulations. These dynamic models will be used in controller designs in chapter 4 and chapter 5. Analysis of the dynamic models show that FG-FAQ is overactuated since it has 16 actuation motors and 10 DOF, while FG-MAQ is underactuated with 16 actuation motors and 18 DOF as each quadrotor gains 2 more DOF in pitch and roll rotation. However, this redundancy will be further analyzed in chapter 3.

WRENCH CAPABILITY ANALYSIS OF FLYING GRIPPER

3.1 Introduction to wrench capability analysis	76
3.2 Wrench capability analysis of a Planar Aerial Manipulator (PAM)	82
3.3 Wrench capability analysis of FG-FAQ and FG-MAQ	100
3.4 Conclusions	106

This chapter proposes a wrench capability analysis method to analyze the manipulability of the FG-FAQ and FG-MAQ robots based on their static model developed in chapter 2. We analyze the manipulability from the available wrench set that can be applied on the robot by quadrotors, which is called the available body wrench set. This method is called wrench capability analysis.

This chapter introduces a geometrical and visual approach using polytopes to compute the available body wrench set of the robot. The main challenges of this study are: *i*) the high number of actuators, *ii*) how to consider the mobility of quadrotors authorized by the introduction of passive universal joints between the quadrotor and the body structure in FG-MAQ, *iii*) how to consider the effect of the yaw torque applied to drive fingers. In this method, equalities are used to model the last two constraints.

Section 3.1 introduces the background of the wrench capability analysis. It reviews previous works on the analysis of the wrench capability and the connections between grasping, cable robots and aerial robots. Then, we introduce an overview of the proposed method that will be further detailed to analyze the wrench capability of the Flying Gripper robot. In order to better visualize and illustrate the proposed wrench analysis method, we introduce two different architectures of a Planar Aerial Manipulator in section 3.2: one with Fixed-Attitude Birotors (PAM-FAB) and one with Mobile-Attitude Birotors (PAM-MAB). The method is illustrated by showing the result at each step and performance criteria are used to evaluate and compare the wrench capabilities of the two robots.

Finally, we use this method to analyze the available body wrench sets of the FG-FAQ and FG-MAQ robots while grasping and manipulating an object respectively in section 3.3.

3.1 Introduction to wrench capability analysis

In this chapter, we want to qualify and quantify the manipulability of the Flying Gripper, in positioning and orienting a grasped object (assumed rigidly attached to the robot’s body). The manipulability of a robot is associated to its capability to move an end-effector in all directions.

Considering a serial manipulator, the manipulability analysis generally consists in studying the condition number of the Jacobian matrix. This permits to evaluate the velocity isotropy [Yoshikawa, 1985]. Due to the duality of force and velocity, it is also related to the force isotropy of the mechanism.

When considering more complex mechanisms, such as parallel manipulators with actuation redundancy (PMAR), the condition number of the Jacobian matrix is no longer relevant to analyze the manipulability nor the force capability, since the velocity/force duality no longer holds. In this case, a useful tool consists in studying the dimensions of the largest ellipsoid inscribed in the operational velocity polytope [Krut et al., 2004]. This method can be used in the dual force space, to obtain the available wrench space [Krut et al., 2004], that is the set of wrenches that can be exerted on the movable platform.

3.1.1 Connections between grasping, cable robots and aerial robots

Methods based on the analysis of a wrench set are well indicated in the study of the manipulability of Cable-Driven Parallel Robots (CDPRs), in that it permits to deal with actuation redundancy, but also with the unilaterality of cable forces. Indeed, when using a CDPR, the platform is said to be in a manipulable (controllable) pose, if it is wrench-closure, i.e. if a wrench can be applied in any direction of $SE(3)$ while cables are tensed [Shen et al., 1994, Gallina and Rosati, 2002]. This property depends on the robot’s architecture and on the robot’s pose, it can be used to draw the workspace of a robot [Gouttefarde and Gosselin, 2006].

This wrench-closure property is actually derived from the similar force-closure property defined to analyze the stability of a grasp [Nguyen, 1988]. Indeed, because of the

unidirectionality of contact constraints, many tools obtained to analyze a grasp have been transposed to analyze a CDPR where the same type of unilateral constraints hold to maintain tension in cables [Ebert-Uphoff and Voglewede, 2004]. However, force-closure used in the grasping community is slightly different from wrench-closure used in CDPR community, in that it does not imply manipulability of the grasped object [Murray et al., 1994], since it relies on uncontrollable forces such as frictional forces. The difference is made between passive and active force-closure [Shapiro et al., 2001]. While active force-closure is related to the manipulability, passive force-closure related to the capability of the grasping mechanism to counteract any external wrench exerted on the grasped object by an appropriate combination of contact forces. In the study of CDPRs, wrench-closure is by nature active since all forces are independently controllable.

To continue with the analogy between grasping mechanisms and CDPRs, the so-called "Grasp Wrench Space" (GWS) [Ferrari and Canny, 1992, Pollard, 1996] obtained from the grasp map \mathbf{G} (mapping the vector of fingers' forces to the wrench exerted on the object) corresponds to the "Available Wrench Set" (AWS) used for CDPRs [Bosscher and Ebert-Uphoff, 2004, Bouchard et al., 2010] that can be computed from the so-called wrench matrix \mathbf{W} (mapping the vector of cables' forces to the wrench exerted on the movable platform). These two sets GWS and AWS are interesting in that they take into account unilateral constraints but also actuators limits.

Coming back to our concern that is the manipulability of an aerial robot actuated by multiple UAVs, it appears that the same type of unilateral constraints hold. Especially for those robots with multiple UAVs, each rotor can be considered as an actuator and its capability can be taken into account in the manipulability analysis. Indeed, a propeller is generally designed to exert a force in a single direction. The range of force that it can apply depends on the minimal and maximal velocity of the associated motor. No direct relation can be written between the velocity of the robot's body and actuators velocities. It remains no other choice than that to analyze the operational wrench set. Such a method has been recently applied on the analysis of a simpler version of Flying Gripper [Saint-Sevin et al., 2019] and to analyze the wrench capability of an Aerial Cable-Towed Robot (ACTR) [Erskine et al., 2019]. Interestingly, in [Nguyen et al., 2018], authors introduce a mechanism based on three (or two) quadrotors linked to a common movable platform through spherical joints which lets each quadrotor modify its attitude. Quadrotors are thus used as thrust generators and the thrust orientation can be freely chosen in space. Since, spherical joints have mechanical limits, they use a linearized cone to represent the

set of thrust that can be exerted on the platform, this is again inspired from the works on grasping mechanism, that introduce a friction cone to model constraints on contact forces [Murray et al., 1994]. However, as we later point it out, this method is based on the assumption that each quadrotor can instantly modify its orientation.

3.1.2 Introduction to polytope's notations

The aforementioned wrench capability analysis method is based on the concept of polytopes. A polytope is a bounded convex set (see Appendix A). It can be represented mathematically in two different manners: using the \mathcal{H} -representation (as the intersection of a set of halfspaces \mathcal{HS} and hyperplanes \mathcal{HP}) or using the \mathcal{V} -representation (as the convex hull of a set of vertices) [Grünbaum, 2003]. See Appendix A about polytope notations and operations.

Let first introduce halfspaces and hyperplanes:

— a halfspace in \mathbb{R}^n is represented by a linear inequality

$$\mathcal{HP} = \left\{ \mathbf{x} \in \mathbb{R}^{n \times 1} \mid \mathbf{a}^T \mathbf{x} \leq b \right\}, \quad (3.1)$$

— a hyperplane in \mathbb{R}^n is represented by a linear equality

$$\mathcal{HS} = \left\{ \mathbf{x} \in \mathbb{R}^{n \times 1} \mid \mathbf{c}^T \mathbf{x} = d \right\}, \quad (3.2)$$

where $\mathbf{a}, \mathbf{c} \in \mathbb{R}^{n \times 1}$ are normal vectors of the halfspace and hyperplane, $b, d \in \mathbb{R}$ are two scaled values associated with halfspace and hyperplane.

Then, a polytope can be represented in \mathcal{H} -representation and \mathcal{V} -representation respectively as follows:

1. \mathcal{H} -representation

$$\mathcal{P} = \left\{ \mathbf{x} \in \mathbb{R}^{n \times 1} \mid \mathbf{A}\mathbf{x} \leq \mathbf{b}, \mathbf{C}\mathbf{x} = \mathbf{d} \right\} \quad (3.3)$$

where $\mathbf{A} \in \mathbb{R}^{m \times n}$ and $\mathbf{b} \in \mathbb{R}^{m \times 1}$ represent m halfspaces in \mathbb{R}^n , while $\mathbf{C} \in \mathbb{R}^{p \times n}$ and $\mathbf{d} \in \mathbb{R}^{p \times 1}$ represent p halfplanes in \mathbb{R}^n . Rows of matrix \mathbf{A} (respectively \mathbf{C}) contain each normal vector associated to a corresponding halfspace (respectively hyperplane).

2. \mathcal{V} -representation

$$\mathcal{P} = \text{conv}(\mathcal{S}) \quad (3.4)$$

where \mathcal{S} is a set of vertices and \mathcal{P} is the convex hull noted $\mathbf{conv}(\mathcal{S})$

$$\mathbf{conv}(\mathcal{S}) = \left\{ \sum_{i=1}^k \alpha_i \mathbf{x}_i \mid \mathbf{x}_i \in \mathcal{S}, \alpha_i \geq 0, \sum_{i=1}^k \alpha_i = 1 \right\} \quad (3.5)$$

Given a certain convex polytope in the \mathcal{H} -representation, computing its \mathcal{V} -representation is called the vertex enumeration problem. The reverse problem is referred to as the facet enumeration problem [Fukuda, 2020].

3.1.3 Overview of the proposed method to obtain the available body wrench set

With the aim of analyzing the manipulability, this chapter proposes a geometric method to compute the available wrench set, which we refer to as the available body wrench set. The available body wrench set is the set of wrenches that can be applied by quadrotors on the robot's body, considering the following constraints: actuators' capabilities, the yaw torque that must be applied by each quadrotor to drive the opening/closing motion of the corresponding finger and static equilibrium conditions that apply for each quadrotor when passive joints are introduced between quadrotors and the robot's body.

A general overview of the proposed method is given here:

1. This method uses convex sets to model the available actuation set of quadrotors and obtain the available body wrench set of the robot.
2. There are multiple steps in this method that successively transform the available actuation set to compute the available body wrench set using different operations (see Appendix A). These steps are based on equations given in the static model in chapter 2.
3. It is also worthy to mention that one can start from a 16D space (Flying Gripper has 16 actuators $\boldsymbol{\Omega} \in \mathbb{R}^{16 \times 1}$) and want to obtain a 6D body wrench polytope (${}^b\mathbf{w}_b \in \mathbb{R}^{6 \times 1}$). We can apply a projection of a 16D available actuation set in the body wrench space using a 6×16 matrix. However, this requires vertex enumeration and generates a very large number of vertices 2^{16} , which is not computationally effective. Instead, we prefer to begin with the available actuation set in a 4D space for each quadrotor (one quadrotor has 4 actuators $\boldsymbol{\Omega}_i \in \mathbb{R}^{4 \times 1}$), then we study the set of wrenches that can be applied on the robot's body by each UAV one after

the other and, at a final step, sum all these sets using the Minkowski sum (refer to Appendix A).

4. We choose to represent polytopes using \mathcal{H} -representation instead of \mathcal{V} -representation. The advantage of the \mathcal{H} -representation is that it gives an exact representation, whereas \mathcal{V} -representation is an approximation. Vertex enumeration can generate numeric difficulties. The second advantage is that \mathcal{H} -representation permits an easier analysis of the dimension of the polytope and thus of manipulability. Full manipulability requires that the dimension of the available body wrench set is equal to the dimension of the body wrench space. In our method, we decide to use the \mathcal{H} -representation as far as it is computationally efficient. In any case, at the end, \mathcal{H} -representation of the available body wrench set is required to compute performance criteria.

Here, we shortly explain each step of the proposed method as follows (see Table 3.1)

1. Step 1: modeling the available actuation set in \mathbb{R}^4 for each quadrotor considering inequality constraints imposed on motor speed squares $\Omega_i \in \mathbb{R}^{4 \times 1}$ with \mathcal{H} -representation.
2. Step 2: linear bijection using $\Gamma_i \in \mathbb{R}^{4 \times 4}$ to map the available actuation set in the UAV reduced wrench space in \mathbb{R}^4 expressed in \mathcal{F}_i (using \mathcal{H} -representation, see Appendix A), which gives the available UAV reduced wrench set.
3. Step 3: lifting the available UAV reduced wrench set from \mathbb{R}^4 to \mathbb{R}^6 in the local UAV wrench space, which gives the available UAV wrench set. This operation permits to apply a simple linear bijection at step 4 while preserving the use of the \mathcal{H} -representation.
 - (a) Step 3-bis : imposing the yaw torque equality constraint that is required to close or open the finger. This can be geometrically interpreted as the intersection of a polytope with a hyperplane.
 - (b) Step 3-ter : imposing equality constraints required to satisfy the UAV static equilibrium. This step applies only for robots with mobile attitude UAVs, when a passive joint is introduced between the UAV and the worm screw.
4. Step 4: linear bijection, using ${}^b\mathbf{W}_i \in \mathbb{R}^{6 \times 6}$ to map the available UAV wrench set in the body wrench space (in \mathbb{R}^6). It should be noted that for the robot with mobile attitude quadrotors, ${}^b\mathbf{W}_i$ depends on the attitude of the corresponding UAV.

5. Step 5: Minkowski sum of multiple available UAV wrench sets in the body wrench space. Note that the obtained available body wrench set is a polytope in \mathbb{R}^6 . This later operation can be achieved using \mathcal{V} -representation or \mathcal{H} -representation [Fukuda, 2020]. In the former case, vertex enumeration of each UAV wrench set has to be applied first.

Table 3.1 – Wrench capability analysis scheme for FG-FAQ and FG-MAQ at an instant configuration

	Studied space	Available set
	step 1: model actuators capabilities using polytopes in \mathcal{H} -representation	
UAV actuation space	$\Omega_i \in \mathbb{R}^{4 \times 1}$	$\mathcal{A}_i \subset \mathbb{R}^4$
	step 2: linear bijection $\Gamma_i \in \mathbb{R}^{4 \times 4}$	
UAV reduced wrench space in \mathcal{F}_i	${}^i\mathbf{w}_i^r \in \mathbb{R}^{4 \times 1}$	$\mathcal{W}_i^r \subset \mathbb{R}^4$
	step 3: lifting	
UAV wrench space in \mathcal{F}_i	${}^i\mathbf{w}_i \in \mathbb{R}^{6 \times 1}$	$\mathcal{W}_i \subset \mathbb{R}^6$
	step 3-bis: intersection with yaw torque equality constraint	
	${}^i\mathbf{w}_i \in \mathbb{R}^{6 \times 1} (\tau_{i,z} = \pm\tau_f)$	$\mathcal{W}_i^{\text{yaw}} \subset \mathbb{R}^6$
	step 3-ter*: intersection with UAV static equilibrium equality constraint	
	${}^i\mathbf{w}_i \in \mathbb{R}^{6 \times 1} (\tau_{i,x} = \tau_{i,y} = 0)$	$\mathcal{W}_i^{\text{eq}} \subset \mathbb{R}^6$
	step 4: linear bijection ${}^b\mathbf{W}_i \in \mathbb{R}^{6 \times 6}$	
Body wrench space in \mathcal{F}_b	${}^b\mathbf{w}_{i,b} \in \mathbb{R}^{6 \times 1}$	$\mathcal{W}_i^b \subset \mathbb{R}^6$
	step 5: Minkowski sum	
	${}^b\mathbf{w}_b \in \mathbb{R}^{6 \times 1}$	$\mathcal{W}_b \subset \mathbb{R}^6$

* step 3-ter only for FG-MAQ

The approach presented in Table 3.2 computes the available body wrench set for FG-MAQ at an instant configuration. Then, another approach is proposed that considers all admissible configurations allowed by mechanical stops of universal joints. This approach shares the same steps 1 to 3-bis with the above one, and it is presented as follows:

1. Step 3-quater: linear bijection ${}^s\mathbf{W}_i(\boldsymbol{\eta}_i) \in \mathbb{R}^{6 \times 6}$ maps the available UAV wrench set in \mathcal{F}_{s_i} which is a frame attached to the worm screw linked with quadrotor i . The available UAV wrench set considering all admissible configurations is obtained computing the convex hull of union of ${}^s\mathbf{W}_i(\boldsymbol{\eta}_i)$.
2. Step 4: linear bijection, using ${}^b\mathbf{W}_{s_i} \in \mathbb{R}^{6 \times 6}$ to map the available UAV wrench set computed in the previous step in the body wrench space.

3. Step 5: Minkowski sum of multiple available UAV wrench sets in the body wrench space.

Table 3.2 – Wrench capability analysis scheme for FG-MAQ for all admissible configurations

	Studied space	Available set
	step 3-quad: linear bijection ${}^s\mathbf{W}_i \in \mathbb{R}^{6 \times 6}$	
UAV wrench space in \mathcal{F}_{s_i}	${}^s\mathbf{w}_i \in \mathbb{R}^{6 \times 1}$	$\mathcal{W}_i^s(\boldsymbol{\eta}_i) \subset \mathbb{R}^6$
	convex hull of union	
	${}^s\mathbf{w}_i \in \mathbb{R}^{6 \times 1}$	$\mathcal{W}_i^s \subset \mathbb{R}^6$
	step 4: linear bijection ${}^b\mathbf{W}_{s_i} \in \mathbb{R}^{6 \times 6}$	
Body wrench space in \mathcal{F}_b	${}^b\mathbf{w}_{i,b} \in \mathbb{R}^{6 \times 1}$	$\mathcal{W}_i^b \subset \mathbb{R}^6$
	step 5: Minkowski sum	
	${}^b\mathbf{w}_b \in \mathbb{R}^{6 \times 1}$	$\mathcal{W}_b \subset \mathbb{R}^6$

\mathcal{F}_{s_i} is a frame attached to the worm screw linked with quadrotor i . Its origin coincides with the CoM of the quadrotor. It should be noted that \mathcal{F}_{s_i} is fixed with respect to \mathcal{F}_b .

3.2 Wrench capability analysis of a Planar Aerial Manipulator (PAM)

In this section, we apply our method to a Planar Aerial Manipulator (PAM) and analyze its wrench capability in $SE(2)$. The analysis for this robot offers a simple way to explain this method and studying in $SE(2)$ permits to visualize all steps.

We present three different cases: the first applies to a Planar Aerial Manipulator with Fixed-Attitude Birotors (PAM-FAB); the second applies to a Planar Aerial Manipulator with Mobile-Attitude Birotors (PAM-MAB) and considers an instant configuration of the mechanism; the third is the same PAM-MAB robot but considers all admissible configurations of the mechanism.

3.2.1 Available body wrench set of PAM-FAB

In the following, we build, in 5 steps, the available body wrench set of PAM-FAB (see Fig. 3.1). Each birotor has two propellers and has a fixed attitude w.r.t the robot's body given by angle α .

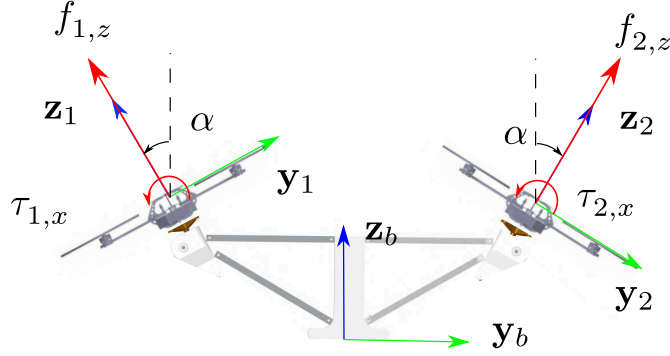


Figure 3.1 – CAD view of Planar Aerial Manipulator with Fixed-Attitude Birotors (PAM-FAB) that consists of a body structure and two birotors that are linked to the body structure with a tilting angle α . Each birotor can generate a thrust force $f_{i,z}$ and a roll torque $\tau_{i,x}$ in \mathcal{F}_i .

Step 1. Available UAV Actuation Set \mathcal{A}_i

The first step of the method consists in determining the available actuation set of one UAV.

For the PAM-FAB robot, each birotor actuation capacity is saturated by the two motors' limits. We use the vector $\boldsymbol{\Omega}_i = [\omega_{i,1}^2 \ \omega_{i,2}^2]^T \in \mathbb{R}^{2 \times 1}$ to represent the birotor actuation state, where $\omega_{i,1}$ and $\omega_{i,2}$ are the two motors' speed of the i^{th} birotor. Thus, each birotor's capability is modeled by a lower bound $\underline{\boldsymbol{\Omega}} = [\omega_{\min}^2 \ \omega_{\min}^2]^T \in \mathbb{R}^{2 \times 1}$ and an upper bound $\overline{\boldsymbol{\Omega}} = [\omega_{\max}^2 \ \omega_{\max}^2]^T \in \mathbb{R}^{2 \times 1}$ as

$$\underline{\boldsymbol{\Omega}} \leq \boldsymbol{\Omega}_i \leq \overline{\boldsymbol{\Omega}}. \quad (3.6)$$

We define the available UAV actuation set \mathcal{A}_i for birotor i as follows

$$\mathcal{A}_i = \left\{ \boldsymbol{\Omega}_i \in \mathbb{R}^{2 \times 1} \mid \underline{\boldsymbol{\Omega}} \leq \boldsymbol{\Omega}_i \leq \overline{\boldsymbol{\Omega}} \right\}. \quad (3.7)$$

This set of inequalities is rewritten in \mathcal{H} -representation of a polytope using notations introduced in section 3.1.2:

$$\mathcal{A}_i = \left\{ \boldsymbol{\Omega}_i \in \mathbb{R}^{2 \times 1} \mid \mathbf{A}_{\Omega_i} \boldsymbol{\Omega}_i \leq \mathbf{b}_{\Omega_i} \right\} \quad (3.8)$$

in which $\mathbf{b}_{\Omega_i} = [\overline{\boldsymbol{\Omega}}^T \ \vdots \ -\underline{\boldsymbol{\Omega}}^T]^T \in \mathbb{R}^{4 \times 1}$, $\mathbf{A}_{\Omega_i} = [\mathbf{I}_2 \ \vdots \ -\mathbf{I}_2]^T \in \mathbb{R}^{4 \times 2}$ and 4 stands for the number of inequalities and 2 is for the dimension of the UAV actuation space. The

available UAV actuation set \mathcal{A}_i is a square in the 2D space $(\omega_{i,1}^2, \omega_{i,2}^2)$ (see Fig. 3.2).

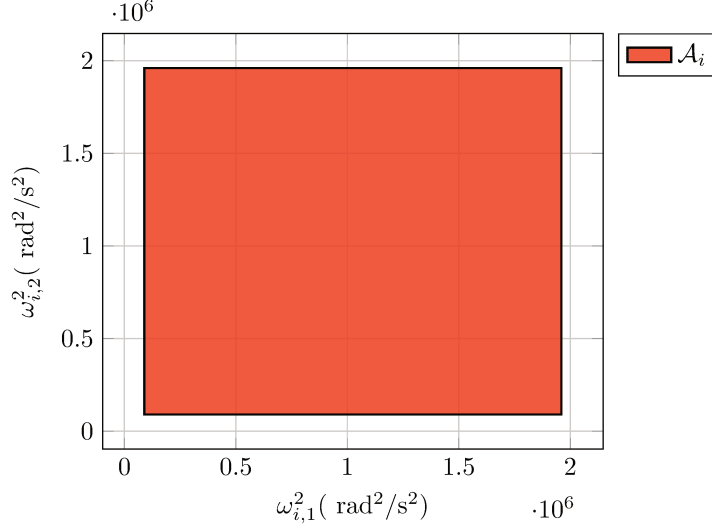


Figure 3.2 – \mathcal{A}_i : available UAV actuation set of birotor i . \mathcal{A}_i is a square in the 2D space $(\omega_{i,1}^2, \omega_{i,2}^2)$ where $\omega_{i,1}$ and $\omega_{i,2}$ are the two motors' speed of birotor i . This figure is obtained with a minimal and maximal motor speeds of respectively 300 rad/sec and 1400 rad/sec for each rotor.

Step 2. Linear mapping of \mathcal{A}_i in UAV reduced local wrench space

There exists a constant linear relation between $\mathbf{\Omega}_i$ and the birotor's reduced wrench ${}^i\mathbf{w}_{i,r} = [f_{i,z} \quad \tau_{i,x}]^T$ expressed in \mathcal{F}_i (see Fig. 3.1)

$${}^i\mathbf{w}_{i,r} = \mathbf{\Gamma}_i \mathbf{\Omega}_i \quad (3.9)$$

where $\mathbf{\Gamma}_i \in \mathbb{R}^{2 \times 2}$ is a square and invertible matrix

$$\mathbf{\Gamma}_i = \begin{bmatrix} c_t & c_t \\ -c_t d_q & c_t d_q \end{bmatrix}. \quad (3.10)$$

Considering this linear bijective relation, the available UAV reduced wrench set for ${}^i\mathbf{w}_{i,r}$, can be developed as

$$\mathcal{W}_i^r = \left\{ {}^i\mathbf{w}_{i,r} \in \mathbb{R}^{2 \times 1} \mid \mathbf{A}_{i,r}^i {}^i\mathbf{w}_{i,r} \leq \mathbf{b}_{\Omega_i} \right\} \quad (3.11)$$

where $\mathbf{A}_{i,r}^i = \mathbf{A}_{\Omega_i} \mathbf{\Gamma}_i^{-1} \in \mathbb{R}^{4 \times 2}$ (see Appendix about linear mapping of polytopes).

As we can see, the above polytope using the \mathcal{H} -representation is made of 4 inequalities in \mathbb{R}^2 . These inequalities correspond to the actuators' capabilities. Therefore, \mathcal{W}_i^r describes the set of possible wrenches that the i^{th} birotor is able to produce in \mathcal{F}_i under the motor limits, which is a rhombus in the 2D space $(f_{i,z}, \tau_{i,x})$ (see Fig.3.3).

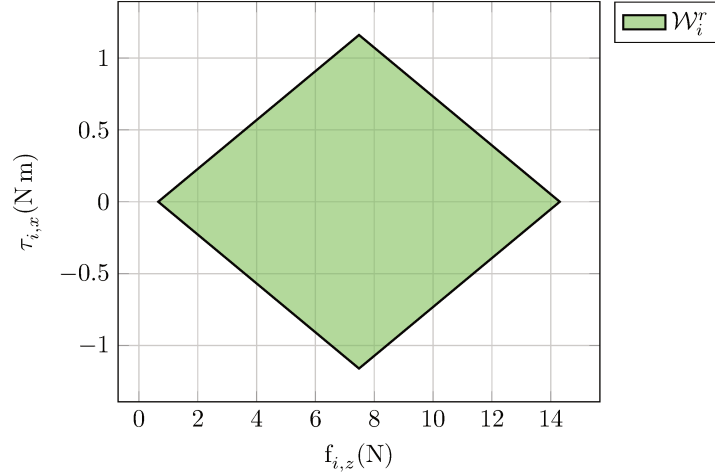


Figure 3.3 – \mathcal{W}_i^r : available UAV reduced wrench set of birotor i of PAM-FAB. \mathcal{W}_i^r is a planar rhombus in the 2D space $(f_{i,z}, \tau_{i,x})$ where $f_{i,z}$ and $\tau_{i,x}$ are the i^{th} UAV's thrust force and roll torque expressed in \mathcal{F}_i .

Step 3 : Lifting of \mathcal{W}_i^r in UAV 3D Local Wrench Space

We introduce this intermediate step before mapping the available UAV reduced wrench set $\mathcal{W}_i^r \subset \mathbb{R}^2$ in the body wrench space (in \mathbb{R}^3) whose dimension is larger than that of \mathcal{W}_i^r . A linear mapping from a low dimensional space to a high dimensional space cannot apply to a polytope while keeping \mathcal{H} -representation (see Appendix about linear mapping on polytopes).

It is shown that the UAV reduced wrench ${}^i\mathbf{w}_i^r = [f_{i,z} \ \tau_{i,x}]^T$ is a 2×1 vector in \mathcal{F}_i , whereas the UAV wrench is a 3×1 vector ${}^i\mathbf{w}_i = [f_{i,y} \ f_{i,z} \ \tau_{i,x}]^T$ in \mathcal{F}_i , where $f_{i,y}$ is the force produced by the UAV along \mathbf{y}_i in \mathcal{F}_i (see Fig. 3.1). Thus, we first modify the \mathcal{H} -representation of the polytope \mathcal{W}_i^r in order to express the available UAV wrench set in the 3D space $(f_{i,y}, f_{i,z}, \tau_{i,x})$ which will permit us to apply a simple linear bijective application at the next step to obtain the corresponding polytope in the body wrench space as both of them are in \mathbb{R}^3 . This permits to keep using the \mathcal{H} -representation and avoid vertex enumeration. We further call this operation as lifting operation.

This lifting operation requires increasing the dimension of all row vectors of matrix $\mathbf{A}_{i,r}^i$, namely the normal vectors¹, such that inequalities remain true whatever the value of the additional component of the wrench $f_{i,y}$. This is achieved by simply adding a zero to the component corresponding to $f_{i,y}$. This permits to obtain the following matrix, whose rows are the lifted normal vectors:

$$\mathbf{A}_i^i = \left[\mathbf{0}_{4 \times 1} \mid \mathbf{A}_{i,r}^i \right] \quad (3.12)$$

Thus, \mathbf{A}_i^i is now a 4×3 matrix. The following inequality generates an unbounded tube with a rhombus section (see Fig. 3.4)

$$\mathbf{A}_i^i \mathbf{w}_i \leq \mathbf{b}_{\Omega_i} \quad (3.13)$$

We now apply the equality $f_{i,y} = 0$, which remains true whatever the values of $f_{i,z}$ and $\tau_{i,x}$, since a birotor cannot produce a thrust force along the \mathbf{y}_i direction. This is achieved by introducing a supplementary halfplane in the \mathcal{H} -representation of \mathcal{W}_i , which results in the available UAV wrench set in \mathcal{F}_i :

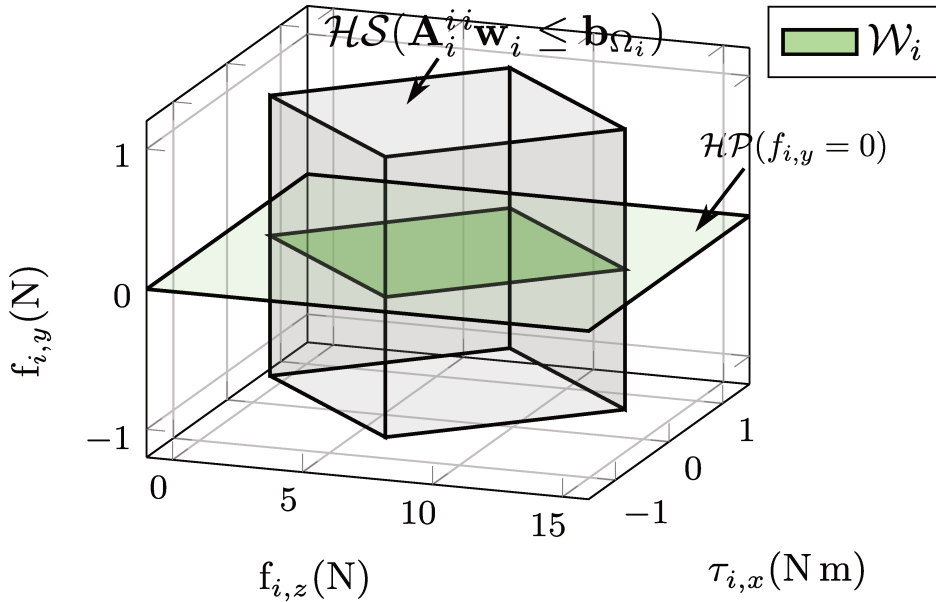


Figure 3.4 – \mathcal{W}_i : available UAV wrench set \mathcal{W}_i of birotor i of PAM-FAB after lifting and it remains a planar rhombus in the 3D space $(f_{i,y}, f_{i,z}, \tau_{i,x})$.

1. each row vector of $\mathbf{A}_{i,r}^i$ matrix corresponds to a normal vector of the corresponding halfspace

$$\mathcal{W}_i = \left\{ {}^i\mathbf{w}_i \in \mathbb{R}^{3 \times 1} \mid \mathbf{A}_i^i {}^i\mathbf{w}_i \leq \mathbf{b}_{\Omega_i}, \mathbf{C}_i^i {}^i\mathbf{w}_i = 0 \right\} \quad (3.14)$$

with $\mathbf{A}_i^i = \begin{bmatrix} \mathbf{0} & \mathbf{A}_{i,r}^i \end{bmatrix} = \begin{bmatrix} \mathbf{0} & \mathbf{A}_{\Omega_i} \mathbf{\Gamma}_i^{-1} \end{bmatrix} \in \mathbb{R}^{4 \times 3}$ from the actuators' capabilities and $\mathbf{C}_i^i = \mathbf{e}_1^T \in \mathbb{R}^{1 \times 3}$ imposed by $f_{i,y} = 0$. So, the \mathcal{H} -representation is conserved and the linear mapping operations can still be found in \mathbf{A}_i^i .

It is interesting to note that, in Eq.(3.14), there is 1 equality represented by \mathbf{C}_i^i . Thus, \mathcal{W}_i is a polytope with a dimension of 2 in \mathbb{R}^3 . As we can see from Fig. 3.4, \mathcal{W}_i is a planar rhombus in the 3D space $(f_{i,y}, f_{i,z}, \tau_{i,x})$.

Step 4 : Linear mapping of \mathcal{W}_i in body wrench space

The term ${}^b\mathbf{w}_{i,b} \in \mathbb{R}^{3 \times 1}$ refers to the wrench applied to the body structure by the i^{th} birotor, which is computed by applying a linear 3×3 bijection to ${}^i\mathbf{w}_i$ that

$${}^b\mathbf{w}_{i,b} = {}^b\mathbf{W}_i {}^i\mathbf{w}_i \quad (3.15)$$

where ${}^b\mathbf{W}_i \in \mathbb{R}^{3 \times 3}$ is a square and invertible matrix

$${}^b\mathbf{W}_i = \begin{bmatrix} {}^b\mathbf{R}_i & \mathbf{0} \\ [{}^b\mathbf{r}_i]_{\times} & {}^b\mathbf{R}_i \quad \mathbf{1} \end{bmatrix}. \quad (3.16)$$

We can now compute the available set for ${}^b\mathbf{w}_{i,b}$ that can be applied by the i^{th} birotor to the robot's body, expressed in the body frame \mathcal{F}_b , by applying the linear bijection ${}^b\mathbf{W}_i$ to \mathcal{W}_i on the set of halfspaces (inequalities) and on the set of hyperplanes (equalities):

$$\mathcal{W}_i^b = \left\{ {}^b\mathbf{w}_{i,b} \in \mathbb{R}^{3 \times 1} \mid \mathbf{A}_i^i {}^b\mathbf{W}_i^{-1} {}^b\mathbf{w}_{i,b} \leq \mathbf{b}_{\Omega_i}, \mathbf{C}_i^i {}^b\mathbf{W}_i^{-1} {}^b\mathbf{w}_{i,b} = 0 \right\} \quad (3.17)$$

where

1. matrix $\mathbf{A}_i^i {}^b\mathbf{W}_i^{-1} = \begin{bmatrix} \mathbf{0} & \mathbf{A}_{\Omega_i} \mathbf{\Gamma}_i^{-1} \end{bmatrix} {}^b\mathbf{W}_i^{-1} = \begin{bmatrix} \mathbf{0} & \mathbf{A}_{\Omega_i} \mathbf{\Gamma}_i^{-1} {}^b\mathbf{W}_i^{-1} \end{bmatrix} \in \mathbb{R}^{4 \times 3}$ refers to 4 inequality constraints on wrench ${}^b\mathbf{w}_{i,b} \in \mathbb{R}^{3 \times 1}$,
2. vector $\mathbf{C}_i^i {}^b\mathbf{W}_i^{-1} \in \mathbb{R}^{1 \times 3}$ refers to 1 equality constraint.

At this step, we can use \mathcal{W}_i^b to represent the wrench set that can be applied to the robot body by quadrotor i . Since there is 1 equality shown in Eq.(3.17), \mathcal{W}_i^b is a 2D polytope in the 3D space. As shown in Fig.3.5, \mathcal{W}_1^b and \mathcal{W}_2^b are two 2D polytopes in the 3D wrench space $({}^b f_{b,y}, {}^b f_{b,z}, {}^b \tau_{b,x})$.

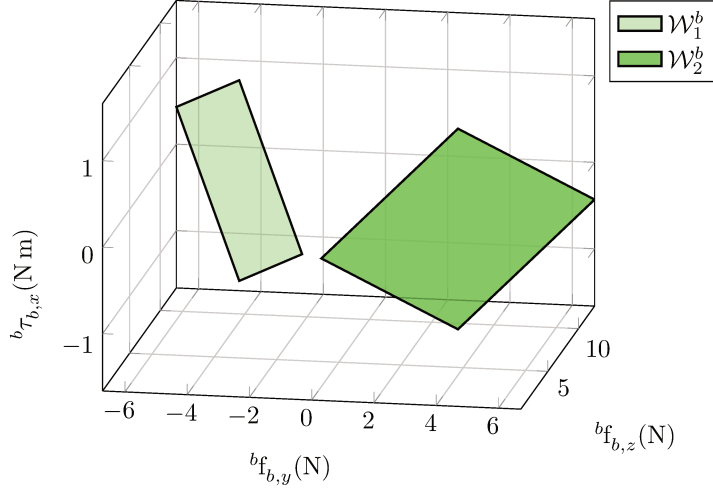


Figure 3.5 – \mathcal{W}_1^b and \mathcal{W}_2^b : available UAV wrench sets mapped in the body wrench space of PAM-FAB robot ($\alpha = 28^\circ$). Each set \mathcal{W}_i^b is a 2D polytope in the 3D wrench space (${}^b f_{b,y}, {}^b f_{b,z}, {}^b \tau_{b,x}$).

Step 5 : Minkowski Sum of \mathcal{W}_1^b and \mathcal{W}_2^b

The resulting body wrench vector ${}^b \mathbf{w}_b$ is simply obtained as the sum of ${}^b \mathbf{w}_{i,b}$ for each birotor

$${}^b \mathbf{w}_b = {}^b \mathbf{w}_{1,b} + {}^b \mathbf{w}_{2,b}. \quad (3.18)$$

Thus, the set of feasible resulting body wrenches applied by birotors can be obtained using the Minkowski sum of both sets \mathcal{W}_1^b and \mathcal{W}_2^b (see Appendix A about the Minkowski sum of polytopes). The Minkowski sum gives all linear combinations of ${}^b \mathbf{w}_{1,b} \in \mathcal{W}_1^b$ and ${}^b \mathbf{w}_{2,b} \in \mathcal{W}_2^b$:

$$\mathcal{W}_b = \mathcal{W}_1^b \oplus \mathcal{W}_2^b \quad (3.19)$$

where \oplus stands for the Minkowski sum (see Fig. 3.6). There is no equality constraint in the \mathcal{H} -representation of \mathcal{W}_b , so \mathcal{W}_b is a 3D polytope, which can be seen in Fig. 3.6. Furthermore, \mathcal{W}_b is a 3D polytope including the wrench compensating gravity in its interior, showing that PAM-FAB is able to produce a wrench in any direction (${}^b f_{b,y}, {}^b f_{b,z}, {}^b \tau_{b,x}$) and the robot achieves full manipulability in $SE(2)$.

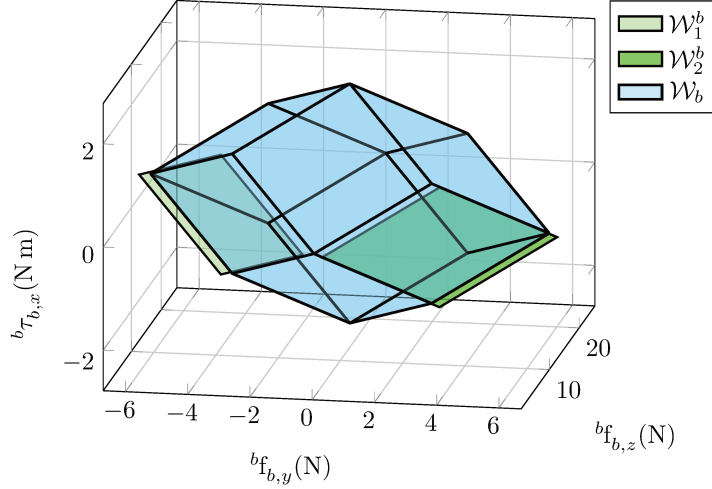


Figure 3.6 – \mathcal{W}_b : available body wrench set of PAM-FAB robot ($\alpha = 28^\circ$). In the 3D wrench space $(b^f_{I_{b,y}}, b^f_{I_{b,z}}, b^{\tau_{b,x}})$, each \mathcal{W}_i^b is a 2D polytope, while \mathcal{W}_b is a 3D polytope with the wrench compensating gravity is strictly inside, which demonstrates that the robot achieves full manipulability in $SE(2)$.

3.2.2 Available body wrench set of PAM-MAB

In this section, we introduce the PAM-MAB robot, shown in Fig. 3.7. It consists of a body structure and two birotors each one being linked to the body structure through one revolute joint (R-joint).

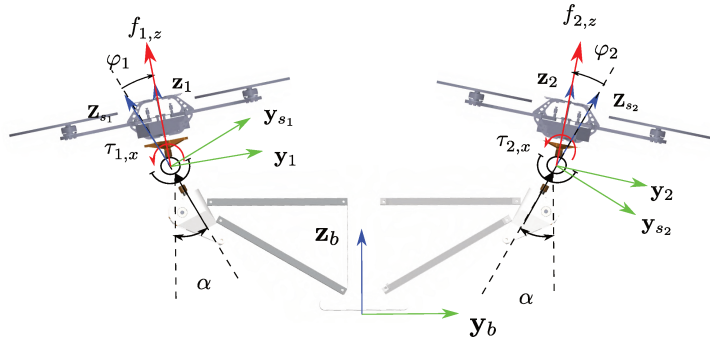


Figure 3.7 – CAD view of Planar Aerial Manipulator with Mobile-Attitude Birotors (PAM-MAB): consisting of a body structure and two birotors that are linked to the body structure through revolute joints. Each birotor generates a thrust force $f_{i,z}$ and a roll torque $\tau_{i,x}$ in frame \mathcal{F}_i , and its rotation w.r.t \mathcal{F}_{s_i} is represented by φ_i .

We introduce a new frame \mathcal{F}_{s_i} , which indicates the central attitude of the birotor w.r.t the body structure. We assume that the origins of \mathcal{F}_i and \mathcal{F}_{s_i} coincide with the CoM of the UAV whose \mathbf{z}_{s_i} axis coincides with the worm screw axis. It should be noted, that \mathcal{F}_{s_i}

is fixed with respect to \mathcal{F}_b , its attitude α is a design parameter, whereas the attitude \mathcal{F}_i depends on the variable φ_i . Mechanical stops impose $-\varphi_{\max} < \varphi_i < \varphi_{\max}$.

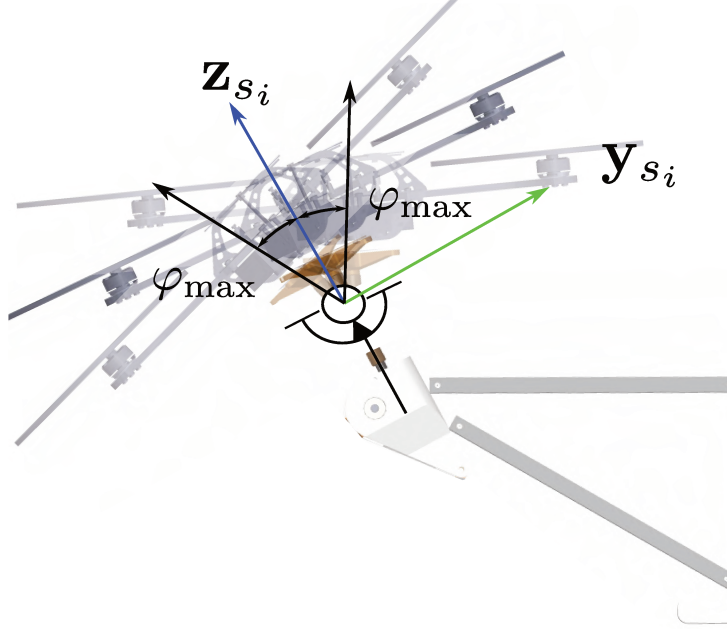


Figure 3.8 – Available rotation range of birotor i in \mathcal{F}_{s_i} : φ_{\max} is the maximal rotation angle allowed by the mechanical stop of revolute joint.

Since we implement the same birotors as for the PAM-FAB robot, both robots share the same actuation capacities. Thus, steps 1, 2 and 3 of the analysis of the PAM-FAB robot presented in the previous section, can be reproduced identically to obtain \mathcal{W}_i that is given in Eq. (3.14).

Step 3-bis : Introducing UAV static equilibrium condition

Due to the introduction of passive joints, each birotor gains an additional DOF: the roll rotation about \mathbf{x}_i axis of its local frame. This implies that no torque around \mathbf{x}_i can be transmitted to the robot's body by the i^{th} birotor. Static equilibrium imposes

$$\tau_{i,x} = 0. \quad (3.20)$$

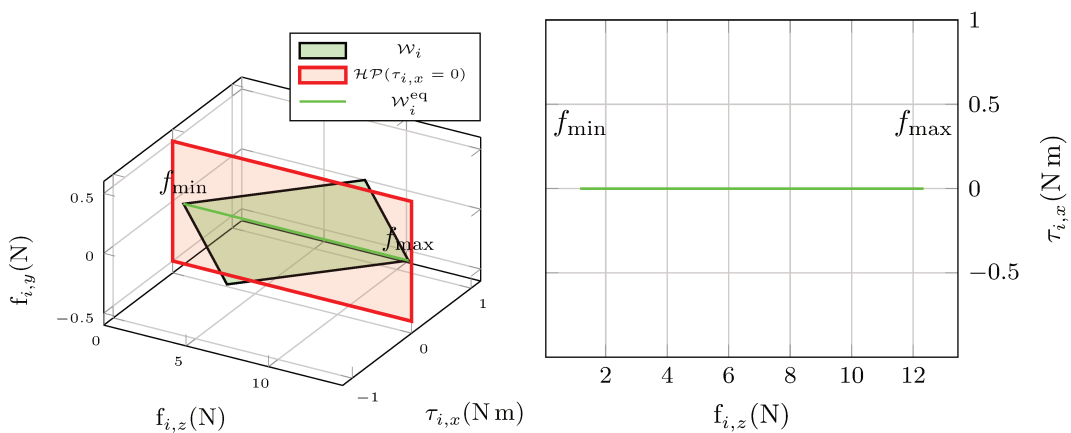
Considering this additional equality constraint, the available UAV wrench set satisfying equality constraints can be rewritten using the following \mathcal{H} -representation:

$$\mathcal{W}_i^{\text{eq}} = \left\{ {}^i\mathbf{w}_i \in \mathbb{R}^{3 \times 1} \mid \mathbf{A}_i^{ii} \mathbf{w}_i \leq \mathbf{b}_{\Omega_i}, \mathbf{C}_i^{\text{eq}i} \mathbf{w}_i = \mathbf{0} \right\} \quad (3.21)$$

where

1. $\mathbf{A}_i^i = \begin{bmatrix} \mathbf{0} & \mathbf{A}_{i,r}^i \end{bmatrix} = \begin{bmatrix} \mathbf{0} & \mathbf{A}_{\Omega_i} \mathbf{\Gamma}_i^{-1} \end{bmatrix} \in \mathbb{R}^{4 \times 3}$,
2. $\mathbf{C}_i^{\text{eq}} = \begin{bmatrix} \mathbf{e}_1 & \mathbf{e}_3 \end{bmatrix}^T \in \mathbb{R}^{2 \times 3}$.

Since there exist 2 equalities in $\mathcal{W}_i^{\text{eq}}$, we can conclude that $\mathcal{W}_i^{\text{eq}}$ is a polytope of dimension 1, i.e. 1 dimension set, in the 3D space. As illustrated by the polytope $\mathcal{W}_i^{\text{eq}}$ plotted in Fig. 3.9, each birotor i can only generate a thrust force $f_{i,z} \in [f_{\min} \ f_{\max}]$ along \mathbf{z}_i direction.



(a) Intersection of \mathcal{W}_i with $\mathcal{HP}(\tau_{i,x} = 0)$ (b) Minimal and maximal thrust forces of $\mathcal{W}_i^{\text{eq}}$

Figure 3.9 – $\mathcal{W}_i^{\text{eq}}$: available UAV wrench set of PAM-MAB in \mathcal{F}_i satisfying static equilibrium. This polytope is obtained as the intersection of \mathcal{W}_i with the static equilibrium hyperplane $\mathcal{HP}(\tau_{i,x} = 0)$. It finally is a line segment in the 3D wrench space $(f_{i,y}, f_{i,z}, \tau_{i,x})$.

Step 4 : Linear mapping of $\mathcal{W}_i^{\text{eq}}$ in body wrench space

In this case, step 4 differs slightly from the previous method, in that the attitude of birotor i is now represented by φ_i . Indeed, matrix \mathbf{W}_i now depends on φ_i . To insist on this point, it will be further written as $\mathbf{W}_i(\varphi_i)$

$${}^b\mathbf{w}_{i,b} = \mathbf{W}_i(\varphi_i) {}^i\mathbf{w}_i. \quad (3.22)$$

The available UAV wrench set \mathcal{W}_i^b is written as follows

$$\mathcal{W}_i^b(\varphi_i) = \left\{ {}^b\mathbf{w}_{i,b} \in \mathbb{R}^{3 \times 1} \mid \mathbf{A}_i^{ib} \mathbf{W}_i^{-1}(\varphi_i) {}^b\mathbf{w}_{i,b} \leq \mathbf{b}_{\Omega_i}, \mathbf{C}_i^{\text{eq}} \mathbf{W}_i^{-1}(\varphi_i) {}^b\mathbf{w}_{i,b} = \mathbf{0} \right\} \quad (3.23)$$

where

1. matrix $\mathbf{A}_i^{ib}\mathbf{W}_i^{-1}(\varphi_i) = \begin{bmatrix} \mathbf{0} & \mathbf{A}_{\Omega_i}\mathbf{\Gamma}_i^{-1} \end{bmatrix}^b\mathbf{W}_i^{-1}(\varphi_i) = \begin{bmatrix} \mathbf{0} & \mathbf{A}_{\Omega_i}\mathbf{\Gamma}_i^{-1}{}^b\mathbf{W}_i^{-1}(\varphi_i) \end{bmatrix} \in \mathbb{R}^{4 \times 3}$ refers to 4 inequality constraints on wrench ${}^b\mathbf{w}_{i,b} \in \mathbb{R}^{3 \times 1}$,
2. vector $\mathbf{C}_i^{\text{eq}b}\mathbf{W}_i^{-1}(\varphi_i) \in \mathbb{R}^{2 \times 3}$ refers to 2 equality constraints.

Again, we find that $\mathcal{W}_i^b(\varphi_i)$ is a 2D polytope in the 3D body wrench space.

It is interesting to compare \mathcal{W}_i^b of PAM-FAB in Eq. (3.17) and PAM-MAB in Eq. (3.23). Both have the same inequality constraints expression, while \mathcal{W}_i^b of the PAM-MAB robot has an additional equality constraint imposed by static equilibrium of the passive R-joint.

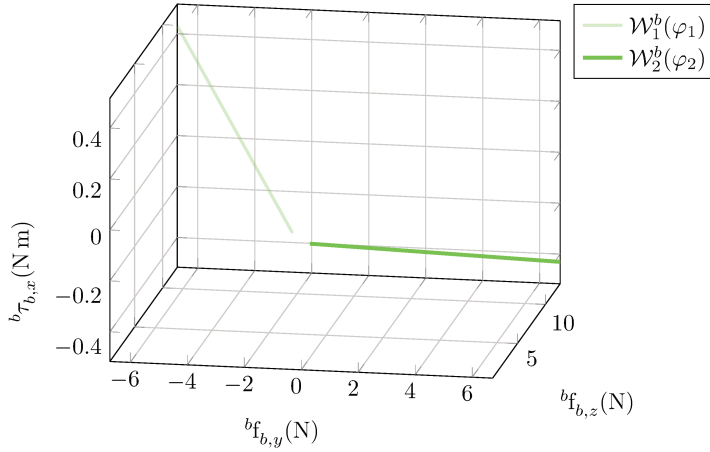


Figure 3.10 – $\mathcal{W}_i^b(\varphi_i)$: Available UAV wrench set mapped in the body wrench space of PAM-MAB robot for the configuration $\varphi_1 = 0^\circ, \varphi_2 = 0^\circ$. $\mathcal{W}_i^b(\varphi_i)$ is a line segment in the 3D wrench space $({}^b f_{b,y}, {}^b f_{b,z}, {}^b \tau_{b,x})$.

Step 5 : Minkowski sum of \mathcal{W}_1^b and \mathcal{W}_2^b

Again, we apply the Minkowski sum to compute the available body wrench set $\mathcal{W}_b = \mathcal{W}_1^b \oplus \mathcal{W}_2^b$

The resulting sets are plotted for two different attitudes of the birotors :

1. when $\varphi_1 = 0^\circ, \varphi_2 = 0^\circ$, see Fig. 3.11a;
2. when $\varphi_1 = -28^\circ, \varphi_2 = 28^\circ$ (the birotors are in the horizontal plane), see Fig. 3.11b.

Since \mathcal{W}_1^b and \mathcal{W}_2^b are two polytopes of dimension 1, \mathcal{W}_b can be a polytope with a dimension of at most 2. This result illustrates that the PAM-MAB robot cannot generate any independent wrench in $SE(2)$ and does not achieve full manipulability in $SE(2)$. This is true whatever the attitude of each birotor.

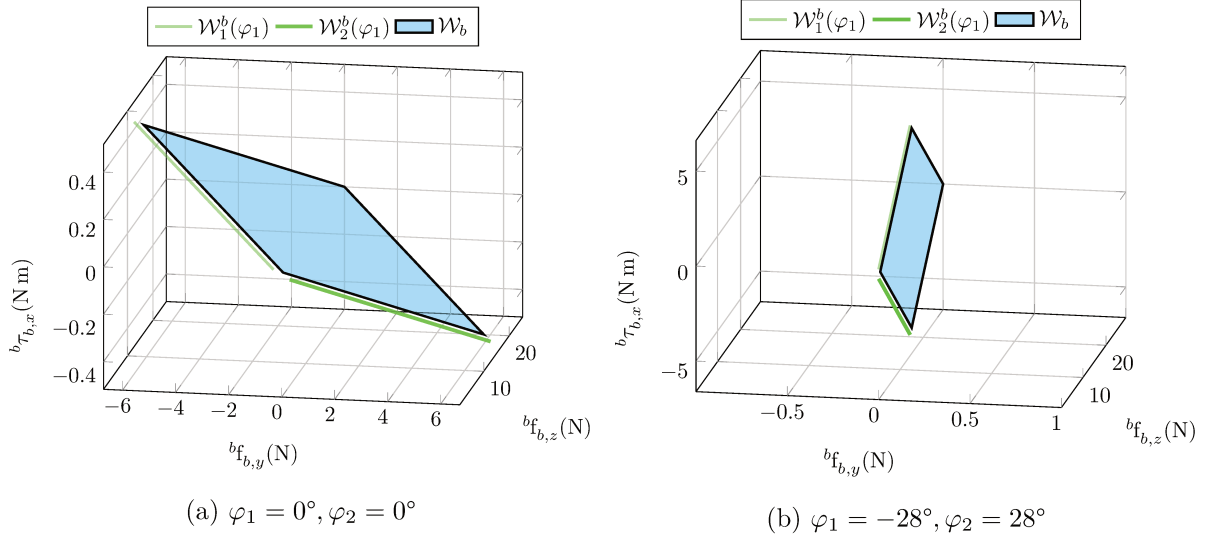


Figure 3.11 – \mathcal{W}_b : available body wrench set of PAM-MAB robot for configurations (a) $\varphi_1 = 0^\circ, \varphi_2 = 0^\circ$ and (b) $\varphi_1 = -28^\circ, \varphi_2 = 28^\circ$. In both cases, \mathcal{W}_b is a 2D polytope in the 3D wrench space $({}^b f_{b,y}, {}^b f_{b,z}, {}^b \tau_{b,x})$, showing that this robot does not allow full manipulability in $SE(2)$.

3.2.3 Available body wrench set of PAM-MAB for all admissible configurations

This section proposes a new method to analyze the manipulability of the PAM-MAB robot. Whereas the method presented in 3.2.2 considers a given attitude for each birotor, the method presented below considers all admissible attitudes of birotors under constraints imposed by mechanical stops restraining birotors' attitudes. Therefore, we assume that each birotor can instantly switch from a configuration to another, i.e. neglecting its rotational dynamics. This assumption is done in [Nguyen et al., 2018] but not explicitly.

Since, we analyze the same mechanism analyzed in section 3.2.2, the result of the step 3bis will be the starting point. It gives the available UAV wrench set $\mathcal{W}_i^{\text{eq}}$ satisfying the UAV static equilibrium condition (see Eq. (3.21)).

Step 3-ter: Linear mapping in \mathcal{F}_s and consideration of R-joint mechanical stops

We first express the available UAV wrench in \mathcal{F}_{s_i} as ${}^s \mathbf{w}_i = [{}^s f_{i,y} \quad {}^s f_{i,z} \quad {}^s \tau_{i,x}]^T \in \mathbb{R}^{3 \times 1}$ that

$${}^s \mathbf{w}_i = {}^s \mathbf{W}_i(\varphi_i) {}^i \mathbf{w}_i \quad (3.24)$$

where ${}^s\mathbf{W}_i(\varphi_i) = \begin{bmatrix} {}^s\mathbf{R}_i & \mathbf{0} \\ \mathbf{0} & 1 \end{bmatrix} \in \mathbb{R}^{3 \times 3}$ is a square and invertible matrix.

The available UAV wrench set $\mathcal{W}_i^s(\varphi_i)$ expressed in \mathcal{F}_{s_i} is calculated as

$$\mathcal{W}_i^s(\varphi_i) = \left\{ {}^s\mathbf{w}_i \in \mathbb{R}^{3 \times 1} \mid \mathbf{A}_i^i {}^s\mathbf{W}_i^{-1}(\varphi_i) {}^s\mathbf{w}_i \leq \mathbf{b}_{\Omega_i}, \mathbf{C}_i^{\text{eq}s} {}^s\mathbf{W}_i^{-1}(\varphi_i) {}^s\mathbf{w}_i = \mathbf{0} \right\}. \quad (3.25)$$

In order to consider all admissible attitude φ_i of birotor i , we compute multiple $\mathcal{W}_i^s(\varphi_i)$ with $-\varphi_{\max} \leq \varphi_i \leq \varphi_{\max}$ (see Fig. 3.12). The interval is discretized to approximate the final set. We then build the union of these sets of polytopes. Since, the resulting union set is not necessarily convex, we further compute its convex hull. As it can be seen in Fig. 3.12, the convex hull of union of $\mathcal{W}_i^s(\varphi_i)$ is actually close to the original non-convex set.

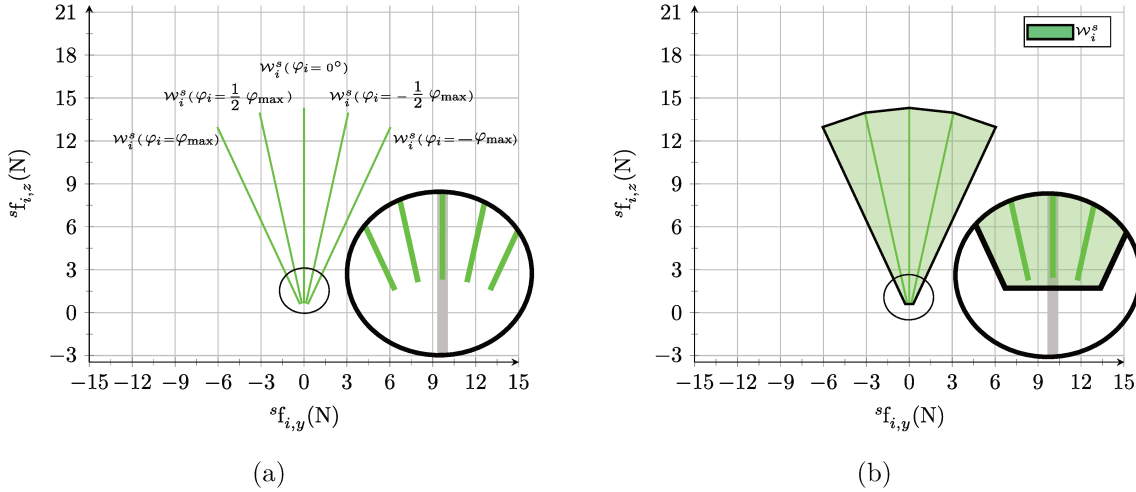


Figure 3.12 – (a) Available UAV wrench set $\mathcal{W}_i^s(\varphi)$ in \mathcal{F}_{s_i} at different admissible attitudes of PAM-MAB: $\varphi_i = 0^\circ, \pm \frac{1}{2}\varphi_{\max}, \pm \varphi_{\max}$. Each $\mathcal{W}_i^s(\varphi)$ is a line segment. (b) Available UAV wrench set \mathcal{W}_i^s is the convex hull of union of multiple admissible configurations of PAM-MAB expressed in frame \mathcal{F}_{s_i} .

$$\mathcal{W}_i^s = \mathbf{conv} \left(\bigcup_{\varphi_i \in [-\varphi_{\max}, \varphi_{\max}]} \mathcal{W}_i^s(\varphi_i) \right) = \mathbf{conv}(\mathcal{S}_i^p), \quad (3.26)$$

At this stage, \mathcal{W}_i^s is defined using the \mathcal{V} -representation with \mathcal{S}_i^p being the set of vertices of the union's convex hull for the birotor i of PAM-MAB². In the following, we'll keep on using the \mathcal{V} -representation for computational efficiency. It is important to note that \mathcal{W}_i^s

2. the output of the convex hull operation of the union is a set of vertices

is an linearized approximation for the available UAV wrench set. Also, \mathcal{W}_i^s does not rely on the attitude of the birotor φ_i , but solely on the actuators' capabilities, the mechanical stops of revolute joints and the number of generators used in the union.

Step 4 : Linear mapping of \mathcal{W}_i^s in body wrench space

The UAV wrench expressed in the body frame ${}^b\mathbf{w}_{i,b}$ can be obtained using the following formula:

$${}^b\mathbf{w}_{i,b} = {}^b\mathbf{W}_{s_i} {}^s\mathbf{w}_i. \quad (3.27)$$

where ${}^b\mathbf{W}_{s_i} = \begin{bmatrix} {}^b\mathbf{R}_{s_i} & \mathbf{0} \\ \mathbf{0} & 1 \end{bmatrix} \in \mathbb{R}^{3 \times 3}$ is a constant square and invertible matrix.

The set \mathcal{W}_i^b expressed in \mathcal{F}_b is obtained as follows (see Appendix A about linear mapping on polytopes using \mathcal{V} -representation)

$$\mathcal{W}_i^b = \text{conv}({}^b\mathbf{W}_{s_i}(\mathcal{S}_i^p)). \quad (3.28)$$

Even though we express \mathcal{W}_i^b using \mathcal{V} -representation, we can still tell that \mathcal{W}_i^b is a 2D polytope from Fig. 3.13.

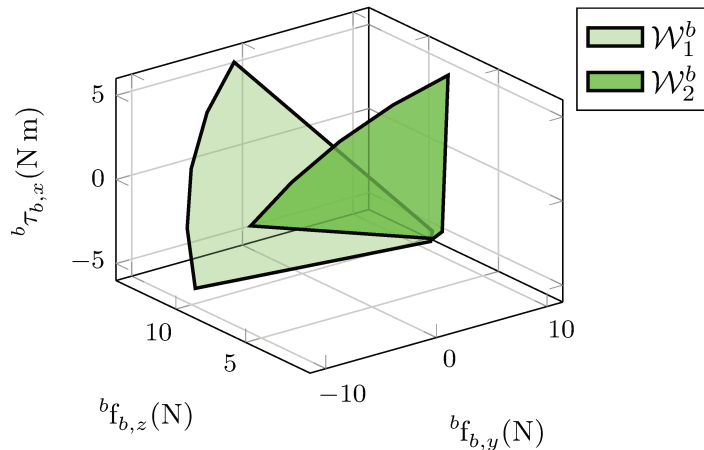


Figure 3.13 – Available UAV wrench sets mapped in the body wrench space $\mathcal{W}_1^b, \mathcal{W}_2^b$ for PAM-MAB. $\mathcal{W}_i^b, i = 1, 2$, is a 2D polygon in the 3D wrench space $({}^b f_{b,y}, {}^b f_{b,z}, {}^b \tau_{b,x})$.

Step 5 : Minkowski sum of \mathcal{W}_1^b and \mathcal{W}_2^b

The available body wrench set \mathcal{W}_b is obtained using the Minkowski sum $\mathcal{W}_b = \mathcal{W}_1^b \oplus \mathcal{W}_2^b$. It is recalled that this set does not rely on attitudes of birotors φ_i but depends on

the mechanical stops imposed on birotors' attitudes.

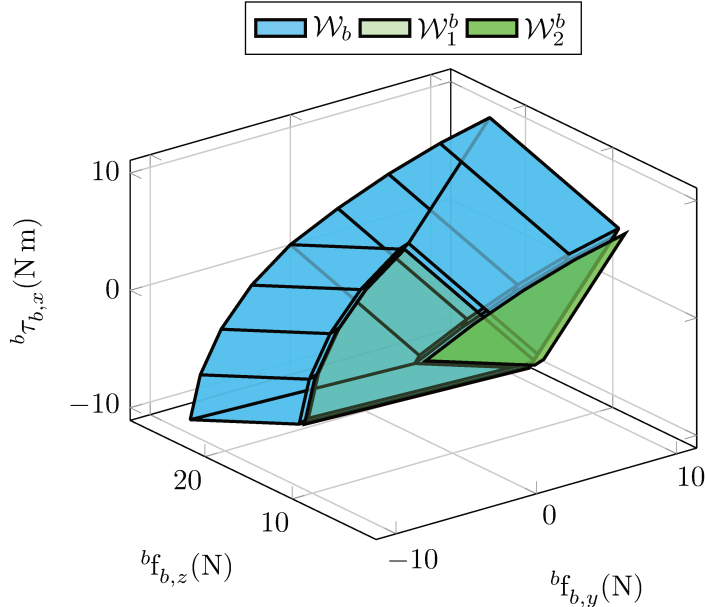


Figure 3.14 – \mathcal{W}_b : available body wrench set of PAM-MAB robot for all admissible configurations. In wrench space $({}^b f_{b,y}, {}^b f_{b,z}, {}^b \tau_{b,x})$, \mathcal{W}_b is obtained using the Minkowski sum of the available wrench sets applied to body structure by each birotor: \mathcal{W}_1^b and \mathcal{W}_2^b . \mathcal{W}_b is a 3D polytope containing the wrench compensating gravity in its interior, indicating that the PAM-MAB robot allows full manipulability in $SE(2)$.

Analyzing the result in Fig. 3.14, we can find that the available body wrench set \mathcal{W}_b of the PAM-MAB robot is a 3D polytope in the 3D wrench space $({}^b f_{b,y}, {}^b f_{b,z}, {}^b \tau_{b,x})$ containing the wrench compensating gravity in its interior. It demonstrates that the robot achieves full manipulability and its DOF can be fully controlled in $SE(2)$.

3.2.4 Discussion on results

First, the available UAV wrench sets of the three cases are discussed. Then, a qualitative criterion is used to check if full manipulability is achieved and a quantitative criterion is used to compare the manipulability.

Available UAV wrench sets of PAM-FAB and PAM-MAB

The available UAV wrench sets of PAM-FAB and PAM-MAB are illustrated in Fig. 3.15. For the PAM-FAB robot, \mathcal{W}_i expressed in \mathcal{F}_i is a 2D polytope (in the plane $\mathcal{HP}(f_{i,y} = 0)$)

in the space $(f_{i,y}, f_{i,z}, \tau_{i,x})$. It is worthy to note that $\mathcal{W}_i^{\text{eq}}$ expressed in \mathcal{F}_i of the PAM-MAB robot is a 1D set. If we consider all admissible configurations allowed by the mechanical stops of revolute joints, \mathcal{W}_i^s expressed in \mathcal{F}_{s_i} of PAM-MAB is a 2D polytope (in the plane $\mathcal{HP}({}^s\tau_{i,x} = 0)$) in the space $({}^s f_{i,y}, {}^s f_{i,z}, {}^s \tau_{i,x})$.

Comparing the results in Fig. 3.15, it shows that the mechanical design of PAM influences the available UAV wrench set. For the PAM-FAB robot, a birotor cannot generate a force along \mathbf{y}_i . For the PAM-MAB robot for an instant configuration, a birotor can not produce any force along \mathbf{y}_i or any torque along \mathbf{x}_i (loose 1 degree of actuation), while for the PAM-MAB robot for all admissible configurations, a birotor generates no torque along \mathbf{x}_{s_i} .

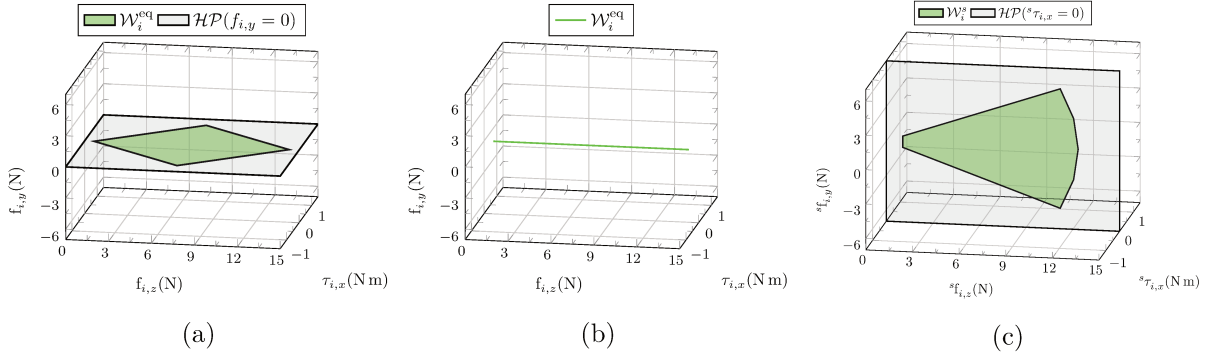


Figure 3.15 – Available UAV wrench sets of PAM: (a) \mathcal{W}_i of PAM-FAB in \mathcal{F}_i , (b) $\mathcal{W}_i^{\text{eq}}$ of PAM-MAB at an instant configuration in \mathcal{F}_i , (c) \mathcal{W}_i^s of PAM-MAB for all admissible configurations in \mathcal{F}_{s_i} .

A qualitative performance criteria to check full manipulability of PAM-FAB and PAM-MAB

Furthermore, we analyze the robot's manipulability and we use a sufficient and necessary condition for full manipulability: checking if the wrench compensating gravity is strictly inside \mathcal{W}_b . If it is strictly inside of \mathcal{W}_b , then the robot is able to generate a wrench with any direction while compensating gravity. Also, there is a necessary condition for full manipulability: the dimension of \mathcal{W}_b equals to the dimension of the body wrench space. Thus, it is possible to check the \mathcal{H} -representation of \mathcal{W}_b using this necessary condition. Indeed, if the set of linearly independent equalities describing \mathcal{W}_b is not empty, it means that the dimension of \mathcal{W}_b is lower than the space in which it is represented and only wrenches that satisfy the set of inequalities can be applied. In other words, if the dimension of \mathcal{W}_b

is smaller than that of the space, then the robot cannot achieve full manipulability.

As shown in Table 3.3, the PAM-FAB robot and PAM-MAB robot for all admissible configurations allow full manipulability in $SE(2)$ as the wrench compensating gravity is strictly inside \mathcal{W}_b , while \mathcal{W}_b of the PAM-MAB robot for an instant configuration has a dimension of 2 which is smaller than that of $SE(2)$, demonstrating that the robot does not allow full manipulability in $SE(2)$.

A quantitative performance criterion to compare the wrench capabilities of PAM-FAB and PAM-MAB

Since both PAM-FAB and PAM-MAB robots allow full manipulability in $SE(2)$, we now use a quantitative criterion to compare their capabilities to generate a set of wrenches. We therefore use a performance index presented in [Saint-Sevin et al., 2019] that is the radius r_c of the largest circle included in three polytopes defined as the intersections of the available body wrench set \mathcal{W}_b respectively and each of the three planes defined by $\tau_{i,x} = 0 \text{ N m}$, $\tau_{i,x} = \pm 1 \text{ N m}$ (see Table 3.3).

In order to take into account the gravity, the center of the inscribed circle is imposed at point $[0 \ m_t g]$ (see Appendix A about how to compute r_c). Indeed, r_c stands for the maximal force that the robot is able to exert in any direction while compensating gravity and exerting a torque $\tau_{i,x}$ between -1 N m and 1 N m . This method permits to avoid analyzing a polytope with heterogeneous units. The results are given in Table 3.3.

The result demonstrates that the PAM-MAB robot has a larger manipulability than the PAM-FAB robot does.

3.2. Wrench capability analysis of a Planar Aerial Manipulator (PAM)

Table 3.3 – Comparing manipulability of PAM-FAB and PAM-MAB

	PAM-FAB	PAM-MAB	PAM-MAB*
\mathcal{W}_b			
Dimension of \mathcal{W}_b polytope	3	2	3
Full manipulability in $SE(2)$	Yes	No	Yes
		\emptyset	
		\emptyset	
r_c	3.1 N	\emptyset	4.9 N

* consider all admissible configurations of quadrotor imposed by R-joints

3.3 Wrench capability analysis of FG-FAQ and FG-MAQ

In this section, we now study the Flying Gripper robot using 4 quadrotors that are presented in chapter 2. We again compare both architectures with Fixed-Attitude Quadrotors (FG-FAQ) and with Mobile-Attitude Quadrotors (FG-MAQ). The method used to analyze the Flying Gripper robot is similar to the method presented in section 3.2 to analyze the illustrative example of the PAM robot. However, the following differences need to be considered:

1. The Flying Gripper robot is actuated by 4 quadrotors, whereas the PAM robot is actuated by 2 birotors.
2. The manipulability of Flying Gripper is studied in $SE(3)$, whereas the manipulability of PAM was studied in $SE(2)$ for a visualization purpose.
3. The Flying Gripper robot is equipped with 4 fingers actuated by the yaw torque generated by the corresponding quadrotor, therefore these constraints have to be considered in the construction of the available UAV wrench sets.
4. In the case of the Flying Gripper with Mobile-Attitude Quadrotors (FG-MAQ), a passive universal joint is introduced between each quadrotor and its corresponding finger, which modifies the static equilibrium conditions given in section 3.2.2 for the PAM robot which uses passive revolute joints.

This section directly gives the available UAV wrench sets, but more details can be found in Appendix B. In Appendix B, a Planar Flying Gripper actuated by two quadrotors (PFG) is introduced and a full analysis of the following cases is given: one with Fixed-Attitude Quadrotors (PFG-FAQ), one with Mobile-Attitude Quadrotors (PFG-MAQ) and PFG-MAQ for all admissible configurations.

3.3.1 Available body wrench sets of FG-FAQ and FG-MAQ

As introduced in chapter 2, the Flying Gripper is designed to grasp and manipulate a large size object and it has four different operating modes: free flight, grasping, manipulation, placing. In the free flight and placing modes, each quadrotor keeps its yaw rotation fixed, while it produces a yaw rotation to close or open the corresponding finger in the grasping and placing modes.

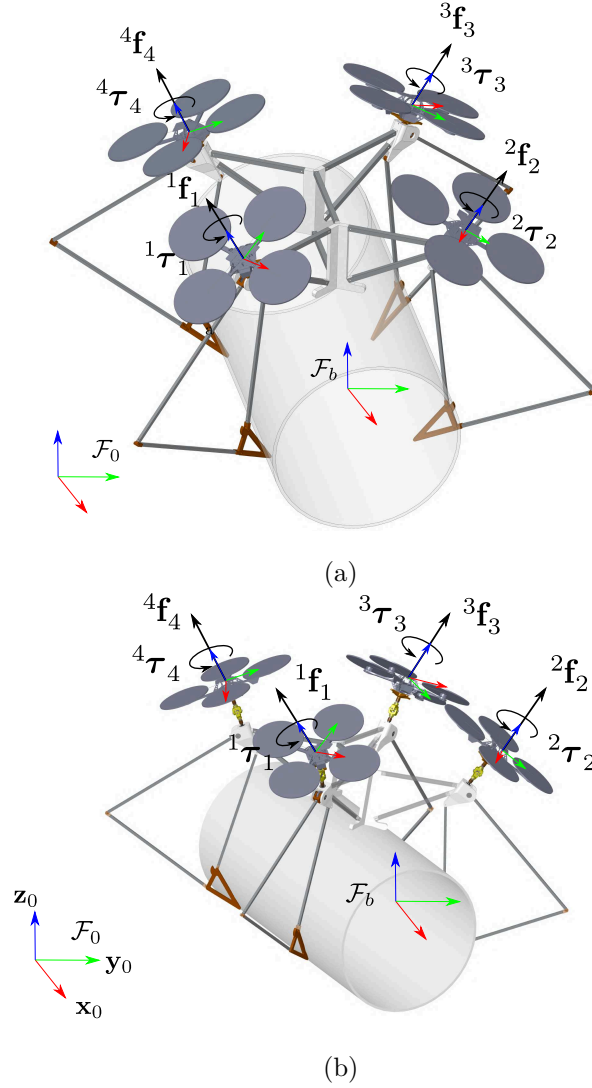


Figure 3.16 – Representation of FG-FAQ robot in (a) and FG-MAQ robot in (b). Each quadrotor generates a thrust force ${}^i\mathbf{f}_i$ and a torque ${}^i\tau_i$ expressed in frame \mathcal{F}_i .

Thus, a simple model is proposed to describe the available UAV wrench sets in the different operating modes:

1. in the grasping or placing mode, each quadrotor produces a yaw torque
 - in the grasping mode: $\tau_{1,z} = \tau_{3,z} = \tau_f, \tau_{2,z} = \tau_{4,z} = -\tau_f$,
 - in the placing mode: $\tau_{1,z} = \tau_{3,z} = -\tau_f, \tau_{2,z} = \tau_{4,z} = \tau_f$,
2. in the free flight or manipulation mode, each quadrotor generates a zero yaw torque

$$\tau_{i,z} = 0. \quad (3.29)$$

Here, the wrench capability of the robot is compared using two quantitative criteria that are the largest sphere inscribed in the available force set \mathcal{W}_f and the largest sphere inscribed in the available force set \mathcal{W}_τ , where

1. \mathcal{W}_f is the available force set when the robot generates zero torque: it is computed as the intersection of \mathcal{W}_b with $\mathcal{HP}({}^b\tau_{b,x} = 0, {}^b\tau_{b,y} = 0, {}^b\tau_{b,z} = 0)$,
2. \mathcal{W}_τ is the available torque set when the robot generates a force that compensates gravity: it is computed as the intersection of \mathcal{W}_b with $\mathcal{HP}({}^bf_{b,x} = 0, {}^bf_{b,y} = 0, {}^bf_{b,z} = m_t g)$ and m_t stands for the mass of the whole robot.

Then, two criteria to compare the wrench capability of the robot are introduced here:

1. r_f is the radius of the largest sphere centered on $(f_x, f_y, f_z) = (0, 0, m_t g)$ inscribed in \mathcal{W}_f ,
2. r_τ is the radius of the largest sphere centered on the origin $(\tau_x, \tau_y, \tau_z) = (0, 0, 0)$ inscribed in \mathcal{W}_τ .

Such spheres represent the maximal force (torque) that the robot is able to exert in any direction: r_f describes the maximal force that the robot is able to exert in any direction apart from when the robot generates no torque, while r_τ describes the maximal torque that the robot is able to exert in any direction when the robot compensates gravity.

3.3.2 Discussion on results

Available UAV wrench sets of FG-FAQ and FG-MAQ

The available UAV wrench sets of FG-FAQ and FG-MAQ when grasping are shown in Fig. 3.17. For the FG-FAQ robot, $\mathcal{W}_i^{\text{yaw}}$ is the available UAV wrench set expressed in \mathcal{F}_i that considers the actuators' capabilities, the yaw torque constraints. However, for the FG-MAQ robot at an instant configuration, $\mathcal{W}_i^{\text{eq}}$ is the available UAV wrench set expressed in \mathcal{F}_i that considers also mobility imposed by the passive U-joint, while \mathcal{W}_i^s is the available UAV wrench set of the FG-MAQ robot for all admissible configurations expressed in \mathcal{F}_{s_i} .

In the 6D space $(f_{i,x}, f_{i,y}, f_{i,z}, \tau_{i,x}, \tau_{i,y}, \tau_{i,z})$, $\mathcal{W}_i^{\text{yaw}}$ is a 3D polytope and, interestingly, $\mathcal{W}_i^{\text{eq}}$ is a 1D set. It means that a quadrotor of FG-MAQ can only generate a 1D force while producing a constant yaw torque. When considering all admissible configurations allowed by the mechanical stops of the U-joints, \mathcal{W}_i^s is a linearized approximation of a cone in the space $({}^s f_{i,x}, {}^s f_{i,y}, {}^s f_{i,z})$.

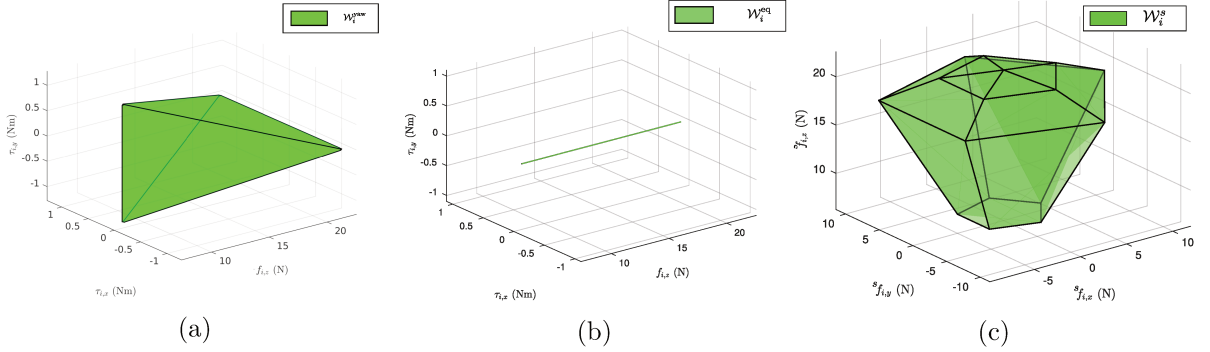


Figure 3.17 – Available UAV wrench sets of Flying Gripper: (a) \mathcal{W}_i of FG-FAQ in the 3D space $(f_{i,z}, \tau_{i,x}, \tau_{i,y})$, (b) $\mathcal{W}_i^{\text{faq}}$ of FG-MAQ at an instant configuration in the 3D space $(f_{i,z}, \tau_{i,x}, \tau_{i,y})$, (c) \mathcal{W}_i^s of FG-MAQ for all admissible configurations in \mathcal{F}_{s_i} in the 3D space $({}^s f_{i,x}, {}^s f_{i,y}, {}^s f_{i,z})$.

Analyzing manipulability of FG-FAQ and FG-MAQ

In order to analyze the robot's manipulability, a sufficient and necessary condition for full manipulability is used: checking if the wrench $\mathbf{w}_0 = [m_t \mathbf{g}^T \quad \mathbf{0}]^T \in \mathbb{R}^{6 \times 1}$ is strictly inside \mathcal{W}_b . Also, we can check the robot's manipulability using the dimension of \mathcal{W}_b in \mathbb{R}^6 . If the dimension is smaller than 6, then the robot does not have full manipulability in $SE(3)$: a 6D polytope is a necessary condition for full manipulability.

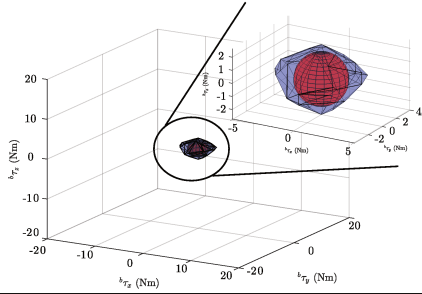
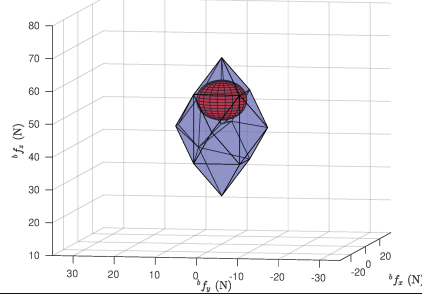
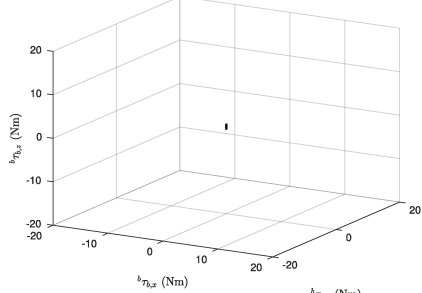
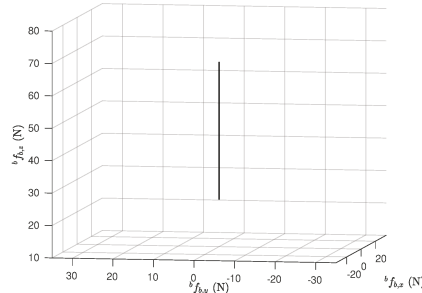
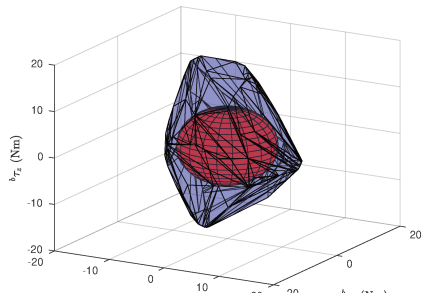
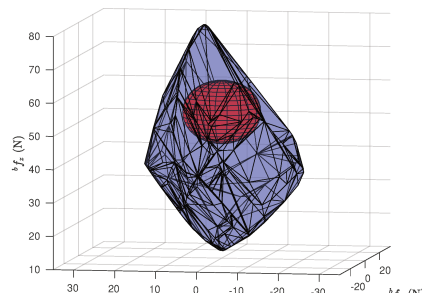
The FG-FAQ and FG-MAQ (all admissible configurations) robots allow full manipulability in $SE(3)$, as \mathbf{w}_0 is strictly inside \mathcal{W}_b . Nevertheless, it is interesting to note that, the FG-MAQ robot at an instant configuration cannot achieve full manipulability because the dimension of \mathcal{W}_b is 4 that is smaller than the dimension of the body wrench space (in \mathbb{R}^6).

Comparing wrench capabilities of FG-FAQ and FG-MAQ

The available force set \mathcal{W}_f and the available torque set \mathcal{W}_τ are visualized in Table 3.4 (for the grasping mode) and Table 3.5 (for the manipulation mode) respectively. Concerning r_f and r_τ , we find that the FG-MAQ robot has a larger wrench capacity than the FG-FAQ does. Since none of these mechanisms dimensions is optimized, it is difficult to compare the wrench capabilities of these two robots. However, if one consider dimensions based on Table 3.4 and Table 3.5, one can conclude that FG-MAQ has larger capabilities in force and torque.

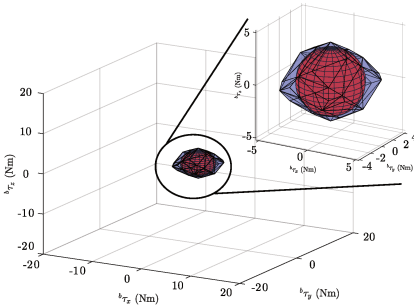
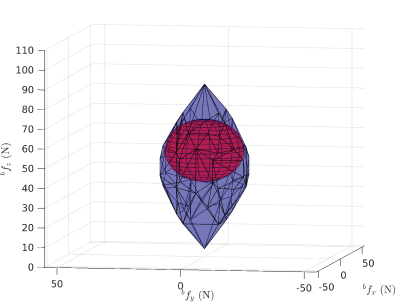
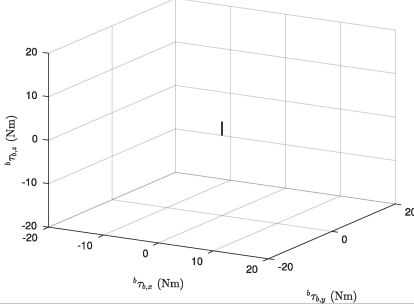
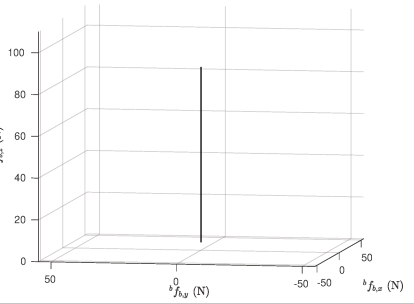
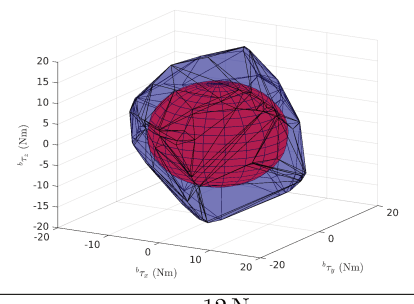
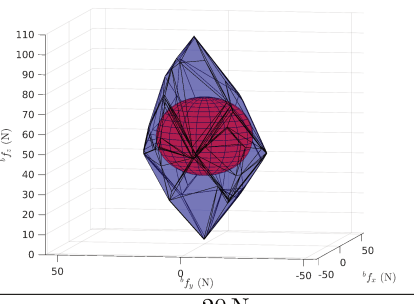
It is important to note that the superiority of FG-MAQ is based on the assumption

Table 3.4 – When closing fingers, \mathcal{W}_f and \mathcal{W}_τ of FG-FAQ and FG-MAQ robots. The available torque set \mathcal{W}_τ is computed as the intersection of \mathcal{W}_b with $\mathcal{HP}({}^b f_{b,x} = 0, {}^b f_{b,y} = 0, {}^b f_{b,z} = m_t g)$, and the available force set \mathcal{W}_f is calculated as the intersection of \mathcal{W}_b with $\mathcal{HP}({}^b \tau_{b,x} = 0, {}^b \tau_{b,y} = 0, {}^b \tau_{b,z} = 0)$

	full manipulability in $SE(3)$	\mathcal{W}_τ	\mathcal{W}_f
FG-FAQ $\dim(\mathcal{W}_b) = 6$	Yes	 <p style="text-align: center;">$r_\tau = 2.0 \text{ N m}$</p>	 <p style="text-align: center;">$r_f = 6.1 \text{ N}$</p>
FG-MAQ $\dim(\mathcal{W}_b) = 4$	No	 <p style="text-align: center;">$r_\tau = \emptyset$</p>	 <p style="text-align: center;">$r_f = \emptyset$</p>
FG-MAQ* $\dim(\mathcal{W}_b) = 6$	Yes	 <p style="text-align: center;">$r_\tau = 8.1 \text{ N m}$</p>	 <p style="text-align: center;">$r_f = 9.5 \text{ N}$</p>

* consider all admissible configuration of quadrotor imposed by U-joints
 $\dim(\mathcal{W}_b)$ means the dimension of the \mathcal{W}_b polytope

Table 3.5 – In manipulation mode, \mathcal{W}_f and \mathcal{W}_τ of FG-FAQ and FG-MAQ robots. The available torque set \mathcal{W}_τ is computed as the intersection of \mathcal{W}_b with $\mathcal{HP}(b_{f_{b,x}} = 0, b_{f_{b,y}} = 0, b_{f_{b,z}} = m_t g)$, and the available force set \mathcal{W}_f is calculated as the intersection of \mathcal{W}_b with $\mathcal{HP}(b_{\tau_{b,x}} = 0, b_{\tau_{b,y}} = 0, b_{\tau_{b,z}} = 0)$

	full manipulability in $SE(3)$	\mathcal{W}_τ	\mathcal{W}_f
FG-FAQ $\dim(\mathcal{W}_b) = 6$	Yes	 <p style="text-align: center;">$r_\tau = 3.1 \text{ N m}$</p>	 <p style="text-align: center;">$r_f = 16 \text{ N}$</p>
FG-MAQ $\dim(\mathcal{W}_b) = 4$	No	 <p style="text-align: center;">$r_\tau = \emptyset$</p>	 <p style="text-align: center;">$r_f = \emptyset$</p>
FG-MAQ* $\dim(\mathcal{W}_b) = 6$	Yes	 <p style="text-align: center;">$r_\tau = 12 \text{ N m}$</p>	 <p style="text-align: center;">$r_f = 20 \text{ N}$</p>

* consider all admissible configuration of quadrotor imposed by U-joints
 $\dim(\mathcal{W}_b)$ means the dimension of the \mathcal{W}_b polytope

that quadrotors can change their attitude instantly. An allocation algorithm is proposed in chapter 5 that permits to optimize the wrenches applied by each quadrotor taking into account the continuity of the quadrotor wrenches.

3.4 Conclusions

This chapter has presented a geometric and visual approach for analyzing the manipulability of the FG-FAQ and FG-MAQ robots, which considers the actuators' capabilities, the quadrotors' yaw torque constraints for driving fingers in closing/opening and the static equilibrium conditions when passive joints are introduced between the UAV and the robot's body.

We began modeling the available actuation set for one quadrotor as a set of inequalities. Then we computed the available UAV wrench set of each quadrotor taking into account equality constraints to model:

- the constraint on the yaw torque that must be exerted by the quadrotor to open or close the associated finger,
- the static equilibrium condition when a universal joint is introduced between the quadrotor and the robot's frame.

For mobile-attitude quadrotors, we explained how to draw the set of wrenches that can be applied by each quadrotor while satisfying mechanical stops. This is achieved using the union of multiple UAV wrench sets computed for various attitudes satisfying the mechanical stops.

All available UAV wrench sets are then mapped in the body wrench space before being summed using the Minkowski sum to obtain the final available body wrench set, that is the set of wrenches that can be applied by UAVs on the body structure. This method was illustrated on simpler versions of the Flying Gripper: PAM and PFG in Appendix B. In this process, we represented polytopes with \mathcal{H} -representation as far it was computationally efficient with respect to a method that uses \mathcal{V} -representation. \mathcal{H} -representation permits to avoid approximations due to vertex enumeration algorithms, it permits to analyze directly the dimension of polytopes obtained at each step and also compute performance indices.

Based on the obtained available body wrench set that is a polytope, we utilized a qualitative criterion to check if the robot achieves full manipulability in $SE(3)$: if and only if the wrench compensating gravity is strictly inside the available body wrench set. One necessary condition for full manipulability is that the dimension of the available body

wrench set equals to the dimension of the body wrench space. The results showed that both FG-FAQ and FG-MAQ robots obtain full manipulability in $SE(3)$.

Then, quantitative criteria to compare the wrench capabilities are used: the maximal sphere inscribed inside the available force set with zero torque and the maximal sphere inscribed inside the available torque set with gravity compensation. Even if both robots are not optimized, we can still reach the conclusion that the FG-MAQ robot has a better manipulability than the FG-FAQ robot does based on these two criteria.

MODEL PREDICTIVE CONTROL OF FLYING GRIPPER WITH FIXED-ATTITUDE QUADROTORS (FG-FAQ)

4.1 Control scheme of FG-FAQ	110
4.2 Model Predictive Control of FG-FAQ	114
4.3 Co-simulation of FG-FAQ robot	118
4.4 Conclusions	131

This chapter develops a controller for the Flying Gripper with Fixed-Attitude Quadrotors (FG-FAQ) robot based on the robot’s dynamic model previously developed in chapter 2. The main objectives of the controller are to control the robot’s motion and to close/open the robot’s fingers in different working modes. Based on the dynamic properties and over-actuation of the robot, we develop a general control scheme in section 4.1 that consists in two modules: a high motion controller module and a control allocation module. The high motion controller module enables the robot to move from an initial pose to a final pose following a reference trajectory. Then, the control allocation module not only to distribute control efforts, but also to ensure closing/opening fingers during the trajectory tracking. The main contribution of the chapter lies on the proposition of a model predictive control in the high motion controller module in section 4.2. In order to test our designed controller, we conduct several simulations using ADAMS-SIMULINK co-simulations in section 4.3. The co-simulation results validate the effectiveness of our controller and its robustness¹ against external disturbances and noise.

We note that the control method and its numerical validation presented in this chapter were published in [Li et al., 2020b].

1. Robustness refers to the robot’s performance dealing with disturbances and noise in this thesis.

4.1 Control scheme of FG-FAQ

The controller design is based on the FG-FAQ robot’s dynamic model that is developed in chapter 2. The robot’s configuration is characterized by the general coordinate vector $\mathbf{q}^f = [\mathbf{p}_b^T \ \mathbf{q}_a^{fT}]^T \in \mathbb{R}^{10 \times 1}$ where $\mathbf{p}_b \in \mathbb{R}^{6 \times 1}$ describes the body structure pose and $\mathbf{q}_a^f \in \mathbb{R}^{4 \times 1}$ represents all quadrotors’ yaw angles. The robot is overactuated as it has 10 DOF and 16 motors and there exists a redundancy of actuation.

We recall the dynamic model of the FG-FAQ that is modeled by Eq. (2.26) and Eq. (2.27) in chapter 2

$$\mathbf{M}_t \ddot{\mathbf{p}}_b + \mathbf{c}_t = \mathbf{w}_b \quad (4.1)$$

$$\mathbf{w}_b = \mathbf{W}_\Omega \Omega \quad (4.2)$$

where

1. The vector $\mathbf{w}_b = [\mathbf{}^0\mathbf{f}_b^T \ \mathbf{}^b\boldsymbol{\tau}_b^T]^T \in \mathbb{R}^{6 \times 1}$ represents the body wrench acting on the body structure applied by quadrotors, the force $\mathbf{}^0\mathbf{f}_b \in \mathbb{R}^{3 \times 1}$ is expressed in the world frame \mathcal{F}_0 , and the torque $\mathbf{}^b\boldsymbol{\tau}_b \in \mathbb{R}^{3 \times 1}$ is expressed in the body frame \mathcal{F}_b ;
2. The input of the dynamic model $\Omega = [\Omega_1^T \ \Omega_2^T \ \Omega_3^T \ \Omega_4^T]^T \in \mathbb{R}^{16 \times 1}$ is a vector regrouping all quadrotors’ motor speed squares and $\Omega_i \in \mathbb{R}^{4 \times 1}$, see page 60, represents the four motors’ speed squares of quadrotor i .

As we explained earlier in chapter 2, we do not consider the rotational dynamics of quadrotors in the dynamic model, since we assume that quadrotors produce yaw rotations slowly to close and open fingers when grasping or releasing the object, and quadrotors’ yaw angles are kept fixed in the other working modes. As a consequence, we neglect the dynamics of quadrotors’ yaw rotations and fingers and we consider the whole system as a single body.

Based on these properties above, we propose a control scheme for the FG-FAQ robot which consists in two modules (see Fig. 4.1):

1. The high-level motion controller enables the FG-FAQ robot to move from an initial pose to a final pose following a reference trajectory $\mathbf{p}_b^* \in \mathbb{R}^{6 \times 1}$ by computing the body wrench $\mathbf{w}_b \in \mathbb{R}^{6 \times 1}$;
2. The control allocation module, using the actuation redundancy, computes the robot control input Ω for two objectives: 1) ensure opening/closing fingers by generating $\boldsymbol{\tau}_z = [\tau_{1,z} \ \tau_{2,z} \ \tau_{3,z} \ \tau_{4,z}]^T \in \mathbb{R}^{4 \times 1}$ that is a vector of yaw torques exerted by the four

quadrotors along \mathbf{z}_i axis and is developed according to the task; 2) distribute the body wrench \mathbf{w}_b to the actuators;

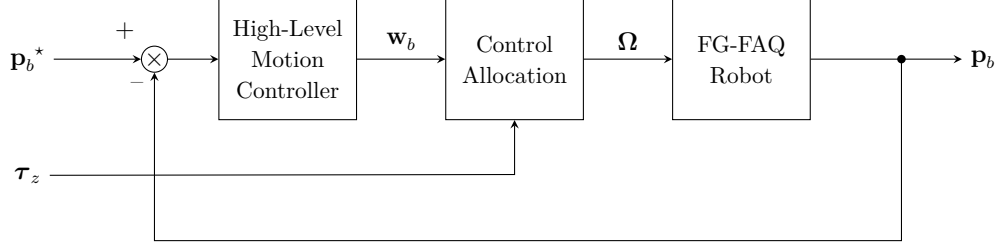


Figure 4.1 – General control scheme of Flying Gripper with Fixed-Attitude Quadrotors (FG-FAQ) robot. High-level motion controller module computes the body wrench $\mathbf{w}_b \in \mathbb{R}^{6 \times 1}$ to track a reference trajectory $\mathbf{p}_b^* \in \mathbb{R}^{6 \times 1}$. The control allocation module computes the robot control input $\mathbf{\Omega} \in \mathbb{R}^{16 \times 1}$ from inputs \mathbf{w}_b and $\boldsymbol{\tau}_z \in \mathbb{R}^{4 \times 1}$ that specifies quadrotors' yaw torques.

4.1.1 High-level motion controller

As shown in the control scheme (see Fig. 4.1), the high-level motion controller's main objective is to control the robot's motion to track a reference trajectory \mathbf{p}_b^* .

Let first consider the dynamic model given by Eq.(4.1) is recalled

$$\mathbf{M}_t \ddot{\mathbf{p}}_b + \mathbf{c}_t = \mathbf{w}_b \quad (4.3)$$

where we find $\dim(\mathbf{p}_b) = \dim(\mathbf{w}_b) = 6$ and that makes \mathbf{p}_b fully controllable w.r.t \mathbf{w}_b .

Control methods used in the high-level motion controller have to deal with variations of dynamic parameters: CoM and inertia of the robot, configuration of fingers (cannot be measured) and unknown mass of the object. Those variations, together with model mismatch caused by simplifying the robot dynamic model, are considered as uncertainties and disturbances in the controller design.

For the high-level motion controller of the FG-FAQ robot, we first introduce a virtual input \mathbf{v}_b to compute the body wrench \mathbf{w}_b

$$\mathbf{w}_b = \mathbf{M}_t \mathbf{v}_b + \mathbf{c}_t. \quad (4.4)$$

Substituting \mathbf{w}_b computed by Eq.(4.4) into Eq. (4.3) gives

$$\ddot{\mathbf{p}}_b = \mathbf{v}_b \quad (4.5)$$

Then, we apply a standard PID control law to get virtual input \mathbf{v}_b as

$$\mathbf{v}_b = \ddot{\mathbf{p}}_b^* + \mathbf{K}_{b,p}\mathbf{e}_p + \mathbf{K}_{b,d}\dot{\mathbf{e}}_p + \mathbf{K}_{b,i} \int \mathbf{e}_p \quad (4.6)$$

where \mathbf{p}_b^* is the reference trajectory and $\mathbf{e}_p = \mathbf{p}_b^* - \mathbf{p}_b$ is the corresponding tracking error. The terms $\mathbf{K}_{b,p}$, $\mathbf{K}_{b,d}$, $\mathbf{K}_{b,i}$ are matrices including the proportional, derivative and integral gains. These matrices must be chosen to ensure the convergence of the tracking error \mathbf{e}_p .

However, note that the convergence of the tracking error \mathbf{e}_p will be guaranteed if and only if the body wrench \mathbf{w}_b is well generated by the actuators of the FG-FAQ robot.

4.1.2 Control allocation

The FG-FAQ robot has 16 actuation motors and 10 DOF, which makes the robot overactuated or redundant. This redundancy can be used to achieve secondary objectives, close/open fingers for grasping/releasing objects, when the robot is tracking a reference trajectory. We propose a two-step approach that is based on the two main objectives of the control allocation module which are explained in the previous section.

Firstly, the control allocation module distributes the body wrench $\mathbf{w}_b \in \mathbb{R}^{6 \times 1}$ to the robot control input $\mathbf{\Omega} \in \mathbb{R}^{16 \times 1}$. This relation is modeled as

$$\mathbf{w}_b - \mathbf{W}_\Omega \mathbf{\Omega} = 0. \quad (4.7)$$

Secondly, self-adaptive fingers of the robot are driven by quadrotors' yaw rotations, but we can not measure fingers' configuration or deduce that from quadrotors' yaw angles. Indeed, we can exert a yaw torque of each quadrotor to open or close the corresponding fingers. Thus, we decide to actuate fingers' closing/opening motion by exerting quadrotors' yaw torques instead of controlling their yaw angles.

Therefore, we choose to actuate the closing/opening motion of fingers by quadrotors' yaw torques in the control allocation module. Let us recall that $\boldsymbol{\tau}_z = [\tau_{1,z} \ \tau_{2,z} \ \tau_{3,z} \ \tau_{4,z}]^T \in \mathbb{R}^{4 \times 1}$ the vector of yaw torques exerted by the four quadrotors along \mathbf{z}_i axis, which is an input of the control allocation module. As previously explained in chapter 3, each yaw torque $\tau_{i,z}$ is defined according to the task:

1. When the robot is in the grasping mode, then the i^{th} quadrotor generates a yaw torque to close the corresponding finger

$$\tau_{i,z} = s_i \cdot \tau_f, \quad (4.8)$$

where τ_f is a resisting torque due to the friction inside the worm-gear mechanism, and s_i is a constant variable depending on the hand of the worm-gear ($s_1 = s_3 = 1, s_2 = s_4 = -1$).

2. When the robot releases the object in the placing mode, then the i^{th} quadrotor generates a yaw torque with the opposite direction from that of the grasping case to open

$$\tau_{i,z} = -s_i \cdot \tau_f. \quad (4.9)$$

It results in an opposite directional yaw rotation of the quadrotor transmitted through the worm-gear to the actuation bar to open fingers, such that the grasped object can be released.

3. When the robot is in the manipulation or free flight modes, the robot follows a given reference trajectory with or without the object. In these two modes, the fingers are kept closed and each quadrotor's yaw rotation is kept fixed. We simply define the i^{th} quadrotor's yaw torque as zero in the manipulation and free flight modes as

$$\tau_{i,z} = 0. \quad (4.10)$$

The relation between the yaw torques $\boldsymbol{\tau}_z$ and the robot control input $\boldsymbol{\Omega}$ can be modeled as

$$\boldsymbol{\tau}_z = \mathbf{C}_z \boldsymbol{\Omega}, \quad (4.11)$$

where $\mathbf{C}_z = \text{diag}(\mathbf{c}_{z_i}) \in \mathbb{R}^{4 \times 16}$ with $\mathbf{c}_{z_i} \in \mathbb{R}^{1 \times 4}$ being the last row of matrix $\mathbf{\Gamma}_i$ introduced in Eq. (2.11).

Finally, in the control allocation module, the relation between the two objectives control the robot's motion and close/open the robot's fingers. The robot control input $\boldsymbol{\Omega}$ is represented by the following equation:

$$\begin{bmatrix} \mathbf{w}_b \\ \boldsymbol{\tau}_z \end{bmatrix} = \begin{bmatrix} \mathbf{W}_\Omega \\ \mathbf{C}_z \end{bmatrix} \boldsymbol{\Omega} = \mathbf{H} \boldsymbol{\Omega}. \quad (4.12)$$

Since the dimension of $\boldsymbol{\Omega} \in \mathbb{R}^{16 \times 1}$ is greater than that of $[\mathbf{w}_b^T \ \boldsymbol{\tau}_z^T]^T \in \mathbb{R}^{10 \times 1}$, there exist a redundancy of actuation and exists an infinity of solutions for $\boldsymbol{\Omega}$ to Eq. (4.12).

The robot control input $\boldsymbol{\Omega}$ is restricted by the limits of the motors speed and must satisfy $\underline{\boldsymbol{\Omega}} \leq \boldsymbol{\Omega} \leq \overline{\boldsymbol{\Omega}}$. The terms $\underline{\boldsymbol{\Omega}} \in \mathbb{R}^{16 \times 1}$ and $\overline{\boldsymbol{\Omega}} \in \mathbb{R}^{16 \times 1}$ are respectively the lower and upper bounds to the rotor speed squares.

Cable driven parallel robots are well known overactuated robots and numerous allocation methods were developed for their control. However, the FG-FAQ robot has a degree of redundancy of 6 ($\dim(\boldsymbol{\Omega}) - \dim(\mathbf{q}^f) = 6$), while most of existing redundant cable driven parallel robots have a degree of redundancy of 1 or 2. As a consequence, methods developed for cable driven parallel robots such as [Gouttefarde et al., 2015b] cannot be applied directly to the FG-FAQ robot. In this section, we apply the algorithm presented in [Pott et al., 2009] to compute $\boldsymbol{\Omega}$. This algorithm is computationally efficient and a closed-form algorithm. It will give the closest solution to $\boldsymbol{\Omega}_m$ using the 2-norm

$$\boldsymbol{\Omega} = \boldsymbol{\Omega}_m + \mathbf{H}^+ \left(\begin{bmatrix} \mathbf{w}_b \\ \boldsymbol{\tau}_z \end{bmatrix} - \mathbf{H}\boldsymbol{\Omega}_m \right) \quad (4.13)$$

where $\boldsymbol{\Omega}_m = (\underline{\boldsymbol{\Omega}} + \overline{\boldsymbol{\Omega}}) / 2$ and \mathbf{H}^+ is the Pseudo-Inverse of \mathbf{H} .

Section 4.1 has presented the general control scheme of the FG-FAQ with a standard high-level motion controller and a control allocation module. In order to deal with model uncertainties, disturbances and noise, we propose to introduce, use and implement a Model Predictive Control (MPC) strategy in the high-level motion controller, which will be developed in the following section.

4.2 Model Predictive Control of FG-FAQ

4.2.1 Introduction to Model Predictive Control

The term Model Predictive Control (MPC) does not refer to a specific control strategy but rather to a wide variety of control methods that explicitly use a prediction model of the process in order to obtain the control signal by minimizing an objective function [Morales, 2019]. It is an optimization control method determining the best control input signal to be applied by considering the future evolution of its state with a prediction model. Due to its conceptual simplicity and its ability to handle easily and effectively complex systems with hard control constraints and many inputs and outputs [Mayne, 2014], it has been applied

in various areas, such as visual servoing [Allibert et al., 2010], quadrotor control [Selfridge and Tao, 2016], humanoid robot [Naveau et al., 2016], cable-driven parallel robots [Santos et al., 2020].

The basic concept of MPC is to use a prediction dynamic model to forecast system behavior at future time instants up to a given horizon, then to compute a control sequence to optimize a given objective function (see Fig. 4.2). This approach considers a receding future horizon. At each step, it calculates the optimal control sequence to a particular time point in the future and it applies the first control signal of the computed control sequence. This self-correcting process of recalculating the control sequence can handle misspecified and simplified dynamic models.

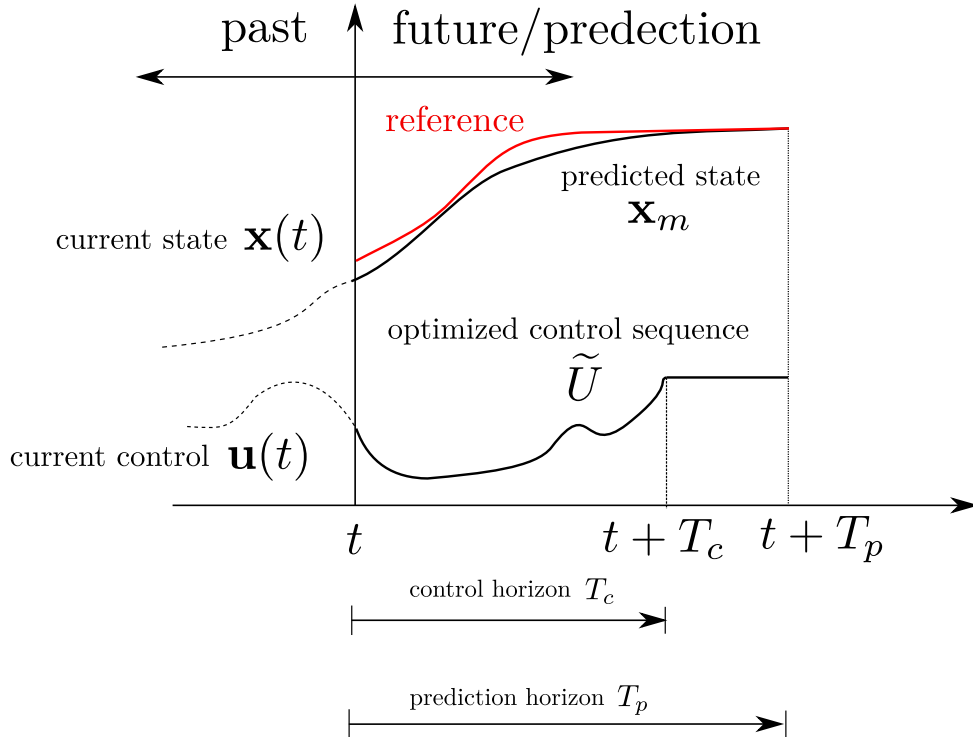


Figure 4.2 – Temporal diagram of the finite-horizon prediction [Findeisen and Allgöwer, 2002]. Model Predictive Control computes the optimized input sequence to be applied in order to force predicted system state track a reference.

4.2.2 Application of Model Predictive Control for FG-FAQ

As mentioned in chapter 2, when the robot grasps an object, variations of dynamic parameters caused by holding the object are considered as model mismatch and uncertainty.

This section proposes a model predictive controller based on [Allibert et al., 2010] in the high-level motion controller module to track the reference trajectory (see Fig. 4.3), dealing with the model mismatch and varying dynamic parameters, in presence of disturbances and noise.

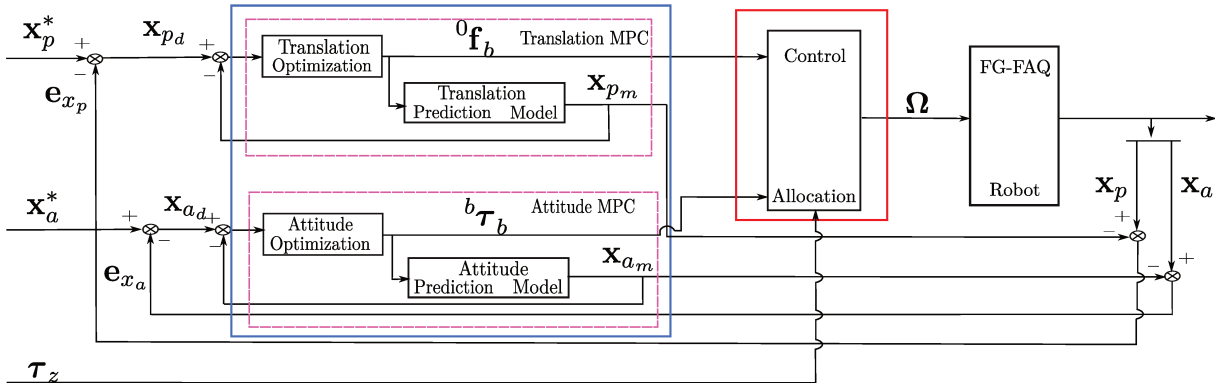


Figure 4.3 – Application of a model predictive controller in the high-level motion controller module of Flying Gripper with Fixed-Attitude Quadrotors (FG-FAQ) robot. The model predictive controller consists in a translation model predictive controller (translation MPC) and an attitude model predictive controller (attitude MPC) that calculate the force ${}^0\mathbf{f}_b$ and the torque ${}^b\boldsymbol{\tau}_b$.

More precisely, this model predictive controller consists in two submodules a translation MPC and an attitude MPC (see Fig. 4.3) that calculate components of the required body wrench $\mathbf{w}_b = [{}^0\mathbf{f}_b^T \quad {}^b\boldsymbol{\tau}_b^T]^T \in \mathbb{R}^{6 \times 1}$: the force ${}^0\mathbf{f}_b \in \mathbb{R}^{3 \times 1}$ and the torque ${}^b\boldsymbol{\tau}_b \in \mathbb{R}^{3 \times 1}$ in order to track the reference trajectory.

In the translation MPC, we introduce the translation state variable $\mathbf{x}_p = [{}^0\mathbf{x}_b^T \quad 0\dot{\mathbf{x}}_b^T]^T \in \mathbb{R}^{6 \times 1}$, $\mathbf{x}_{p_m} \in \mathbb{R}^{6 \times 1}$ is the predicted translation state variable, and $\mathbf{x}_p^* \in \mathbb{R}^{6 \times 1}$ is the corresponding reference translation trajectory.

Let us express the k^{th} sample of the variable x as $x[k]$. Then, we linearize the translation dynamic model of the FG-FAQ robot in Eq.(4.3) to obtain the discrete prediction model as

$$\mathbf{x}_{p_m}[k] = \mathbf{A}_p \mathbf{x}_{p_m}[k-1] + \mathbf{B}_p {}^0\mathbf{f}_b[k-1] + \mathbf{g}_p \quad (4.14)$$

where $\mathbf{x}_{p_m}[k], \mathbf{x}_{p_m}[k-1] \in \mathbb{R}^{6 \times 1}$ are the k^{th} and $k-1^{\text{th}}$ predicted translation state samples, and ${}^0\mathbf{f}_b[k-1]$ is the $k-1^{\text{th}}$ sample of the force ${}^0\mathbf{f}_b$. The terms $\mathbf{A}_p \in \mathbb{R}^{6 \times 6}$, $\mathbf{B}_p \in \mathbb{R}^{6 \times 3}$ and $\mathbf{g}_p \in \mathbb{R}^{6 \times 1}$ are the state transition matrix, the input matrix, and the constant vector of the translation prediction model respectively. We define $\mathbf{e}_{x_p} \in \mathbb{R}^{6 \times 1}$ as the error between

the translation state \mathbf{x}_p and the prediction \mathbf{x}_{p_m}

$$\mathbf{e}_{x_p}[k] = \mathbf{x}_p[k] - \mathbf{x}_{p_m}[k]. \quad (4.15)$$

The correction of the reference trajectory \mathbf{x}_p^* with the error \mathbf{e}_{x_p} is defined as $\mathbf{x}_{p_d} \in \mathbb{R}^{6 \times 1}$

$$\mathbf{x}_{p_d}[k] = \mathbf{x}_p^*[k] - \mathbf{e}_{x_p}[k]. \quad (4.16)$$

The objective function is defined to minimize the error between the correction \mathbf{x}_{p_d} and the predictive state \mathbf{x}_{p_m}

$$\underset{\tilde{U}_f}{\text{minimize}} \sum_{k=n_p+1}^{n_p+N_p} [\mathbf{x}_{p_d}[k] - \mathbf{x}_{p_m}[k]]^T \mathbf{Q}_p [\mathbf{x}_{p_d}[k] - \mathbf{x}_{p_m}[k]], \quad (4.17)$$

$$\mathbf{x}_{p_m}[k] = \mathbf{A}_p \mathbf{x}_{p_m}[k-1] + \mathbf{B}_p {}^0\mathbf{f}_b[k-1] + \mathbf{g}_p \quad (4.18)$$

$$\text{subject to: } \mathbf{e}_{x_p}[k] = \mathbf{x}_p[k] - \mathbf{x}_{p_m}[k] \quad (4.19)$$

$$\mathbf{x}_{p_d}[k] = \mathbf{x}_p^*[k] - \mathbf{e}_{x_p}[k] \quad (4.20)$$

where

1. n_p is the current sample, $N_p \in \mathbb{N}$ is the prediction horizon, $N_c \in \mathbb{N}$ is the control horizon, and $\mathbf{Q}_p \in \mathbb{R}^{6 \times 6}$ is the weighting matrix that can be tuned for tracking the reference \mathbf{x}_p^* ;
2. the optimized control sequence $\tilde{U}_f = \{ {}^0\mathbf{f}_b[n_p], {}^0\mathbf{f}_b[n_p+1], \dots, {}^0\mathbf{f}_b[k], \dots, {}^0\mathbf{f}_b[n_p+N_c-1] \}$ is a set of the forces, but only the first element ${}^0\mathbf{f}_b[n_p]$ will be applied;

Then we apply the same method to develop the attitude MPC in the high-level motion controller. As shown in Fig. 4.3, the attitude state variable is $\mathbf{x}_a = [\boldsymbol{\eta}_b^T \ \dot{\boldsymbol{\eta}}_b^T]^T$ and the reference is \mathbf{x}_a^* . The attitude prediction model is based on the linearization of the dynamic model in Eq. (4.3) at the horizontal attitude ($\phi_b = \theta_b = \psi_b = 0$) and its output is the prediction state \mathbf{x}_{a_m} .

The attitude MPC can be modeled as

$$\underset{\tilde{U}_a}{\text{minimize}} \sum_{k=n_a+1}^{n_a+N_a} [\mathbf{x}_{a_d}[k] - \mathbf{x}_{a_m}[k]]^T \mathbf{Q}_a [\mathbf{x}_{a_d}[k] - \mathbf{x}_{a_m}[k]], \quad (4.21)$$

$$\mathbf{x}_{a_m}[k] = \mathbf{A}_a \mathbf{x}_{a_m}[k-1] + \mathbf{B}_a {}^b\boldsymbol{\tau}_b[k-1] + \mathbf{g}_a \quad (4.22)$$

$$\text{subject to: } \mathbf{e}_{x_a}(k) = \mathbf{x}_a[k] - \mathbf{x}_{a_m}[k] \quad (4.23)$$

$$\mathbf{x}_{a_d}[k] = \mathbf{x}_a^*[k] - \mathbf{e}_{x_a}[k] \quad (4.24)$$

where

1. the terms $\mathbf{A}_a \in \mathbb{R}^{6 \times 6}$, $\mathbf{B}_a \in \mathbb{R}^{6 \times 3}$ and $\mathbf{g}_a \in \mathbb{R}^{6 \times 1}$ are the state transition matrix, the input matrix, and the constant vector of the attitude prediction model that are obtained from linearizing the dynamic model in Eq. (4.3);
2. the optimized control sequence $\tilde{U}_a = \left\{ {}^b\boldsymbol{\tau}_b[n_a], {}^b\boldsymbol{\tau}_b[n_a + 1], \dots, {}^b\boldsymbol{\tau}_b[k], \dots, {}^b\boldsymbol{\tau}_b[n_a + N_c - 1] \right\}$, with n_a being the current sample, is a set of the torque ${}^b\boldsymbol{\tau}_b$;
3. we tune the weighting matrix \mathbf{Q}_a for tracking the reference \mathbf{x}_a^* and we can balance the position tracking and the attitude tracking by tuning the two weighting matrices \mathbf{Q}_p and \mathbf{Q}_a .

The outputs of the designed model predictive controller are the first elements of optimized control sequences \tilde{U}_p and \tilde{U}_a : ${}^0\mathbf{f}_b[n_p]$ and ${}^b\boldsymbol{\tau}_b[n_a]$, which are sent to the control allocation module.

4.3 Co-simulation of FG-FAQ robot

A simulator is developed with MATLAB-SIMULINK and ADAMS co-simulation. The dynamic of the FG-FAQ robot is simulated by ADAMS, while the controller is implemented in MATLAB-SIMULINK. We introduce a white noise to each measurement of \mathbf{q}^f and an external and varying disturbance force ${}^0\mathbf{f}_{ext}$ is applied to the CoM of the robot expressed in frame \mathcal{F}_0 in the ADAMS model.

4.3.1 Case study: FG-FAQ robot grasping a 1kg object with disturbances

The first co-simulation is developed to test a simple grasping sequence described below (see Fig. 4.5). The dynamic parameters of the FG-FAQ robot are given in Table 4.1.

In this co-simulation, the robot's initial position is assumed to be above the object. The robot is required to perform a downward trajectory (0s - 2s) and then close its fingers while maintaining its position above the object (2s - 5s) under a disturbance force ${}^0\mathbf{f}_{ext}$

Table 4.1 – Dynamic parameters of FG-FAQ robot in co-simulation

Parameter	Value
Mass of the body structure m_b (kg)	2.3
Inertia of the body structure in \mathcal{F}_b (kg m^2)	$\begin{bmatrix} 0.98 & 0 & 0 \\ 0 & 0.84 & 0 \\ 0 & 0 & 0.77 \end{bmatrix}$
Mass of one quadrotor m_i (kg)	0.70
Inertia of one quadrotor in \mathcal{F}_i (kg m^2)	$\begin{bmatrix} 0.010 & 0 & 0 \\ 0 & 0.010 & 0 \\ 0 & 0 & 0.020 \end{bmatrix}$
Mass of a tube object (kg)	1
Inertia of a tube object (kg m^2)	$\begin{bmatrix} 0.067 & 0 & 0 \\ 0 & 0.067 & 0 \\ 0 & 0 & 0.020 \end{bmatrix}$
Minimal motor speed ω_{\min} (rad s^{-1})	0
Maximal motor speed ω_{\max} (rad s^{-1})	1000
Friction torque to actuate one finger τ_f (N m)	0.0010

(see Fig. 4.4). Furthermore, we introduce a white noise on each state measurement to simulate sensor noise and its amplitude is chosen as $\pm 10^3$ (m or rad), which is based on measurement precision.

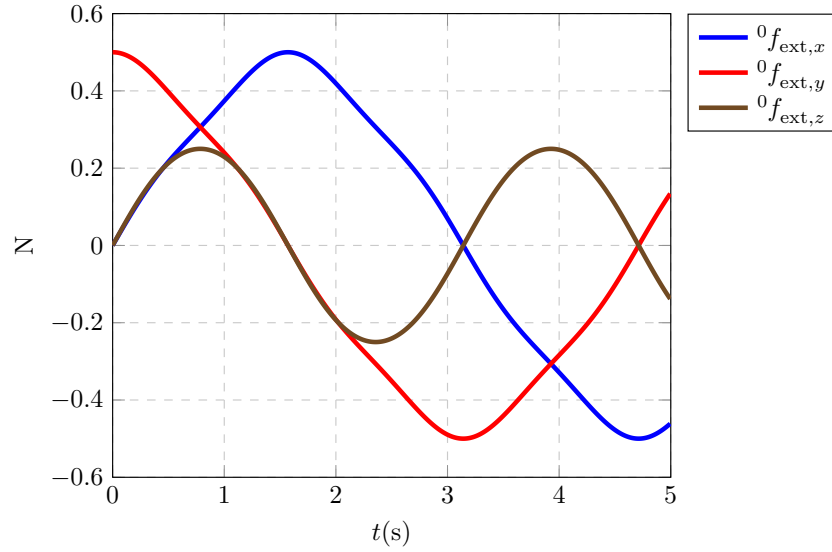


Figure 4.4 – External and varying disturbance force ${}^0\mathbf{f}_{ext} = \begin{bmatrix} {}^0f_{ext,x} & {}^0f_{ext,y} & {}^0f_{ext,z} \end{bmatrix}^T$ ($|{}^0\mathbf{f}_{ext}| = 0.5 \text{ N}$) is applied to the robot CoM expressed in \mathcal{F}_0 .

The ADAMS-SIMULINK co-simulation results are shown in Fig.4.6 and in Fig.4.7. As we can see from those figures, with disturbance $|{}^0\mathbf{f}_{ext}| = 0.5 \text{ N}$ and the white noise of amplitude $\pm 10^3$ (m or rad) on each state measurement, the controller shows that the error interval of translation coordinates $\mathbf{x}_b, \mathbf{y}_b$ is $\begin{bmatrix} -2 \times 10^{-3} \text{ m} & 2 \times 10^{-3} \text{ m} \end{bmatrix}$, and that of

\mathbf{z}_b is $[-5 \times 10^{-2} \text{ m} \quad 1 \times 10^{-2} \text{ m}]$, while the error interval of attitude coordinates $\boldsymbol{\eta}_b$ is $[-3 \times 10^{-3} \text{ rad} \quad 4 \times 10^{-3} \text{ rad}]$. The control input, see Fig. 4.8 and Fig. 4.9, respect the mechanical limits of motor speed. Note that, when the robot performs grasping during (2s - 5s), the controller enables the robot to deal with external disturbances and noise while generating exerting yaw torques of quadrotors to close fingers. For instance, see Fig. 4.8 and Fig. 4.9, quadrotor 1 controls speed of motor 2 and motor 4 to be larger than that of motor 1 and motor 3, in order to generate a positive yaw torque, see Eq.(4.8), for closing fingers: motors 2 and 4 contribute to positive yaw torques, while motors 1 and 3 contribute to negative ones, which can be found in $\boldsymbol{\Gamma}_i$ in Eq.(2.11).

These co-simulation results validate that the controller is able to complete the task under disturbances and sensor noise and respect the actuator mechanical constraints.

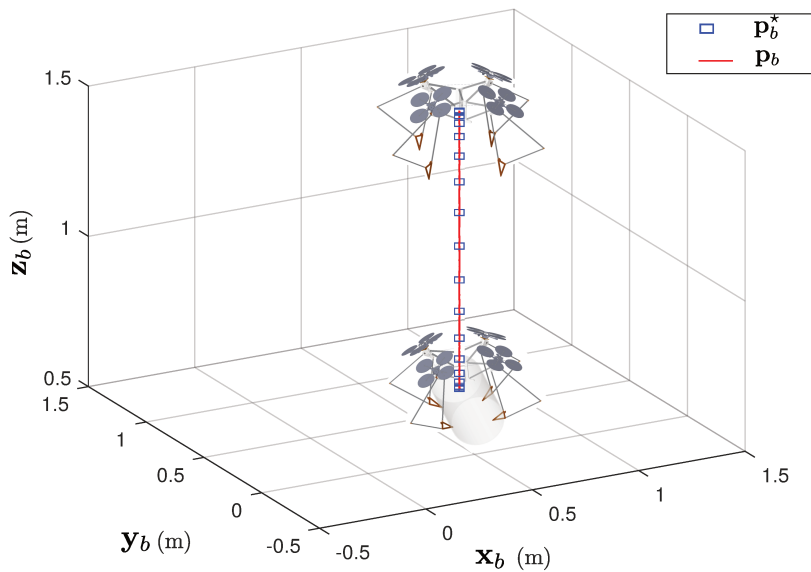


Figure 4.5 – FG-FAQ robot grasping a 1 kg object with external force disturbances and sensor noise in ADAMS-SIMULINK co-simulation

In order to test the controller’s robustness, we conducted several simulations under different disturbance forces ${}^0\mathbf{f}_{ext}$ and Table 4.2 gives the mean of absolute value of the tracking error for each coordinate when we apply different amplitudes of the disturbance force.

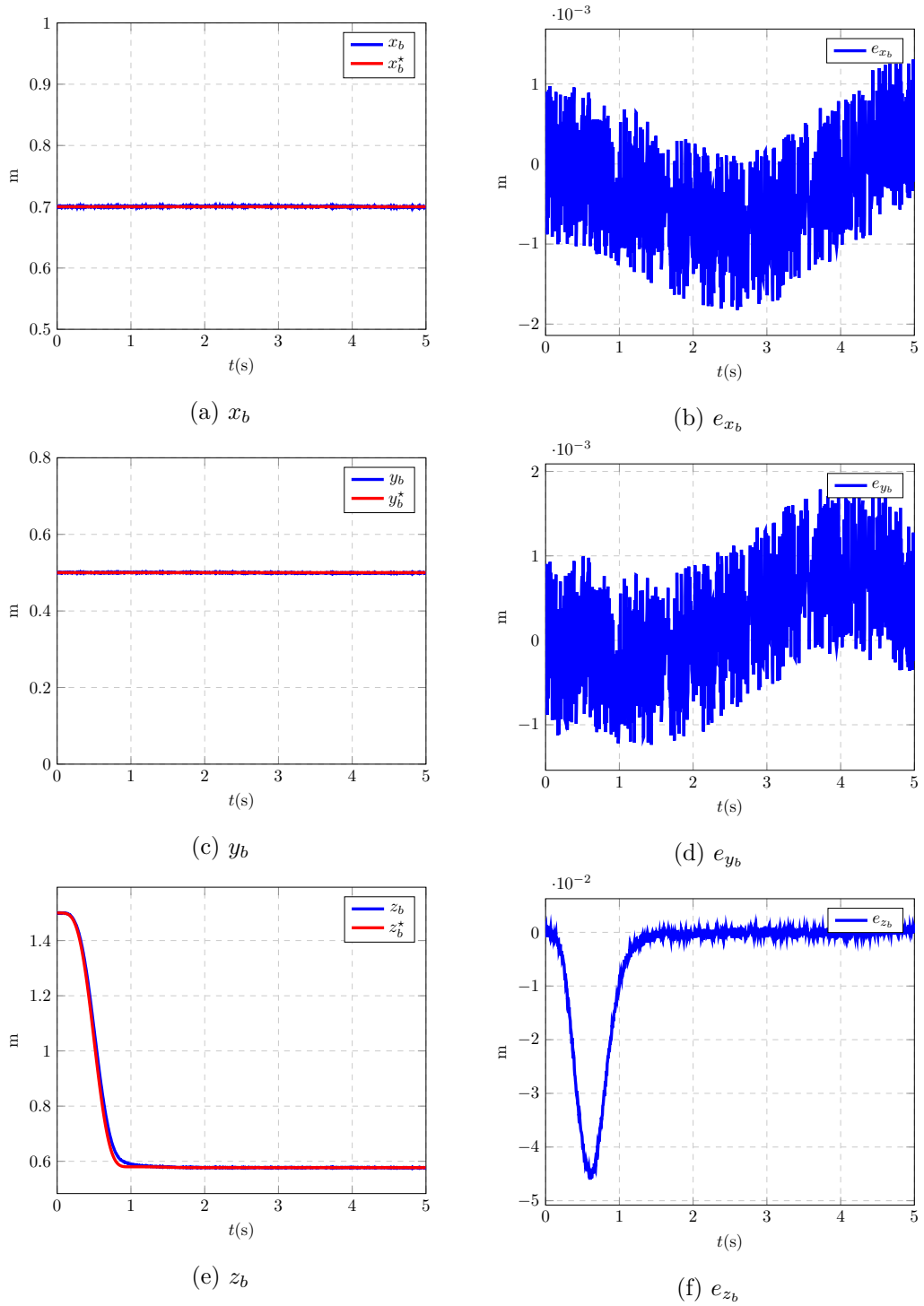


Figure 4.6 – Co-simulation of FG-FAQ robot grasping a 1 kg object under external force disturbances and sensor noise: reference trajectory and tracking errors of translation coordinates of vector \mathbf{p}_b

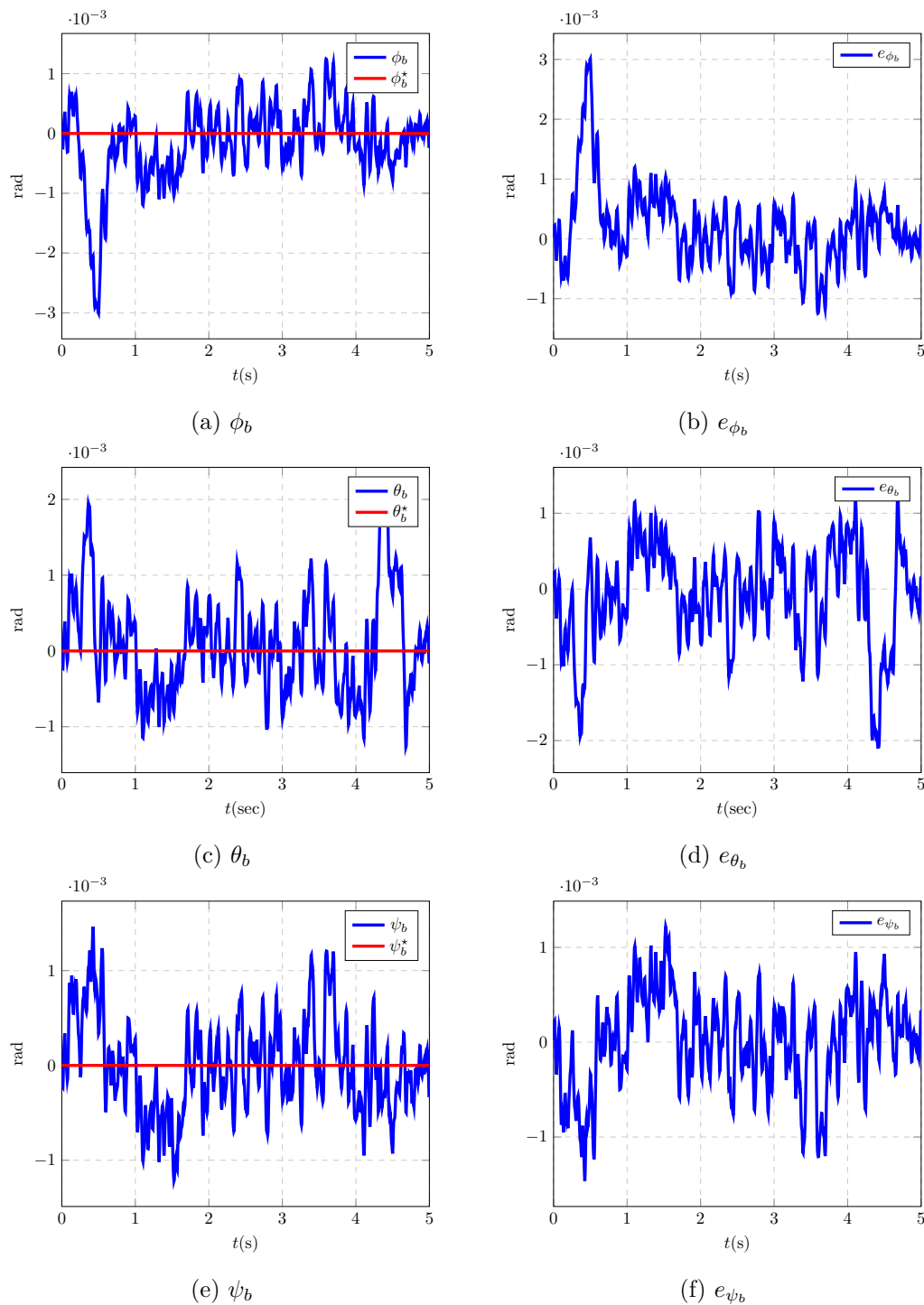
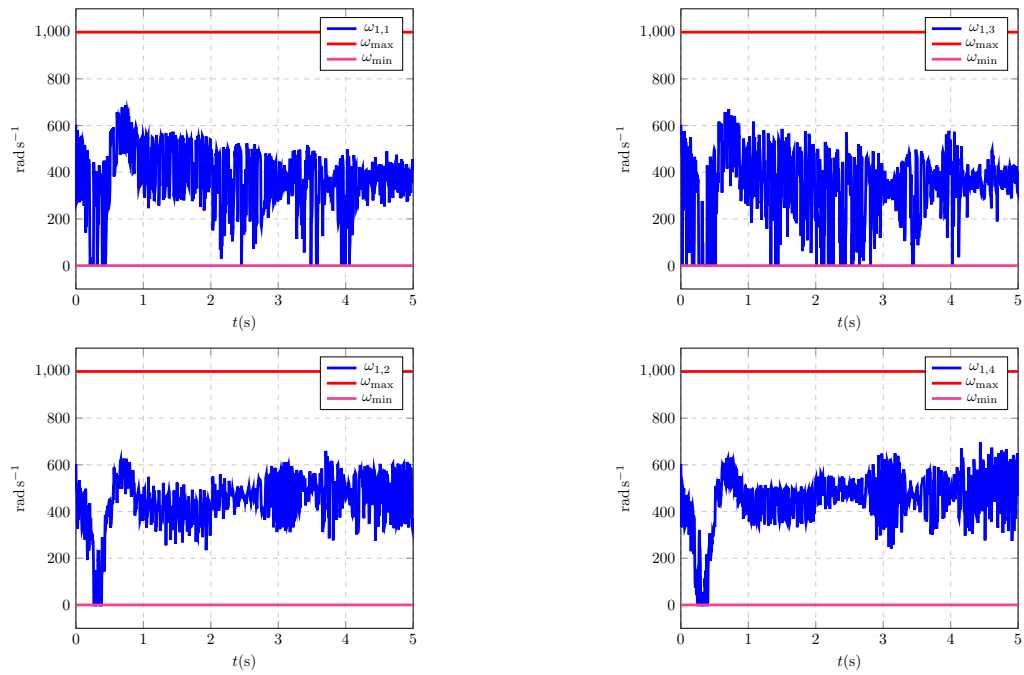
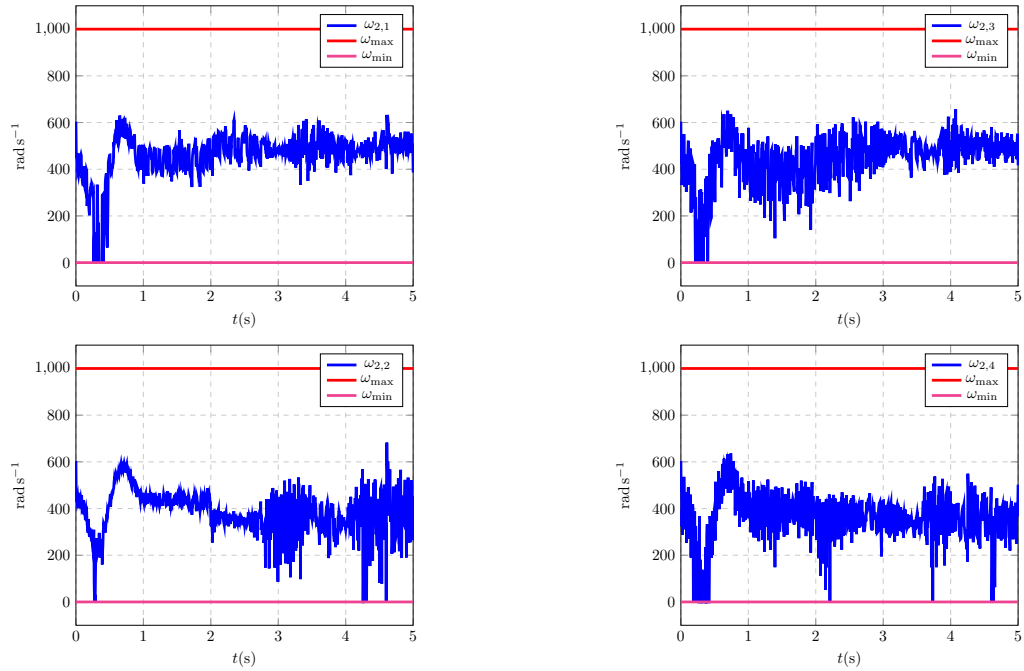


Figure 4.7 – Co-simulation of FG-FAQ robot grasping a 1 kg object under external force disturbances and sensor noise: reference trajectory and tracking errors of attitude coordinates of vector \mathbf{p}_b

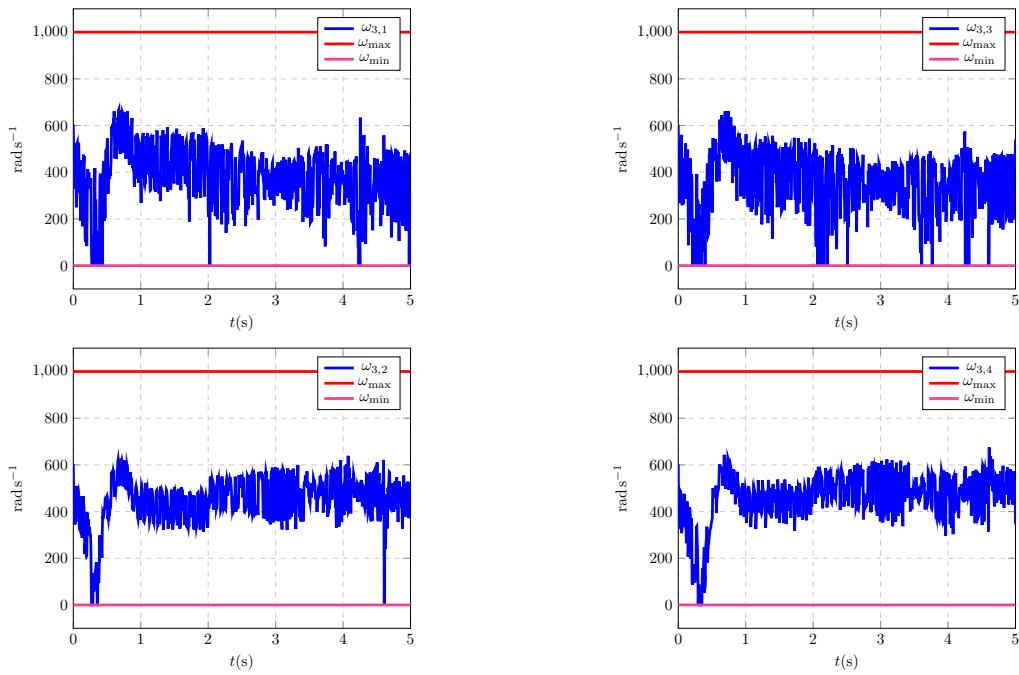


(a) motor speed of quadrotor 1

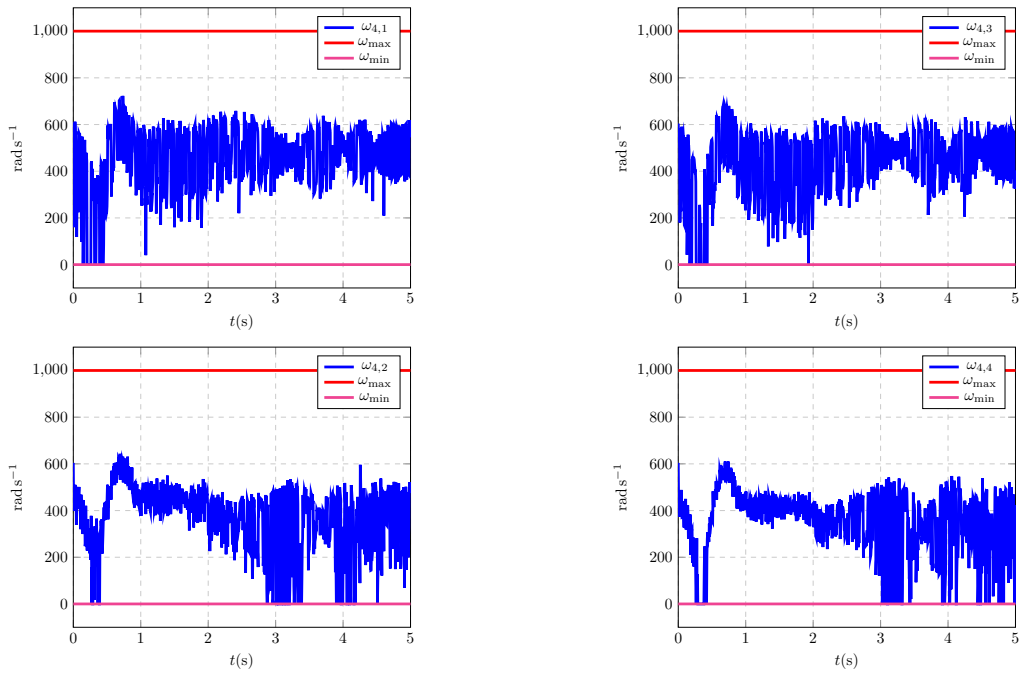


(b) motor speed of quadrotor 2

Figure 4.8 – Co-simulation of FG-FAQ robot grasping a 1 kg object under external force disturbances and sensor noise: motor speed of quadrotor 1 and 2 where $\omega_{i,j}$ is the j^{th} motor's speed of the i^{th} quadrotor



(a) motor speed of quadrotor 3



(b) motor speed of quadrotor 4

Figure 4.9 – Co-simulation of FG-FAQ robot grasping a 1 kg object under external force disturbances and sensor noise: motor speed of quadrotor 3 and 4 where $\omega_{i,j}$ is the j^{th} motor’s speed of the i^{th} quadrotor

Table 4.2 – Mean of absolute value of tracking error of each coordinate of FG-FAQ robot grasping a 1 kg object with different disturbance forces

	Amplitude of force disturbances $ \mathbf{f}_{ext} $ (N)				
	0.1	0.5	1	3	5
Mean error x_b (m)	4.9e-04	6.1e-04	9.7e-04	2.8e-03	6.3e-03
Mean error y_b (m)	5.0e-04	6.0e-04	9.5e-04	2.9e-03	6.0e-03
Mean error z_b (m)	5.1e-03	5.1e-03	5.2e-03	8.4e-03	2.2e-02
Mean error ϕ_b (rad)	4.5e-04	4.7e-04	6.0e-04	1.6e-03	8.3e-03
Mean error θ_b (rad)	4.9e-03	5.0e-03	5.9e-04	2.6e-03	3.2e-03
Mean error ψ_b (rad)	3.7e-03	3.9e-03	3.9e-04	4.0e-04	5.1e-04

* Mechanical motor speed limits are satisfied.

4.3.2 Case study: FG-FAQ robot grasping, transporting and placing a 1kg object

In reality, aerial manipulation robots always accomplish more complex tasks, for instance to grasp, manipulate and place an object. Thus, in this simulation, the FG-FAQ robot is supposed to approach the object (1 kg), close the fingers, transport the object and place the object under external force disturbances (see Fig.4.4) and sensor noise.

The reference trajectory is defined as follows (see Fig. 4.10):

1. in 0s-3s, the robot approaches to the object from its initial pose;
2. in 3s-6s, the quadrotors produce the yaw rotations to close the fingers while maintaining the robot pose;
3. in 6s-21s, the robot manipulates and transports the object following a reference trajectory;
4. in 21s-25s, the quadrotors produce the inverse yaw rotations to open the fingers while maintaining the robot pose.

The dynamic parameters of the FG-FAQ robot in this co-simulation are the same as those in Table 4.1. The co-simulation results are shown in Fig. 4.11 and in Fig. 4.12 and the control input is illustrated in Fig. 4.13 and Fig. 4.14. It can be seen from Fig. 4.11 and Fig. 4.12 that, with disturbance $|\mathbf{f}_{ext}| = 0.5$ N and a white noise noise of amplitude $\pm 10^3$ (m or rad) on the robot state measurements, the controller shows that the error interval of translation is $[-3 \times 10^{-3} \text{ m} \quad 7 \times 10^{-3} \text{ m}]$ and that of attitude is $[-3 \times 10^{-3} \text{ rad} \quad 4 \times 10^{-3} \text{ rad}]$ during trajectory tracking and grasping/manipulating/releasing the object. It validates that the designed controller achieves tracking reference position trajectories and maintaining the robot's attitude, while rotating quadrotors to close or

open fingers to grasp and manipulate a large size object under external disturbances and noise.

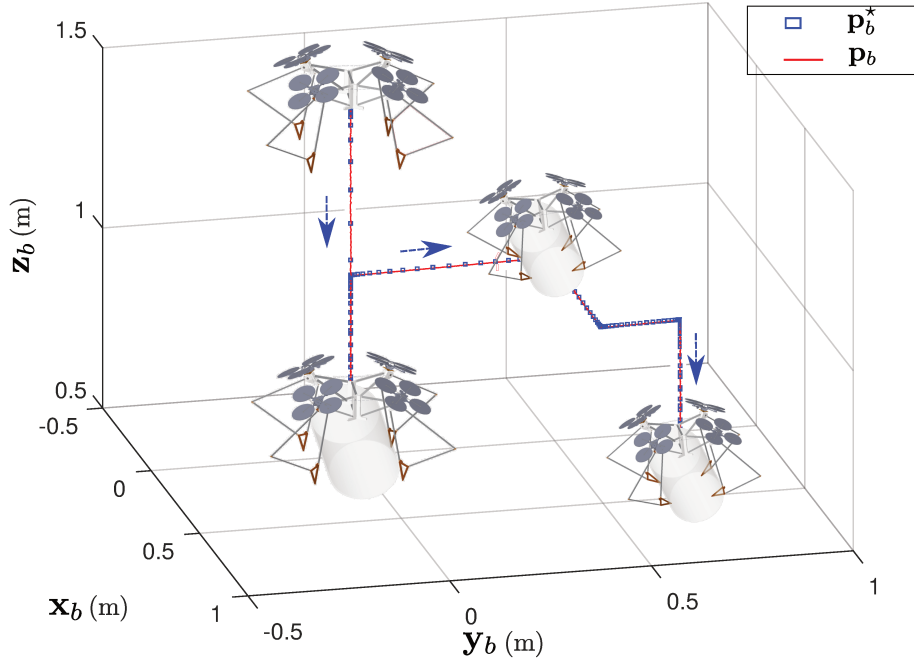


Figure 4.10 – FG-FAQ robot grasping, transporting and placing a 1 kg object under external force disturbances and sensor noise in ADAMS-SIMULINK co-simulation

4.3.3 Discussion on co-simulation results of FG-FAQ robot

As shown in the co-simulation results, the FG-FAQ robot, with the designed controller, is capable of grasping and manipulating a 1 kg object, dealing with the variation of dynamics caused by the object in the manipulation. Even though the used control allocation algorithm does not guarantee that actuators' limits will be satisfied, it shows that they are satisfied considering the simulated scenarios.

Thus, the co-simulation results demonstrate the effectiveness of the designed controller and its robustness against noise and disturbance. A video of these two co-simulations is available online with the link ².

After the co-simulations, we build a prototype of the FG-FAQ robot and apply the controller in that prototype. However, failure in controlling motor speed of quadrotors

2. https://youtu.be/ziYE_SF3t4c

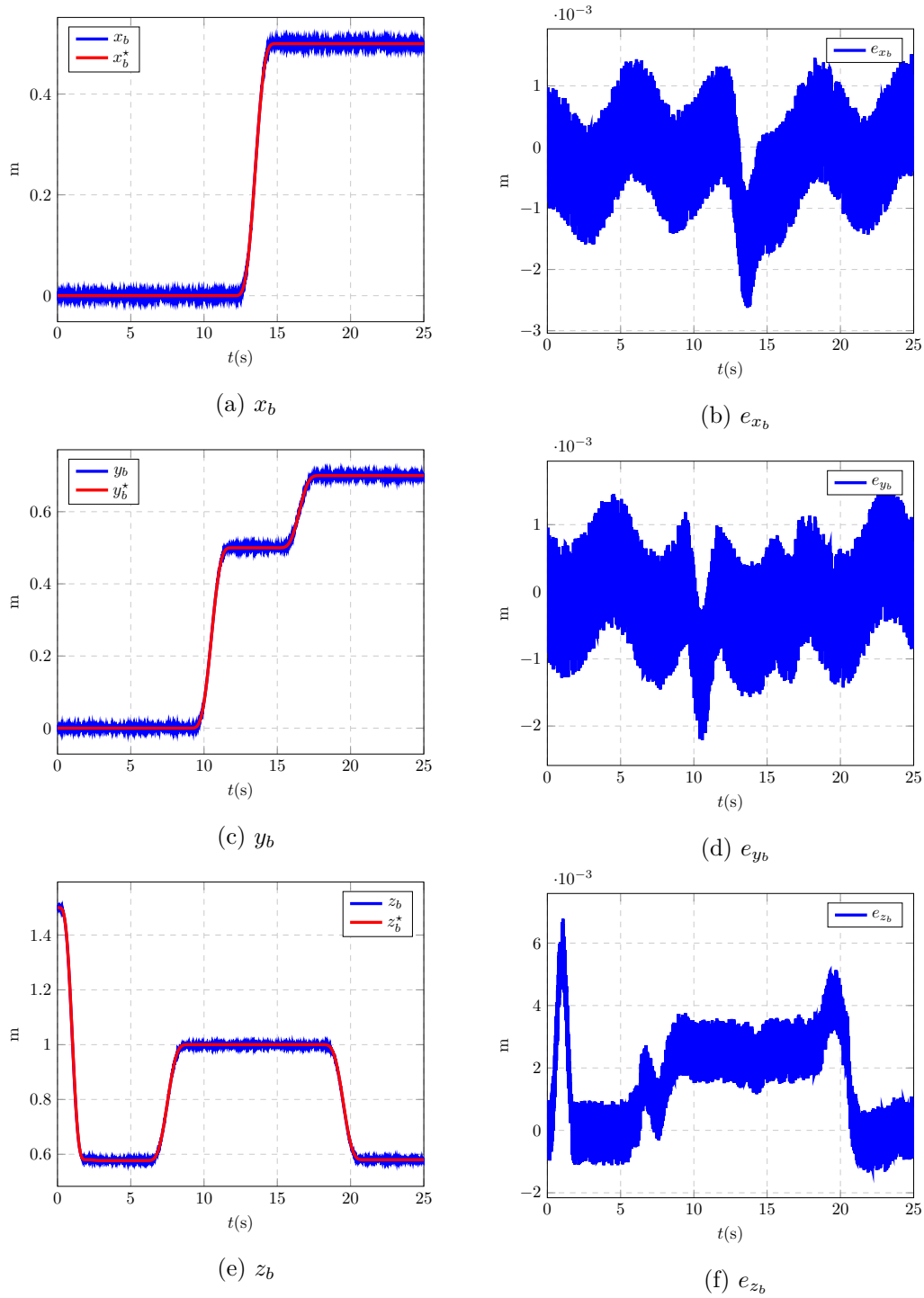


Figure 4.11 – Co-simulation of FG-FAQ robot grasping, transporting and placing a 1 kg object under external force disturbances and sensor noise: reference trajectory and tracking errors of translation coordinates of the vector \mathbf{p}_b

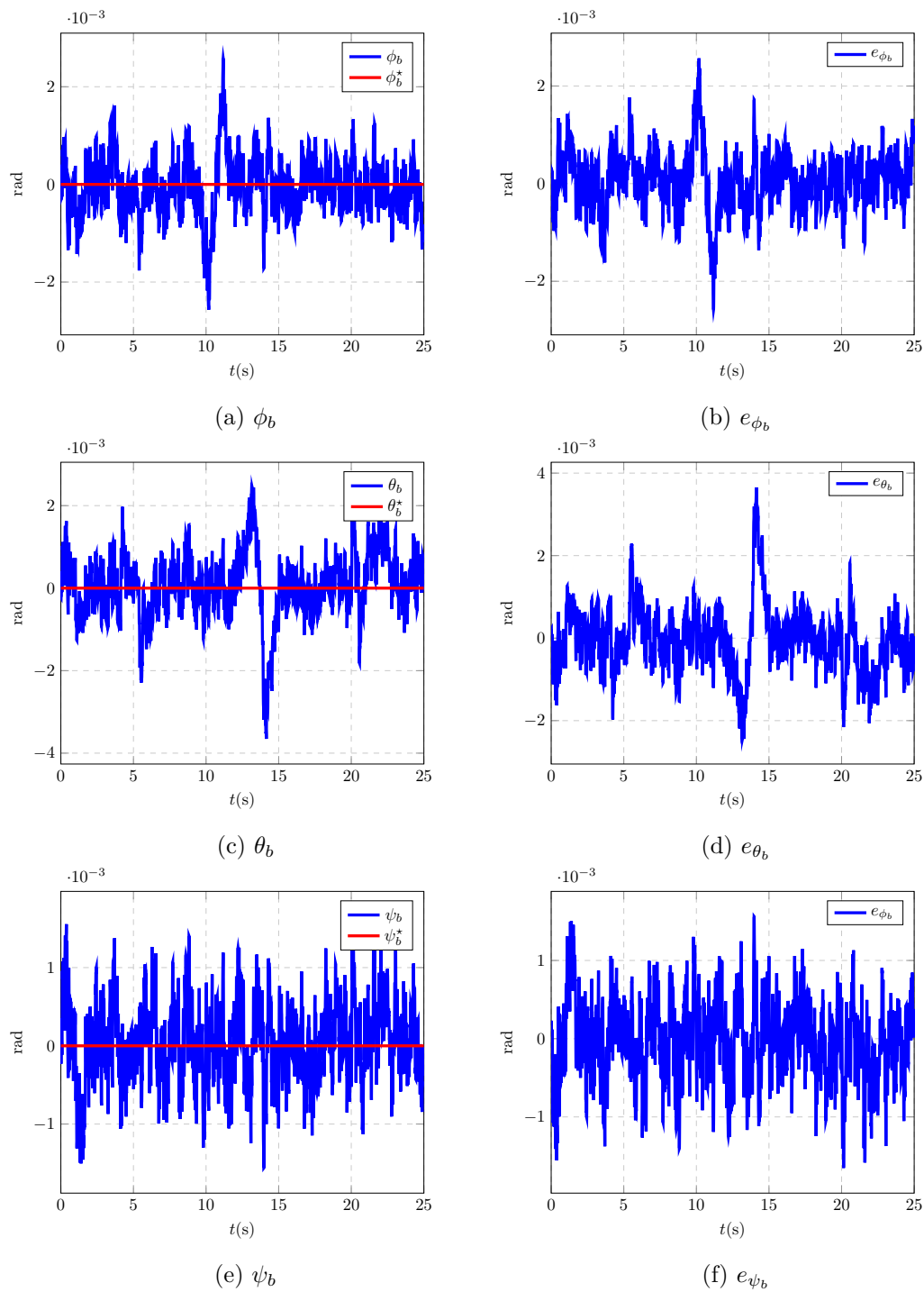
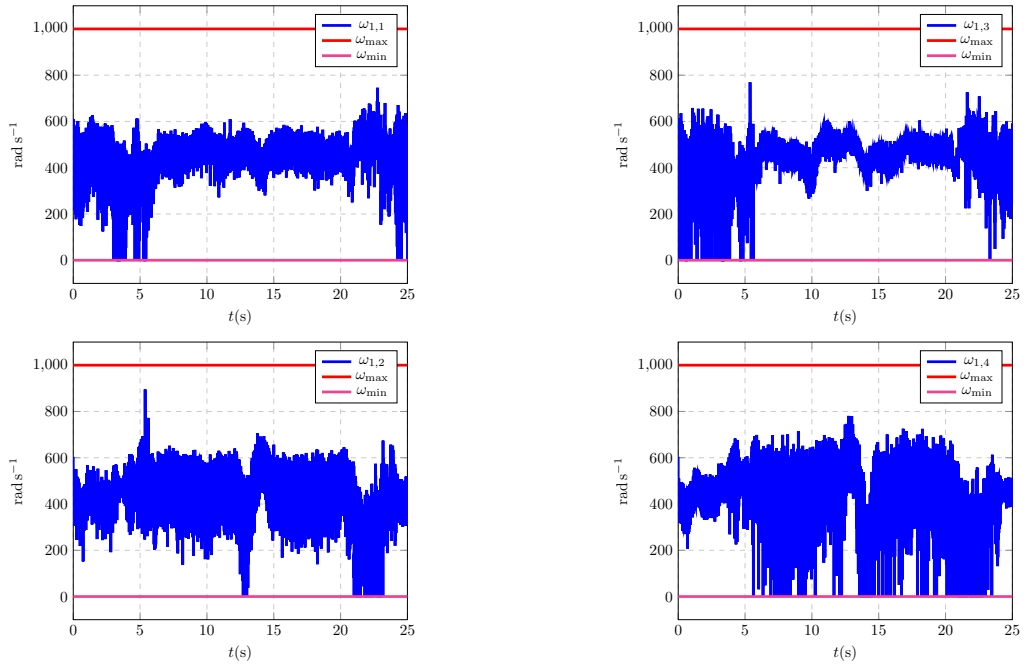
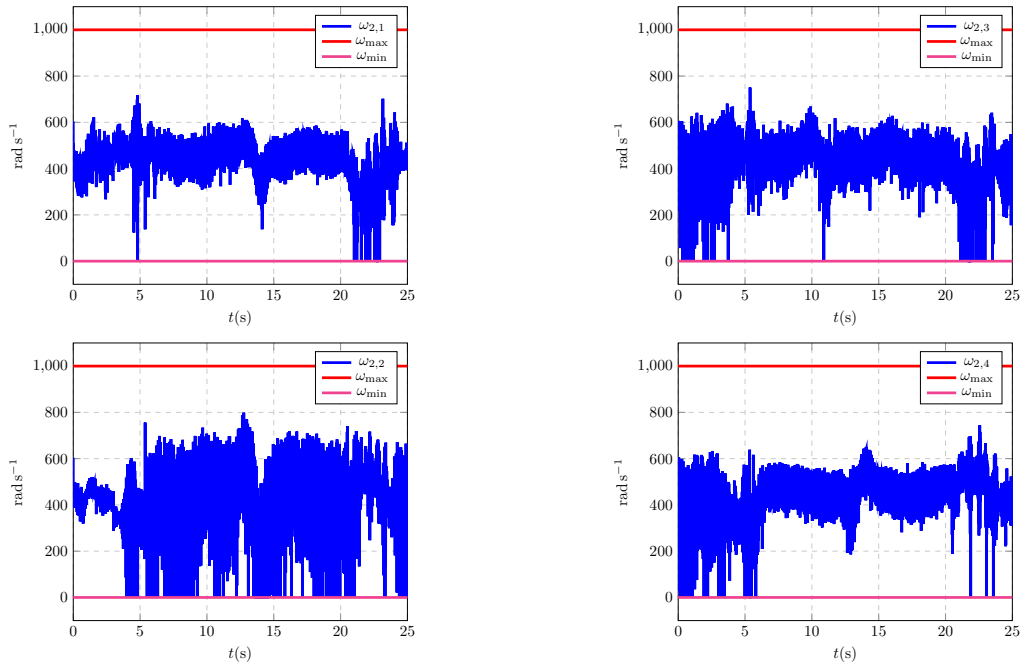


Figure 4.12 – Co-simulation of FG-FAQ robot grasping, transporting and placing a 1 kg object under external force disturbances and sensor noise: reference trajectory and tracking errors of attitude coordinates of the vector \mathbf{p}_b

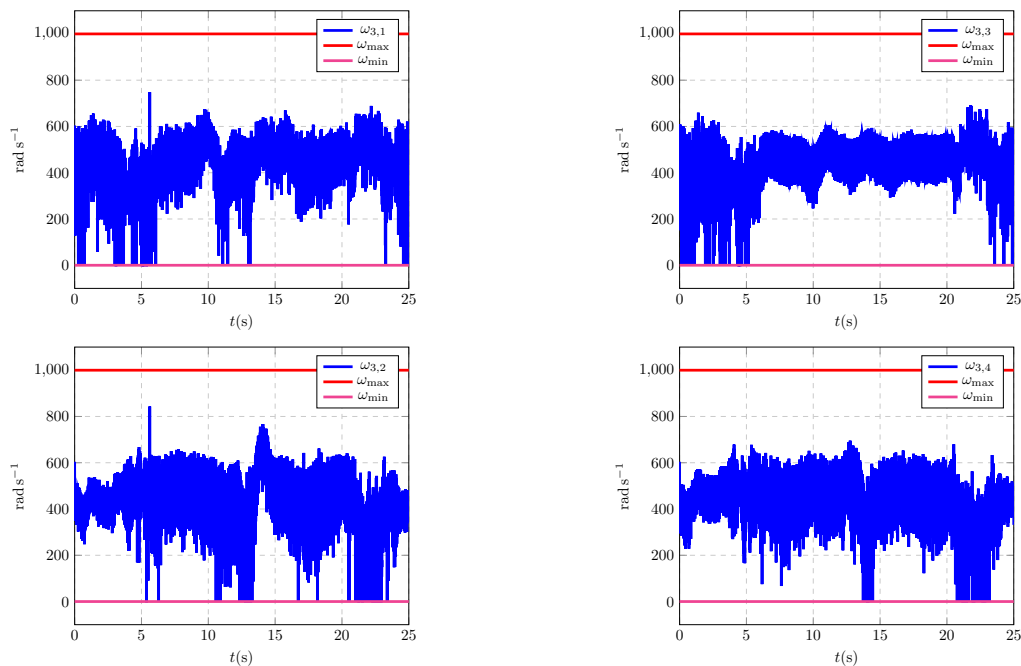


(a) motor speed of quadrotor 1

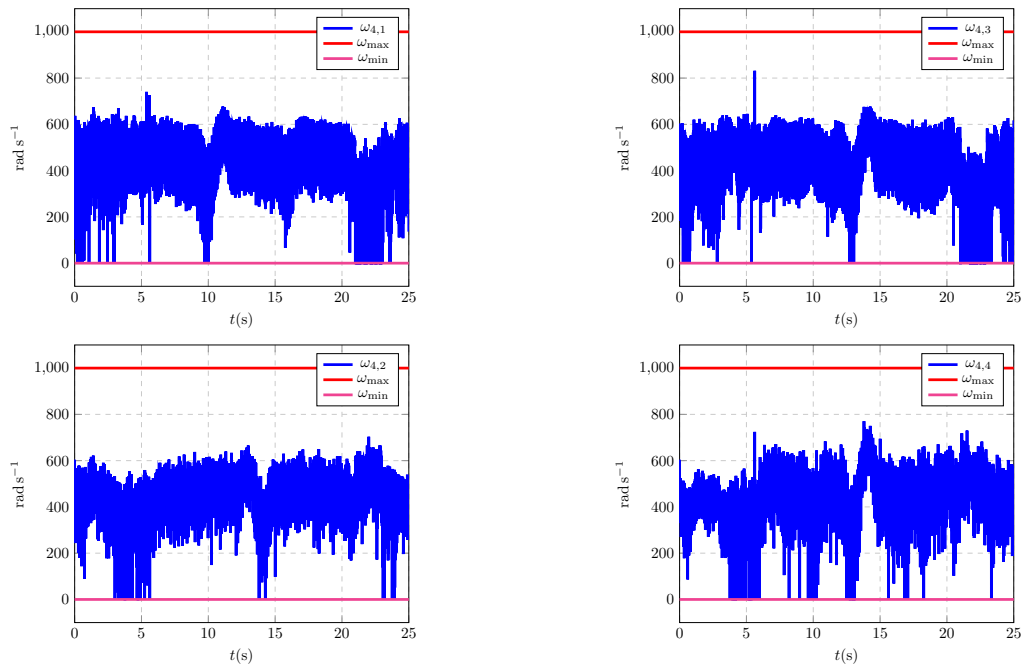


(b) motor speed of quadrotor 2

Figure 4.13 – Co-simulation of FG-FAQ robot grasping, transporting and placing a 1 kg object under external force disturbances and sensor noise: motor speed of quadrotor 1 and 2 where $\omega_{i,j}$ is the j^{th} motor's speed of the i^{th} quadrotor.



(a) motor speed of quadrotor 3



(b) motor speed of quadrotor 4

Figure 4.14 – Co-simulation of FG-FAQ robot grasping, transporting and placing a 1 kg object under external force disturbances and sensor noise: motor speed of quadrotor 3 and 4 where $\omega_{i,j}$ is the j^{th} motor’s speed of the i^{th} quadrotor.

stops implementing the controller furthermore. One reason is the used autopilot, further explained in chapter 5, which provides only an open loop for motor speed control and results in unacceptable performances. It is still worthy to mention that numerous work are done in controlling UAVs' motor speed such as [Herrmann et al., 2019, Franchi and Mallet, 2017].

4.4 Conclusions

In this chapter, we developed a controller design method for the FG-FAQ robot to control the robot's motion and to close/open the robot's fingers.

The designed controller scheme consists in two modules: a high motion controller to enable the robot to move from an initial pose to a final pose following a reference trajectory and a control allocation to distribute actuators' commands while ensuring closing fingers during the trajectory tracking. We have applied a model predictive controller in the high motion controller module to enable the robot to track a reference trajectory and deal with the variation of dynamics caused by the object during the manipulation, which is the main contribution of this chapter. An allocation algorithm has been applied in the control allocation module that is computationally efficient and is a closed-form algorithm. The effectiveness of the designed controller and its robustness against noise and disturbances have been validated in ADAMS-SIMULINK co-simulation, and the actuators satisfied their limits in the co-simulations.

Indeed, the controller scheme, proposed in this chapter, provides a systematical and flexible method for designing a controller for the FG-FAQ robot: diverse control methods can be implemented in the high motion controller module and the control allocation module. The next chapter will be devoted to a more advanced method for the control allocation module, which will be applied to a different version of our flying gripper since it will concern the Flying Gripper with Mobile-Attitude Quadrotors (FG-MAQ).

DYNAMIC CONTROL ALLOCATION AND EXPERIMENTATION OF FLYING GRIPPER WITH MOBILE-ATTITUDE QUADROTORS (FG-MAQ)

5.1 Control scheme of FG-MAQ	134
5.2 Dynamic Control Allocation of FG-MAQ	139
5.3 Co-simulation of a Rigid Platform with Mobile-Attitude Quadrotors (RP-MAQ)	146
5.4 Experimentations with RP-MAQ robot	150
5.5 Experimentations with FG-MAQ robot	161
5.6 Conclusions	174

This chapter is dedicated to the design and the implementation of a controller for the Flying Gripper with Mobile-Attitude Quadrotors (FG-MAQ) robot whose dynamic model is built in chapter 2. The objective of the controller is to allow the FG-MAQ robot to track a reference trajectory while closing or opening fingers by controlling the quadrotors' yaw rotations.

Section 5.1 presents a strategy to control the body structure's motion for trajectory tracking and the quadrotors' yaw rotations for driving fingers independently. The developed controller includes three modules: a high motion controller module, a control allocation module and a quadrotor controller module. The high motion controller computes the wrench that must be applied on the robot's body to follow a trajectory. The control allocation distributes this wrench to the quadrotors. For each quadrotor, the quadrotor controller control its thrust and attitude in order to fulfill the control signal revived from control allocation as well as to track a reference yaw angle trajectory for closing/opening

the corresponding finger.

Regarding the control allocation module, Dynamic Control Allocation (DCA) is applied in section 5.2, which is the main contribution of this chapter. It is a 2-step optimization method based on quadratic programming algorithm that considers actuators' limits and mechanical limits of U-joints (approximated with a linearized cone) and continuity of control. In section 5.3, a prototype is built using a Rigid Platform with Mobile-Attitude Quadrotors (RP-MAQ) and each quadrotor is connected to the rigid platform through a spherical joint. Fingers are not considered, but, thanks to spherical joints quadrotors can execute yaw motion to simulate closing or opening fingers.

The designed controller is first tested on the RP-MAQ robot using ADAMS-SIMULINK co-simulations in section 5.3, then it is tested on a prototype of RP-MAQ experimentally in section 5.4. Finally, a prototype of the FG-MAQ robot is built in section 5.5. Several experimental tests are conducted on the FG-MAQ prototype.

5.1 Control scheme of FG-MAQ

As presented previously in chapter 2, the robot's configuration is characterized by the general coordinate vector $\mathbf{q}^m = [\mathbf{p}_b^T \quad \mathbf{q}_a^{mT}]^T \in \mathbb{R}^{18 \times 1}$ where $\mathbf{p}_b \in \mathbb{R}^{6 \times 1}$ describes the pose of the body structure, $\mathbf{q}_a^m \in \mathbb{R}^{12 \times 1}$ describes the attitudes of the quadrotors.

We recall that the FG-MAQ dynamic model is represented by the following system of equations (see chapter 2 for details)

$$\mathbf{M}_b \ddot{\mathbf{p}}_b + \mathbf{c}_b = \mathbf{w}_b \quad (5.1)$$

$$\mathbf{M}_a \ddot{\mathbf{q}}_a^m + \mathbf{c}_a = {}^q \boldsymbol{\tau}_q \quad (5.2)$$

$$\mathbf{w}_b = \mathbf{W}_f {}^0 \mathbf{f}_q \quad (5.3)$$

$${}^0 \mathbf{f}_q = \mathbf{R}_r \mathbf{f}_z, \quad (5.4)$$

where the inputs of the dynamic systems are

1. $\mathbf{f}_z = [f_{1,z} \quad f_{2,z} \quad f_{3,z} \quad f_{4,z}]^T \in \mathbb{R}^{4 \times 1}$ where $f_{i,z}$ is the thrust of each quadrotor i ;
2. ${}^q \boldsymbol{\tau}_q = [{}^1 \boldsymbol{\tau}_1^T \quad {}^2 \boldsymbol{\tau}_2^T \quad {}^3 \boldsymbol{\tau}_3^T \quad {}^4 \boldsymbol{\tau}_4^T]^T \in \mathbb{R}^{12 \times 1}$ where ${}^i \boldsymbol{\tau}_i \in \mathbb{R}^{3 \times 1}$ stands for the torque of the i^{th} quadrotor expressed in \mathcal{F}_i .

In controller design, the inputs of the FG-MAQ dynamic model \mathbf{f}_z and ${}^q \boldsymbol{\tau}_q$ can be regrouped in ${}^q \mathbf{w}_q^r = [{}^1 \mathbf{w}_1^r{}^T \quad {}^2 \mathbf{w}_2^r{}^T \quad {}^3 \mathbf{w}_3^r{}^T \quad {}^4 \mathbf{w}_4^r{}^T]^T \in \mathbb{R}^{16 \times 1}$ with ${}^i \mathbf{w}_i^r = [f_{i,z} \quad {}^i \boldsymbol{\tau}_i^T]^T \in \mathbb{R}^{4 \times 1}$.

The dynamic model in chapter 2 shows two key properties of the FG-MAQ robot:

1. The FG-MAQ robot's pose is described by the vector \mathbf{p}_b . Since the rotational dynamics of quadrotors are independent from the dynamics of the body structure in chapter 2, then we can assume that \mathbf{p}_b is fully controllable by ${}^0\mathbf{f}_q$ (vector grouping thrust forces of all quadrotors). There exist an actuation redundancy of ${}^0\mathbf{f}_q$ because $\dim(\mathbf{p}_b) < \dim({}^0\mathbf{f}_q)$: with a given \mathbf{p}_b , an infinity of solutions for ${}^0\mathbf{f}_q$ exists.
2. The yaw angles ψ_i of the quadrotors do not influence the robot's motion, and therefore can be used to control the fingers' closing/opening motion.

Based on these properties, a strategy is proposed to control the FG-MAQ robot by a trajectory specifying:

1. the robot's motion by \mathbf{p}_b^* ,
2. the quadrotors' yaw rotations by $\boldsymbol{\psi}^* = [\psi_1^* \ \psi_2^* \ \psi_3^* \ \psi_4^*] \in \mathbb{R}^{4 \times 1}$.

In order to achieve the strategy above, we propose a control scheme for the FG-MAQ robot which consists in three modules (see Fig. 5.1):

1. The high-level motion controller enables the FG-MAQ robot to track a reference trajectory $\mathbf{p}_b^* \in \mathbb{R}^{6 \times 1}$ by computing the body wrench $\mathbf{w}_b \in \mathbb{R}^{6 \times 1}$;
2. The control allocation distributes the body wrench \mathbf{w}_b to the thrust forces of all quadrotors ${}^0\mathbf{f}_q$ that ${}^0\mathbf{f}_q = [{}^0\mathbf{f}_1^T \ {}^0\mathbf{f}_2^T \ {}^0\mathbf{f}_3^T \ {}^0\mathbf{f}_4^T]^T \in \mathbb{R}^{12 \times 1}$ where ${}^0\mathbf{f}_i \in \mathbb{R}^{3 \times 1}$ is the thrust force of quadrotor i expressed in the world frame \mathcal{F}_0 ;
3. The quadrotor controller embedded in each quadrotor i computes the quadrotor reduced wrench ${}^i\mathbf{w}_i^r$ for realizing the thrust force ${}^0\mathbf{f}_i$ and tracking the reference yaw angle ψ_i^* .

For this part of the work, we implement a PID controller in the high-level motion controller module (first module), a DCA algorithm to perform allocation in the control allocation module, and a PD controller in the quadrotor controller module.

5.1.1 High-level motion controller

As the control scheme depicted in Fig. 5.1, the high-level motion controller controls the robot's pose in order to track a reference trajectory \mathbf{p}_b^* .

Let us start by recalling Eq.(2.40) which expresses the dynamic model of the FG-MAQ robot

$$\mathbf{M}_b \ddot{\mathbf{p}}_b + \mathbf{c}_b = \mathbf{w}_b \quad (5.5)$$

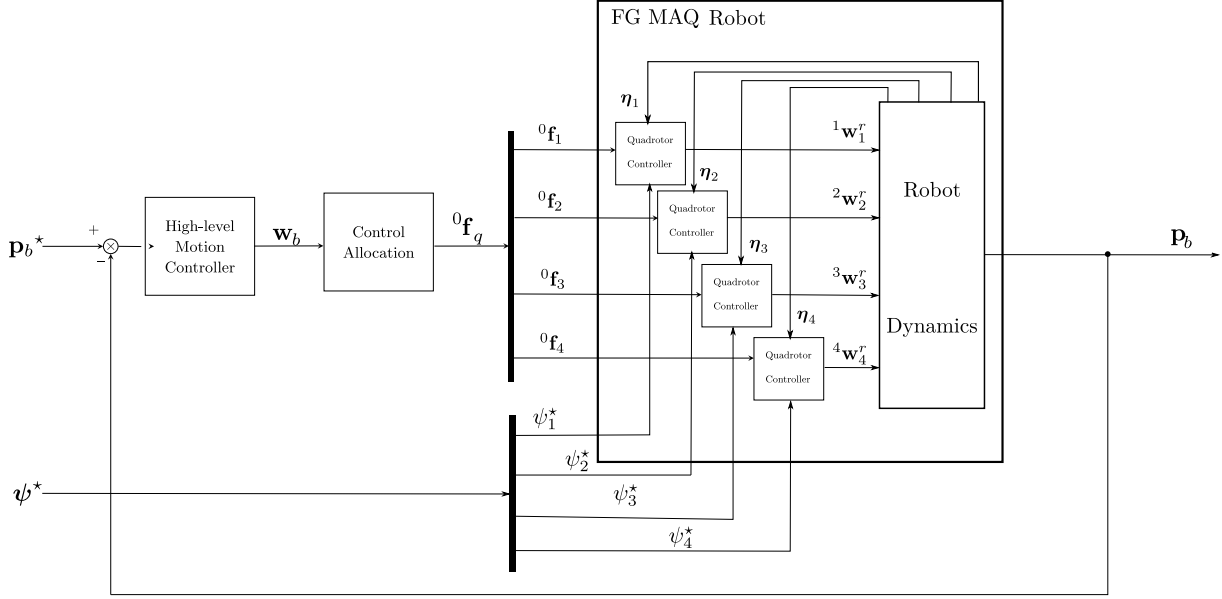


Figure 5.1 – General control scheme of Flying Gripper with Mobile-Attitude Quadrotors (FG-MAQ) consisting of a high-level motion controller module, a control allocation module and a quadrotor controller module. The high-level motion controller module computes the body wrench $\mathbf{w}_b \in \mathbb{R}^{6 \times 1}$ to track a reference trajectory $\mathbf{p}_b^* \in \mathbb{R}^{6 \times 1}$. The control allocation module distributes \mathbf{w}_b ${}^0\mathbf{f}_q \in \mathbb{R}^{12 \times 1}$ that is the vector regrouping all quadrotors' thrust force vectors expressed in \mathcal{F}_0 . Then, for each quadrotor i , the quadrotor controller computes the dynamic system input ${}^i\mathbf{w}_i^r \in \mathbb{R}^{4 \times 1}$ from the inputs ${}^0\mathbf{f}_i \in \mathbb{R}^{4 \times 1}$, the reference yaw angle ψ_i^* , and the attitude angle $\eta_i \in \mathbb{R}^{3 \times 1}$. Note that closing/opening the fingers is imposed by $\boldsymbol{\psi}^* = [\psi_1^* \ \psi_2^* \ \psi_3^* \ \psi_4^*] \in \mathbb{R}^{4 \times 1}$.

where we find $\dim(\mathbf{p}_b) = \dim(\mathbf{w}_b) = 6$ for the body structure and that makes \mathbf{p}_b fully controllable w.r.t \mathbf{w}_b . This property allows choosing various control methods for the high-level motion controller.

Control methods used in the high-level motion controller have to deal with variations of dynamic parameters caused by holding the object and change of fingers' configurations. Those variations are considered as uncertainties and disturbances in the controller design.

For the high-level motion controller, let first introduce a virtual input \mathbf{v}_b such that

$$\mathbf{w}_b = \mathbf{M}_b \mathbf{v}_b + \mathbf{c}_b \quad (5.6)$$

Substituting \mathbf{w}_b computed by Eq.(5.6) into Eq. (5.5) gives

$$\ddot{\mathbf{p}}_b = \mathbf{v}_b \quad (5.7)$$

A standard PID control law can be implemented

$$\mathbf{v}_b = \ddot{\mathbf{p}}_b^* + \mathbf{K}_{b,p}\mathbf{e}_p + \mathbf{K}_{b,d}\dot{\mathbf{e}}_p + \mathbf{K}_{b,i} \int \mathbf{e}_p \quad (5.8)$$

where \mathbf{p}_b^* is the reference trajectory and \mathbf{e}_p is the corresponding tracking error. The terms $\mathbf{K}_{b,p}$, $\mathbf{K}_{b,d}$, $\mathbf{K}_{b,i}$ are matrices corresponding to the proportional, derivative and integral gains. These matrices must be tuned to ensure the convergence of the tracking error \mathbf{e}_p .

5.1.2 Control allocation

The control allocation module, in Fig. 5.1, is built to distribute the body wrench \mathbf{w}_b among quadrotors. It distributes the body wrench $\mathbf{w}_b \in \mathbb{R}^{6 \times 1}$ to the quadrotors' thrust forces ${}^0\mathbf{f}_q \in \mathbb{R}^{12 \times 1}$. The relation between \mathbf{w}_b and ${}^0\mathbf{f}_q$ is modeled as

$$\mathbf{w}_b - \mathbf{W}_f {}^0\mathbf{f}_q = 0. \quad (5.9)$$

Since $\dim(\mathbf{w}_b) < \dim({}^0\mathbf{f}_q)$, there exists a certain amount of redundancy of ${}^0\mathbf{f}_q$ for producing \mathbf{w}_b . Because of this actuation redundancy, there exists an infinity of solutions for ${}^0\mathbf{f}_q$. We will discuss the control allocation module of FG-MAQ in section 5.2.

5.1.3 Quadrotor controller

As we can see in Fig. 5.1, the quadrotor controller is implemented for each quadrotor i and permits to

1. produce a thrust force ${}^0\mathbf{f}_i \in \mathbb{R}^{3 \times 1}$ (element of ${}^0\mathbf{f}_q \in \mathbb{R}^{12 \times 1}$) that is previously computed by the control allocation module,
2. follow a reference yaw angle ψ_i^* (element of $\boldsymbol{\psi}^* \in \mathbb{R}^{4 \times 1}$).

In terms of producing ${}^0\mathbf{f}_i$, each quadrotor i can merely generate a thrust force $f_{i,z}$ along its \mathbf{z}_i axis. For instance, one quadrotor cannot provide forces in a horizontal plane without changing its attitude. The relation between ${}^0\mathbf{f}_i$ and $f_{i,z}$ is modeled by Eq.(2.46) that is recalled here

$${}^0\mathbf{f}_i = \begin{bmatrix} \cos \phi_i \sin \theta_i \\ -\sin \phi_i \\ \cos \phi_i \cos \theta_i \end{bmatrix} f_{i,z}. \quad (5.10)$$

From this relation we find that ${}^0\mathbf{f}_i$ depends on the thrust $f_{i,z}$, the roll angle ϕ_i , and

the pitch angle θ_i , but it is independent of the yaw angle ψ_i . Considering this property, we propose a control strategy for the quadrotors (see Fig. 5.2):

1. controlling the quadrotor's thrust $f_{i,z}$, roll and pitch angles ϕ_i, θ_i in order to generate the required thrust force ${}^0\mathbf{f}_i$.
2. controlling the quadrotor's yaw angle ψ_i to track ψ_i^* .

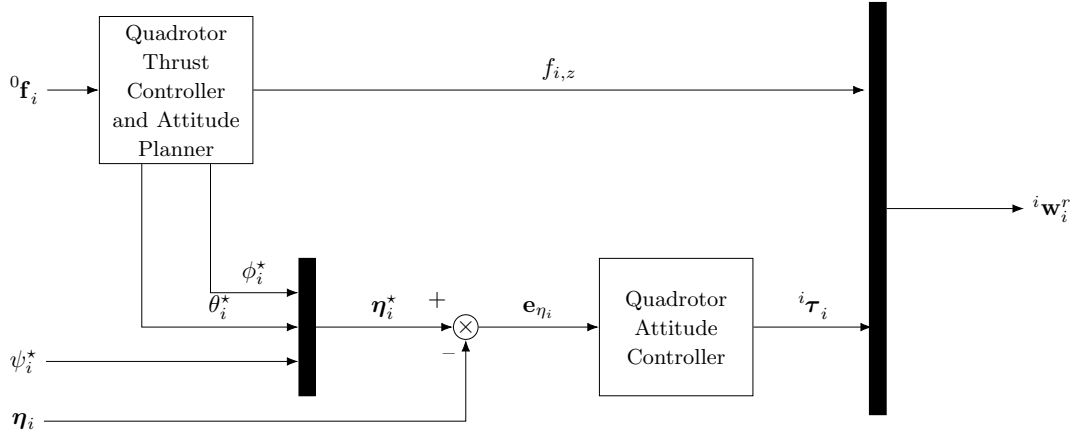


Figure 5.2 – Schematic representation of Quadrotor Controller of quadrotor i of the FG-MAQ robot that consists of i) a quadrotor thrust controller and attitude planner; ii) a quadrotor attitude controller. The quadrotor thrust controller and attitude planner computes the thrust force $f_{i,z} \in \mathbb{R}$ and the angles $\phi_i^*, \theta_i^* \in \mathbb{R}$, then the quadrotor attitude controller calculates the quadrotor torque ${}^i\boldsymbol{\tau}_i \in \mathbb{R}^{3 \times 1}$ to track the reference angle vector $\boldsymbol{\eta}_i^* = [\phi_i^* \quad \theta_i^* \quad \psi_i^*]^T \in \mathbb{R}^{3 \times 1}$. Finally, the output of the quadrotor controller module is the quadrotor reduced wrench ${}^i\mathbf{w}_i^r \in \mathbb{R}^{4 \times 1}$.

As the quadrotor controller's scheme shown in Fig. 5.2, there are two submodules in the quadrotor controller: i) a quadrotor thrust controller and attitude planner; ii) a quadrotor attitude controller.

Firstly, the quadrotor thrust controller and attitude planner computes the thrust $f_{i,z}$ and the desired roll and pitch angles ϕ_i^*, θ_i^* with a given thrust force ${}^0\mathbf{f}_i$

$$f_{i,z} = \| {}^0\mathbf{f}_i \| \quad (5.11)$$

$$\phi_i^* = -\sin^{-1} \left({}^0f_{i,x} \right) \quad (5.12)$$

$$\theta_i^* = \text{atan2} \left({}^0f_{i,x}, {}^0f_{i,z} \right). \quad (5.13)$$

Secondly, with ϕ_i^*, θ_i^* , computed by Eq.(5.12) and Eq.(5.13) in the quadrotor thrust

controller and attitude planner, and ψ_i^* from the reference trajectory, the quadrotor attitude controller calculates the torque ${}^i\boldsymbol{\tau}_i$ for forcing the quadrotor's attitude $\boldsymbol{\eta}_i$ to track the reference $\boldsymbol{\eta}_i^* = [\phi_i^* \quad \theta_i^* \quad \psi_i^*]^T$.

Let us recall the attitude dynamic model of quadrotor i in Eq.(2.38)

$$\mathbf{M}_i \ddot{\boldsymbol{\eta}}_i + \mathbf{c}_i = {}^i\boldsymbol{\tau}_i. \quad (5.14)$$

Note that the attitude of quadrotor i is fully controllable by ${}^i\boldsymbol{\tau}_i$ as $\dim(\boldsymbol{\eta}_i) = \dim({}^i\boldsymbol{\tau}_i) = 3$. This allows to use various control methods. In this section, we introduce a virtual input \mathbf{v}_{η_i} such that

$${}^i\boldsymbol{\tau}_i = \mathbf{M}_i \mathbf{v}_{\eta_i} + \mathbf{c}_i. \quad (5.15)$$

With ${}^i\boldsymbol{\tau}_i$ computed in Eq.(5.15), the attitude dynamic model becomes

$$\ddot{\boldsymbol{\eta}}_i = \mathbf{v}_{\eta_i}. \quad (5.16)$$

So, a standard PD control law is applied to obtain the virtual input \mathbf{v}_{η_i} as

$$\mathbf{v}_{\eta_i} = \ddot{\boldsymbol{\eta}}_i^* + \mathbf{K}_{\eta,p} \mathbf{e}_{\eta_i} + \mathbf{K}_{\eta,d} \dot{\mathbf{e}}_{\eta_i} \quad (5.17)$$

where $\mathbf{K}_{\eta,p}, \mathbf{K}_{\eta,d} \in \mathbb{R}^{3 \times 3}$ are matrices with gains to be tuned in order to correctly track the attitude of for quadrotor i and $\mathbf{e}_{\eta_i} = \boldsymbol{\eta}_i^* - \boldsymbol{\eta}_i$. Consequently, we obtain the torque ${}^i\boldsymbol{\tau}_i$ as

$${}^i\boldsymbol{\tau}_i = \mathbf{M}_i \left(\ddot{\boldsymbol{\eta}}_i^* + \mathbf{K}_{\eta,p} \mathbf{e}_{\eta_i} + \mathbf{K}_{\eta,d} \dot{\mathbf{e}}_{\eta_i} \right) + \mathbf{c}_i \quad (5.18)$$

Finally, for each quadrotor i , the proposed quadrotor controller composed of the quadrotor thrust controller and attitude planner (Eq.(5.11), Eq.(5.12) and Eq.(5.13)) and the quadrotor attitude controller (Eq.(5.18)) computes the control input ${}^i\mathbf{w}_i^r$. The input ${}^q\mathbf{w}_q^r$ of the FG-MAQ robot regrouping the ${}^i\mathbf{w}_i^r$ of all quadrotors is finally given as follows

$${}^q\mathbf{w}_q^r = \left[{}^1\mathbf{w}_1^r \quad {}^2\mathbf{w}_2^r \quad {}^3\mathbf{w}_3^r \quad {}^4\mathbf{w}_4^r \right]^T.$$

5.2 Dynamic Control Allocation of FG-MAQ

In chapter 4, the control allocation algorithm distributes the actuators' speed to produce a wrench on the body and apply yaw torques of quadrotors to close/open fingers.

This algorithm cannot deal with inequality constraints. Thus, Dynamic Control Allocation (DCA) is used in the control allocation module of FG-MAQ in order to take into account the actuators' capabilities, mechanical stops of U-joints and continuity of control.

5.2.1 Introduction to Dynamic Control Allocation

Control allocation is raised for overactuated systems whose number of DOF is smaller than the number of actuators. This type of algorithm has been used in particular on aircrafts [Chen, 2015a], aerial vehicles [Ryll et al., 2014], marine vessels [Johansen et al., 2004], submarine vehicles [Fossen and Johansen, 2006], cable-driven parallel robots [Caverly and Forbes, 2014]. Control Allocation is often formulated as an optimization problem where redundant degrees of actuation are used to achieve secondary objectives. The main objectives of Control Allocation are summarized in [Johansen and Fossen, 2013, Sadien, 2017]:

1. Achieve the desired control signal computed by the high-level motion controller.
2. Produce smoothly and reliably varying control distributions, that do not chatter back and forth from one time step to the next.
3. Solve secondary objectives that are often chosen from an operational perspective in order to minimize power or fuel consumption, minimization of actuator/effector tear and wear, or other criteria.
4. Require an acceptable computing power, especially for real-time computation.
5. Be compatible with the existing generalized control structure such that allocation algorithms can be designed without detailed knowledge about actuators.

If the allocation problem is modeled by linear systems, explicit solutions can be found in some cases [Johansen and Fossen, 2013]. However, for nonlinear systems several difficulties may occur like numerical robustness, convergence to a local minimum, computational complexity. Control allocation algorithms can be divided into different groups such as the unconstrained methods, the constrained methods (like cascaded generalized inverse), the optimization-based methods, the iterative methods, and the update law-based methods. A general panorama on these different control allocation techniques can be found in [Johansen and Fossen, 2013, Sadien, 2017].

When choosing an allocation algorithm for FG-MAQ robot, the optimization-based methods is one of the best choices. In recent years, they are widely used and developed in practice because the computational efficiency of computers has largely increased. Among

optimization-based methods, quadratic optimization is famous for its time-effective property, when dealing with linear constraints. Within this category, DCA is the most natural pick as it can ensure a good tracking accuracy, guarantee continuity of the control input, and, especially, consider the system constraints. Differently from allocation algorithms that consider only the current step, DCA takes into account the change in control inputs from the previous sample to the current sample, which is referred to the term "dynamic" [Härkegård, 2004].

Let us introduce DCA with a general allocation problem modeled by

$$\mathbf{v} = \mathbf{W}\mathbf{u}$$

where \mathbf{W} is the control effectiveness matrix, \mathbf{v} is the required control effort, \mathbf{u} is the control input of the system with $\dim(\mathbf{v}) < \dim(\mathbf{u})$. The method Dynamic Control Allocation (DCA) is proposed by Ola Härkegård in [Härkegård, 2004], which is a 2-step optimization method:

1. Ensure producing total control effort \mathbf{v} by minimizing $\mathbf{W}\mathbf{u} - \mathbf{v}$ in the 1st optimization as

$$\mathbf{u}_\Lambda = \underset{\mathbf{u}(t)}{\operatorname{argmin}} \|\mathbf{W}\mathbf{u}(t) - \mathbf{v}(t)\|^2 \quad (5.19)$$

$$\text{s.t. } \mathbf{A}\mathbf{u}(t) \leq \mathbf{b} \quad (5.20)$$

where $\mathbf{A}\mathbf{u}(t) \leq \mathbf{b}$ are linear inequalities that describe constraints of the system. In this step, $\Lambda = \left\{ \mathbf{u}(t) \mid \mathbf{u}(t) = \mathbf{u}_\Lambda(t) + \mathbf{Z}\mathbf{u}_0(t) \right\}$ is the set of feasible control inputs minimizing $\|\mathbf{W}\mathbf{u}(t) - \mathbf{v}(t)\|^2$, where the columns of \mathbf{Z} are bases of kernel of \mathbf{W} ($\mathbf{W}\mathbf{Z} = \mathbf{0}$) and $\mathbf{u}_0(t)$ is an arbitrary vector.

2. Select the control input \mathbf{u} inside the set Λ (the solution of the previous optimization) for the 2nd optimization to guarantee continuity of the control input and to keep the solution close to a desired state as

$$\mathbf{u}(t) = \underset{\mathbf{u}(t) \in \Lambda}{\operatorname{argmin}} \left\| \mathbf{W}_1^{-\frac{1}{2}} \left(\mathbf{u}(t) - \mathbf{u}_{des}(t) \right) \right\|^2 + \left\| \mathbf{W}_2^{-\frac{1}{2}} \left(\mathbf{u}(t) - \mathbf{u}(t - T_u) \right) \right\|^2 \quad (5.21)$$

$$\text{s.t. } \mathbf{A}\mathbf{u}(t) \leq \mathbf{b} \quad (5.22)$$

$$\Lambda = \left\{ \mathbf{u}(t) \mid \mathbf{u}(t) = \mathbf{u}_\Lambda(t) + \mathbf{Z}\mathbf{u}_0(t) \right\} \quad (5.23)$$

where \mathbf{W}_1 and \mathbf{W}_2 are weighting matrices allowing to manage the trade-off between keeping the control input \mathbf{u} close to a desired control input \mathbf{u}_{des} and minimizing the change in control input distribution from the previous time sample. We will discuss the choice of \mathbf{u}_{des} in section 5.2.3. The term T_u stands for control sampling period. If $\mathbf{W}_1, \mathbf{W}_2$ are symmetric and $\sqrt{\mathbf{W}_1^2 + \mathbf{W}_2^2}$ is non nonsingular, then it certifies that there is a unique optimal solution to the control allocation problem [Härkegård, 2004].

The objective function in Eq.(5.21) can be rewritten as

$$\left\| \mathbf{W}_1^{-\frac{1}{2}} (\mathbf{u}(t) - \mathbf{u}_{des}(t)) \right\|^2 + \left\| \mathbf{W}_2^{-\frac{1}{2}} (\mathbf{u}(t) - \mathbf{u}(t - T_u)) \right\|^2 \quad (5.24)$$

$$\Leftrightarrow \left\| \begin{bmatrix} \mathbf{W}_1^{-\frac{1}{2}} (\mathbf{u}(t) - \mathbf{u}_{des}(t)) \\ \mathbf{W}_2^{-\frac{1}{2}} (\mathbf{u}(t) - \mathbf{u}(t - T_u)) \end{bmatrix} \right\|^2 \quad (5.25)$$

$$\Leftrightarrow \left\| \begin{bmatrix} \mathbf{W}_1^{-\frac{1}{2}} \\ \mathbf{W}_2^{-\frac{1}{2}} \end{bmatrix} \mathbf{u}(t) - \begin{bmatrix} \mathbf{W}_1^{-\frac{1}{2}} \mathbf{u}_{des}(t) \\ \mathbf{W}_2^{-\frac{1}{2}} \mathbf{u}(t - T_u) \end{bmatrix} \right\|^2. \quad (5.26)$$

Therefore, the 2nd optimization is represented as

$$\mathbf{u}(t) = \underset{\mathbf{u}(t) \in \Lambda}{\operatorname{argmin}} \left\| \mathbf{Q} \mathbf{u}(t) - \boldsymbol{\delta} \right\|^2 \quad (5.27)$$

$$\text{s.t.} \quad \mathbf{A} \mathbf{u}(t) \leq \mathbf{b} \quad (5.28)$$

$$\Lambda = \left\{ \mathbf{u}(t) \mid \mathbf{u}(t) = \mathbf{u}_\Lambda(t) + \mathbf{Z} \mathbf{u}_0(t) \right\} \quad (5.29)$$

$$\text{where } \mathbf{Q} = \begin{bmatrix} \mathbf{W}_1^{-\frac{1}{2}} \\ \mathbf{W}_2^{-\frac{1}{2}} \end{bmatrix} \text{ and } \boldsymbol{\delta} = \begin{bmatrix} \mathbf{W}_1^{-\frac{1}{2}} \mathbf{u}_{des}(t) \\ \mathbf{W}_2^{-\frac{1}{2}} \mathbf{u}(t - T_u) \end{bmatrix}.$$

As we can see, the 2nd optimization is solved inside the solution set of the 1st optimization, which shows that the 1st optimization has a higher priority than the 2nd optimization does. Finally, the solution given by DCA ensures the production of the control effort \mathbf{v} satisfying the 1st priority, guarantees the continuity of the control input and approaches to a desired control input with the 2nd priority.

Here, a hierarchy approach can be used to solve this two step optimization problem as follows:

1. Obtain $\mathbf{u}_\Lambda(t)$ by solving the first step optimization in Eq.(5.19), which is aimed to minimize $\| \mathbf{W} \mathbf{u}(t) - \mathbf{v}(t) \|^2$

2. Calculating matrix \mathbf{Z} whose columns are bases of kernel of \mathbf{W} such that $\mathbf{WZ} = \mathbf{0}$.
3. The final solution can be represented as $\mathbf{u}(t) = \mathbf{u}_\Lambda(t) + \mathbf{Zu}_0(t)$ where $\mathbf{u}_0(t)$ is an arbitrary vector. It is worthy to mention that $\mathbf{Wu}(t) = \mathbf{W}(\mathbf{u}_\Lambda(t) + \mathbf{Zu}_0(t)) = \mathbf{Wu}_\Lambda(t)$, which means $\mathbf{u}_0(t)$ can be chosen for the 2nd optimization without influencing the 1st one.

By substituting $\mathbf{u}_0(t)$ for $\mathbf{u}(t)$, the 2nd optimization can be represented as

$$\mathbf{u}_0(t) = \operatorname{argmin} \|\mathbf{QZu}_0(t) - \boldsymbol{\delta} + \mathbf{Qu}_\Lambda(t)\|^2 \quad (5.30)$$

$$\text{s.t. } \mathbf{AZu}_0(t) \leq \mathbf{b} - \mathbf{Au}_\Lambda(t) \quad (5.31)$$

from which we can calculate the solution $\mathbf{u}_0(t)$.

4. Computing the final solution $\mathbf{u}(t) = \mathbf{u}_\Lambda(t) + \mathbf{Zu}_0(t)$ where $\mathbf{u}_\Lambda(t)$ is computed in step 1 and $\mathbf{u}_0(t)$ is computed in step 3.

5.2.2 Constraints in Dynamic Control Allocation of FG-MAQ

The most important objective of the control allocation module is to distribute the body wrench \mathbf{w}_b to the 4 quadrotors' thrust forces ${}^0\mathbf{f}_q$, which is modeled in Eq.(5.9)

$$\mathbf{w}_b - \mathbf{W}_f {}^0\mathbf{f}_q = \mathbf{0}. \quad (5.32)$$

In this section, the goal is to design a new control allocation module having the following characteristics:

- Ability to satisfy the physical limits of the robot (U-joint mechanical limits and the motor speed limits of the quadrotors);
- Continuity in the control;
- Computational efficiency/real-time capability for the experimentation.

Therefore, DCA is implemented for the FG-MAQ robot. In DCA, distributing the body wrench to all quadrotors is realized in the 1st optimization, which is formulated as

$$\mathbf{u}_\Lambda = \operatorname{argmin}_{{}^0\mathbf{f}_q(t)} \|\mathbf{W}_f {}^0\mathbf{f}_q(t) - \mathbf{w}_b(t)\|^2 \quad (5.33)$$

$$\text{s.t. } \mathbf{A}_f {}^0\mathbf{f}_q(t) \leq \mathbf{b}_f \quad (5.34)$$

As it can be seen from Eq.(5.33), the distribution of the body wrench is modeled as

a quadratic programming problem aiming to minimize the virtual control error function $\|\mathbf{W}_f {}^0\mathbf{f}_q - \mathbf{w}_b\|^2$. Physical constraints concerning the decision variable ${}^0\mathbf{f}_q$ are modeled using linear inequalities: $\mathbf{A}_f {}^0\mathbf{f}_q \leq \mathbf{b}_f$.

For the FG-MAQ robot, there are two main constraints of the FG-MAQ robot: the actuators' capabilities of quadrotors and the U-joints mechanical rotation limits. For each quadrotor i , there is a linear mapping between the quadrotor's reduced wrench and the motors' speed square (see Eq.(2.9)). Thus, the available thrust force of quadrotor i depends on its motor speed limits. For each U-joint i , it only allows for a certain range of the i^{th} quadrotor's rotation.

In chapter 3, we computed the available set \mathcal{W}_i^s of ${}^s\mathbf{f}_i$ that is the force that quadrotor i can produce considering the actuators' capabilities and the U-joint constraint in \mathcal{F}_{s_i} (see section B.1.3 and Fig. 3.17c), which is a linearized cone in \mathcal{F}_{s_i} . Indeed, we can compute the \mathcal{H} -representation of \mathcal{W}_i^s in order to obtain the inequality constraints for ${}^s\mathbf{f}_i$ (see Appendix about operations on polytopes)

$$\mathbf{A}_{f_s} {}^s\mathbf{f}_i \leq \mathbf{b}_{f_s}, \quad (5.35)$$

which can be rewritten as

$$\mathbf{A}_{f_s} {}^{s_i}\mathbf{R}_0 {}^0\mathbf{f}_i \leq \mathbf{b}_{f_s} \quad (5.36)$$

where ${}^{s_i}\mathbf{R}_0 \in \mathbb{R}^{3 \times 3}$ is the rotation matrix of \mathcal{F}_0 w.r.t \mathcal{F}_{s_i} .

Till now, we obtain the linear inequalities for ${}^0\mathbf{f}_i$. It should be noted that Eq.(5.36) gives a linearized approximation of the available thrust force set in frame \mathcal{F}_0 . The dimension of matrix \mathbf{A}_{f_s} and vector \mathbf{b}_{f_s} depend on the approximation.

Extending this model from quadrotor i to all quadrotors permits to obtain a linearized approximation of the available set of all quadrotors' thrust force ${}^0\mathbf{f}_q$ as

$$\begin{bmatrix} \mathbf{A}_{f_s} {}^{s_1}\mathbf{R}_0 & \mathbf{0} & \mathbf{0} & \mathbf{0} \\ \mathbf{0} & \mathbf{A}_{f_s} {}^{s_2}\mathbf{R}_0 & \mathbf{0} & \mathbf{0} \\ \mathbf{0} & \mathbf{0} & \mathbf{A}_{f_s} {}^{s_3}\mathbf{R}_0 & \mathbf{0} \\ \mathbf{0} & \mathbf{0} & \mathbf{0} & \mathbf{A}_{f_s} {}^{s_4}\mathbf{R}_0 \end{bmatrix} {}^0\mathbf{f}_q \leq \begin{bmatrix} \mathbf{b}_{f_s} \\ \mathbf{b}_{f_s} \\ \mathbf{b}_{f_s} \\ \mathbf{b}_{f_s} \end{bmatrix} \quad (5.37)$$

Therefore, the 1st optimization of DCA for FG-MAQ robot based on the objective

function in Eq.(5.33) and the constraint model in Eq.(5.37) is proposed as

$$\mathbf{u}_\Lambda = \underset{{}^0\mathbf{f}_q}{\operatorname{argmin}} \|\mathbf{W}_f {}^0\mathbf{f}_q(t) - \mathbf{w}_b(t)\|^2 \quad (5.38)$$

$$\text{s.t. } \mathbf{A}_f {}^0\mathbf{f}_q(t) \leq \mathbf{b}_f \quad (5.39)$$

where $\mathbf{A}_f = \operatorname{diag}(\mathbf{A}_{f_s}{}^{s1}\mathbf{R}_0, \mathbf{A}_{f_s}{}^{s2}\mathbf{R}_0, \mathbf{A}_{f_s}{}^{s3}\mathbf{R}_0, \mathbf{A}_{f_s}{}^{s4}\mathbf{R}_0)$, $\mathbf{b}_f = [\mathbf{b}_{f_s}^T \ \mathbf{b}_{f_s}^T \ \mathbf{b}_{f_s}^T \ \mathbf{b}_{f_s}^T]^T$ and the objective function in Eq.(5.38) is to minimize $\|\mathbf{W}_f {}^0\mathbf{f}_q - \mathbf{w}_b\|$ in order to produce the required body wrench to track a reference trajectory, while the set of the linear inequalities $\mathbf{A}_f {}^0\mathbf{f}_q \leq \mathbf{b}_f$ describes the constraints imposed by the mechanical limits of U-joints and the motor speed limits.

5.2.3 Continuity of control in Dynamic Control Allocation of FG-MAQ

As explained previously in section 5.1.3, each quadrotor controller i computes the thrust force $f_{i,z}$ and θ_i^*, ψ_i^* : the quadrotor needs to change its thrust force, roll and pitch angles in order to produce ${}^0\mathbf{f}_i$. Thus, it is significant for the control allocation's solution ${}^0\mathbf{f}_q$ to be continuous, as large and instant change in ${}^0\mathbf{f}_q$ might cause instability for the quadrotor controllers. Thus, we aim to penalize the change in ${}^0\mathbf{f}_q$ by minimizing

$$\mathbf{g}_1(t) = {}^0\mathbf{f}_q(t) - {}^0\mathbf{f}_q(t - T_u). \quad (5.40)$$

Also, DCA offers a choice to keep the solution ${}^0\mathbf{f}_q$ close to a desired steady state ${}^0\mathbf{f}_{q_{\text{des}}}$. This is conducted by minimizing

$$\mathbf{g}_2(t) = {}^0\mathbf{f}_q(t) - {}^0\mathbf{f}_{q_{\text{des}}}. \quad (5.41)$$

where

$${}^0\mathbf{f}_{q_{\text{des}}} = \begin{bmatrix} {}^0\mathbf{f}_{\text{des},1}^T & {}^0\mathbf{f}_{\text{des},2}^T & {}^0\mathbf{f}_{\text{des},3}^T & {}^0\mathbf{f}_{\text{des},4}^T \end{bmatrix}^T \quad (5.42)$$

and ${}^0\mathbf{f}_{\text{des},i}$ represents the desired state for ${}^0\mathbf{f}_i$, which specifies the desired thrust, roll and pitch angles for quadrotor i . It permits to specify the desired thrust forces of all quadrotors ${}^0\mathbf{f}_{q_{\text{des}}}$. Here, ${}^0\mathbf{f}_{q_{\text{des}}}$ is chosen based on an energy effective point of view: all quadrotors are horizontal and generate thrust forces to compensate the gravity, which is represented by

equation

$${}^0\mathbf{f}_{\text{des},i} = \frac{m_t}{4} \mathbf{g} \quad (5.43)$$

such that

$$\mathbf{W}_f {}^0\mathbf{f}_{q_{\text{des}}} = m_t \mathbf{g}. \quad (5.44)$$

Therefore, the 2nd optimization of DCA based on Eq.(5.40) and Eq.(5.41) is proposed in the form

$${}^0\mathbf{f}_q(t) = \underset{{}^0\mathbf{f}_q(t) \in \Lambda}{\text{argmin}} \left\| \mathbf{W}_1^{-\frac{1}{2}} \mathbf{g}_1(t) \right\|^2 + \left\| \mathbf{W}_2^{-\frac{1}{2}} \mathbf{g}_2(t) \right\|^2 \quad (5.45)$$

$$\text{s.t. } \mathbf{A}_f {}^0\mathbf{f}_q(t) \leq \mathbf{b}_f \quad (5.46)$$

Where \mathbf{W}_1 and \mathbf{W}_2 are two weighting matrices to manage the trade-off between two requirements modeled in Eq.(5.40) and Eq.(5.41). We can tune these two matrices to change the trade-off according to the task.

5.3 Co-simulation of a Rigid Platform with Mobile-Attitude Quadrotors (RP-MAQ)

5.3.1 Introduction to RP-MAQ

We decide to take a step-by-step approach for implementing the designed controller for the FG-MAQ robot. Before building the final FG-MAQ robot, we choose to build a prototype to test and validate the designed controller.

This prototype is named in the sequel the Rigid Platform with Mobile-Attitude Quadrotors (RP-MAQ). The RP-MAQ robot is a rigid platform linked with 4 quadrotors through spherical joints (S-joints) and its CAD model is shown in Fig. 5.3. All quadrotors are linked to the platform through S-joints. The RP-MAQ robot can be viewed as a simple version of FG-MAQ without fingers.

The difference between the center of one S-joint and the CoM of one quadrotor, (see Fig. 5.3b), is viewed as a modeling error. It is worthy to mention that S-joints permit yaw rotations of quadrotors, therefore we can simulate the closing sequence by controlling quadrotors' yaw rotations, even if the RP-MAQ robot does not actuate a finger.

The parameters of the RP-MAQ robot is given in the Table 5.1. The designed controller is tested on the RP-MAQ robot in co-simulation between MATLAB-SIMULINK and

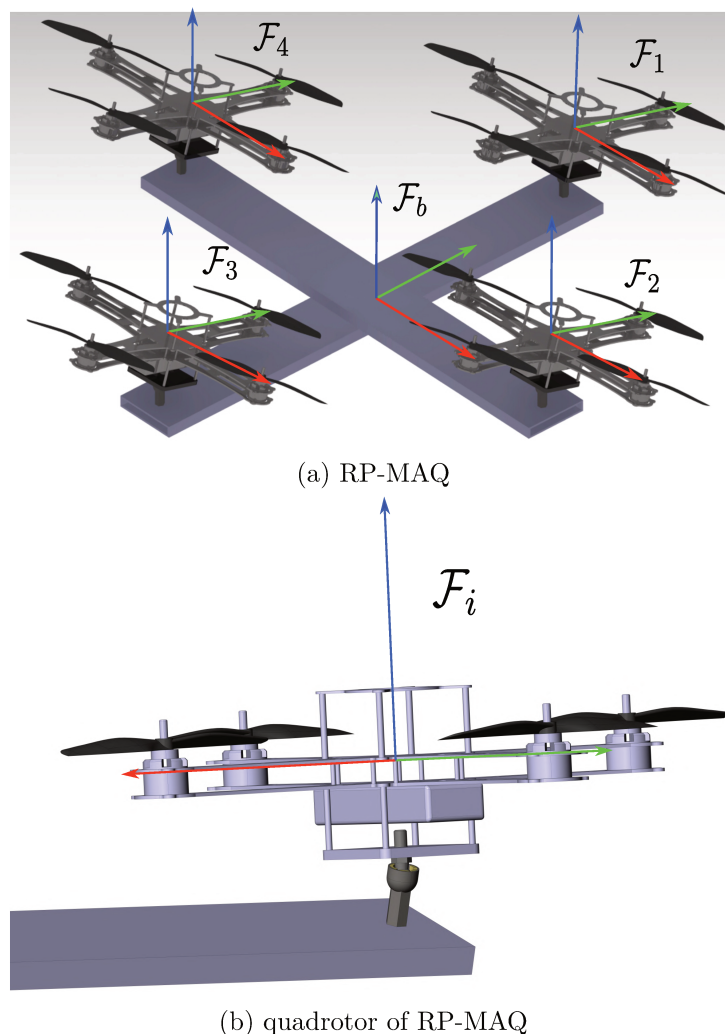


Figure 5.3 – CAD view of RP-MAQ and its main frames. The RP-MAQ robot is a rigid platform linked with 4 quadrotors through spherical joints.

ADAMS (see the controller scheme in Fig. 5.1). In this co-simulation, the controller is implemented in MATLAB-SIMULINK, while the dynamics of RP-MAQ is simulated in ADAMS. The DCA is solved using the *quadprog* function in MATLAB that provides different algorithms, such as interior point convex algorithm and active set algorithm. Inputs of the dynamic co-simulation is represented by the vector regrouping wrenches of the quadrotors ${}^q\mathbf{w}_q^r$ and we consider that all elements of \mathbf{q}^m can be measured directly. In order to simulate the practical experiment condition, a uniformly distributed noise was added to each variable of \mathbf{q}^m . The amplitude of the uniform distribution was defined according to the Motion Capture System (MOCAP) precision with the following values:

Table 5.1 – Dynamic parameters of RP-MAQ in co-simulation

Parameter	Value
m_i (kg)	1.0
\mathbf{I}_i (kg m ²)	diag(0.0010, 0.0010, 0.0020)
d_q (m)	0.17
m_b (kg)	1.2
\mathbf{I}_b (kg m ²)	diag(0.035, 0.035, 0.069)
${}^b\mathbf{r}_1$ (m)	$\begin{bmatrix} 0.40 & 0 & 0.050 \end{bmatrix}$
${}^b\mathbf{r}_2$ (m)	$\begin{bmatrix} 0 & 0.40 & 0.050 \end{bmatrix}$
${}^b\mathbf{r}_3$ (m)	$\begin{bmatrix} -0.40 & 0 & 0.050 \end{bmatrix}$
${}^b\mathbf{r}_4$ (m)	$\begin{bmatrix} 0 & -0.40 & 0.050 \end{bmatrix}$
φ_{\max} (°)	25

10^{-3} m for position, 10^{-3} rad for attitude and 10^{-3} rad s⁻¹ for the body rate.

5.3.2 Discussion on co-simulation results of RP-MAQ robot

This simulation is conducted to test the designed controller and energy efficiency of DCA in trajectory tracking. A reference trajectory is designed to include two segments

1. 0 sec – 2 sec: taking off,
2. 2 sec – 15 sec: following a square trajectory in the horizontal plane.

The trajectory tracking of the body structure is given in Fig. 5.4 and Fig. 5.5. The U-joints rotations are shown in Fig. 5.6 and the control input is given in Fig. 5.7 and Fig. 5.8. We can see from those results that the error interval of translation is $[-4 \times 10^{-2}$ m, 4×10^{-2} m] and that of attitude is $[-8 \times 10^{-2}$ rad, 9×10^{-2} rad]. The mechanical limits of U-joint are satisfied in the co-simulation. One video of this co-simulation is available with link¹.

1. <https://youtu.be/ZKi1EiNYYyM>

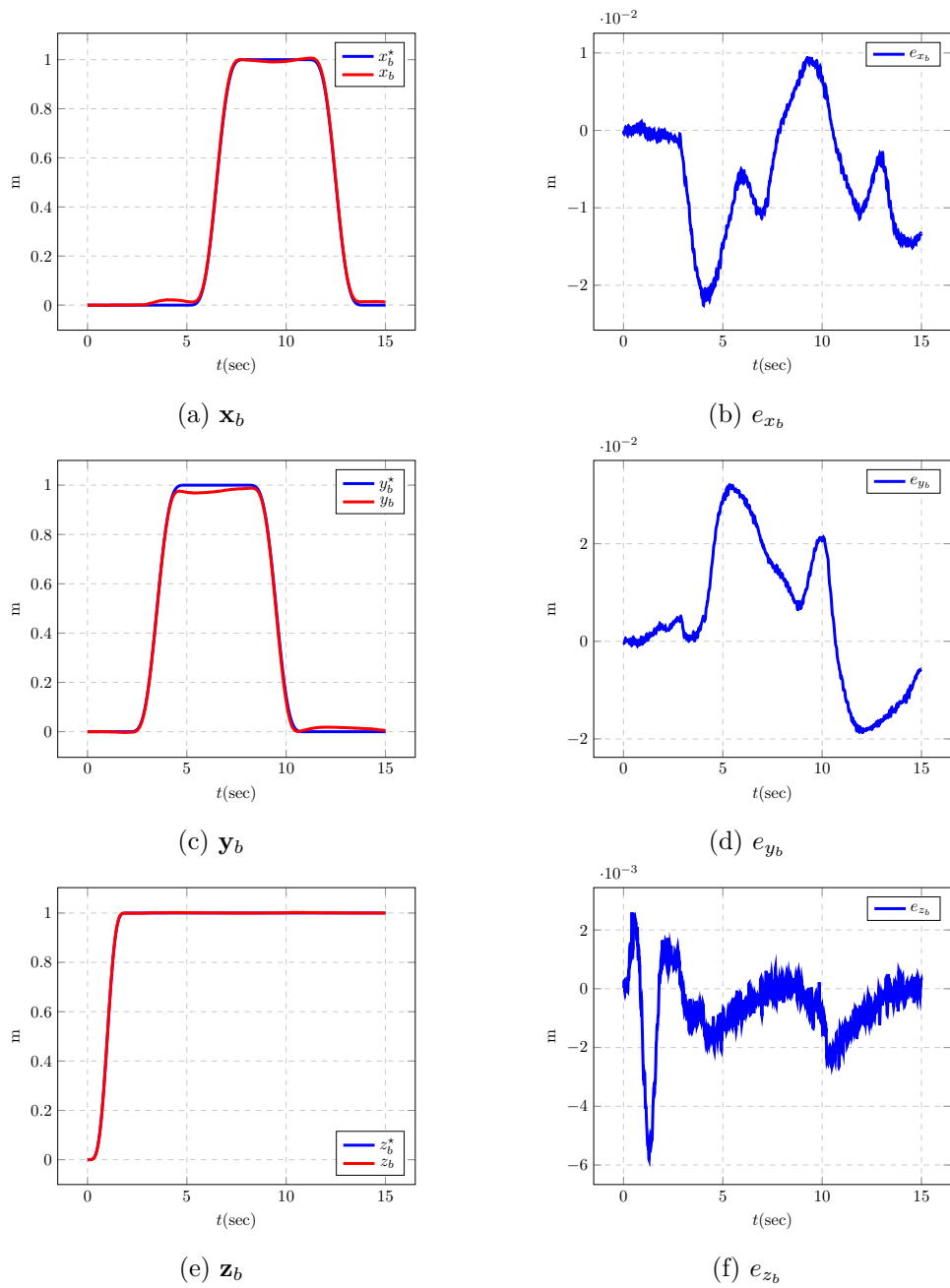


Figure 5.4 – Co-simulation of Rigid Platform with Mobile-Attitude Quadrotors following a square trajectory under sensor noise: reference trajectory and tracking errors of translation coordinates of the vector \mathbf{p}_b

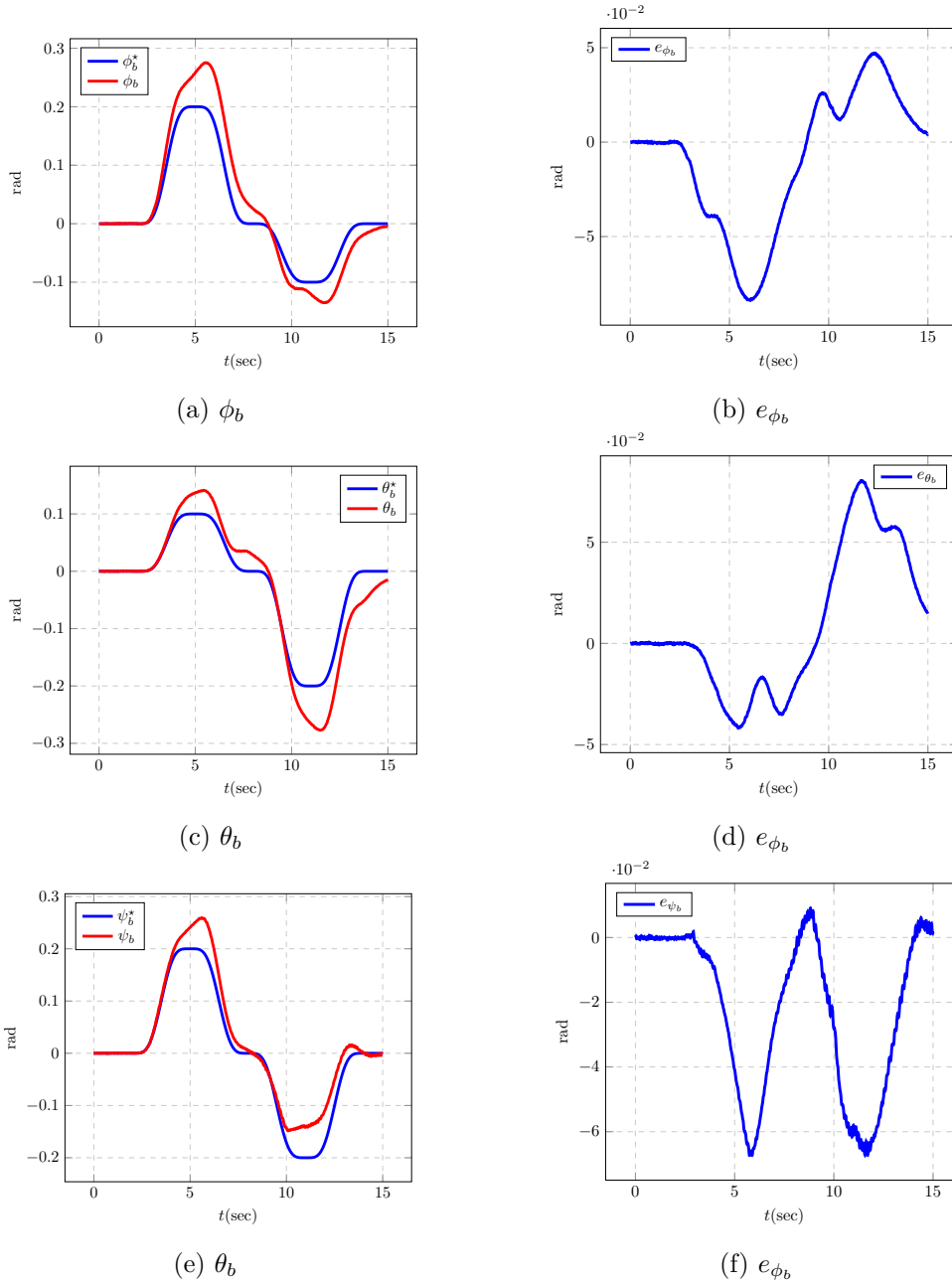


Figure 5.5 – Co-simulation of Rigid Platform with Mobile-Attitude Quadrotors following a square trajectory under sensor noise: reference trajectory and tracking errors of attitude coordinates of the vector \mathbf{p}_b

5.4 Experimentations with RP-MAQ robot

This section sets out to build the RP-MAQ robot for experiments and test the designed controller (see its scheme in Fig. 5.1) in real-time experiments. It is of importance to note

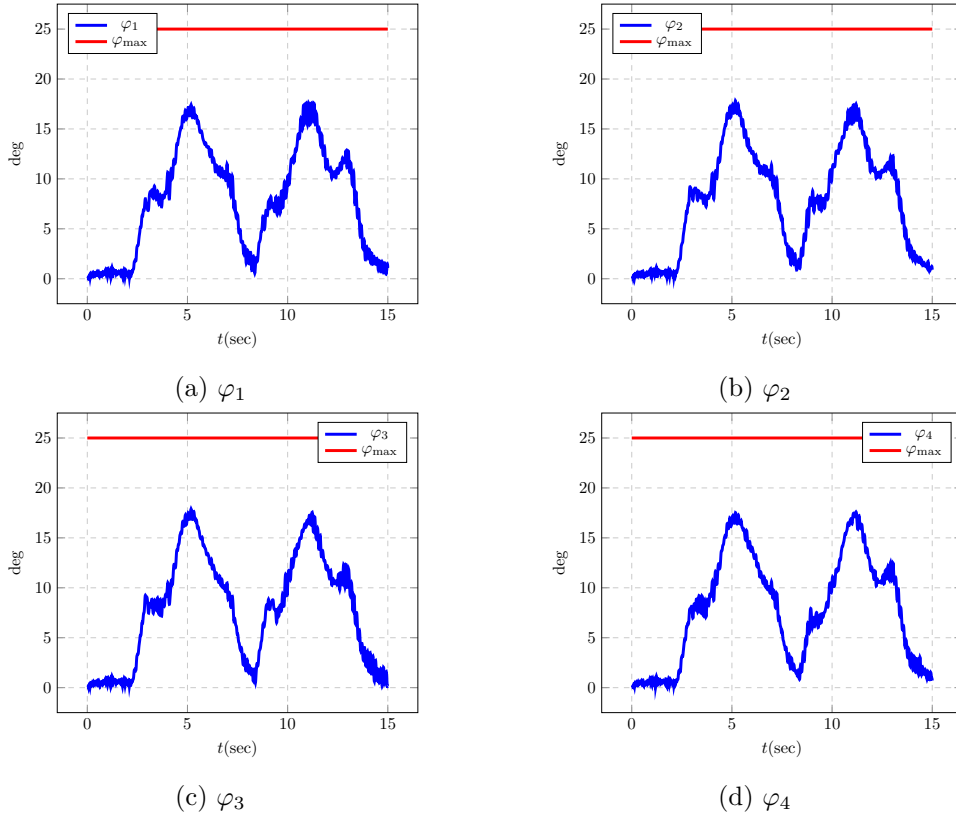


Figure 5.6 – Co-simulation of Rigid Platform with Mobile-Attitude Quadrotors following a square trajectory under sensor noise: rotation angles of U-joints $\varphi_i, i = 1 \dots 4$.

that a quadrotor controller module is designed for each quadrotor i to compute ${}^i\mathbf{w}_i^r$ that is the input of the robot dynamic system. In experiments, instead of programming such a controller, we embed an autopilot Pixhawk—introduced later in this section—in each quadrotor to compute ${}^i\mathbf{w}_i^r$ and then transform ${}^i\mathbf{w}_i^r$ to the physical robot system input $\mathbf{\Omega}_i$.

We detail in the next section the main components of the RP-MAQ robot. This is followed by the introduction of the sensor and communication system used in the experiment. The previously designed controller is tested in the experiment and the results are presented and analyzed.

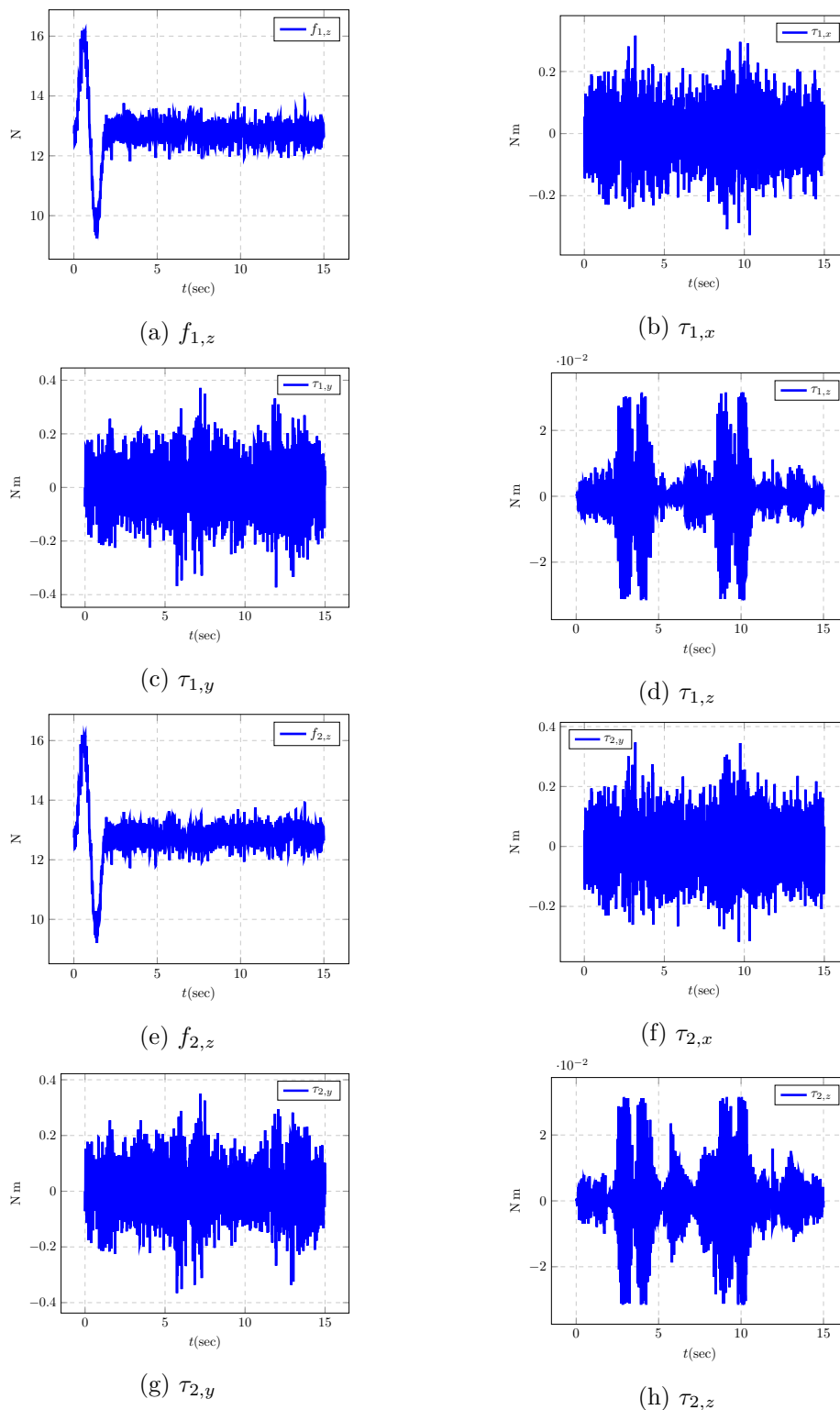


Figure 5.7 – Co-simulation of Rigid Platform with Mobile-Attitude Quadrotors following a square trajectory under sensor noise: reduced wrenches of quadrotors 1 and 2

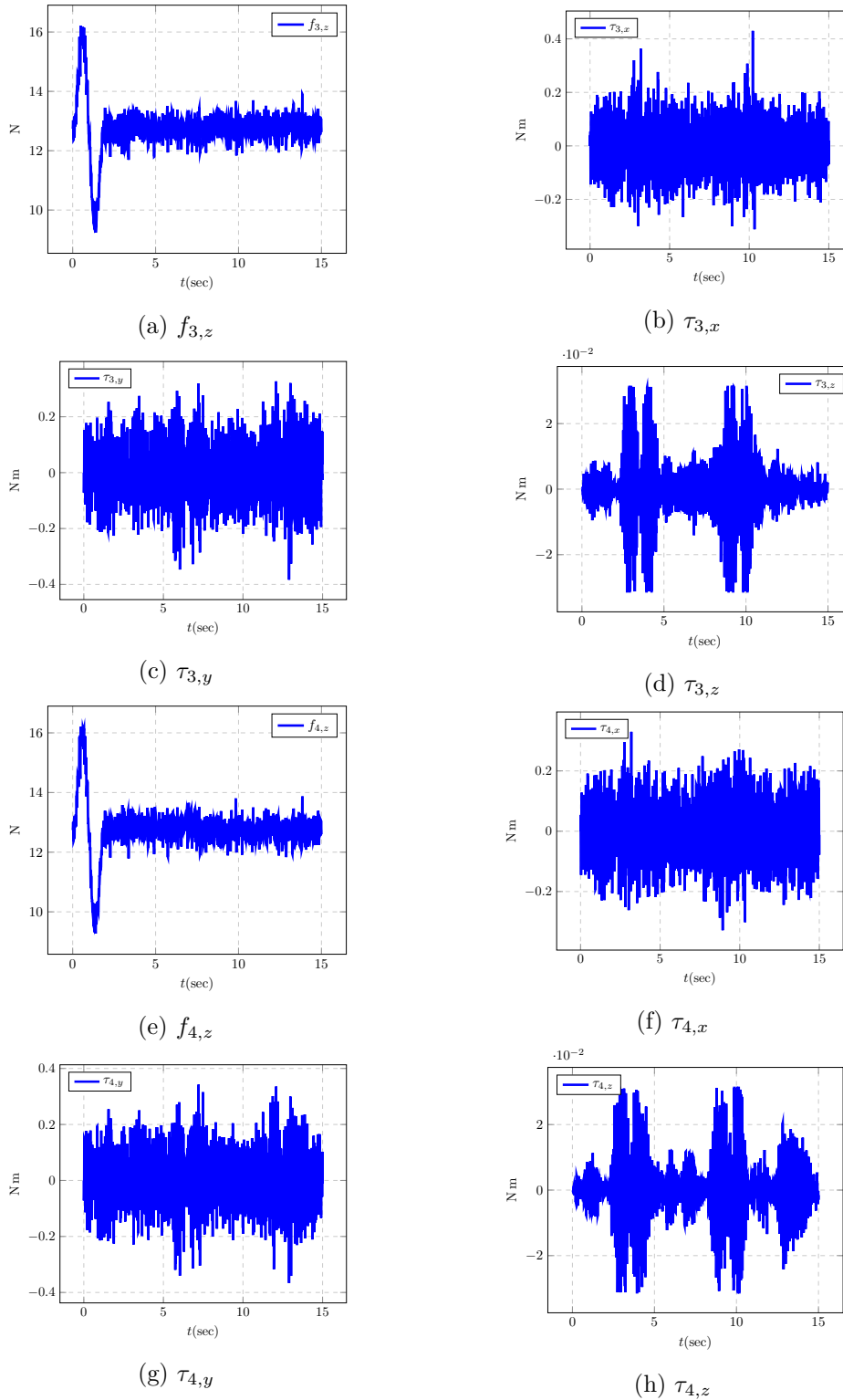


Figure 5.8 – Co-simulation of Rigid Platform with Mobile-Attitude Quadrotors following a square trajectory under sensor noise: reduced wrenches of quadrotors 3 and 4

5.4.1 Experimental setup

Quadrotors

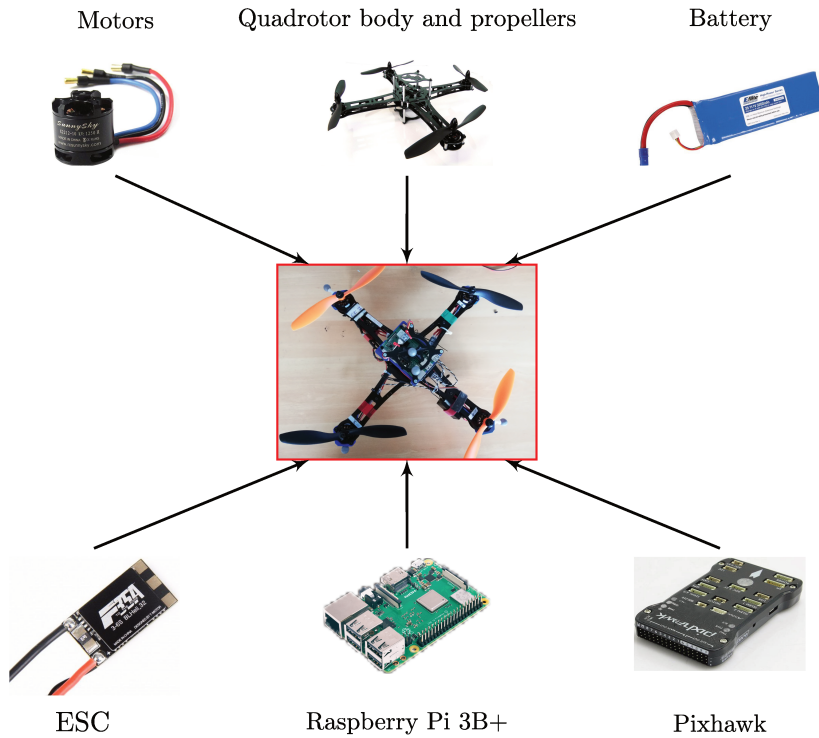


Figure 5.9 – Main components of quadrotors of RP-MAQ

Quadrotors are the key components and actuators of the RP-MAQ robot. The main physical elements of one quadrotor include 1 quadrotor body, 4 motors, 2 pairs of propellers, an autopilot, an onboard computer, 4 Electronic Speed Controllers (ESC), which are shown in Fig. 5.9. The key components of the quadrotor in this experiment, (see Table 5.2), are listed as follows:

1. The quadrotor body used in this experiment is the Lynxmotion Crazy2fly with 34 cm between opposing motors;
2. The brushless motors (X2212-kv1250 from Sunnysky), the ESC (F35A from T-Motor) and the propellers (8 inch \times 4.5 inch)² are chosen. They are able to produce a maximal 6 N force for each propeller (estimation in tests).
3. The Pixhawk is an open-source autopilot for diverse UAVs and other autonomous

2. propeller has a length of 8 inch and it would move forward 4.5 inches in one revolution.

vehicles. It provides a low-level quadrotor controller and sensors to control the motors' speed by generating Pulse Width Modulation (PWM) signals.

4. A Raspberry Pi 3B+ (RPi) has a 1.4 GHz 64-bit quad-core processor that is used onboard the quadrotor for communicating with the working station over a local 5 GHz WIFI channel and the autopilot Pixhawk of the quadrotor.

Table 5.2 – Main components of the RP-MAQ robot's quadrotors in experiments

Components	Parameters
Quadrotor body	Lynxmotion Crazy2Fly
Onboard computer	Raspberry Pi 3 Model B+
Autopilot	Pixhawk 1 Flight Controller
ESC	F35A from T-Motor
Motors	X2212-kv1250 from Sunnysky
Propellers	8×4.5
Battery	LiPo Battery (11.1 V, 3200 mA h)

One quadrotor of the RP-MAQ robot is assembled as shown in Fig. 5.10.

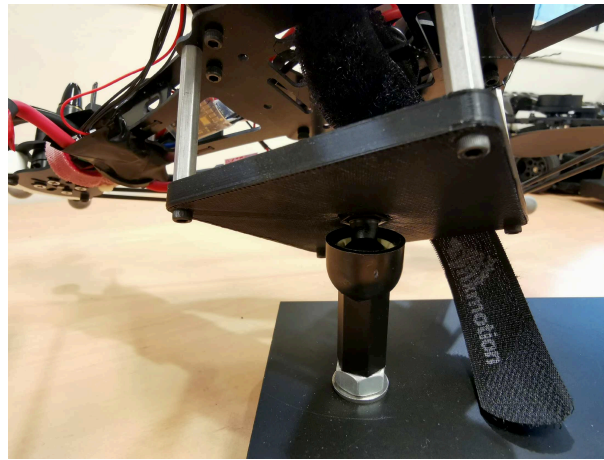


Figure 5.10 – Quadrotor of RP-MAQ

Body structure of the RP-MAQ robot

We build an aluminum body structure with dimension $1\text{ m} \times 1\text{ m}$ and a mass of 1.5 kg. As mentioned in the previous chapter, each quadrotor of the RP-MAQ robot is linked to the body structure through one S-joint and the quadrotor's attitude must fulfill the mechanical limits of the S-joint (see Fig. 5.10 and Fig. 5.11a), which is represented by the angle φ_{\max} . Note that the angle φ_{\max} depends on the chosen S-joint.

The main parameters of the RP-MAQ robot are listed in Table 5.3.



(a) S-joint of RP-MAQ



(b) RP-MAQ

Figure 5.11 – Prototype of RP-MAQ and S-joints in red circles. Each quadrotor is linked to the RP-MAQ body through a S-joint.

5.4.2 Sensors and communication protocol

Motion Capture System and Flight Control Unit

We utilize a Motion Capture System (MOCAP) called Qualisys that consists of 8 infrared cameras to localize the robot. The cameras are placed on the bounds of an enclosed volume of approximately $4\text{ m} \times 4\text{ m} \times 4\text{ m}$ (see Fig. 5.12). With the images taken by the cameras, the Qualisys software calculates the pose of each registered body in a predefined reference frame (see Fig. 5.13).

The Flight Control Unit (FCU) of the Pixhawk is a combination of accelerometers, gyroscopes, magnetometers, and barometers, to measure acceleration, orientation, angular

Table 5.3 – Main parameters of the RP-MAQ robot in experiments

Parameter	Value
m_i (kg)	1.1
\mathbf{I}_i (kg m ²)	diag(0.012, 0.012, 0.025)
d_q (m)	0.17
m_b (kg)	1.2
\mathbf{I}_b (kg m ²)	diag(0.14, 0.14, 0.28)
${}^b\mathbf{r}_1$ (m)	$\begin{bmatrix} 0.40 & 0 & 0.05 \end{bmatrix}$
${}^b\mathbf{r}_2$ (m)	$\begin{bmatrix} 0 & 0.40 & 0.05 \end{bmatrix}$
${}^b\mathbf{r}_3$ (m)	$\begin{bmatrix} -0.40 & 0 & 0.050 \end{bmatrix}$
${}^b\mathbf{r}_4$ (m)	$\begin{bmatrix} 0 & -0.40 & 0.050 \end{bmatrix}$
φ_{\max} (°)	25



Figure 5.12 – Quadrotor arena and Motion Capture System cameras (in the red circles)

velocity, the magnetic field to find the north direction, and air pressure of the environment. An Extended Kalman Filter algorithm embedded in the Pixhawk processes those sensor measurements and provides an estimation of the quadrotor's pose, translational and angular velocities.

In experiments, it is worthy to mention that the Pixhawk plays as a part of the quadrotor controller (see Fig. 5.2). Indeed, for each quadrotor i , the Pixhawk offers a "thrust and attitude" mode, which takes the thrust force $f_{i,z}$ and the attitude $\boldsymbol{\eta}_i^*$ as the inputs and then controls the motors' speed to finally produce the needed wrench ${}^i\mathbf{w}_i^r$.

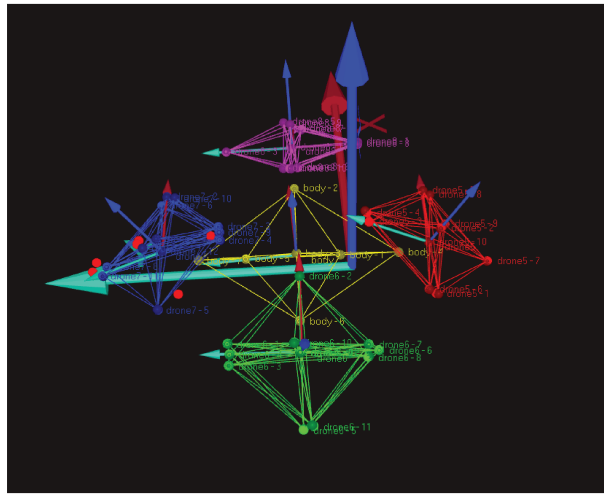


Figure 5.13 – RP-MAQ visualized in Motion Capture System system interface

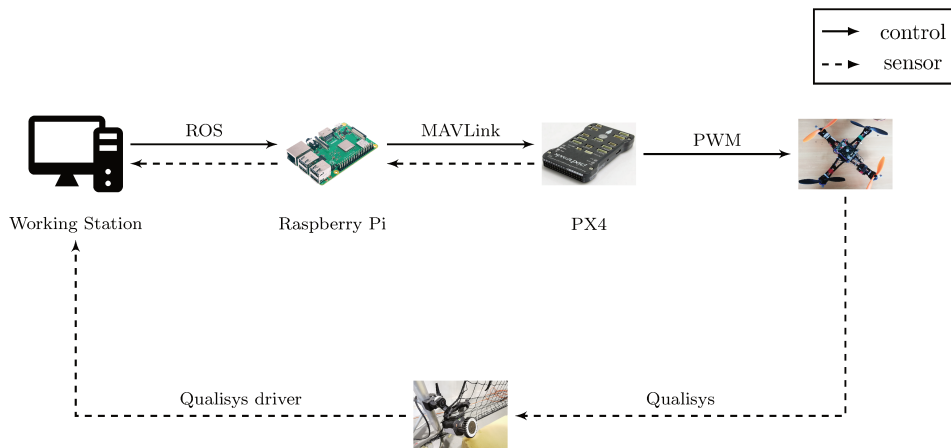


Figure 5.14 – Information flow diagram of each RP-MAQ quadrotor in experiment

Communications and control via ROS

Robot Operating System (ROS) is an open-source, meta-operating system for robots. It provides the services as hardware abstraction, low-level device control message-passing between processes, and communication among devices. Also, it offers tools and libraries for building, writing, and running codes for robot real-time experiments.

We utilize ROS in this experiment for the following two objectives:

1. Communication among the working station, the RPi, and the Qualisys is developed in the framework of ROS;
2. Controller is programmed in C++ ROS libraries and nodes.

Communication among our working station, the RPi, and the Qualisys is built using ROS and the information flow diagram is shown in Fig. 5.14. With regard to the information between the Qualisys and our working station through WIFI, the qualisys ROS package interprets and publishes the robot pose information as ROS topics in the working station. In the working station, a ROS node computes the control signal for the 4 quadrotors and sends that to each quadrotor's RPi. For each quadrotor, a ROS node in RPi builds the communication between each Pixhawk and our working station. The communication between the RPi and our working station is based on ROS messages, while that between the Pixhawk and the RPi is through MAVLINK protocol (the ROS package MAVROS is used as the bridge between MAVLINK and ROS). Thus, it transfers the control input from our working station to the Pixhawk. The flight firmware PX4 on the Pixhawk, realizes the control signal and generates the PWM signals to control the motors' speed. Also, the flight firmware PX4 sends the sensor information measured by FCU to the RPi through MAVLink.

As indicated previously, the working station ROS node runs the designed controller programs. The designed controller for the RP-MAQ robot, shown in Fig. 5.1, includes three main modules: the high motion controller, the control allocation, and the low-level quadrotor controller. As explained before, the Pixhawk on each quadrotor works as the low-level quadrotor controller. With regard to the high motion controller and the control allocation, they are both programmed in C++ and run in the working station ROS node, where DCA is solved using ViSP [Marchand et al., 2005] libraries.

5.4.3 Discussion on experimental results of RP-MAQ robot

We design a reference trajectory for the RP-MAQ robot to test the controller

1. 0 sec – 3 sec: taking off,
2. 3 sec – 35 sec: following a square trajectory in horizontal plane while keeping the body structure flat.

The tracking of the body structure pose \mathbf{p}_b is shown in Fig. 5.15 and Fig. 5.16. As we can see, the controller enables the robot to follow the square reference trajectory approximately, even there exists significant static error in the tracking of \mathbf{z}_b coordinate and attitude coordinates. It offers a preliminary attempt to validate the designed controller, even though it shows that the controller should be tuned with more tests. The experiment

is recorded in a video that can be found with link³. After that, we get a better performance after tuning the controller gains, which can be seen in the video with link⁴.

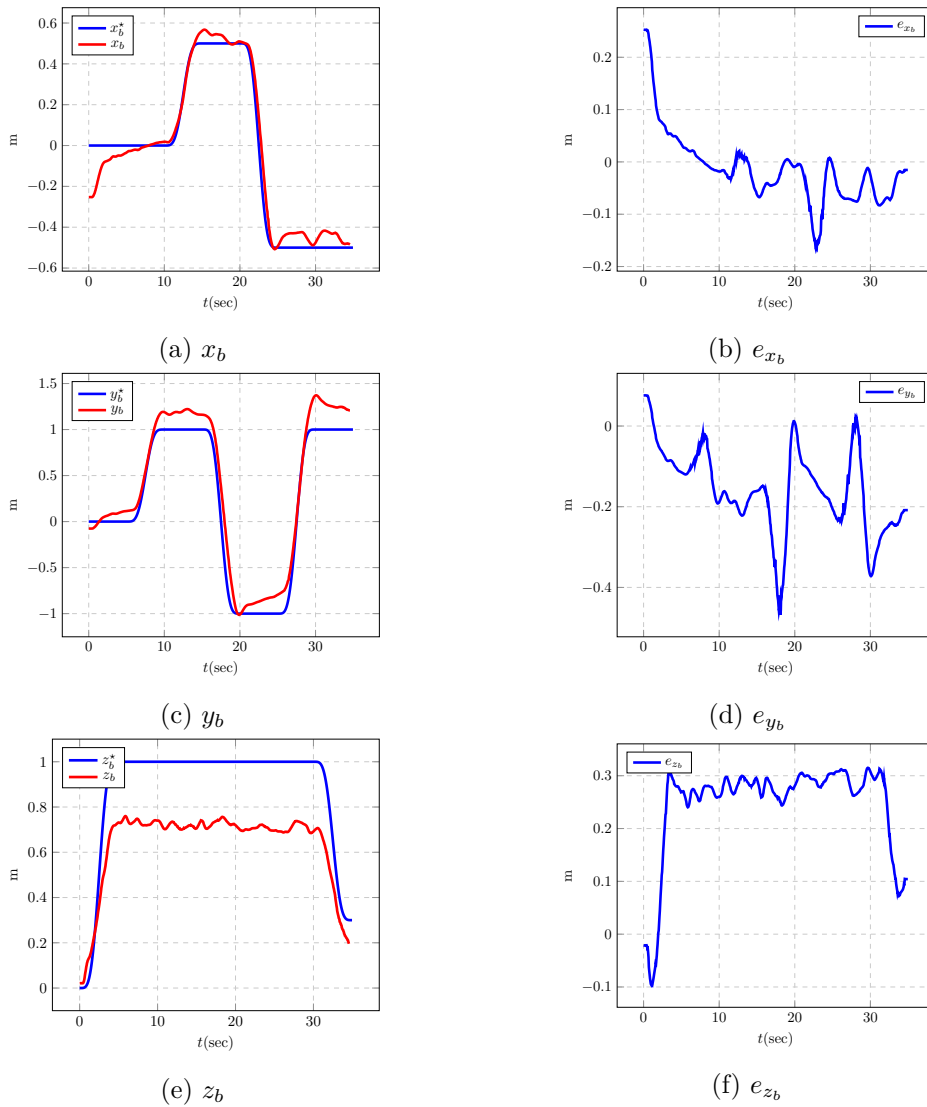


Figure 5.15 – Experimentation of Rigid Platform with Mobile-Attitude Quadrotors: reference trajectory and tracking errors of translation coordinates of vector \mathbf{p}_b .

3. <https://youtu.be/Cec6t1WNw-Y>

4. <https://youtu.be/JiJNpb-qq-k>

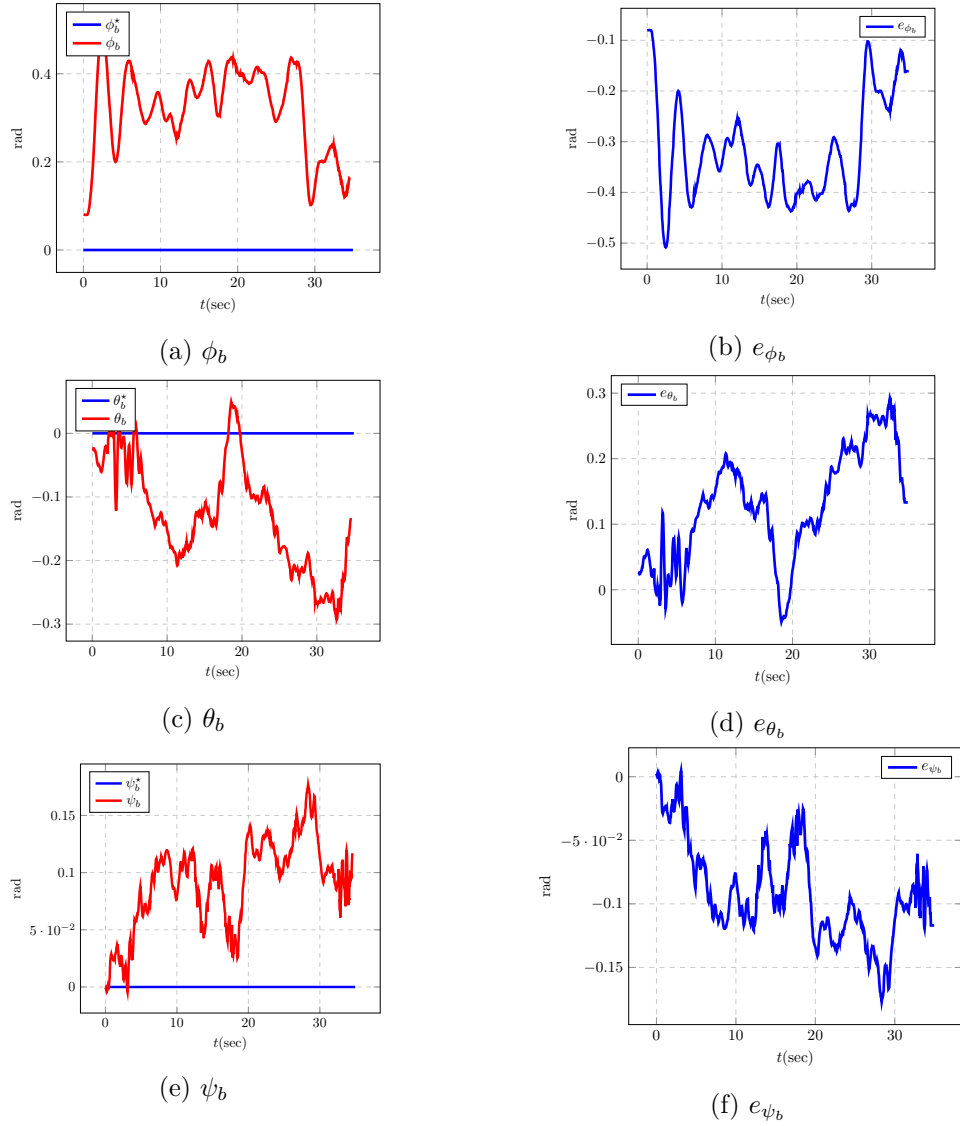


Figure 5.16 – Experimentation of Rigid Platform with Mobile-Attitude Quadrotors: reference trajectory and tracking errors of attitude coordinates of vector \mathbf{p}_b .

5.5 Experimentations with FG-MAQ robot

We develop the RP-MAQ robot, as a simplified version of the FG-MAQ robot, and the experiment set-up in the previous section. It offers an intermediate step to test and tune our designed controller with a simple object. Based on such foundation, we present the process of building a prototype of the FG-MAQ robot and testing the designed controller on this prototype in experiments.

5.5.1 Prototype of FG-MAQ

CAD modeling of robot

First, the design process and CAD models of the full FG-MAQ robot is presented.

According to the CAD model for prototyping the FG-MAQ robot in Fig. 5.20, the robot is thus composed as follows:

1. one body structure of dimension equal to 0.8 m;
2. four gear boxes containing a worm-gear and the worm is linked to the U-joint, and the gear is attached to the actuation bar;
3. four self-adaptive fingers;
4. four quadrotors' whose bases are linked to the worm-screws through the U-joints.

We design a new body structure as a truss (see Fig. 5.17). The previous design in chapter 2, the connections between quadrotors and the body structure are proved to be fragile during experiment and they are easily broken when the robot falls from the air to the ground. Therefore, we propose this truss body structure uses multiple bars to enhance the structure's rigidity and reduce the weight.

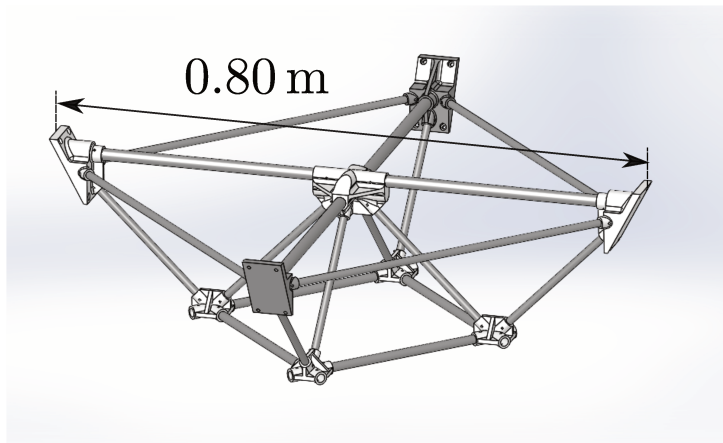


Figure 5.17 – CAD view of new body structure of FG-MAQ robot: a symmetric truss.

The gear box including a worm screw and a gear is presented in Fig. 5.18. As we can see from Fig. 5.18, two bearings are introduced between the worm screw and the gear box which permit the relative rotation between the worm screw and the gear box. Thanks to the worm-gear mechanism, the rotation is transformed from the worm screw to the gear and its direction is rotated by 90° through transmission between worms of

the screw and teeth of the gear. The screw is linked to one quadrotor through a U-joint, while the gear is linked to an actuation bar of finger: the worm-gear mechanism is the transmission unit between the quadrotor and the actuation bar. Thus, we design the worm-gear mechanism to be non-backdrivable such that it only permits the worms motion driven by the quadrotors to be transmitted to the gears motion for actuating the fingers, but not the other way back. It means that once phalanxes are in contact with the object, the actuation cannot move backwards anymore.

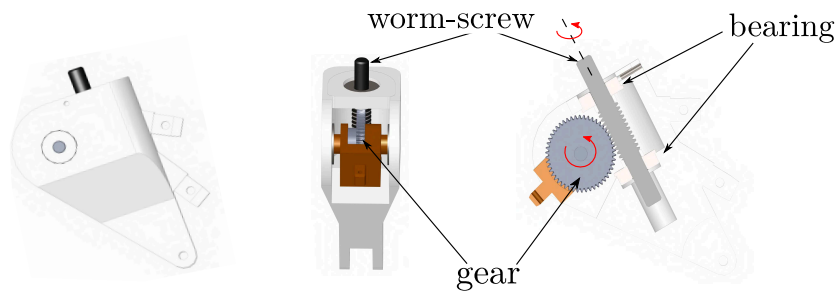


Figure 5.18 – CAD view of gear box of FG-MAQ robot

The self-adaptive fingers of the FG-MAQ robot are shown in Fig. 5.19. Here, we recall the introduction of self-adaptive finger in chapter 2 (see page 49). Bar (1) is the actuation bar of a four-bar mechanism that is used to introduce self-adaptation between both phalanxes of each finger. This actuation bar is driven by the yaw torque of each quadrotor through a worm-gear mechanism.

Finally, the CAD model of the FG-MAQ robot is shown in Fig. 5.20. We can obtain dynamic parameters of the robot, such as the CoM, the inertia matrix. It gives a guideline to assembly the fingers, the gear boxes and the body structure to build the prototype of the FG-MAQ robot.

Prototyping of robot

We manufacture components of FG-MAQ robot based on their CAD models presented in the previous section. Most of these components are manufactured by 3D printing in developing the FG-MAQ robot.

In the first step, we manufacture the body structure and the gear boxes with 3D printers, which are assembled according the designed in Fig. 5.20. Four quadrotors are linked to the worm-screws through U-joints⁵ (see Fig. 5.21).

5. <https://fr.rs-online.com/web/p/cardans-universels/0689035>

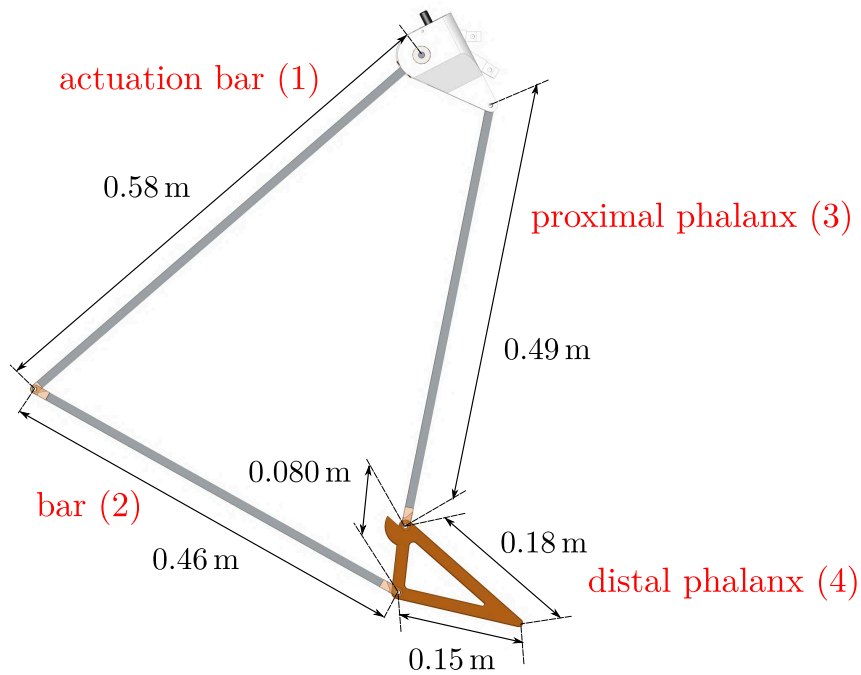


Figure 5.19 – CAD view of self-adaptive finger of FG-MAQ robot



Figure 5.20 – CAD view of FG-MAQ with new structure

In the second step, we 3D print all distal phalanges of fingers, and we construct all bars and proximal phalanges from aluminum tubes. Then we assemble these components to build the fingers. Based on the design in Fig. 5.19, we link the finger to the gear box: the actuation bar is linked to the gear, while the proximal phalanx is linked to the gear box with a bearing (see Fig. 5.22).

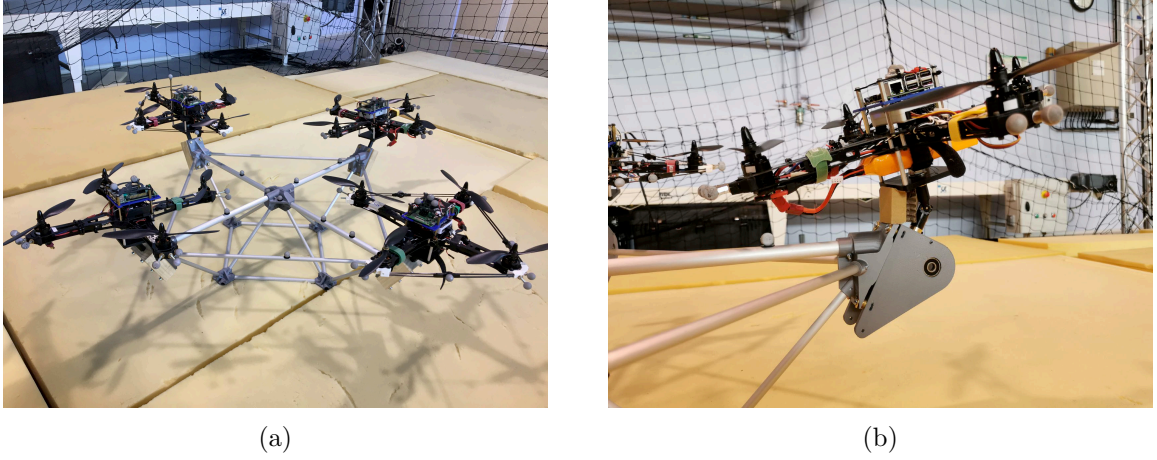


Figure 5.21 – Body structure (with gear boxes) and quadrotors that are linked through U-joints of FG-MAQ robot. The body structure and the gear boxes are 3D printed, then they are assembled together. The quadrotors are linked to the gear boxes of the body structure through the U-joints whose maximal shaft alignment angle $\varphi_{\text{mas}} = 45^\circ$.

Finally, we assemble four fingers to the gear boxes of the robot's body structure: we obtain the prototype of the FG-MAQ robot (see Fig. 5.23).

5.5.2 Case study: FG-MAQ robot hovering under disturbances

For the first test of our controller, we design a taking off and hovering reference trajectory for its robustness under disturbances. Based on the control strategy in section 5.1, the reference trajectory is represented by $\mathbf{p}_b^* \in \mathbb{R}^{6 \times 1}$ that specifies the motion of the robot in $\text{SO}(3)$, and $\boldsymbol{\psi}^* \in \mathbb{R}^{4 \times 1}$ that controls the closing fingers to grasp an object. The reference trajectory is defined as as

1. 0 sec – 5 sec: taking off from the ground,
2. 5 sec – 20 sec: hovering in the air.

Since this task does not involve grasping, so we keep the yaw angles of quadrotors fixed to be zeros $\boldsymbol{\psi}^* = [\psi_1^* \ \psi_2^* \ \psi_3^* \ \psi_4^*]^T = [0 \ 0 \ 0 \ 0]^T$.

In this experiment, disturbances are applied to the robot by using a wooden bar manually. We use a wooden bar to push the robot at its body structure horizontally at $t = 8 \text{ sec}$, $t = 13 \text{ sec}$, while we push the robot downwards $t = 18 \text{ sec}$ (see Fig. 5.24).

The main results are visualized in Fig. 5.25 and Fig. 5.26. As we can see from the results, the robot takes off vertically during 0 sec – 5 sec and hovers during 5 sec – 20 sec in the air. The controller enables the robot to take off and hover under disturbances,

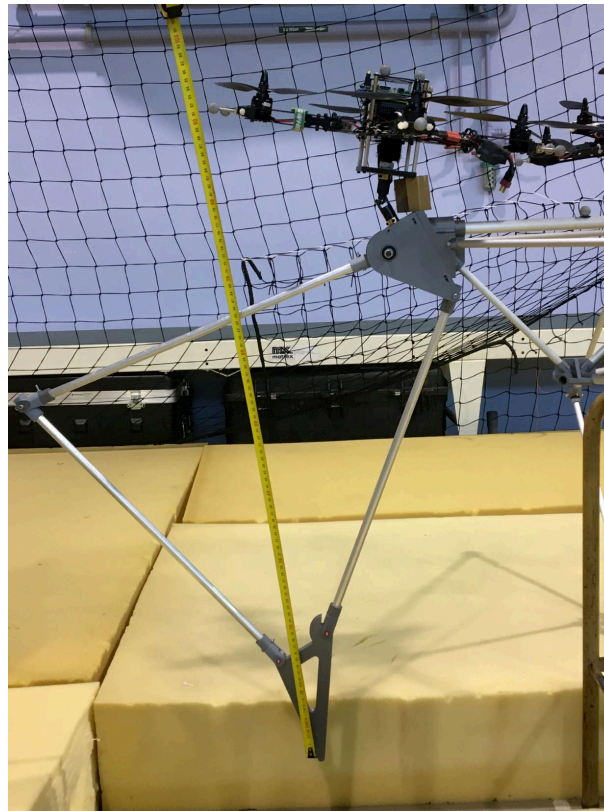


Figure 5.22 – Self-adaptive finger linked to gear box of FG-MAQ robot

stabilizing the robot's attitude. Two videos recording this experimentation can be found with link ⁶ (a up view) and with link ⁷ (a side view).

It is interesting to note the robot's performance under applied disturbances at $t = 8$ sec, $t = 14$ sec, $t = 18$ sec. After that we apply disturbances whose projections are in \mathbf{x}_0 and $-\mathbf{y}_0$ directions at $t = 8$ sec, $t = 14$ sec, the robot is pushed away from the hovering position. Even there are negligible static errors in translation tracking, the controller still enables the robot to be back to the desired position in 2 sec-3 sec. We pushed the robot downwards at $t = 18$ sec, as we can see from Fig. 5.25, and the robot spends less time to recover from disturbances. This is because at hovering, the robot's quadrotors are in horizontal plane and their thrust forces are in the vertical direction. Facing the downward disturbances, the quadrotors are able to increase their thrust forces without changing their attitudes to deal with the disturbances. However, when there are the horizontal disturbances, the quadrotors must generate torques to change their attitudes in order to

6. <https://youtu.be/F1A8A2USego>

7. <https://youtu.be/BeMqwYIcTPw>

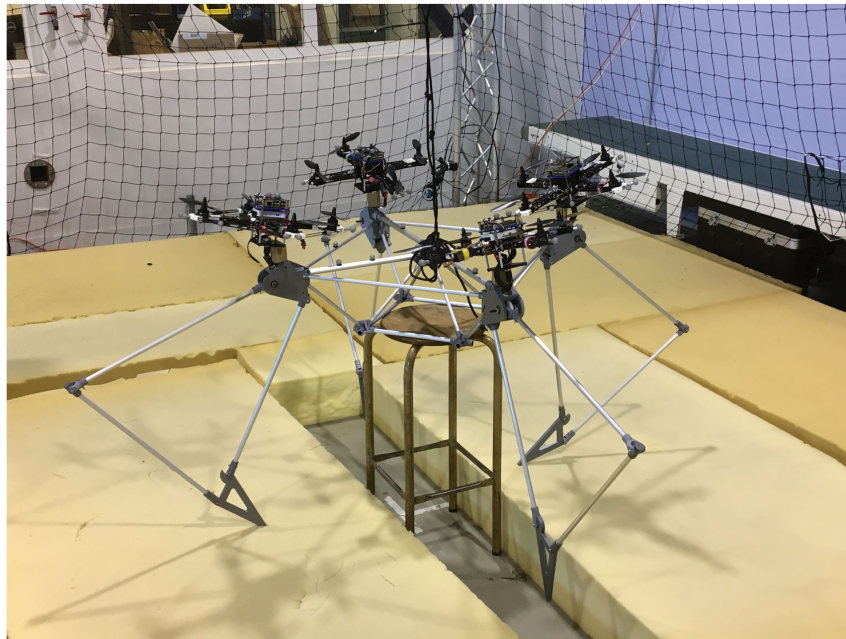


Figure 5.23 – Prototype of FG-MAQ robot

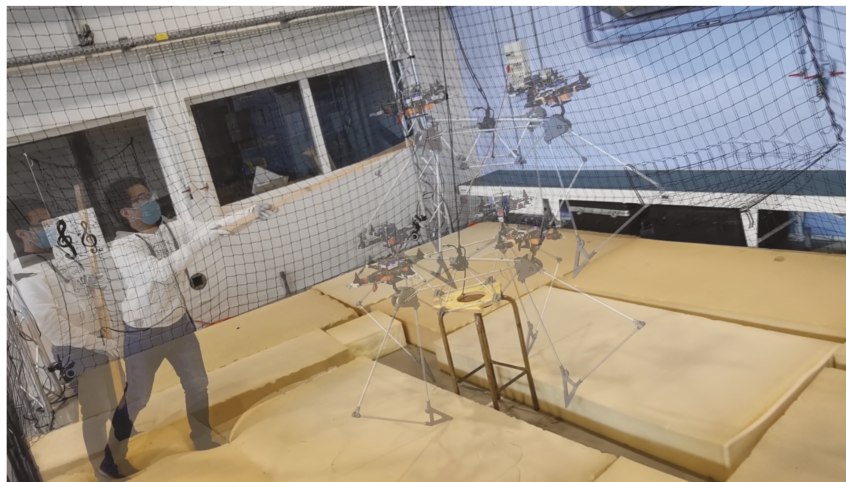


Figure 5.24 – Experiment of FG-MAQ robot under disturbances

produce the thrust forces in the horizontal plane to compensate the disturbances.

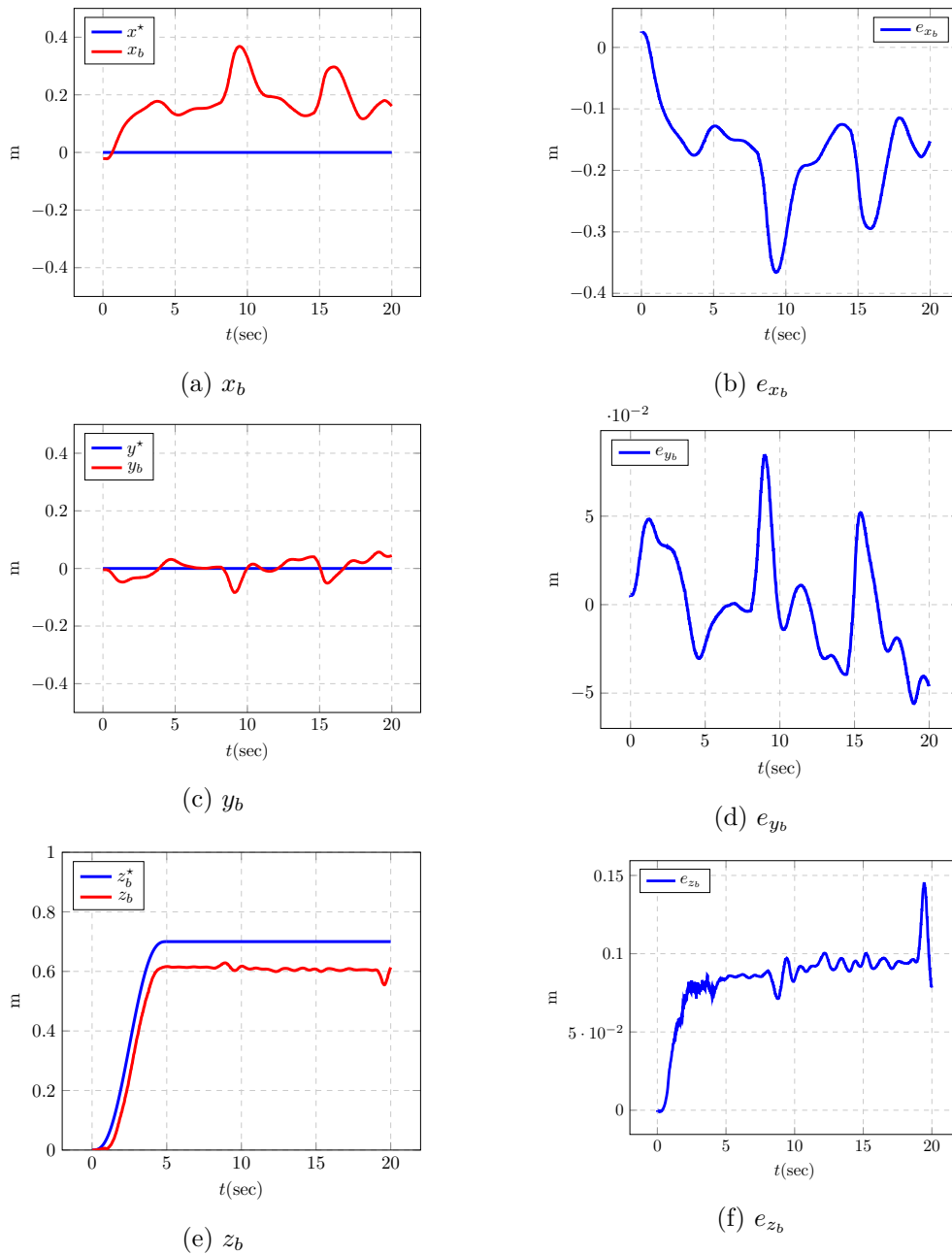


Figure 5.25 – Experiment of FG-MAQ robot hovering under disturbances: reference trajectory and tracking errors of translation coordinates of vector \mathbf{p}_b

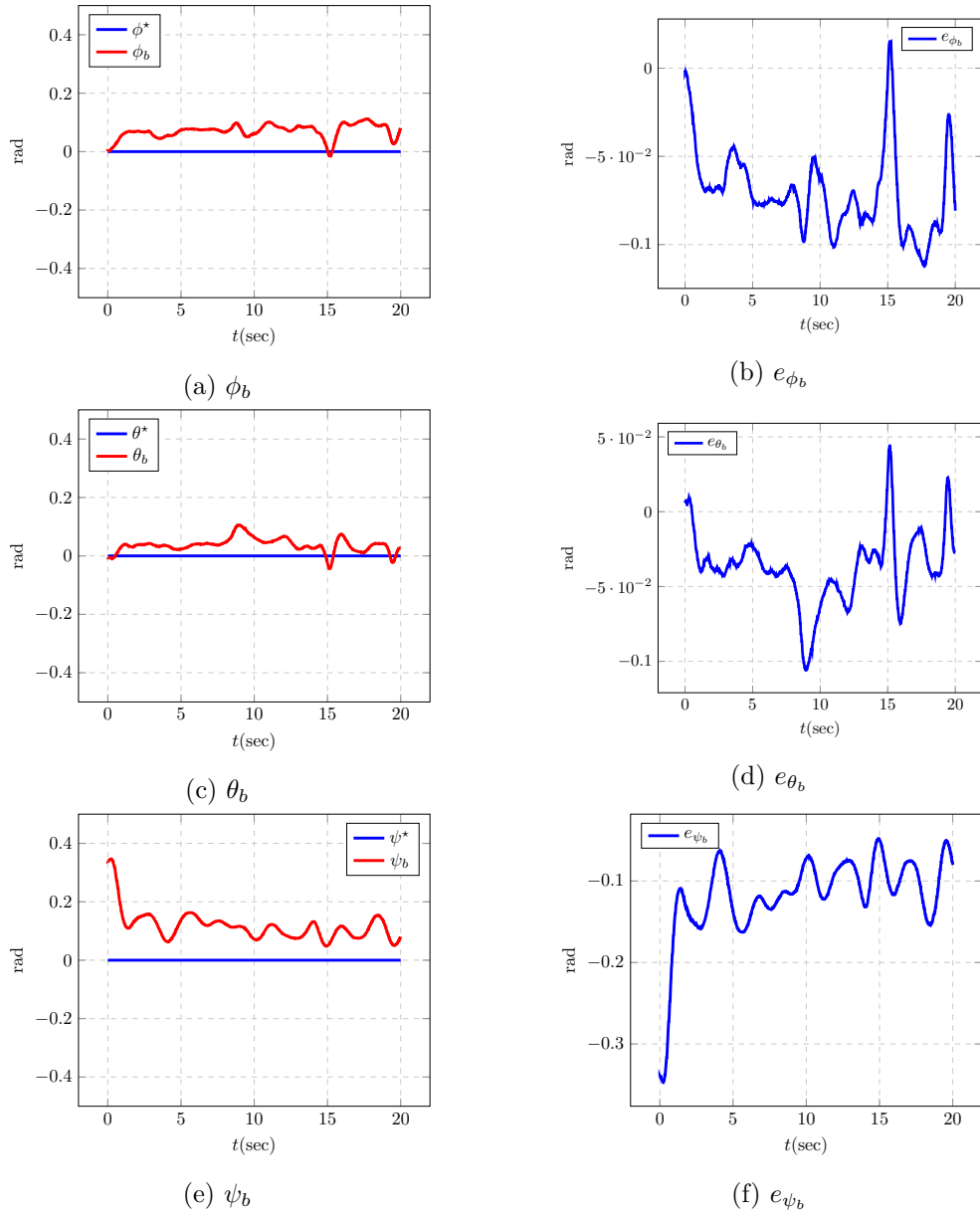


Figure 5.26 – Experiment of FG-MAQ robot hovering under disturbances: reference trajectory and tracking errors of attitude coordinates of vector \mathbf{p}_b

5.5.3 Case study: FG-MAQ robot approaching and grasping a large size object

For the second test, we assume that the robot is located differently from an object (see Fig. 5.27). In order to perform grasping, the robot needs to take off and moves to the above of the object in the first step. Then, the robot stabilizes its position and attitude,

while closing fingers to grasp the object in the air. In this context, we design a reference trajectory for the robot as follows

1. 0 sec – 5 sec: it takes off from the ground,
2. 5 sec – 20 sec: it moves to the above of the object to grasp,
3. 20 sec – 27 sec: it grasps the object,
4. 27 sec – 30 sec: it stabilizes the robot's pose above the object.

Note that the reference yaw angles of quadrotors are set as $\psi^* = [0 \ 0 \ 0 \ 0]^T$ during 0 sec – 20 sec and 27 sec – 30 sec.

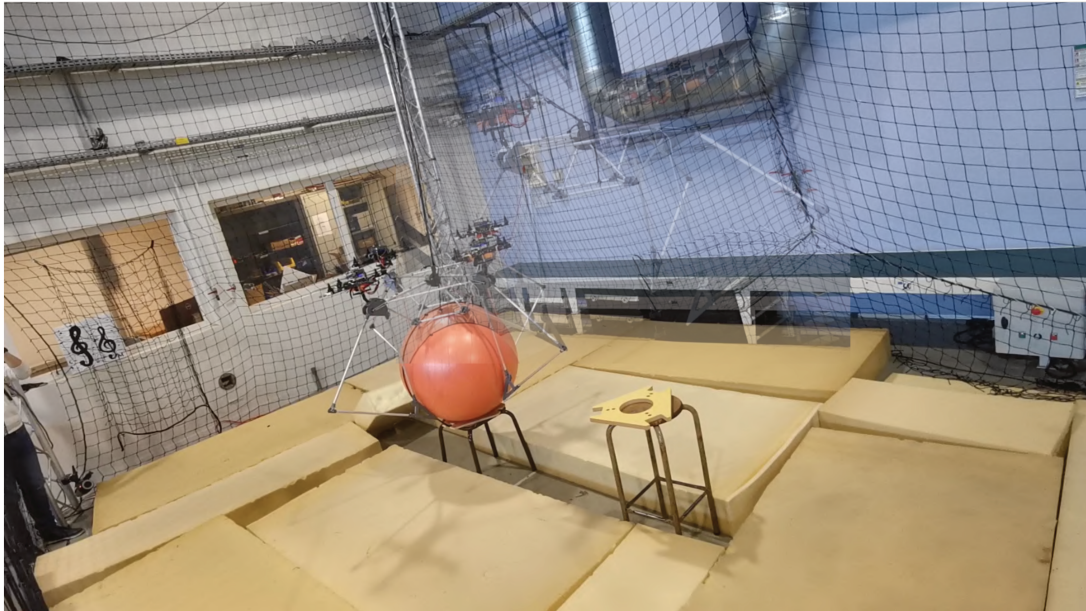


Figure 5.27 – Experiment of FG-MAQ robot grasping a large size object

The tracking results of coordinates of \mathbf{p}_b are shown in Fig. 5.28 and Fig. 5.29, while those of ψ are illustrated in Fig. 5.30. The mean and maximal values of the absolute errors of \mathbf{p}_b are given in Table 5.4. We can conclude based on these results that the controller enables the robot to track a reference trajectory and the tracking precision is enough for the robot before conduct grasping. The experiment is recorded in two videos: one from a up view (link⁸), and the other with a side view (link⁹).

It is of great significance of this test to study the controller's performance when the robot conducts grasping during 20 sec – 27 sec. It can be seen from Fig. 5.30 that the

8. <https://youtu.be/nvdsKQ-XwJw>

9. <https://youtu.be/pQhE0mZLnMA>

quadrotors' yaw angles are kept around zeros before 20 sec, then the quadrotors begin to generate yaw rotations following the reference ψ^* during 20 sec-27 sec. As the consequence, the attitude tracking error increases during this period of time (see Fig. 5.29).

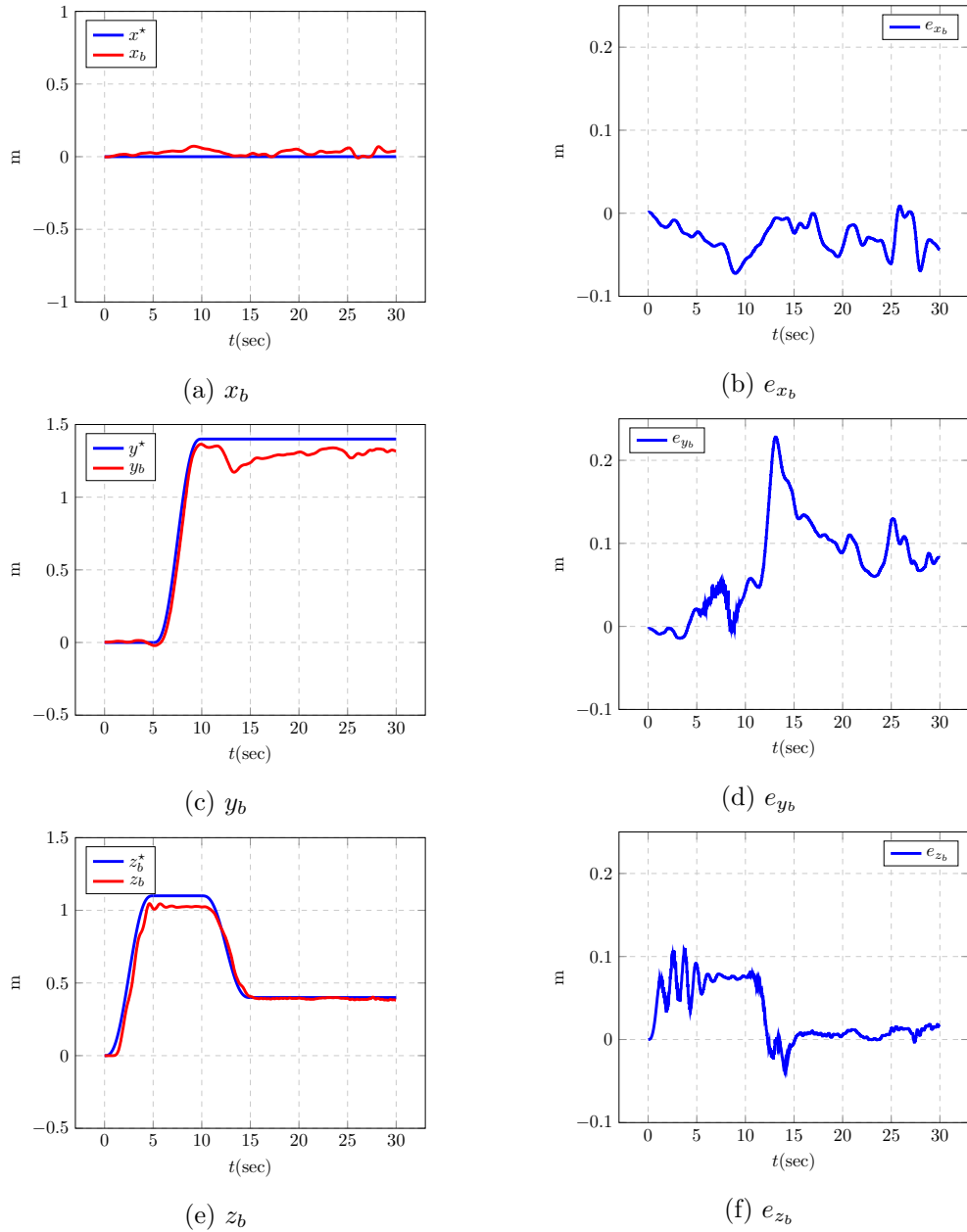


Figure 5.28 – Experiment of FG-MAQ robot grasping: reference trajectory and tracking errors of translation coordinates of vector \mathbf{p}_b

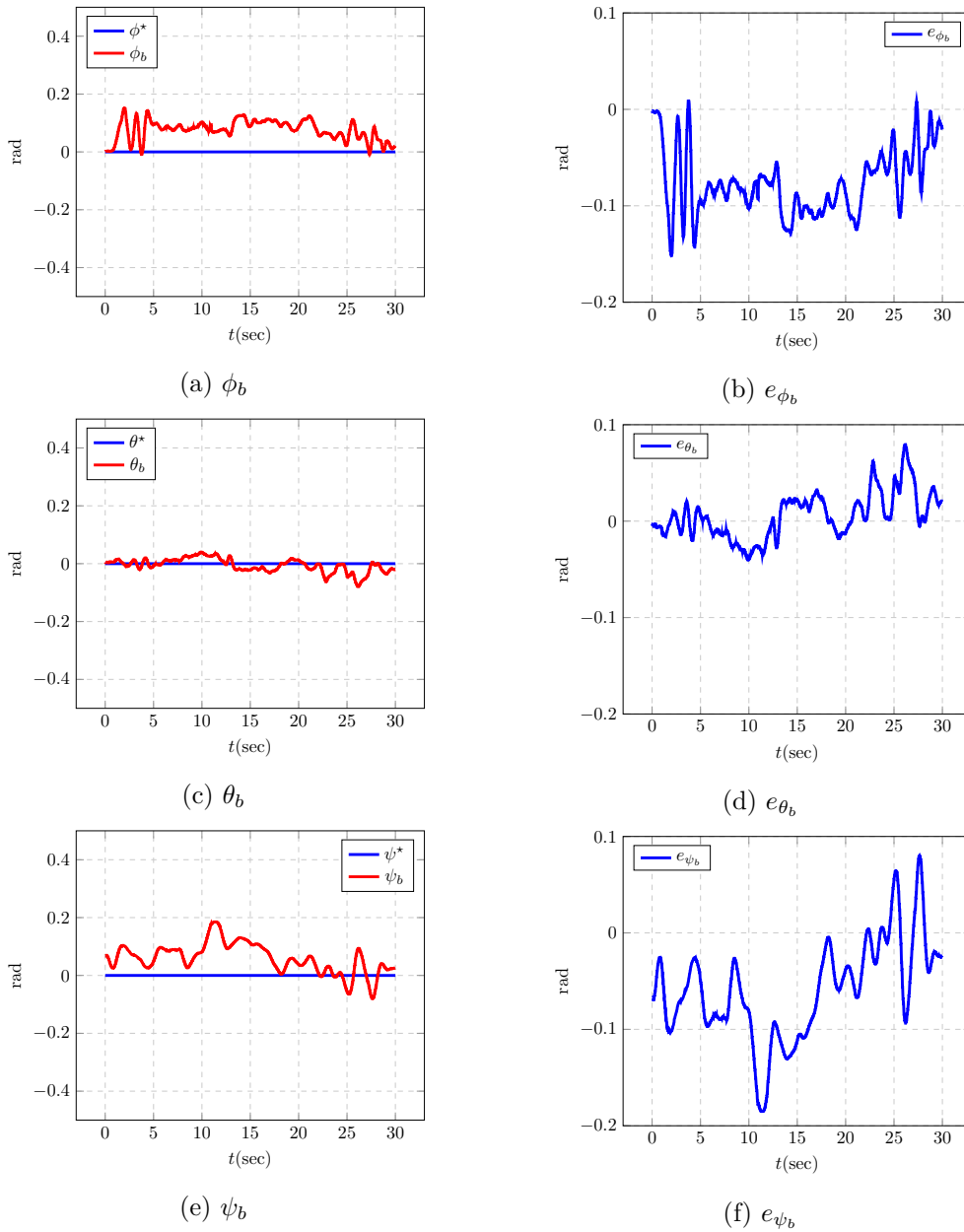


Figure 5.29 – Experiment of FG-MAQ robot grasping: reference trajectory and tracking errors of attitude coordinates of vector \mathbf{p}_b

5.5.4 Discussion on experimental results of FG-MAQ robot

We conducted two experiments to test the designed controller for the FG-MAQ robot: the first test is to test the controller’s robustness under external disturbances, and the second test is to test the controller’s capacity of closing fingers in grasping.

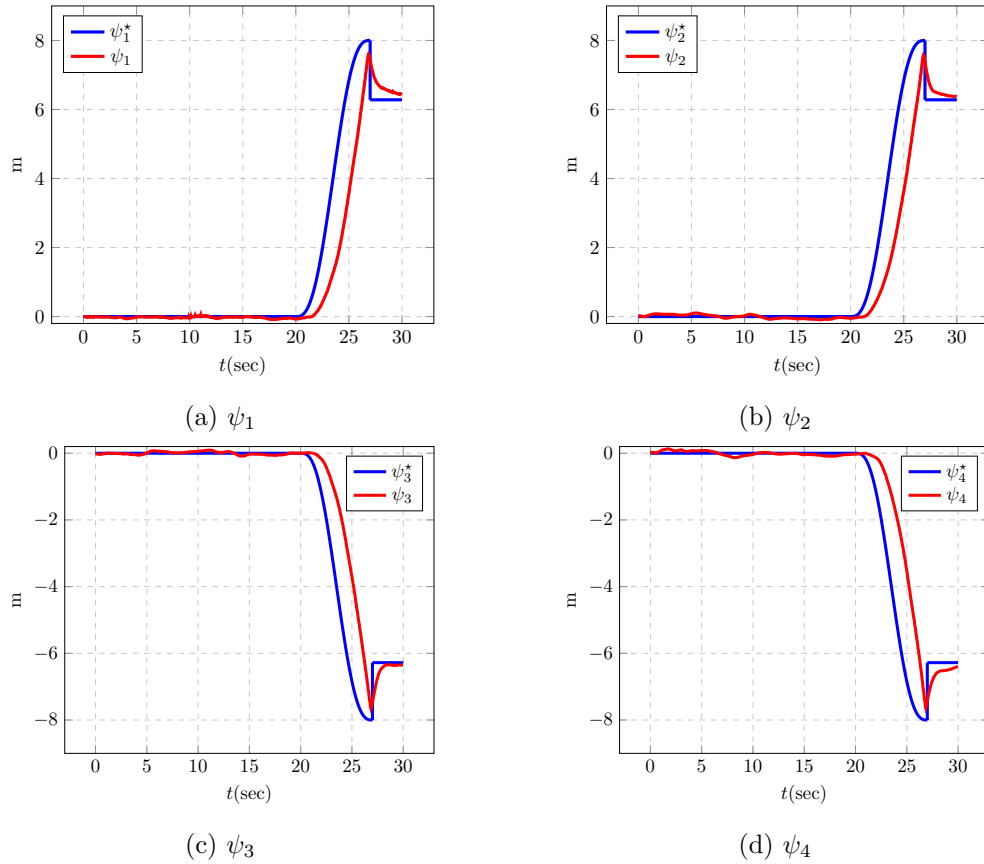


Figure 5.30 – Experiment of FG-MAQ robot grasping: reference trajectory and tracking errors of yaw angle of all quadrotors ψ

In the first test, the robot controlled by the designed controller takes off and hovers in the air under the external disturbances exerted on the robot body. After being applied the external disturbances, the robot moves away from the desired pose, while the controller enables the robot recover its desired pose. It is worthy to mention that, if the robot is forced to move horizontally, the quadrotors will need to change their attitudes to compensate influences caused by such disturbances. Compared the disturbances vertically that does not need to change the quadrotors' attitudes, the recovering from the horizontal disturbances is more time consuming. It is also necessary to note that static error exists in translation tracking, which requires tuning the controller in the future work.

In the second test, the robot is controlled to perform a more complex task that involves taking off, approaching the object and grasping the object. The robot takes off from its initial position that is assumed to be different from the object. Following the defined trajectory, the robot approaches the object from the air, and stabilizes its position and

Table 5.4 – Mean and maximal values of absolute value of tracking error of each coordinate of FG-MAQ robot pose in grasping experiment

	Translation			Attitude		
	x_b	y_b	z_b	ϕ_b	θ_b	ψ_b
Mean error (m/rad)	2.9e-02	7.6e-02	3.2e-02	7.6e-02	1.9e-02	6.6e-02
Maximal error (m/rad)	7.2e-02	2.3e-01	1.1e-01	1.5e-01	7.9e-02	1.9e-01

attitude above the object while producing the quadrotor’s yaw rotations to close the fingers.

However, two things in the second test should be noticed with great attention. First, we recall that we set the elements of ψ^* to be zeros¹⁰ except in grasping (see Fig. 5.30). Thus, once after grasping, the quadrotors’ yaw angles are forced to become zeros from their current values, which cannot be predicted. Thus, if the quadrotors’ yaw angles are far away from zeros, This may lead to discontinuity in the ψ tracking. Second, as we analyzed in the previous chapter for the FG-FAQ robot with tilted quadrotors in grasping, the yaw rotations of the quadrotors 1 and 3 should have the same rotational direction, which is the opposite to the quadrotors 2 and 4, in order to cancel the resultant yaw torques applied to the robot. Even ψ^* defined in this section does not follow this rule, it stills performs grasping successfully as the quadrotors are all in the same horizontal plane-the resultant yaw torques can be canceled as well.

5.6 Conclusions

A controller was designed and tested for the FG-MAQ robot in both co-simulations and experiments. This controller includes three modules: a high motion controller, a control allocation and a quadrotor controller. The high motion controller module considers the robot to be fully controllable and computes the wrench that must be applied on the robot’s body to track a trajectory, the control allocation module distributes this wrench to the quadrotor controllers that are embedded in the robot to fulfill the wrench and to track a reference yaw angle trajectory to close/open the corresponding finger.

One main contribution of this chapter is applying Dynamic Control Allocation in the control allocation module for control effort distribution, while reducing energy consumption and managing the control input continuity, considering the constraints imposed by

10. In representing angles, 0 and 2π correspond to the same configuration

mechanical limits and actuators' capabilities. This controller was tested on a simplified prototype of the FG-MAQ robot called RP-MAQ in both co-simulations and experiments.

Another main contribution of this chapter is that a prototype of the FG-MAQ robot is built based on the design presented in chapter 2. We tested the controller's robustness under disturbances and while conducting a grasping task on the prototype experimentally. A second experiment showed that the controller enables the robot to begin from a different position from that of the object, approaches the object from the air and performs grasping while stabilizing the robot's pose.

The experimental results validated the original motivation of the robot to conduct grasping, manipulation and transportation of a large size object.

CONCLUSIONS

Contributions of the Thesis

Aerial manipulation has experienced increasingly rapid advances in recent years. However, aerial manipulation of a large size object is still an open problem: how to perform all of the following phases: grasping, manipulating, and transporting a large size object autonomously?

This thesis has proposed and demonstrated a novel concept of aerial manipulator called Flying Gripper as an effective approach to this open problem. In this thesis, two robot designs based on the concept of Flying Gripper were introduced: one with Fixed-Attitude Quadrotors (FG-FAQ), and one with Mobile-Attitude Quadrotors (FG-MAQ). We have proposed a systematic method for this new concept: introduce the mechanical design, develop the static and dynamic models, analyze manipulability, design and test a controller in co-simulations, build a prototype and test the designed controller in experiments for FG-MAQ. Therefore, this Flying Gripper concept has been realized from a sketch design to a validated prototype.

Chapter 1 was devoted to a review of aerial manipulation and an introduction of self-adaptive fingers. It collected aerial manipulation robots that were developed in recent years. Analysis of these current robots showed that they cannot grasp, manipulate, and transport a large size object autonomously, neither produce a secured grasp. It led to the motivation of this thesis that is to propose a novel robot to address this problem. For this novel robot, we decided to use multiple quadrotors to increase the payload and achieve full manipulability, use yaw rotations of quadrotors to actuate fingers, use self-adaptive fingers to produce an enveloping grasp, use non-backdrivable mechanisms in the transmission of closing motion between quadrotors and fingers to obtain a secured grasp.

Chapter 2 detailed the concept of Flying Gripper (FG-FAQ and FG-MAQ) that is intended to perform grasping, manipulating and transporting large objects autonomously. It is composed of four quadrotors, four self-adaptive fingers and a body structure. Quadrotors are arranged so as to achieve full manipulability in $SE(3)$ and the robot can produce secured grasps using self-adaptive fingers and non-backdrivable worm-gear mechanisms.

For the FG-FAQ robot, each quadrotor’s yaw rotation is transmitted by one worm-gear mechanism to actuate the corresponding finger. By contrast, for the FG-MAQ robot, we introduced universal joints to link the quadrotors to the worm screws so that each quadrotor gains two additional DOF (roll and pitch rotations). Therefore, each quadrotor can modify its attitude w.r.t the body structure while transmitting its yaw rotation to the worm screw to open/close the finger. In this chapter, we built a general formulation for the static models for FG-FAQ and FG-MAQ, which lays a foundation for analyzing manipulability in chapter 3. The FG-FAQ robot is a complex system with several different mechanisms. In order to simplify the dynamic model, we neglected dynamics of the fingers, yaw velocities of the quadrotors. We just considered each finger as one single rigid body and the robot was thus simplified to a body structure linked with four quadrotors through resolute joints. By modeling universal joints as spherical joints, the dynamic model of FG-MAQ was simplified to be a body structure linked with four quadrotors by spherical joints. In such a way, we decoupled the rotational dynamics of quadrotors from the rotational dynamics of the robot body for FG-MAQ. It is worthy to note that such modeling errors were treated as disturbances and uncertainties in the controller design in chapter 4 and 5. Analysis of the dynamic models showed that FG-FAQ is overactuated since it has 16 actuation motors and 10 DOF, while FG-MAQ is underactuated with 16 actuation motors and 18 DOF as each quadrotor gains 2 more DOF in pitch and roll rotation. These properties were also taken into account in chapter 4 and 5.

Chapter 3 presented a wrench capability analysis method to analyze the manipulability of FG-FAQ and FG-MAQ considering the actuators’ capabilities and the system mechanical limits. Considering difficulties caused by a large number of actuators 16, we used polytopes to model the actuators’ capabilities for each quadrotor that has 4 actuators. For each quadrotor, we used hyperplanes to model the yaw torque for closing/opening the fingers and the static equilibrium constraint imposed by the introduction of the passive joint respectively. Thanks to the Minkowski Sum, we computed the available body wrench set that is the set of wrenches that can be applied on the robot body by quadrotors. This method is computationally effective and provides visualizable results at each step. In order to facilitate the reader’s comprehension, we introduced a planar aerial manipulator with two birotors which can be viewed as a simplified version of Flying Gripper, then we applied the method and visualized the results in the 3D space at each step. After that, we analyzed and compared the manipulability of the FG-FAQ and FG-MAQ robots by looking at the degree of the available body wrench set and the inclusion of the gravity com-

pensation wrench. The results showed that FG-MAQ with Mobile-Attitude Quadrotors has a better manipulability than FG-FAQ with Fixed-Attitude Quadrotors.

In chapter 4, we developed a controller design method for the FG-FAQ robot and tested this controller in co-simulations. The designed controller scheme consists of two modules: *i*) a high motion controller to enable the robot to move from an initial pose to a final pose following a reference trajectory; *ii*) a control allocation using overactuation of FG-FAQ to distribute the actuators' commands while ensuring closing/opening fingers during trajectory tracking. This controller scheme is a systematic and flexible framework and diverse control methods can be implemented in these two modules. We applied a model predictive controller in the high motion controller module to deal with the variation of dynamics caused by the grasped object, which is the main contribution of this chapter. An allocation algorithm was applied in the control allocation module that is computationally efficient and is a closed-form algorithm. The controller's effectiveness and robustness against noise and disturbances were demonstrated in ADAMS-SIMULINK co-simulations. When building a prototype of FG-FAQ, failure in controlling motor speed of quadrotors prevented us from implementing the controller experimentally.

Chapter 5 proposed a controller design method for the FG-MAQ robot and a prototype of FG-MAQ was built to test the designed controller in both co-simulations and experiments. In chapter 2, the dynamic model of FG-MAQ was simplified to be represented by the body structure linked with four quadrotors through universal joints. The rotational dynamics of quadrotors are decoupled from the rotational dynamics of the robot body. Since the attitude dynamics of quadrotors can be typically controlled much faster than the dynamics of the body structure, we considered that each quadrotor can change its attitude instantly, then the robot body structure is fully controllable and there exists a redundancy of actuation. Therefore, this chapter presented a control strategy for the FG-MAQ robot. The developed control scheme includes three modules: a high motion controller, a control allocation and a quadrotor controller. The high motion controller computes the control efforts in order to track a reference trajectory, which are distributed by the control allocation to the quadrotor controllers. Then, the quadrotor controller embedded in each quadrotor computes the control input based on two signals: *i*) the output of the control allocation module for tracking the reference trajectory; *ii*) the reference yaw angle for closing/opening the finger. In this chapter, Dynamic Control Allocation was utilized in the control allocation module for control effort distribution, energy efficiency and continuity of control, considering the constraints of the robot's mechanical limits and the motor

speed limits of quadrotors. This controller was first tested on a simplified prototype of the FG-MAQ robot in both co-simulations and experiments, whose results demonstrated the designed controller’s effectiveness. Then, another key contribution is that we built a prototype of FG-MAQ. The designed controller was then tested on the prototype of FG-MAQ in experiments. The experiment results demonstrated the robot’s ability to track a trajectory and then keep a fixed position and attitude while keeping rotating quadrotors around their yaw axis in order to close fingers and grasp a large object, which validated the motivation of this thesis.

Perspectives for Future Works

This thesis offered a novel solution to aerial grasping and manipulation of a large size object. Nonetheless, there are still residual works to complete in the experimental validation, theoretical developments, and practical application.

First of all, the most important perspective for future works concerns experiments on FG-MAQ. Due to the time limits as well as the world wide confinement in 2020, we only did two kinds of tests : *i*) we tested the controller’s performances under disturbances; *ii*) we tested the controller’s capability of approaching and grasping a large size object. Further tests are needed to be done, such as if the robot can transport and manipulate the object after grasping it, dealing with dynamic parameters variations. We did not continue experiments for FG-FAQ as we failed in controlling the motor speed of quadrotors. If this problem could be solved, then experiments for FG-FAQ would also be possible and we could compare these two robots’ performances.

Secondly, the dynamic models for FG-FAQ and FG-MAQ can be improved. It could be interesting to consider dynamics of the fingers during grasping as well as the quadrotors’ yaw rotation velocities for FG-FAQ. In addition, one could model universal joints in the dynamic modeling for FG-MAQ so that we can take into account the transmission of the quadrotors’ yaw torques to the worm screws by universal joints. Thus, it would be possible to study dynamics of the fingers driven by the quadrotors’ yaw torques and full dynamics of the robots.

Thirdly, the designed controller schemes presented in chapter 4 and 5 provide a systematical and flexible framework for both FG-FAQ (overactuated) and FG-MAQ (underactuated) robot. Instead of using a one-step approach, we controlled the robot body’s motion in two modules (three modules for FG-MAQ): *i*) the high motion controller mod-

ule considers the robot body as a fully controllable system and computes the wrench that must be applied on the robot’s body to track a trajectory; *ii*) the control allocation module distributes this wrench (together with the quadrotors yaw torques for FG-FAQ); *iii*) for each quadrotor, the quadrotor controller controls its thrust and attitude to fulfill the wrench distributed by control allocation module and track a reference yaw angle to close/open the corresponding finger for the FG-MAQ robot. In these general control schemes, different control methods for fully actuated systems can be applied in the high motion controller module and other allocation algorithms can be used in the control allocation module. On the one hand, it provides flexible schemes for different control methods, on the other hand, these control schemes could be extended to other aerial manipulators that are overactuated or underactuated. Furthermore, Model Predictive Control and Dynamic Control Allocation algorithms that have been used and tested in our work can be applied to other fully actuated or overactuated systems, such as robots in [Hamandi et al., 2020] and [Brescianini and D’Andrea, 2016], which are not necessarily limited to aerial robots.

Fourthly, there are several promising directions to optimize the design of Flying Gripper. Recently in the domain of robot optimal design, there has been increasing interest in taking manipulability into consideration, in objective functions [Brescianini and D’Andrea, 2016, Gouttefarde et al., 2015a], in constraints [Hussein et al., 2018]. The wrench analysis method presented in this thesis permits to analyze the manipulability of an aerial robot using qualitative and quantitative criteria. These criteria, a step further, could be used as performance criteria to optimize the design of Flying Gripper. Additionally, the payload and the flight time are limits for Flying Gripper. Thus, exploring the energy effectiveness of the robot is another research axis, such as in the mechanical design (see [Rajappa et al., 2015, Ryll et al., 2016]), and in motion planning (see [Nguyen et al., 2014]). Apart from adding an energy point of view to the design, it is furthermore significant to take into account the energy consumption in the trajectory generation, which has not been addressed in this thesis.

Finally, it should be noted that the self-adaptive fingers of Flying Gripper are detachable components and grasping performances of Flying Gripper depend on the used fingers. It is possible for Flying Gripper to choose different fingers that can be adapted to different objects and tasks. Thus, designing fingers for different tasks is another promising research area. Moreover, instead of using four-bar rigid mechanisms like this thesis, it could be interesting to use soft grippers, i.e. self-adaptive grippers composed of flexible

bodies that are able to sustain very large deformations. Apart from adaption to any kind of objects and shapes, soft grippers are very lightweight that allow to design grippers of bigger size, thus being able to grasp bigger size objects.

Appendices

OPERATIONS ON POLYTOPES

This Appendix details the main concepts about convex sets and polytopes that are used to model and evaluate the robot manipulability in chapter 3. In particular, we give a brief overview of the definitions of convex sets and polytopes. Then, we discuss two different representations of a polytope \mathcal{H} -representation and \mathcal{V} -representation. Finally, we introduce linear application of polytopes and the Minkowski sum of polytopes.

A.1 Convex set and polytope

A.1.1 Polytope

A set \mathcal{P} is defined as a convex set if the line segment between any two points in \mathcal{P} still lies in \mathcal{P} [Boyd and Vandenberghe, 2004]. For instance, if for any $\mathbf{x}_1, \mathbf{x}_2 \in \mathcal{P}$ and any α with $0 \leq \alpha \leq 1$, we have the following relation

$$\alpha \mathbf{x}_1 + (1 - \alpha) \mathbf{x}_2 \in \mathcal{P}. \quad (\text{A.1})$$

An example of a convex set in \mathbb{R}^2 is shown in Fig. A.1. A polyhedron is a convex set given as the intersection of a finite number of hyperplanes and halfspaces [Boyd and Vandenberghe, 2004] and a polytope is a bounded polyhedron.

A hyperplane in \mathbb{R}^n is defined using the following linear equality

$$\mathcal{HP} = \{ \mathbf{x} \mid \mathbf{c}^T \mathbf{x} = d \}, \quad (\text{A.2})$$

where \mathbf{c} is a $n \times 1$ normal vector to the hyperplane and d is a scalar value (see Fig. A.2). If \mathbf{c} is a unit vector, then d can be interpreted as the minimal signed distance from the origin to the hyperplane. In a general manner, d can be interpreted geometrically as the projection of \mathbf{x}_0 on \mathbf{c} , $d = \mathbf{c}^T \mathbf{x}_0$, where \mathbf{x}_0 is the coordinate of a point located on the hyperplane.

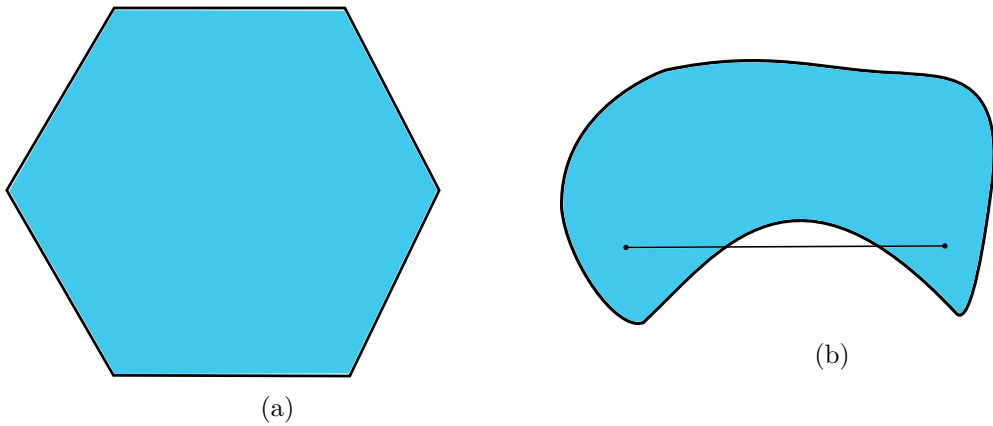


Figure A.1 – (a) Hexagon is a convex set, while (b) kidney shaped set is not a convex set as one line segment between the two points in the set is not contained in the set (b) [Boyd and Vandenberghe, 2004].

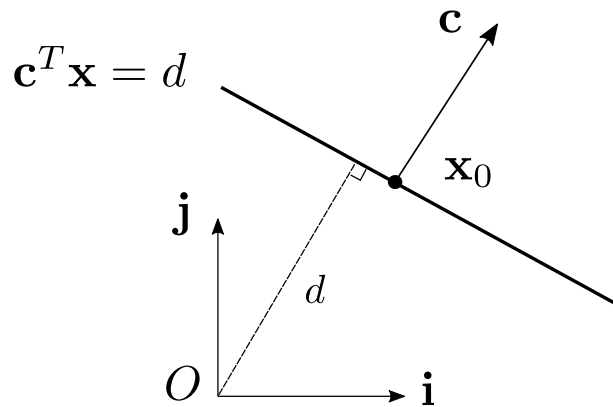


Figure A.2 – Representation of a hyperplane in \mathbb{R}^2 ($O, \mathbf{i}, \mathbf{j}$). The hyperplane is defined as $\mathbf{c}^T \mathbf{x} = d$, which can be rewritten as $\mathbf{c}^T (\mathbf{x} - \mathbf{x}_0) = 0$ as well.

A halfspace in \mathbb{R}^n is defined using the following inequality

$$\mathcal{HS} = \{ \mathbf{x} \mid \mathbf{a}^T \mathbf{x} \leq b \}, \quad (\text{A.3})$$

where \mathbf{a} is a $n \times 1$ unit vector normal to the separating hyperplane, pointing towards the unauthorized halfspace and b is a scalar value referring to the distance from the origin to the hyperplane. Note that the halfspace determined by Eq. (A.3) extends in the direction $-\mathbf{a}$ (see shaded set in Fig. A.3).

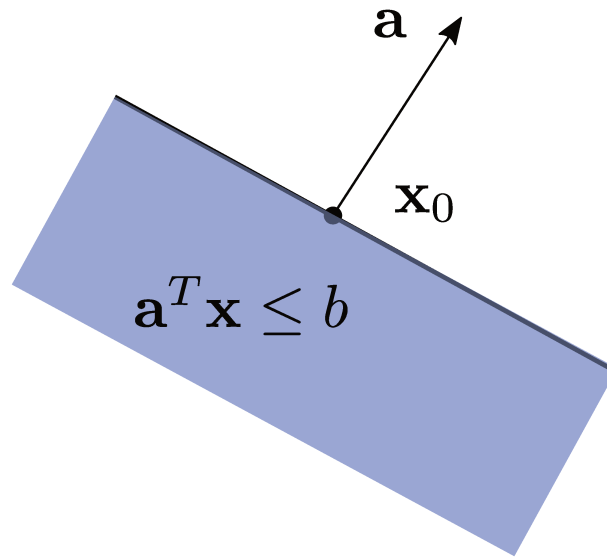


Figure A.3 – Representation of a halfspace in \mathbb{R}^2 . The halfspace is defined as $\mathbf{a}^T \mathbf{x} \leq b$, which can be rewritten as $\mathbf{a}^T (\mathbf{x} - \mathbf{x}_0) \leq 0$. The halfspace determined by $\mathbf{a}^T \mathbf{x} \leq b$ (which is shown shaded) extends in the direction $-\mathbf{a}$.

A.1.2 \mathcal{H} -representation and \mathcal{V} -representation of polytope

A polytope that can be represented mathematically in two different manners : \mathcal{H} -representation (intersection of halfspaces and hyperplanes) or \mathcal{V} -representation (a convex hull of vertices) [Grünbaum, 2003], see Fig. A.4.

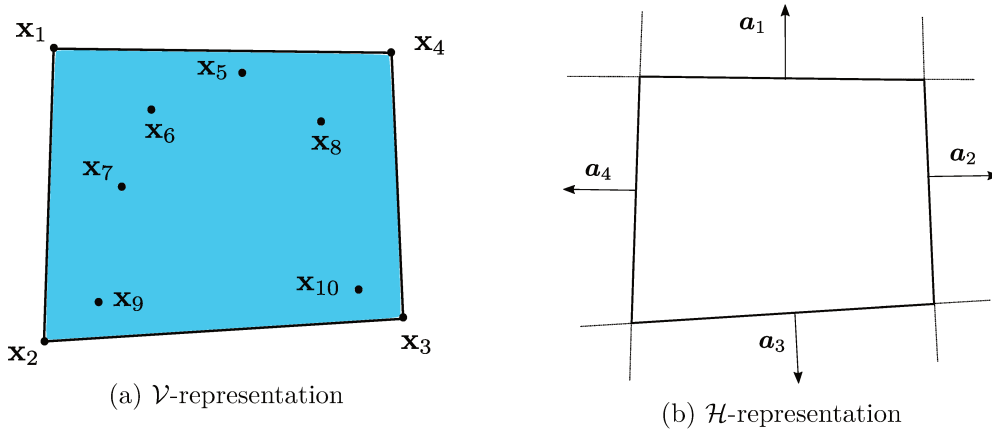


Figure A.4 – Representation of a polytope with (a) \mathcal{V} -representation and (b) \mathcal{H} -representation

Indeed, we can represent a polytope as the intersection of multiple halfspaces and

hyperplanes, namely the \mathcal{H} -representation,

$$\mathcal{P} = \left\{ \mathbf{x} \in \mathbb{R}^{n \times 1} \mid \mathbf{A}\mathbf{x} \leq \mathbf{b}, \mathbf{C}\mathbf{x} = \mathbf{d} \right\} \quad (\text{A.4})$$

where $\mathbf{A} \in \mathbb{R}^{m \times n}$ and $\mathbf{b} \in \mathbb{R}^{m \times 1}$ stand for m halfspaces, while $\mathbf{C} \in \mathbb{R}^{p \times n}$ and $\mathbf{d} \in \mathbb{R}^{p \times 1}$ represent p hyperplanes. Rows of matrix \mathbf{A} (resp. \mathbf{C}) contain each normal vector associated to a corresponding halfspace (resp. hyperplane).

Also, a polytope can also be represented as the convex hull of a set of points, the \mathcal{V} -representation.

$$\mathcal{P} = \mathbf{conv}(\mathcal{S}) \quad (\text{A.5})$$

where \mathcal{S} is the set of vertices of \mathcal{P} and the convex hull $\mathbf{conv}(\mathcal{S})$ is the set of all convex combinations of points

$$\mathbf{conv}(\mathcal{S}) = \left\{ \sum_{i=1}^k \alpha_i \mathbf{x}_i \mid \mathbf{x}_i \in \mathcal{S}, \alpha_i \geq 0, \sum_{i=1}^k \alpha_i = 1 \right\} \quad (\text{A.6})$$

In this thesis, \mathcal{H} -representation and \mathcal{V} -representation are considered equivalent since we study bounded convex sets. Given a certain convex polytope using \mathcal{H} -representation, computing its \mathcal{V} -representation is called the vertex enumeration problem. The reverse problem is referred to as the facet enumeration problem. More details about the vertex enumeration problem and the facet enumeration problem can be found in [Fukuda, 2020].

A.1.3 Maximal inscribed sphere in a polytope

Given a point \mathbf{x}_c and a halfspace $\mathbf{a}^T \mathbf{x} \leq b$, the signed distance from the point to the separating hyperplane $\mathbf{a}^T \mathbf{x} = b$ is along the normal vector \mathbf{a} , which can be computed as

$$r = \frac{b - \mathbf{a}^T \mathbf{x}_c}{|\mathbf{a}|}. \quad (\text{A.7})$$

If \mathbf{a} is a unit vector, then the above equation can be rewritten to be

$$r = b - \mathbf{a}^T \mathbf{x}_c. \quad (\text{A.8})$$

It is possible to find the relation between \mathbf{x}_c and the halfspace based on r :

- $r > 0$ means that \mathbf{x}_c is inside the halfspace,
- $r < 0$ means that \mathbf{x}_c is outside the halfspace,

— $r = 0$ means that \mathbf{x}_c is located on the separating hyperplane $\mathbf{a}^T \mathbf{x} = b$.

A sphere in \mathbb{R}^n ($n \geq 4$) is a generalization of the circle in \mathbb{R}^2 and usual sphere in \mathbb{R}^3 to dimensions n . In \mathbb{R}^n , a sphere with radius r_s centered at \mathbf{x}_s is defined by

$$\| \mathbf{x} - \mathbf{x}_s \|^2 = r_s. \quad (\text{A.9})$$

Let consider that the point \mathbf{x}_c is inside a polytope $\mathcal{P} = \left\{ \mathbf{x} \in \mathbb{R}^{n \times 1} \mid \mathbf{A}\mathbf{x} \leq \mathbf{b} \right\}$. The polytope \mathcal{P} is modeled by intersections of halfspaces and each halfspace is defined by a row of \mathbf{A} and \mathbf{b} . After normalizing normal vectors contained in \mathbf{A} , the shortest signed distance among \mathbf{x}_c and all facets of \mathcal{P} is computed as

$$r = \min \left\{ \mathbf{b} - \mathbf{A}\mathbf{x}_c \right\} \quad (\text{A.10})$$

For the polytope \mathcal{P} , therefore, the largest inscribed sphere centered at \mathbf{x}_c inside can be represented by

$$\| \mathbf{x} - \mathbf{x}_c \|^2 = r. \quad (\text{A.11})$$

A.2 Operations on polytopes

Some operations allow us to construct polytopes from others and some operations used in this thesis are introduced here.

A.2.1 Linear mapping of a polytope

After introducing polytopes, our concern is to define the linear transformation of a polytope. Let's introduce the \mathcal{H} -representation and \mathcal{V} -representation of a polytope \mathcal{P} :

$$\mathcal{P} = \left\{ \mathbf{x} \in \mathbb{R}^{n \times 1} \mid \mathbf{A}\mathbf{x} \leq \mathbf{b}, \mathbf{C}\mathbf{x} = \mathbf{d} \right\} = \mathbf{conv}(\mathcal{S}), \quad (\text{A.12})$$

where $\mathcal{S} = \{\mathbf{x}_1, \dots, \mathbf{x}_k\}$ is the set of k vertices of \mathcal{P} .

Let us introduce a linear mapping $\mathbf{L} \in \mathbb{R}^{m \times n}$ that maps \mathbf{x} to \mathbf{x}'

$$\mathbf{x}' = \mathbf{L}\mathbf{x}. \quad (\text{A.13})$$

1. if \mathbf{L} is a square and invertible matrix with $m = n$. Substituting $\mathbf{x} = \mathbf{L}^{-1}\mathbf{x}'$ into

Eq.(A.12), we obtain the \mathcal{H} -representation of \mathcal{P}' from that of \mathcal{P}

$$\mathcal{P}' = \left\{ \mathbf{x}' \in \mathbb{R}^{m \times 1} \mid \mathbf{A}\mathbf{L}^{-1}\mathbf{x}' \leq \mathbf{b}, \mathbf{C}\mathbf{L}^{-1}\mathbf{x}' = \mathbf{d} \right\}. \quad (\text{A.14})$$

It is also possible to calculate the \mathcal{V} -representation of \mathcal{P}' by using the following relation:

$$\mathcal{P}' = \mathbf{conv}(\mathcal{S}') = \mathbf{conv}(\mathbf{L}(\mathcal{S})) \quad (\text{A.15})$$

where $\mathcal{S}' = \{\mathbf{x}'_1, \dots, \mathbf{x}'_k\}$ is the set of mapped vertices with $\mathbf{x}'_i = \mathbf{L}\mathbf{x}_i \quad \forall i \in \{1, \dots, k\}$. In what follows, we note $\mathcal{S}' = \mathbf{L}(\mathcal{S})$ the set of transformed vertices.

2. If \mathbf{L} is a rectangular matrix and $m < n$. The linear mapping \mathbf{L} is a projection from a higher dimensional space to a lower dimensional space (see Fig. A.5). Since matrix \mathbf{L} is not invertible, the previous method cannot be applied. In this case, one method consists in using the \mathcal{V} -representation to obtain the projected polytope \mathcal{P}' [Huynh et al., 1992]

$$\mathcal{P}' = \mathbf{conv}(\mathcal{S}') = \mathbf{conv}(\mathbf{L}(\mathcal{S})) \quad (\text{A.16})$$

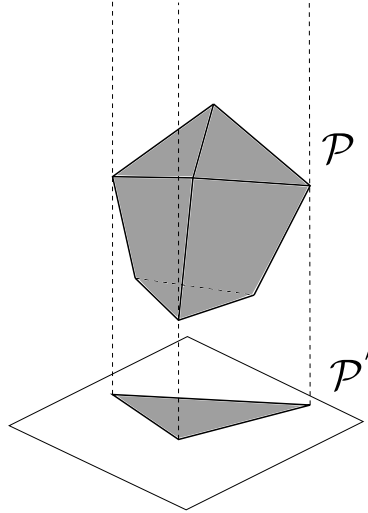


Figure A.5 – Projection of convex polytope \mathcal{P} to \mathcal{P}' in \mathbb{R}^3 .

3. If \mathbf{L} is a rectangular matrix and $m > n$. The polytope \mathcal{P} is mapped to a higher dimensional space, which is called convex lifting. Convex lifting is defined as to find a higher-dimensional polytope \mathcal{P}' whose projection is a given polytope \mathcal{P} [Fawzi, 2016]. However, note that lifting a polytope has an infinity of solution \mathcal{P}' in \mathbb{R}^m

(see Fig. A.6).

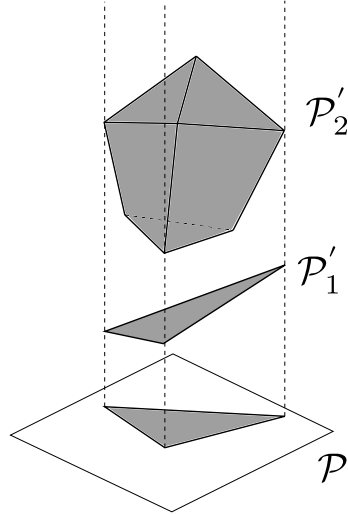


Figure A.6 – Lifting of a convex polytope \mathcal{P} in \mathbb{R}^3 . Lifting \mathcal{P} has an infinity of solution polytope \mathcal{P}' that have the same projection \mathcal{P} in \mathbb{R}^n , such as \mathcal{P}'_1 and \mathcal{P}'_2 .

A.2.2 Minkowski sum

Given two polytopes $\mathcal{P}, \mathcal{P}'$ in \mathbb{R}^n , their Minkowski sum is defined as

$$\mathcal{P} \oplus \mathcal{P}' = \{ \mathbf{x} + \mathbf{x}' \mid \mathbf{x} \in \mathcal{P}, \mathbf{x}' \in \mathcal{P}' \}. \quad (\text{A.17})$$

If both polytopes are defined using the \mathcal{V} -representation, then we can rewrite their Minkowski sum

$$\mathcal{P} \oplus \mathcal{P}' = \{ \mathbf{x} + \mathbf{x}' \mid \mathbf{x} \in \mathcal{S}, \mathbf{x}' \in \mathcal{S}' \} \quad (\text{A.18})$$

where \mathcal{S} and \mathcal{S}' are sets of vertices of \mathcal{P} and \mathcal{P}' respectively. An geometrical example in \mathbb{R}^2 is given in Fig. A.8. It is worthy to mention that computing the Minkowski sum of polytopes defined using the \mathcal{H} -representation is also possible [Tiwary, 2008].

A.2.3 Intersection

The intersection between two polytopes \mathcal{P} and \mathcal{P}' in \mathbb{R}^n is defined as

$$\mathcal{P} \cap \mathcal{P}' = \{ \mathbf{x} \mid \mathbf{x} \in \mathcal{P}, \mathbf{x} \in \mathcal{P}' \}. \quad (\text{A.19})$$

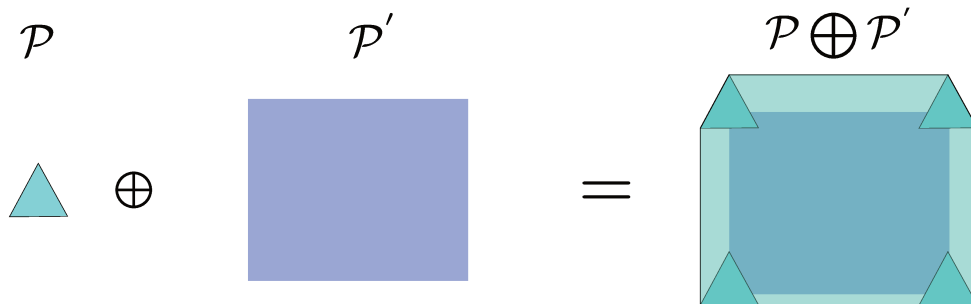


Figure A.7 – Minkowski sum of two polytopes in \mathbb{R}^2 : \mathcal{P} and \mathcal{P}'

If both polytopes are in the \mathcal{H} -representation, then the \mathcal{H} -representation of $\mathcal{P} \cap \mathcal{P}'$ can be computed by collecting the halfspaces and hyperplanes defining \mathcal{P} and \mathcal{P}' .

$$\mathcal{P} \cap \mathcal{P}' = \left\{ \mathbf{x} \in \mathbb{R}^{n \times 1} \mid \begin{bmatrix} \mathbf{A} \\ \mathbf{A}' \end{bmatrix} \mathbf{x} \leq \begin{bmatrix} \mathbf{b} \\ \mathbf{b}' \end{bmatrix}, \begin{bmatrix} \mathbf{C} \\ \mathbf{C}' \end{bmatrix} \mathbf{x} = \begin{bmatrix} \mathbf{d} \\ \mathbf{d}' \end{bmatrix} \right\}, \quad (\text{A.20})$$

where \mathbf{A}' , \mathbf{b}' define the halfspaces and \mathbf{C}' , \mathbf{d}' represent the hyperplanes of \mathcal{P}' . In this case, some inequalities and/or equalities become possibly redundant.

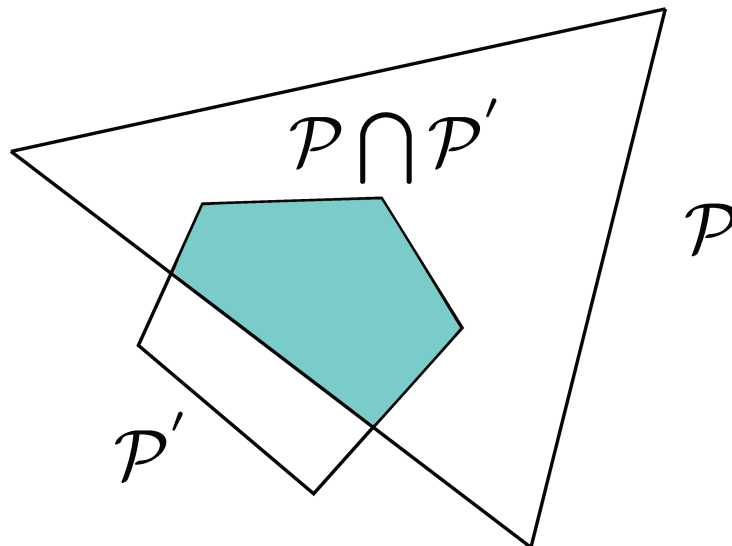


Figure A.8 – Intersection of two polytopes \mathcal{P} and \mathcal{P}' in \mathbb{R}^2 .

A.2.4 Remarks on the complexity of operations on polytopes

It is worthy to note that the complexity of an operation on polytopes depends on representations used (\mathcal{H} or \mathcal{V}). For example, in terms of computational complexity, it is

easier to compute the \mathcal{V} -representation of $\mathcal{P} \oplus \mathcal{P}'$ with input polytopes in \mathcal{V} -representation by solving a polynomial number of linear programs [Tiwary, 2008]. Thus, choosing a proper presentation of polytopes is essential for computational effectiveness (see Table A.1). Some more information can be found in [Tiwary, 2007, Tiwary, 2009, Chen, 2015b, Schupp, 2019].

Table A.1 – Complexities of operations on polytopes [Chen, 2015b]

\mathcal{P}	\mathcal{P}'	$\mathcal{P} \cap \mathcal{P}'$	$\text{conv}(\mathcal{P} \cup \mathcal{P}')$	$\mathcal{P} \oplus \mathcal{P}'$
\mathcal{H}	\mathcal{H}	$+(\mathcal{H})$	–	–
\mathcal{V}	\mathcal{V}	–	$+(\mathcal{V})$	$+(\mathcal{V})$

– means computational heavy.

$+(\mathcal{H})$ means computationally effective with output in \mathcal{H} -representation and $+(\mathcal{V})$ means computationally effective with output in \mathcal{V} -representation.

We use the MPT [Herceg et al., 2013] and benslove [Löhne and WeisSing, 2016, Ciripoi et al., 2018] toolboxes in this thesis to model and perform operations on the polytopes.

WRENCH CAPABILITY ANALYSIS OF A PLANAR FLYING GRIPPER ACTUATED BY TWO QUADROTORS (PFG)

B.1 Wrench capability analysis of a Planar Flying Gripper actuated by two quadrotors (PFG)

Here, a planar version of the Flying Gripper with two fingers and actuated by two quadrotors is introduced. Each finger is driven by one quadrotor's yaw rotation produced by the quadrotor's yaw torque.

The available body wrench sets of two different designs are computed in $SE(3)$: a Planar Flying Gripper with Fixed-Attitude Quadrotors (PFG-FAQ) and a Planar Flying Gripper with Mobile-Attitude Quadrotors (PFG-MAQ), which considers that quadrotors must produce yaw torques in order to actuate fingers to close or open. The results of closing fingers are given.

B.1.1 Available body wrench set of PFG-FAQ

The PFG-FAQ robot is a robot composed of a body structure, two self-adaptive fingers and actuated by two quadrotors (see Fig. B.1). Each quadrotor is linked to the body structure with a tilting angle α . It can generate a thrust force ${}^i\mathbf{f}_i \in \mathbb{R}^{3 \times 1}$ and a torque ${}^i\boldsymbol{\tau}_i \in \mathbb{R}^{3 \times 1}$ in \mathcal{F}_i .

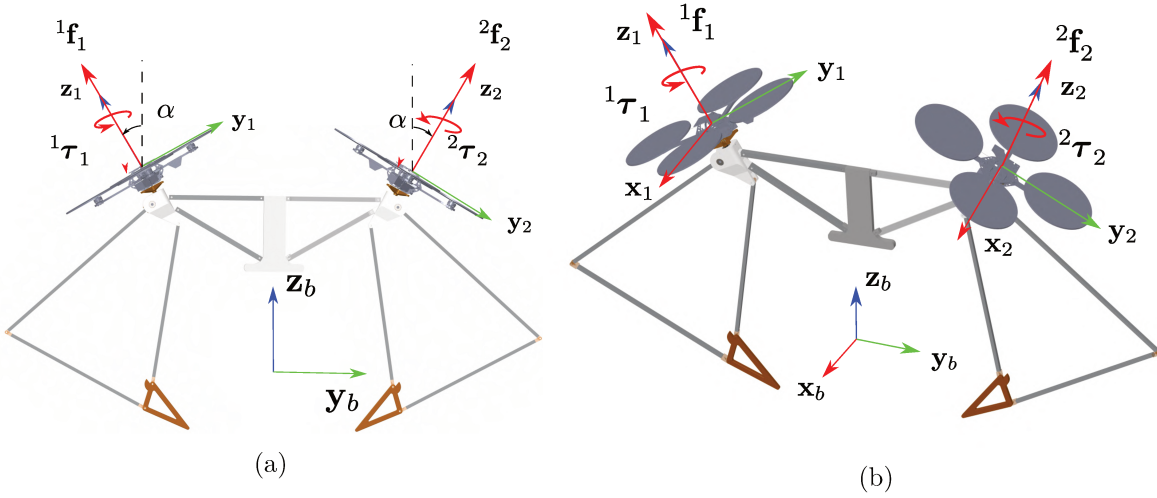


Figure B.1 – CAD view of Planar Flying Gripper with Fixed-Attitude Quadrotors (PFG-FAQ) robot. It is a planar robot composed of a body structure, two self-adaptive fingers, and two quadrotors tilted with angle α . Each quadrotor has four motors such that it generates a thrust force ${}^i\mathbf{f}_i \in \mathbb{R}^{3 \times 1}$ and a torque ${}^i\boldsymbol{\tau}_i \in \mathbb{R}^{3 \times 1}$ in frame \mathcal{F}_i .

Step 1: Available UAV actuation set \mathcal{A}_i

The available actuation set of a quadrotor \mathcal{A}_i is now a 4-cube and can be modeled as

$$\mathcal{A}_i = \left\{ \boldsymbol{\Omega}_i \in \mathbb{R}^{4 \times 1} \mid \mathbf{A}_{\Omega_i} \boldsymbol{\Omega}_i \leq \mathbf{b}_{\Omega_i} \right\} \quad (\text{B.1})$$

where $\mathbf{b}_{\Omega_i} = \left[\overline{\boldsymbol{\Omega}}^T \mid -\underline{\boldsymbol{\Omega}}^T \right]^T \in \mathbb{R}^{8 \times 1}$, $\mathbf{A}_{\Omega_i} = \left[\mathbf{I}_4 \mid -\mathbf{I}_4 \right]^T \in \mathbb{R}^{8 \times 4}$, 8 stands for the number of inequality constraints and 4 is the dimension of the actuation set (see Fig. B.2).

Step 2. Linear mapping of \mathcal{A}_i in UAV local reduced wrench space

Based on the linear mapping $\boldsymbol{\Gamma}_i$ in Eq. (2.9), the available UAV reduced wrench set \mathcal{W}_i^r is obtained as follows

$$\mathcal{W}_i^r = \left\{ {}^i\mathbf{w}_{i,r} \in \mathbb{R}^{4 \times 1} \mid \mathbf{A}_{\Omega_i} \boldsymbol{\Gamma}_i^{-1} {}^i\mathbf{w}_{i,r} \leq \mathbf{b}_{\Omega_i} \right\}, \quad (\text{B.2})$$

and \mathcal{W}_i^r is a 4D parallelotope, which can be visualized in Fig. B.3 showing its intersection with hyperplane $\mathcal{HP}(\tau_{i,y} = 0)$.

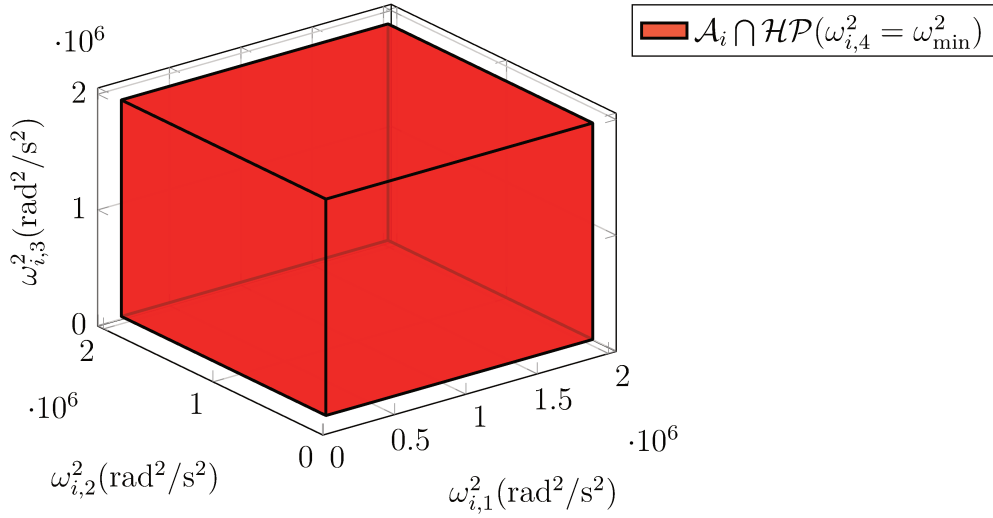


Figure B.2 – Visualization of the available UAV actuation set \mathcal{A}_i for FG-FAQ robot: showing intersection with hyperplane $\mathcal{HP}(\omega_{i,4}^2 = \omega_{\min}^2)$ in space $(\omega_{i,1}^2, \omega_{i,2}^2, \omega_{i,3}^2)$.

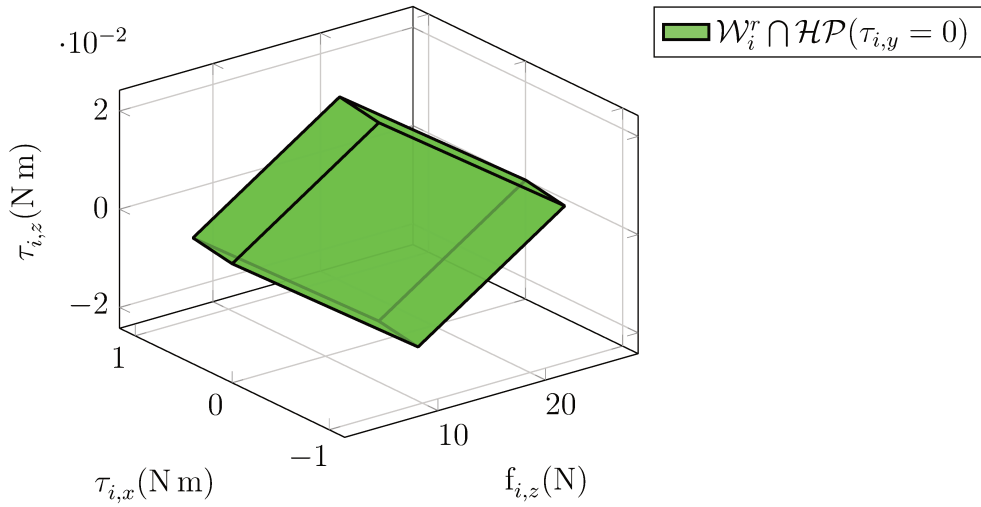


Figure B.3 – Visualization of available UAV reduced wrench set \mathcal{W}_i^r (a 4D parallelepotope): showing the intersection with hyperplane $\mathcal{HP}(\tau_{i,y} = 0)$ in the 3D space $(f_{i,z}, \tau_{i,x}, \tau_{i,z})$.

Step 3 : Lifting \mathcal{W}_i^r in UAV local wrench space

We compute the available UAV wrench set \mathcal{W}_i in a 6D space by lifting \mathcal{W}_i^r along $f_{i,x}$ and $f_{i,y}$ directions.

$$\mathcal{W}_i = \left\{ {}^i\mathbf{w}_i \in \mathbb{R}^{6 \times 1} \mid \mathbf{A}_i^{ii} \mathbf{w}_i \leq \mathbf{b}_{\Omega_i}, \mathbf{C}_i^{ii} \mathbf{w}_i = \mathbf{0} \right\} \quad (\text{B.3})$$

where

1. $\mathbf{A}_i^i = \begin{bmatrix} \mathbf{0}_{8 \times 2} & \vdots & \mathbf{A}_{\Omega_i} \mathbf{\Gamma}_i^{-1} \end{bmatrix} \in \mathbb{R}^{8 \times 6}$ that represents 8 inequality constraints,
2. $\mathbf{C}_i^i = \begin{bmatrix} \mathbf{e}_1 & \mathbf{e}_2 \end{bmatrix}^T \in \mathbb{R}^{2 \times 6}$ stands for 2 equality constraints that are introduced to ensure $f_{i,x} = f_{i,y} = 0$ as the quadrotor cannot produce any thrust force along \mathbf{x}_i or \mathbf{y}_i direction.

We can see in Fig. B.3 that \mathcal{W}_i is a 4D polytope in the 6D space.

Step 3 bis: Introducing UAV yaw torque constraint

Each quadrotor i must generate a yaw torque in order to actuate its corresponding finger when grasping or releasing an object. The available UAV wrench set considering this yaw torque constraint is defined as $\mathcal{W}_i^{\text{yaw}}$.

As explained in chapter 2, we design one worm gear to be left-hand, the other to be right-hand such that the two quadrotors generate two opposite yaw rotations to close/open fingers in order to obtain a zero net yaw torque exerted on the robot's body. In the following, we arbitrary consider a positive yaw torque τ_f for quadrotor i when closing the finger:

$$\tau_{i,z} = \tau_f \quad (\text{B.4})$$

Then, $\mathcal{W}_i^{\text{yaw}}$ is written, introducing this supplementary equality constraint

$$\mathcal{W}_i^{\text{yaw}} = \left\{ {}^i \mathbf{w}_i \in \mathbb{R}^{6 \times 1} \mid \mathbf{A}_i^i \mathbf{w}_i \leq \mathbf{b}_{\Omega_i}, \mathbf{C}_i^{\text{yaw}} \mathbf{w}_i = \mathbf{d}_i^{\text{yaw}} \right\}, \quad (\text{B.5})$$

where $\mathbf{A}_i^i = \begin{bmatrix} \mathbf{0} & \mathbf{A}_{\Omega_i} \mathbf{\Gamma}_i^{-1} \end{bmatrix} \in \mathbb{R}^{8 \times 6}$, $\mathbf{b}_{\Omega_i} \in \mathbb{R}^{8 \times 1}$, $\mathbf{C}_i^{\text{yaw}} = \begin{bmatrix} \mathbf{C}_i^{iT} & \mathbf{e}_6 \end{bmatrix}^T \in \mathbb{R}^{3 \times 6}$ and $\mathbf{d}_i^{\text{yaw}} = \begin{bmatrix} 0 & 0 & \tau_f \end{bmatrix}^T \in \mathbb{R}^{3 \times 1}$. It is shown in Fig. B.4c that $\mathcal{W}_i^{\text{yaw}}$ is a 3D polytope in the 6D space $(f_{i,x}, f_{i,y}, f_{i,z}, \tau_{i,x}, \tau_{i,y}, \tau_{i,z})$. We can visualize the intersection between \mathcal{W}_i^i and $\mathcal{HP}(\tau_{i,z} = \tau_f)$ in the space $(f_{i,z}, \tau_{i,x}, \tau_{i,z})$ in Fig. B.4.

Step 4 : Linear mapping of $\mathcal{W}_i^{\text{yaw}}$ in body wrench space

As ${}^b \mathbf{w}_{i,b}$ represents the wrench applied to the robot's body by quadrotor i expressed in the body frame \mathcal{F}_b , it can be computed with the formula

$${}^b \mathbf{w}_{i,b} = {}^b \mathbf{W}_i^i \mathbf{w}_i, \quad (\text{B.6})$$

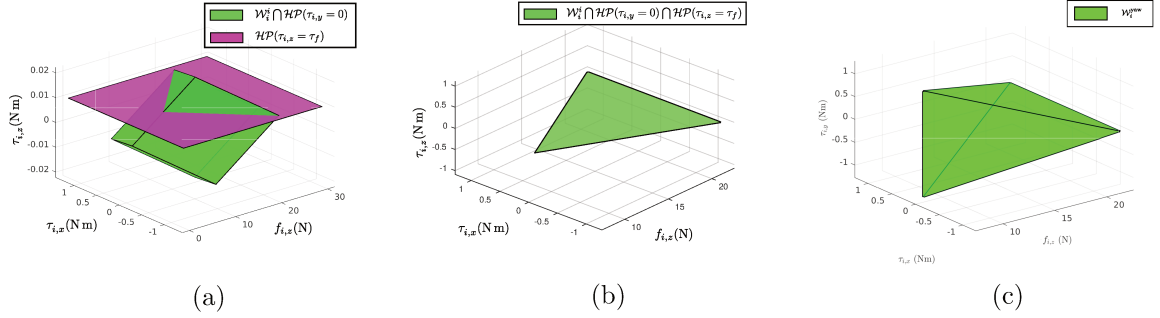


Figure B.4 – $\mathcal{W}_i^{\text{yaw}}$: available UAV wrench set considering equality yaw torque constraint. (a) plot hyperplane $\mathcal{HP}(\tau_{i,z} = \tau_f)$ ($\tau_f = 0.01$ N m) and $\mathcal{W}_i(\tau_{i,y} = 0)$ in the 3D space $(f_{i,z}, \tau_{i,x}, \tau_{i,z})$. (b) $\mathcal{W}_i^{\text{yaw}}$ is a 3D polytope, but its intersection with $\mathcal{HP}(\tau_{i,y} = 0)$ that is a 2D polytope in the 3D space $(f_{i,z}, \tau_{i,x}, \tau_{i,z})$ for visualization. (c) $\mathcal{W}_i^{\text{yaw}}$ in the 3D space $(f_{i,z}, \tau_{i,x}, \tau_{i,y})$

where ${}^b\mathbf{W}_i = \begin{bmatrix} {}^b\mathbf{R}_i & \mathbf{0} \\ [{}^b\mathbf{r}_i]_{\times} & {}^b\mathbf{R}_i \end{bmatrix} \in \mathbb{R}^{6 \times 6}$, defined in Eq. 2.6, is a constant square and invertible matrix.

Thus, we can compute its corresponding available UAV wrench set \mathcal{W}_i^b as

$$\mathcal{W}_i^b = \left\{ {}^b\mathbf{w}_{i,b} \in \mathbb{R}^{6 \times 1} \mid \mathbf{A}_i^i {}^b\mathbf{W}_i^{-1} {}^b\mathbf{w}_{i,b} \leq \mathbf{b}_{\Omega_i}, \mathbf{C}_i^{\text{yaw}} {}^b\mathbf{W}_i^{-1} {}^b\mathbf{w}_{i,b} = \mathbf{d}_i^{\text{yaw}} \right\} \quad (\text{B.7})$$

where

1. matrix $\mathbf{A}_i^i {}^b\mathbf{W}_i^{-1} = \begin{bmatrix} \mathbf{0} & \mathbf{A}_{\Omega_i} \mathbf{\Gamma}_i^{-1} \end{bmatrix} {}^b\mathbf{W}_i^{-1} = \begin{bmatrix} \mathbf{0} & \mathbf{A}_{\Omega_i} \mathbf{\Gamma}_i^{-1} {}^b\mathbf{W}_i^{-1} \end{bmatrix} \in \mathbb{R}^{8 \times 6}$ refers to 8 inequality constraints,
2. vector $\mathbf{C}_i^{\text{eq}} {}^b\mathbf{W}_i^{-1} \in \mathbb{R}^{3 \times 6}$ refers to 3 equality constraints.

Again, we can get a conclusion that \mathcal{W}_i^b is a 3D polytope in the body wrench space (in \mathbb{R}^6).

Step 5 : Minkowski sum of \mathcal{W}_1^b and \mathcal{W}_2^b

For the FG-FAQ robot, we compute the available body wrench set \mathcal{W}^b with the Minkowski sum

$$\mathcal{W}_b = \mathcal{W}_1^b \oplus \mathcal{W}_2^b. \quad (\text{B.8})$$

From the \mathcal{H} -representation of \mathcal{W}_b , we find that \mathcal{W}_b has 1 equality constraint such that \mathcal{W}_b is a 5D polytope in the 6D space. It demonstrates that no full manipulability can be allowed.

B.1.2 Available body wrench set of PFG-MAQ

In this section, we compute the available body wrench set of PFG-MAQ (see Fig. B.5). Differently from PFG-FAQ, each quadrotor of the PFG-MAQ robot is linked to one worm screw through a universal joint (U-joint): each quadrotor thus gains two DOF (roll and pitch rotations).

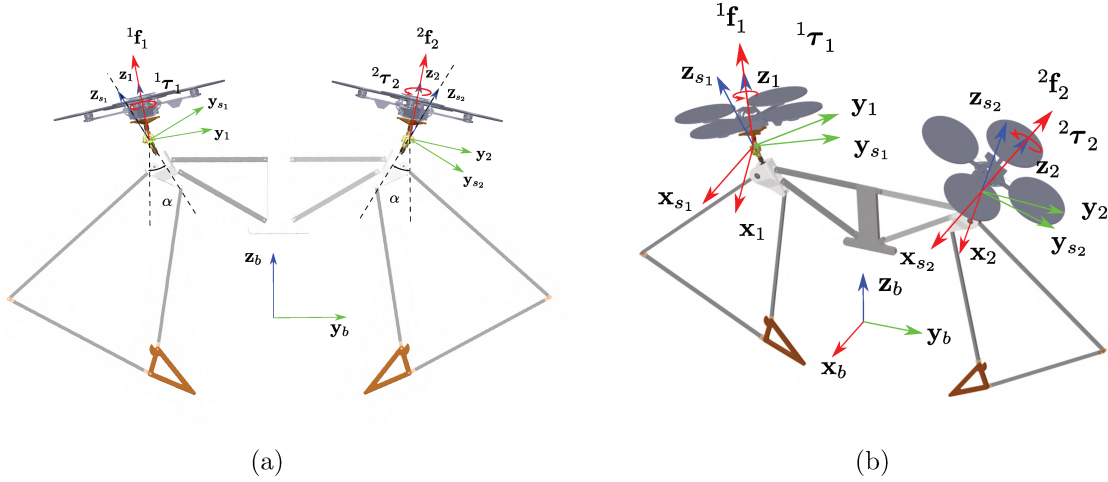


Figure B.5 – CAD view of Planar Flying Gripper with Mobile-Attitude Quadrotors (PFG-MAQ) robot. It is a planar robot composed of a body structure, two self-adaptive fingers, and two quadrotors linked to the body structure through a universal joint. Each quadrotor has four motors such that it generates a thrust force ${}^i\mathbf{f}_i \in \mathbb{R}^{3 \times 1}$ and a torque ${}^i\boldsymbol{\tau}_i \in \mathbb{R}^{3 \times 1}$ in frame \mathcal{F}_i .

In analyzing PFG-MAQ, the frame \mathcal{F}_{s_i} introduced in section 3.2.2 that is attached to the body structure whose \mathbf{z}_{s_i} axis coincides with the worm screw axis and origin coincides with that of \mathcal{F}_i . For quadrotor i , its attitude w.r.t \mathcal{F}_{s_i} is represented by the rotation matrix ${}^s\mathbf{R}_i \in \mathbb{R}^{3 \times 3}$. Due to the mechanical stops of the U-joint, we model the available range of the i^{th} quadrotor's rotation w.r.t \mathcal{F}_{s_i} as a cone (see Fig. B.6b). We can model the mechanical stop by $0 < \varphi_i < \varphi_{\max}$, where φ_i is the angle between \mathbf{z}_{s_i} and \mathbf{z}_i .

Step 3-ter: Introducing static equilibrium conditions

Following steps 1 to 3-bis introduced in the previous section, we compute $\mathcal{W}_i^{\text{yaw}}$ that is the available UAV wrench set expressed in frame \mathcal{F}_i considering the motor speed limit and the yaw torque constraint see Eq. (B.5).

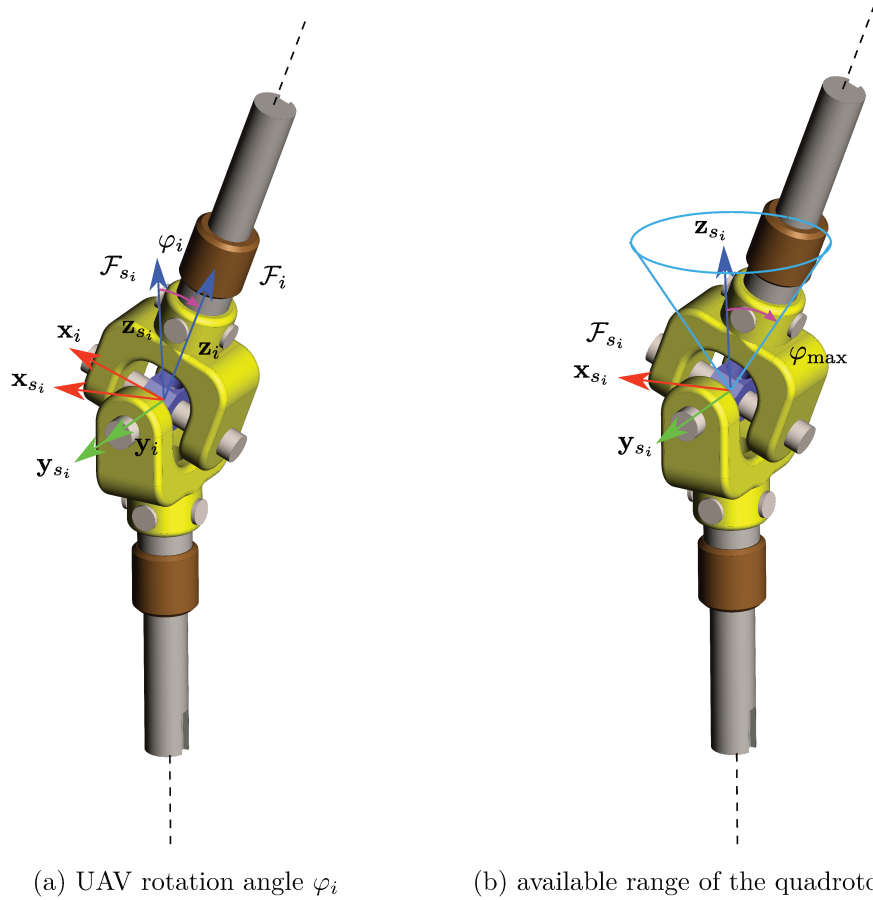


Figure B.6 – Available range of the i^{th} quadrotor's rotation w.r.t the U-joint expressed in frame \mathcal{F}_{s_i} considering the universal joint mechanical limits that is modeled by the maximal angle φ_{\max} .

The static equilibrium of each quadrotor i is modeled by the equations

$$\tau_{i,x} = 0, \quad (\text{B.9})$$

$$\tau_{i,y} = 0. \quad (\text{B.10})$$

Then, we compute the corresponding $\mathcal{W}_i^{\text{eq}}$ that is the available UAV wrench set considering the static equilibrium constraint as

$$\mathcal{W}_i^{\text{eq}} = \left\{ {}^i \mathbf{w}_i \in \mathbb{R}^{6 \times 1} \mid \mathbf{A}_i^{ii} \mathbf{w}_i \leq \mathbf{b}_{\Omega_i}, \mathbf{C}_i^{\text{eq}i} \mathbf{w}_i = \mathbf{d}_i^{\text{eq}} \right\} \quad (\text{B.11})$$

where

- $\mathbf{A}_i^i = \begin{bmatrix} \mathbf{0} & \mathbf{A}_\Omega^i \mathbf{\Gamma}_i^{-1} \end{bmatrix} \in \mathbb{R}^{8 \times 6}$ and $\mathbf{b}_{\Omega_i} \in \mathbb{R}^{8 \times 1}$ represent 8 inequality constraints,
- $\mathbf{C}_i^{\text{eq}} = \begin{bmatrix} \mathbf{C}_i^{\text{yaw}} \\ \mathbf{e}_4^T \\ \mathbf{e}_5^T \end{bmatrix} = \begin{bmatrix} \mathbf{e}_1 & \mathbf{e}_2 & \mathbf{e}_6 & \mathbf{e}_4 & \mathbf{e}_5 \end{bmatrix}^T \in \mathbb{R}^{5 \times 6}$ and $\mathbf{d}_i^{\text{eq}} = \begin{bmatrix} \mathbf{0}_2 & \tau_f & \mathbf{0}_2 \end{bmatrix}^T \in \mathbb{R}^{5 \times 1}$ stands for 5 equality constraints,

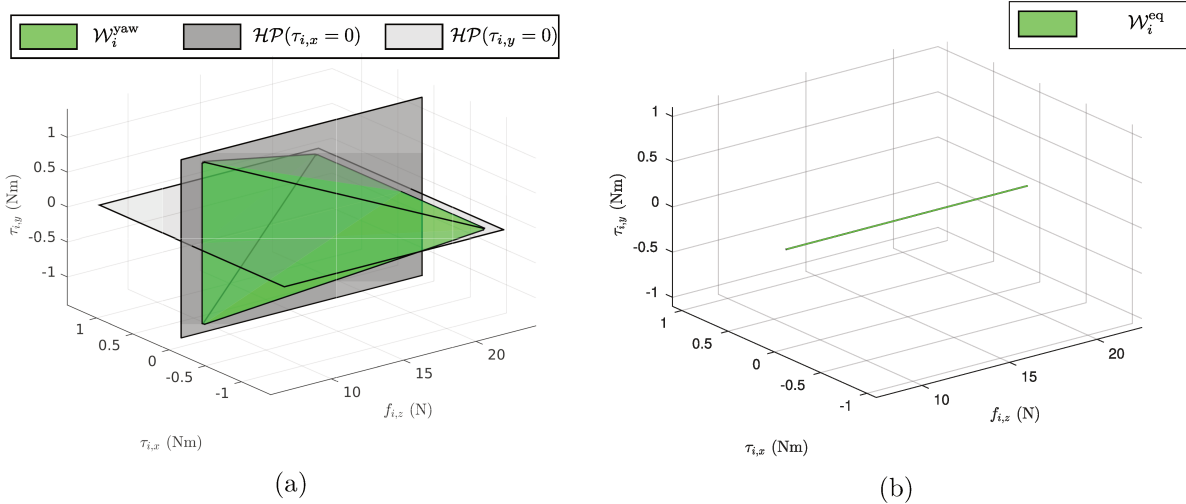


Figure B.7 – $\mathcal{W}_i^{\text{eq}}$: available UAV wrench set considering static equilibrium. We visualize $\mathcal{W}_i^{\text{eq}}$ in the 3D space $(f_{i,z}, \tau_{i,x}, \tau_{i,z})$. $\mathcal{W}_i^{\text{eq}}$ is a line segment in the 3D space $(f_{i,z}, \tau_{i,x}, \tau_{i,z})$.

From the above equation, it can be deduced that $\mathcal{W}_i^{\text{eq}}$ is a 1D polytope. We can visualize $\mathcal{W}_i^{\text{eq}}$ in the 3D space $(f_{i,z}, \tau_{i,x}, \tau_{i,z})$ (see Fig. B.7). Also, we are able to visualize $\mathcal{W}_i^{\text{eq}}$ (see Fig. B.7) in the space $(f_{i,z}, \tau_{i,x}, \tau_{i,y})$ by computing the intersection between $\mathcal{W}_i^{\text{yaw}}$ and $\mathcal{HP}(\tau_{i,x} = \tau_{i,y} = 0 \text{ N m})$ that is imposed by static equilibrium. As we can see in the 3D space $(f_{i,z}, \tau_{i,x}, \tau_{i,y})$, $\mathcal{W}_i^{\text{eq}}$ is a line segment whose extremities are positive values 8.1 N and 21.9 N showing that the quadrotor can only exert a thrust force while applying a constant yaw torque and satisfying equilibrium conditions.

Step 4 : Linear mapping of $\mathcal{W}_i^{\text{eq}}$ in body wrench space

We consider the linear mapping ${}^b\mathbf{W}_i^{-1}(\boldsymbol{\eta}_i)$ between ${}^i\mathbf{w}_i$ and ${}^b\mathbf{w}_{i,b}$ as a function of the quadrotor' configuration, then we can compute the available UAV wrench set \mathcal{W}_i^b expressed in \mathcal{F}_b as

$$\mathcal{W}_i^b(\boldsymbol{\eta}_i) = \left\{ {}^b\mathbf{w}_{i,b} \in \mathbb{R}^{6 \times 1} \mid \mathbf{A}_i^i {}^b\mathbf{W}_i^{-1}(\boldsymbol{\eta}_i) {}^b\mathbf{w}_{i,b} \leq \mathbf{b}_{\Omega_i}, \mathbf{C}_i^{\text{eq}} {}^b\mathbf{W}_i^{-1}(\boldsymbol{\eta}_i) {}^b\mathbf{w}_{i,b} = \mathbf{d}_i^{\text{eq}} \right\}. \quad (\text{B.12})$$

Step 5 : Minkowski Sum of \mathcal{W}_1^b and \mathcal{W}_2^b

Finally, we apply the Minkowski sum to compute the available body wrench set $\mathcal{W}_b = \mathcal{W}_1^b(\boldsymbol{\eta}_1) \oplus \mathcal{W}_2^b(\boldsymbol{\eta}_2)$. Note that the result \mathcal{W}_b depends on the configurations of two quadrotors' attitudes $\boldsymbol{\eta}_1$ and $\boldsymbol{\eta}_2$.

Because $\mathcal{W}_1^b(\boldsymbol{\eta}_1)$ and $\mathcal{W}_2^b(\boldsymbol{\eta}_2)$ are 2 polytopes with dimension of 1, \mathcal{W}_b can have a dimension of at most 2 in \mathbb{R}^6 . So, the robot cannot obtain full manipulability in $SE(3)$.

B.1.3 Available body wrench set of PFG-MAQ for all admissible configurations

The method presented in this section analyzes the PFG-MAQ mechanism. It considers all admissible attitudes of quadrotors under constraints imposed by mechanical stops of U-joints restraining quadrotors' attitudes and neglects quadrotors' rotational dynamics.

Since, we analyze the same mechanism analyzed in section 3.3.2 and we begin with the result of step 3bis (see Eq. (B.11)).

Step 3-quadrotor Available UAV wrench set \mathcal{W}_i^s expressed in \mathcal{F}_{s_i} – linear mapping and union of $\mathcal{W}_i^{\text{eq}}$

We can obtain the expression of UAV wrench in \mathcal{F}_{s_i} as

$${}^s\mathbf{w}_i = {}^s\mathbf{W}_i(\boldsymbol{\eta}_i) {}^i\mathbf{w}_i \quad (\text{B.13})$$

where ${}^s\mathbf{W}_i(\boldsymbol{\eta}_i) = \begin{bmatrix} {}^s\mathbf{R}_i & \mathbf{0} \\ \mathbf{0} & {}^s\mathbf{R}_i \end{bmatrix} \in \mathbb{R}^{6 \times 6}$ is a square and invertible matrix. As a consequence, the available UAV wrench set $\mathcal{W}_i^s(\boldsymbol{\eta}_i)$ expressed in frame \mathcal{F}_{s_i} is calculated as

$$\mathcal{W}_i^s(\boldsymbol{\eta}_i) = \left\{ {}^s\mathbf{w}_i \in \mathbb{R}^{6 \times 1} \mid \mathbf{A}_i^{\text{eq}} {}^s\mathbf{W}_i^{-1}(\boldsymbol{\eta}_i) {}^s\mathbf{w}_i \leq \mathbf{b}_i^{\text{eq}}, \mathbf{C}_i^{\text{eq}} {}^s\mathbf{W}_i^{-1}(\boldsymbol{\eta}_i) {}^s\mathbf{w}_i = \mathbf{d}_i^{\text{eq}} \right\}. \quad (\text{B.14})$$

Then, we find the union of \mathcal{W}_i^s of all admissible configurations and compute its convex hull (see Fig. B.8) in order to consider \mathcal{W}_i^s at all admissible configurations.

$$\mathcal{W}_i^s = \text{conv} \left(\bigcup_{\varphi_i \in [0, \varphi_{\max}]} \mathcal{W}_i^s(\boldsymbol{\eta}_i) \right) = \text{conv} \left(\mathcal{S}_i^f \right), \quad (\text{B.15})$$

where \mathcal{S}_i^f is set of vertices of \mathcal{W}_i^s . In the space $({}^s f_{i,x}, {}^s f_{i,y}, {}^s f_{i,z})$, \mathcal{W}_i^s is a linearized ap-

proximation of a cone and depends on φ_{\max} and the number of generators used in the union.

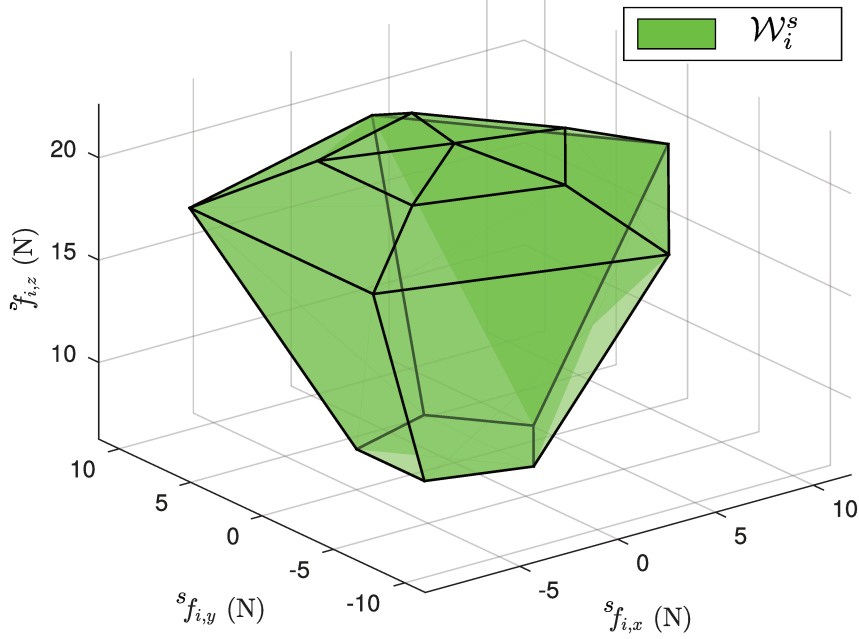


Figure B.8 – Visualization of the available UAV wrench sets \mathcal{W}_i^s with 11 generators expressed in the 3D space $({}^s f_{i,x}, {}^s f_{i,y}, {}^s f_{i,z})$.

Step 4 :Linear Mapping of \mathcal{W}_i^s in the body wrench space

The UAV wrench expressed in the body frame can be obtained using the following formula:

$${}^b \mathbf{w}_{i,b} = {}^b \mathbf{W}_{s_i} {}^s \mathbf{w}_i, \quad (\text{B.16})$$

where ${}^b \mathbf{W}_{s_i} = \begin{bmatrix} {}^b \mathbf{R}_{s_i} & \mathbf{0} \\ \mathbf{0} & {}^b \mathbf{R}_{s_i} \end{bmatrix} \in \mathbb{R}^{6 \times 6}$ is a constant square and invertible matrix.

We recall that the result in the previous step, see Eq.(B.15), is in \mathcal{V} -representation that is a set of vertices. For computational efficiency, we keep this representation for steps 4 and 5. The available UAV wrench set \mathcal{W}_i^b expressed in frame \mathcal{F}_b is obtained as follows

$$\mathcal{W}_i^b = \mathbf{conv}({}^b \mathbf{W}_{s_i} (\mathcal{S}_i^f)). \quad (\text{B.17})$$

Step 5 : Minkowski sum of \mathcal{W}_1^b and \mathcal{W}_2^b

The available body wrench set \mathcal{W}_b is obtained using the Minkowski sum $\mathcal{W}_b = \mathcal{W}_1^b \oplus \mathcal{W}_2^b$. Even \mathcal{W}_b is a 6D polytope in the body wrench space, the wrench compensating gravity is not strictly inside \mathcal{W}_b : no full manipulability is allowed.

B.1.4 Discussion on results

In this section, we compute \mathcal{W}_b in 6D space $({}^b f_{b,x}, {}^b f_{b,y}, {}^b f_{b,z}, {}^b \tau_{b,x}, {}^b \tau_{b,y}, {}^b \tau_{b,z})$ that has different units. That causes difficulties for analyzing \mathcal{W}_b directly. Based on section 3.2, the qualitative index is used to check if the robot allows full manipulability in $SE(3)$. Then, use the quantitative performance index to compare the capabilities.

Analyzing the manipulability of PFG-FAQ and PFG-MAQ

In order to analyze the robot's manipulability, a sufficient and necessary condition for full manipulability is used: checking if the wrench $\mathbf{w}_0 = [m_t \mathbf{g}^T \quad \mathbf{0}]^T \in \mathbb{R}^{6 \times 1}$ is strictly inside \mathcal{W}_b . Also, we can check the robot's manipulability using the dimension of \mathcal{W}_b in \mathbb{R}^6 . If the dimension is smaller than 6, then the robot does not have full manipulability in $SE(3)$: a 6D polytope is a necessary condition for full manipulability.

Therefore, Table. B.1 shows that the PFG-FAQ robot cannot achieve full manipulability in $SE(3)$ as the dimension of \mathcal{W}_b is 5. If consider the PFG-FAQ robot at an instant configuration, the dimension of \mathcal{W}_b is 4 and it cannot achieve full manipulability in $SE(3)$. By contrast, for the PFG-FAQ robot considering all admissible configurations, the dimension is 6 but \mathbf{w}_0 is not strictly inside \mathcal{W}_b . Thus, none of them allow full manipulability in $SE(3)$.

Comparing wrench capabilities of PFG-FAQ and PFG-MAQ

Here, we use two quantitative criteria that are largest spheres inscribed in the available force set \mathcal{W}_f and the available torque set \mathcal{W}_τ , where

1. \mathcal{W}_f is the available force set when the robot generates zero torque: it is computed as the intersection of \mathcal{W}_b with $\mathcal{HP}({}^b \tau_{b,x} = 0, {}^b \tau_{b,y} = 0, {}^b \tau_{b,z} = 0)$,
2. \mathcal{W}_τ is the available torque set when the robot generates a force that compensates gravity: it is computed as the intersection of \mathcal{W}_b with $\mathcal{HP}({}^b f_{b,x} = 0, {}^b f_{b,y} = 0, {}^b f_{b,z} = m_t g)$ and m_t stands for the mass of the whole robot.

Based on the above results, we propose two criteria to evaluate the manipulability of the robot:

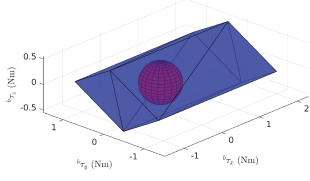
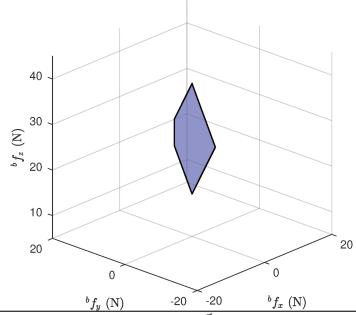
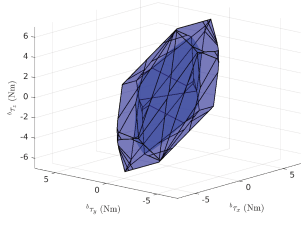
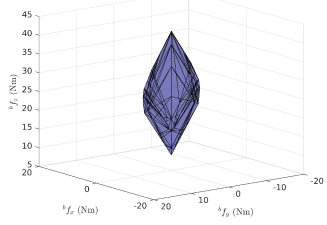
1. we compute r_f , the radius of the largest sphere centered on $({}^b f_{b,x}, {}^b f_{b,y}, {}^b f_{b,z}) = (0, 0, m_t g)$ inscribed in \mathcal{W}_f ,
2. we compute r_τ , the radius of the largest sphere centered on the origin $({}^b \tau_{b,x}, {}^b \tau_{b,y}, {}^b \tau_{b,z}) = (0, 0, 0)$ inscribed in \mathcal{W}_τ .

Such spheres represent the maximal force (torque) that the robot is able to exert in any direction: r_f describes the maximal force that the robot is able to exert in any direction apart from when the robot generates no torque, while r_τ describes the maximal torque that the robot is able to exert in any direction when the robot compensates gravity.

The results in Table B.1 show that for the PFG-FAQ robot, \mathcal{W}_f is a 2D polytope and r_f is empty, while for the PFG-MAQ robot (all admissible configurations), $r_f = 0$ and $r_\tau = 0$. Thus, we can achieve the conclusion that neither of PFG-FAQ or PFG-MAQ cannot allow full manipulability in $SE(3)$.

It is worthy to mention that the PFG-FAQ robot cannot achieve full manipulability as it cannot produce a force long \mathbf{x}_b direction. However, it is able to control its attitude while compensating gravity and closing fingers. Also, it can translate along \mathbf{y}_b and \mathbf{z}_b directions while generating zero torque and closing fingers.

Table B.1 – When closing fingers, \mathcal{W}_f and \mathcal{W}_τ of PFG-FAQ PFG-MAQ robots. The available torque set \mathcal{W}_τ is computed as the intersection of \mathcal{W}_b with $\mathcal{HP}({}^b f_{b,x} = 0, {}^b f_{b,y} = 0, {}^b f_{b,z} = m_t g)$, and the available force set \mathcal{W}_f is calculated as the intersection of \mathcal{W}_b with $\mathcal{HP}({}^b \tau_{b,x} = 0, {}^b \tau_{b,y} = 0, {}^b \tau_{b,z} = 0)$

	full manipulability in $SE(3)$	\mathcal{W}_τ	\mathcal{W}_f
PFG-FAQ $\dim(\mathcal{W}_b) = 5$	No	 <p style="text-align: center;">$r_\tau = 0.40 \text{ N m}$</p>	 <p style="text-align: center;">$r_f = \emptyset$</p>
PFG-MAQ $\dim(\mathcal{W}_b) = 4$	No	\emptyset $r_\tau = \emptyset$	\emptyset $r_f = \emptyset$
PFG-MAQ* $\dim(\mathcal{W}_b) = 6$	No	 <p style="text-align: center;">$r_\tau = 0 \text{ N m}$</p>	 <p style="text-align: center;">$r_f = 0 \text{ N}$</p>

* consider all admissible configuration of quadrotor imposed by U-joints
 $\dim(\mathcal{W}_b)$ means the dimension of the \mathcal{W}_b polytope

BIBLIOGRAPHY

- [Abiko and Harada, 2021] Abiko, S. and Harada, T. (2021). Autonomous flight of a quad tilt-rotor uav at constant altitude. In *ROMANSY 23 - Robot Design, Dynamics and Control*, pages 195–203. Springer International Publishing.
- [Allibert et al., 2010] Allibert, G., Courtial, E., and Chaumette, F. (2010). Predictive control for constrained image-based visual servoing. *IEEE Transactions on Robotics*, 26(5):933–939.
- [Anzai et al., 2018] Anzai, T., Zhao, M., Nozawa, S., Shi, F., Okada, K., and Inaba, M. (2018). Aerial grasping based on shape adaptive transformation by halo: Horizontal plane transformable aerial robot with closed-loop multilinks structure. In *Proceedings of IEEE International Conference on Robotics and Automation (ICRA)*, pages 6990–6996.
- [Begoc et al., 2006] Begoc, V., Durand, C., Krut, S., Dombre, E., and Pierrot, F. (2006). On the form-closure capability of robotic underactuated hands. In *Proceedings of IEEE International Conference on Control, Automation, Robotics and Vision (ICARCV)*, pages 1–8.
- [Bellicoso et al., 2015] Bellicoso, C. D., Buonocore, L. R., Lippiello, V., and Siciliano, B. (2015). Design, modeling and control of a 5-dof light-weight robot arm for aerial manipulation. In *Proceedings of IEEE Mediterranean Conference on Control and Automation (MED)*, pages 853–858.
- [Bicego, 2019] Bicego, D. (2019). *Design and Control of Multi-Directional Thrust Multi-Rotor Aerial Vehicles with applications to Aerial Physical Interaction Tasks*. PhD thesis, Institut national des sciences appliquées de Toulouse.
- [Birglen and Gosselin, 2004] Birglen, L. and Gosselin, C. M. (2004). Kinetostatic analysis of underactuated fingers. *IEEE Transactions on Robotics and Automation*, 20(2):211–221.
- [Birglen and Gosselin, 2006] Birglen, L. and Gosselin, C. M. (2006). Force analysis of connected differential mechanisms: Application to grasping. *The International Journal of Robotics Research*, 25(10):1033–1046.

-
- [Birglen et al., 2008a] Birglen, L., Laliberté, T., and Gosselin, C. (2008). Grasp stability of underactuated fingers. In *Underactuated Robotic Hands*, pages 61–115. Springer Berlin Heidelberg.
- [Birglen et al., 2008b] Birglen, L., Laliberté, T., and Gosselin, C. (2008). Grasping vs. manipulating. In *Underactuated Robotic Hands*, pages 7–31. Springer Berlin Heidelberg.
- [Birglen et al., 2008c] Birglen, L., Laliberté, T., and Gosselin, C. (2008). Kinetostatic analysis of robotic fingers. In *Underactuated Robotic Hands*, pages 33–60. Springer Berlin Heidelberg.
- [Bosscher and Ebert-Uphoff, 2004] Bosscher, P. and Ebert-Uphoff, I. (2004). Wrench-based analysis of cable-driven robots. In *Proceedings of IEEE International Conference on Robotics and Automation (ICRA)*, pages 4950–4955.
- [Bouchard et al., 2010] Bouchard, S., Gosselin, C., and Moore, B. (2010). On the ability of a cable-driven robot to generate a prescribed set of wrenches. *Journal of Mechanisms and Robotics*, 2(1).
- [Boyd and Vandenberghe, 2004] Boyd, S. and Vandenberghe, L. (2004). *Convex Optimization*. Cambridge University Press.
- [Brescianini and D’Andrea, 2016] Brescianini, D. and D’Andrea, R. (2016). Design, modeling and control of an omni-directional aerial vehicle. In *Proceedings of IEEE International Conference on Robotics and Automation (ICRA)*, pages 3261–3266.
- [Caballero et al., 2017] Caballero, A., Béjar, M., Rodriguez-Castaño, A., and Ollero, A. (2017). Motion planning for long reach manipulation in aerial robotic systems with two arms. In *Proceedings of IEEE European Conference on Mobile Robots (ECMR)*, pages 1–7.
- [Caballero et al., 2018] Caballero, A., Suarez, A., Real, F., Vega, V. M., Bejar, M., Rodriguez-Castaño, A., and Ollero, A. (2018). First experimental results on motion planning for transportation in aerial long-reach manipulators with two arms. In *Proceedings of IEEE International Conference on Intelligent Robots and Systems (IROS)*, pages 8471–8477.
- [Car et al., 2018] Car, M., Ivanovic, A., Orsag, M., and Bogdan, S. (2018). Impedance based force control for aerial robot peg-in-hole insertion tasks. In *Proceedings of IEEE International Conference on Intelligent Robots and Systems (IROS)*, pages 6734–6739.

-
- [Carrillo et al., 2013] Carrillo, L. R. G., López, A. E. D., Lozano, R., and Pégard, C. (2013). Modeling the quad-rotor mini-robotcraft. In *Quad Rotorcraft Control*, pages 23–34. Springer.
- [Caverly and Forbes, 2014] Caverly, R. J. and Forbes, J. R. (2014). Dynamic modeling and noncollocated control of a flexible planar cable-driven manipulator. *IEEE Transactions on Robotics*, 30(6):1386–1397.
- [Chen, 2015a] Chen, M. (2015). Constrained control allocation for overactuated aircraft using a neurodynamic model. *IEEE Transactions on Systems, Man, and Cybernetics: Systems*, 46(12):1630–1641.
- [Chen, 2015b] Chen, X. (2015). *Reachability analysis of non-linear hybrid systems using Taylor Models*. Doctoral thesis, RWTH Aachen University, Aachen.
- [Ciripoi et al., 2018] Ciripoi, D., Löhne, A., and WeiSSing, B. (2018). A vector linear programming approach for certain global optimization problems. *Journal of Global Optimization*, 72(2):347372.
- [Danko et al., 2015] Danko, T. W., Chaney, K. P., and Oh, P. Y. (2015). A parallel manipulator for mobile manipulating uavs. In *Proceedings of IEEE international conference on technologies for practical robot applications (TePRA)*, pages 1–6.
- [Deimel and Brock, 2016] Deimel, R. and Brock, O. (2016). A novel type of compliant and underactuated robotic hand for dexterous grasping. *The International Journal of Robotics Research*, 35(1-3):161–185.
- [DJI, 2021a] DJI (2021). Matrice 600 pro - dji. [Online; accessed 15-January-2021].
- [DJI, 2021b] DJI (2021). Mavic mini - dji. [Online; accessed 3-January-2021].
- [DJI, 2021c] DJI (2021). Phantom 4 pro v2.0 - dji. [Online; accessed 3-January-2021].
- [Ebert-Uphoff and Voglewede, 2004] Ebert-Uphoff, I. and Voglewede, P. A. (2004). On the connections between cable-driven robots, parallel manipulators and grasping. In *Proceedings of IEEE International Conference on Robotics and Automation (ICRA)*, volume 5, pages 4521–4526.
- [Erskine et al., 2019] Erskine, J., Chriette, A., and Caro, S. (2019). Wrench Analysis of Cable-Suspended Parallel Robots Actuated by Quadrotor Unmanned Aerial Vehicles. *Journal of Mechanisms and Robotics*, 11(2).
- [Fawzi, 2016] Fawzi, H. (2016). *Power and limitations of convex formulations via linear and semidefinite programming lifts*. Doctoral thesis, Massachusetts Institute of Technology, Massachusetts.

-
- [Ferrari and Canny, 1992] Ferrari, C. and Canny, J. (1992). Planning optimal grasps. In *Proceedings of IEEE International Conference on Robotics and Automation (ICRA)*, pages 2290–2295.
- [Findeisen and Allgöwer, 2002] Findeisen, R. and Allgöwer, F. (2002). An introduction to nonlinear model predictive control. In *Proceedings of 21st Benelux meeting on systems and control*, volume 11, pages 119–141.
- [Fossen and Johansen, 2006] Fossen, T. I. and Johansen, T. A. (2006). A survey of control allocation methods for ships and underwater vehicles. In *Proceedings of IEEE Mediterranean Conference on Control and Automation*, pages 1–6.
- [Franchi and Mallet, 2017] Franchi, A. and Mallet, A. (2017). Adaptive closed-loop speed control of BLDC motors with applications to multi-rotor aerial vehicles. In *Proceedings of IEEE International Conference on Robotics and Automation (ICRA)*, pages 5203–5208.
- [Fukuda, 2020] Fukuda, K. (2020). Polyhedral computation. <https://doi.org/10.3929/ethz-b-000426218>. Online; accessed 21 January 2021.
- [Gabrich et al., 2018] Gabrich, B., Saldana, D., Kumar, V., and Yim, M. (2018). A flying gripper based on cuboid modular robots. In *Proceedings of IEEE International Conference on Robotics and Automation (ICRA)*, pages 7024–7030.
- [Gallina and Rosati, 2002] Gallina, P. and Rosati, G. (2002). Manipulability of a planar wire driven haptic device. *Mechanism and Machine Theory*, 37(2):215–228.
- [Garimella and Kobilarov, 2015] Garimella, G. and Kobilarov, M. (2015). Towards model-predictive control for aerial pick-and-place. In *Proceedings of IEEE International Conference on Robotics and Automation (ICRA)*, pages 4692–4697.
- [Gioioso et al., 2014] Gioioso, G., Franchi, A., Salvietti, G., Scheggi, S., and Prattichizzo, D. (2014). The flying hand: A formation of UAVs for cooperative aerial tele-manipulation. In *Proceedings of IEEE International Conference on Robotics and Automation (ICRA)*, pages 4335–4341.
- [Gosselin, 2005] Gosselin, C. M. (2005). Adaptive Robotic Mechanical Systems: A Design Paradigm. *Journal of Mechanical Design*, 128(1):192–198.
- [Gouttefarde et al., 2015a] Gouttefarde, M., Collard, J.-F., Riehl, N., and Baradat, C. (2015). Geometry selection of a redundantly actuated cable-suspended parallel robot. *IEEE Transactions on Robotics*, 31(2):501–510.

-
- [Gouttefarde and Gosselin, 2006] Gouttefarde, M. and Gosselin, C. M. (2006). Analysis of the wrench-closure workspace of planar parallel cable-driven mechanisms. *IEEE Transactions on Robotics*, 22(3):434–445.
- [Gouttefarde et al., 2015b] Gouttefarde, M., Lamaury, J., Reichert, C., and Bruckmann, T. (2015). A versatile tension distribution algorithm for n -dof parallel robots driven by $n + 2$ cables. *IEEE Transactions on Robotics*, 31(6):1444–1457.
- [Grünbaum, 2003] Grünbaum, B. (2003). *Convex polytopes*. Springer-Verlag New York.
- [Hägele et al., 2016] Hägele, M., Nilsson, K., Pires, J. N., and Bischoff, R. (2016). Industrial robotics. In *Springer Handbook of Robotics*, pages 1385–1422. Springer.
- [Hamandi et al., 2020] Hamandi, M., Sawant, K., Tognon, M., and Franchi, A. (2020). Omni-plus-seven (o7+): An omnidirectional aerial prototype with a minimal number of unidirectional thrusters. In *Proceedings of IEEE International Conference on Unmanned Aircraft Systems (ICUAS)*, pages 754–761.
- [Härkegård, 2004] Härkegård, O. (2004). Dynamic control allocation using constrained quadratic programming. *Journal of Guidance, Control, and Dynamics*, 27(6):1028–1034.
- [Herceg et al., 2013] Herceg, M., Kvasnica, M., Jones, C., and Morari, M. (2013). Multi-Parametric Toolbox 3.0. In *Proceedings of the European Control Conference (ECC)*, pages 502–510.
- [Heredia et al., 2014] Heredia, G., Jimenez-Cano, A., Sanchez, I., Llorente, D., Vega, V., Braga, J., Acosta, J., and Ollero, A. (2014). Control of a multicopter outdoor aerial manipulator. In *Proceedings of IEEE International Conference on Intelligent Robots and Systems (IROS)*, pages 3417–3422.
- [Herrmann et al., 2019] Herrmann, L., Bruckmann, T., Bröcker, M., and Schramm, D. (2019). Development of a Dynamic Electronic Speed Controller for Multicopters. In *Proceedings of IEEE European Control Conference (ECC)*, pages 4010–4015.
- [Hussein et al., 2018] Hussein, H., Santos, J. C., and Gouttefarde, M. (2018). Geometric optimization of a large scale cdpr operating on a building facade. In *Proceedings of IEEE International Conference on Intelligent Robots and Systems (IROS)*, pages 5117–5124.
- [Huynh et al., 1992] Huynh, T., Lassez, C., and Lassez, J.-L. (1992). Practical issues on the projection of polyhedral sets. *Annals of Mathematics and Artificial Intelligence*, 6(4):295–315.

-
- [Jiang and Voyles, 2013] Jiang, G. and Voyles, R. (2013). Hexrotor uav platform enabling dextrous interaction with structures-flight test. In *Proceedings of IEEE international symposium on safety, security, and rescue robotics (SSRR)*, pages 1–6.
- [Johansen and Fossen, 2013] Johansen, T. A. and Fossen, T. I. (2013). Control allocation - a survey. *Automatica*, 49(5):1087–1103.
- [Johansen et al., 2004] Johansen, T. A., Fossen, T. I., and Berge, S. P. (2004). Constrained nonlinear control allocation with singularity avoidance using sequential quadratic programming. *IEEE Transactions on Control Systems Technology*, 12(1):211–216.
- [Kamel et al., 2016] Kamel, M., Alexis, K., and Siegwart, R. (2016). Design and modeling of dextrous aerial manipulator. In *Proceedings of IEEE International Conference on Intelligent Robots and Systems (IROS)*, pages 4870–4876.
- [Kamel et al., 2018] Kamel, M., Verling, S., Elkhatib, O., Sprecher, C., Wulkop, P., Taylor, Z., Siegwart, R., and Gilitschenski, I. (2018). The voliro omniorientational hexacopter: An agile and maneuverable tilttable-rotor aerial vehicle. *IEEE Robotics & Automation Magazine*, 25(4):34–44.
- [Kessens et al., 2016] Kessens, C. C., Thomas, J., Desai, J. P., and Kumar, V. (2016). Versatile aerial grasping using self-sealing suction. In *Proceedings of IEEE International Conference on Robotics and Automation (ICRA)*, pages 3249–3254.
- [Khamseh et al., 2018] Khamseh, H. B., Janabi-Sharifi, F., and Abdessameud, A. (2018). Aerial manipulation - a literature survey. *Robotics and Autonomous Systems*, 107:221–235.
- [Kim et al., 2013] Kim, S., Choi, S., and Kim, H. J. (2013). Aerial manipulation using a quadrotor with a two dof robotic arm. In *Proceedings of IEEE International Conference on Intelligent Robots and Systems (IROS)*, pages 4990–4995.
- [Korpela et al., 2014] Korpela, C., Orsag, M., and Oh, P. (2014). Towards valve turning using a dual-arm aerial manipulator. In *Proceedings of IEEE International Conference on Intelligent Robots and Systems (IROS)*, pages 3411–3416.
- [Krut, 2005] Krut, S. (2005). A force-isotropic underactuated finger. In *Proceedings of IEEE International Conference on Robotics and Automation (ICRA)*, pages 2314–2319.
- [Krut and Begoc, 2011] Krut, S. and Begoc, V. (2011). A Simple Design Rule for 1st Order Form-Closure of Underactuated Hands. *Mechanical Sciences (MS)*, 2:1–8.

-
- [Krut et al., 2010] Krut, S., Bégoc, V., Dombre, E., and Pierrot, F. (2010). Extension of the form-closure property to underactuated hands. *IEEE Transactions on Robotics*, 26(5):853–866.
- [Krut et al., 2004] Krut, S., Pierrot, F., et al. (2004). Velocity performances indexes for parallel mechanisms with actuation redundancy. *Robotica*, 22(Part 2):129–139.
- [Laiacker et al., 2016] Laiacker, M., Huber, F., and Kondak, K. (2016). High accuracy visual servoing for aerial manipulation using a 7 degrees of freedom industrial manipulator. In *Proceedings of IEEE International Conference on Intelligent Robots and Systems (IROS)*, pages 1631–1636.
- [Li et al., 2020a] Li, Z., Erskine, J., Caro, S., and Chriette, A. (2020). Design and control of a variable aerial cable towed system. *IEEE Robotics and Automation Letters*, 5(2):636–643.
- [Li et al., 2020b] Li, Z., Song, X., Begoc, V., Chriette, A., and Fantoni, I. (2020). Dynamic Modeling and Controller Design of a novel aerial grasping robot. In *23rd CISM IFToMM Symposium on Robot Design, Dynamics and Control (RoManSy 2020)*, Sapporo, Japan.
- [Lim et al., 2017] Lim, Y.-H., Kwon, S.-H., Kim, K.-H., and Ahn, H.-S. (2017). Implementation of load transportation using multiple quadcopters. In *Proceedings of IEEE International Conference on Advanced Intelligent Mechatronics (AIM)*, pages 639–644.
- [Lynch and Park, 2017] Lynch, K. M. and Park, F. C. (2017). *Modern Robotics: Mechanics, Planning, and Control*. Cambridge University Press.
- [Löhne and WeiSSing, 2016] Löhne, A. and WeiSSing, B. (2016). Equivalence between polyhedral projection, multiple objective linear programming and vector linear programming. *Mathematical Methods of Operations Research*, 84(2):411–426.
- [Magariyama and Abiko, 2020] Magariyama, T. and Abiko, S. (2020). Seamless 90-degree attitude transition flight of a quad tilt-rotor uav under full position control. In *Proceedings of IEEE International Conference on Advanced Intelligent Mechatronics (AIM)*, pages 839–844.
- [Mahony et al., 2012] Mahony, R., Kumar, V., and Corke, P. (2012). Multirotor aerial vehicles: Modeling, estimation, and control of quadrotor. *IEEE Robotics and Automation mag.*, 19(3):20–32.
- [Manubens et al., 2013] Manubens, M., Devaurs, D., Ros, L., and Cortés, J. (May, 2013). Motion planning for 6-D manipulation with aerial towed-cable systems. In *Robotics: Science and Systems*, Berlin, Germany.

-
- [Marchand et al., 2005] Marchand, E., Spindler, F., and Chaumette, F. (2005). Visp for visual servoing: a generic software platform with a wide class of robot control skills. *IEEE Robotics and Automation Magazine*, 12(4):40–52.
- [Mayne, 2014] Mayne, D. Q. (2014). Model predictive control: Recent developments and future promise. *Automatica*, 50(12):2967–2986.
- [Mellinger et al., 2011] Mellinger, D., Lindsey, Q., Shomin, M., and Kumar, V. (2011). Design, modeling, estimation and control for aerial grasping and manipulation. In *Proceedings of IEEE International Conference on Intelligent Robots and Systems (IROS)*, pages 2668–2673.
- [Meng et al., 2020] Meng, X., He, Y., and Han, J. (2020). Survey on aerial manipulator: System, modeling, and control. *Robotica*, 38(7):1288–1317.
- [Michael et al., 2011] Michael, N., Fink, J., and Kumar, V. (2011). Cooperative manipulation and transportation with aerial robots. *Autonomous Robots*, 30(1):73–86.
- [Morales, 2019] Morales, D. P. (2019). *Multi-sensor-based control in Intelligent Parking applications*. Doctoral thesis, École centrale de Nantes.
- [Murray et al., 1994] Murray, R. M., Li, Z., Sastry, S. S., and Sastry, S. S. (1994). *A mathematical introduction to robotic manipulation*. CRC press.
- [Naveau et al., 2016] Naveau, M., Kudruss, M., Stasse, O., Kirches, C., Mombaur, K., and Souères, P. (2016). A reactive walking pattern generator based on nonlinear model predictive control. *IEEE Robotics and Automation Letters*, 2(1):10–17.
- [Nguyen et al., 2014] Nguyen, D. Q., Gouttefarde, M., Company, O., and Pierrot, F. (2014). On the analysis of large-dimension reconfigurable suspended cable-driven parallel robots. In *Proceedings of IEEE International Conference on Robotics and Automation (ICRA)*, pages 5728–5735.
- [Nguyen et al., 2018] Nguyen, H.-N., Park, S., Park, J., and Lee, D. (2018). A novel robotic platform for aerial manipulation using quadrotors as rotating thrust generators. *IEEE Transactions on Robotics*, 34(2):353–369.
- [Nguyen, 1988] Nguyen, V.-D. (1988). Constructing force-closure grasps. *The International Journal of Robotics Research*, 7(3):3–16.
- [Nonami et al., 2010] Nonami, K., Kendoul, F., Suzuki, S., Wang, W., and Nakazawa, D. (2010). *Autonomous Flying Robots: Unmanned Aerial Vehicles and Micro Aerial Vehicles*. Springer Science & Business Media.

-
- [Oosedo et al., 2015] Oosedo, A., Abiko, S., Narasaki, S., Kuno, A., Konno, A., and Uchiyama, M. (2015). Flight control systems of a quad tilt rotor unmanned aerial vehicle for a large attitude change. In *Proceedings of IEEE International Conference on Robotics and Automation (ICRA)*, pages 2326–2331.
- [Özbek et al., 2016] Özbek, N. S., Önkol, M., and Efe, M. Ö. (2016). Feedback control strategies for quadrotor-type aerial robots: a survey. *Transactions of the Institute of Measurement and Control*, 38(5):529–554.
- [Padfield, 2008] Padfield, G. D. (2008). *Helicopter flight dynamics: the theory and application of flying qualities and simulation modelling*. John Wiley & Sons.
- [Pollard, 1996] Pollard, N. S. (1996). Synthesizing grasps from generalized prototypes. In *Proceedings of IEEE International Conference on Robotics and Automation (ICRA)*, volume 3, pages 2124–2130.
- [Pott et al., 2009] Pott, A., Bruckmann, T., and Mikelsons, L. (2009). Closed-form force distribution for parallel wire robots. In *Computational Kinematics*, pages 25–34. Springer.
- [Pounds et al., 2011] Pounds, P. E., Bersak, D. R., and Dollar, A. M. (2011). The yale aerial manipulator: grasping in flight. In *Proceedings of IEEE International Conference on Robotics and Automation (ICRA)*, pages 2974–2975.
- [Rajappa et al., 2015] Rajappa, S., Ryll, M., Bühlhoff, H. H., and Franchi, A. (2015). Modeling, control and design optimization for a fully-actuated hexarotor aerial vehicle with tilted propellers. In *Proceedings of IEEE International Conference on Robotics and Automation (ICRA)*, pages 4006–4013.
- [Rashad et al., 2020] Rashad, R., Goerres, J., Aarts, R. G., Engelen, J. B., and Stramigioli, S. (2020). Fully actuated multirotor uavs: A literature review. *IEEE Robotics & Automation Magazine*, 27(3):97–107.
- [Rossi et al., 2019] Rossi, E., Tognon, M., Carli, R., Schenato, L., Cortés, J., and Franchi, A. (2019). Cooperative aerial load transportation via sampled communication. *IEEE Control Systems Letters*, 4(2):277–282.
- [Ruggiero et al., 2018] Ruggiero, F., Lippiello, V., and Ollero, A. (2018). Aerial manipulation: A literature review. *IEEE Robotics and Automation Letters*, 3(3):1957–1964.
- [Ruggiero et al., 2015] Ruggiero, F., Trujillo, M. A., Cano, R., Ascorbe, H., Viguria, A., Pérez, C., Lippiello, V., Ollero, A., and Siciliano, B. (2015). A multilayer control for

-
- multirotor uavs equipped with a servo robot arm. In *Proceedings of IEEE international conference on robotics and automation (ICRA)*, pages 4014–4020.
- [Ryll et al., 2016] Ryll, M., Bicego, D., and Franchi, A. (2016). Modeling and control of fast-hex: a fully-actuated by synchronized-tilting hexarotor. In *Proceedings of IEEE International Conference on Intelligent Robots and Systems (IROS)*, pages 1689–1694.
- [Ryll et al., 2012] Ryll, M., Bühlhoff, H. H., and Giordano, P. R. (2012). Modeling and control of a quadrotor uav with tilting propellers. In *Proceedings of IEEE International Conference on Robotics and Automation (ICRA)*, pages 4606–4613.
- [Ryll et al., 2014] Ryll, M., Bühlhoff, H. H., and Giordano, P. R. (2014). A novel over-actuated quadrotor unmanned aerial vehicle: Modeling, control, and experimental validation. *IEEE Transactions on Control Systems Technology*, 23(2):540–556.
- [Sadien, 2017] Sadien, E. (2017). *Design of aircraft integrated ground control laws*. These en préparation, Université de Haute-Alsace, Université de Strasbourg.
- [Saint-Sevin et al., 2019] Saint-Sevin, M., Bégoc, V., Briot, S., Chriette, A., and Fantoni, I. (2019). Design and optimization of a multi-drone robot for grasping and manipulation of large size objects. In *ROMANSY 22 – Robot Design, Dynamics and Control*, pages 458–465. Springer International Publishing.
- [Saldana et al., 2017] Saldana, D., Gabrich, B., Whitzer, M., Prorok, A., Campos, M. F., Yim, M., and Kumar, V. (2017). A decentralized algorithm for assembling structures with modular robots. In *Proceedings of IEEE International Conference on Intelligent Robots and Systems (IROS)*, pages 2736–2743.
- [Šalinić et al., 2017] Šalinić, S., Vranić, A., Nešić, N. D., and Tomović, A. M. (2017). On the torque transmission by a cardan-hooke joint. *FME Transactions*, 45(1):117–121.
- [Sanalitra et al., 2020] Sanalitra, D., Savino, H. J., Tognon, M., Cortés, J., and Franchi, A. (2020). Full-pose manipulation control of a cable-suspended load with multiple uavs under uncertainties. *IEEE Robotics and Automation Letters*.
- [Santos et al., 2020] Santos, J., Chemori, A., and Gouttefarde, M. (2020). Redundancy resolution integrated model predictive control of cdprs: Concept, implementation and experiments. In *IEEE International Conference on Robotics and Automation (ICRA)*, Virtual, France.
- [Schupp, 2019] Schupp, S. (2019). *State set representations and their usage in the reachability analysis of hybrid systems*. Doctoral thesis, RWTH Aachen University, Aachen.

-
- [Selfridge and Tao, 2016] Selfridge, J. M. and Tao, G. (2016). Multivariable output feedback mrac for a quadrotor uav. In *Proceedings of IEEE American Control Conference (ACC)*, pages 492–499.
- [Shapiro et al., 2001] Shapiro, A., Rimon, E., and Burdick, J. W. (2001). Passive force closure and its computation in compliant-rigid grasps. In *Proceedings of IEEE International Conference on Intelligent Robots and Systems (IROS)*, volume 3, pages 1769–1775.
- [Shen et al., 1994] Shen, Y., Osumi, H., and Arai, T. (1994). Set of manipulating forces in wire driven systems. In *Proceedings of IEEE International Conference on Intelligent Robots and Systems (IROS)*, pages 1626–1631.
- [Six et al., 2018] Six, D., Briot, S., Chriette, A., and Martinet, P. (2018). The kinematics, dynamics and control of a flying parallel robot with three quadrotors. *IEEE Robotics and Automation Letters*, 3(1):559–566.
- [Six et al., 2017] Six, D., Chriette, A., Briot, S., and Martinet, P. (2017). Dynamic modeling and trajectory tracking controller of a novel flying parallel robot. *IFAC-PapersOnLine*, 50(1):2241–2246.
- [Sreenath and Kumar, 2013] Sreenath, K. and Kumar, V. (2013). Dynamics, control and planning for cooperative manipulation of payloads suspended by cables from multiple quadrotor robots. In *Proceedings of Robotics: Science and Systems Foundation*, Berlin, Germany.
- [Staub, 2018] Staub, N. (2018). *Models, algorithms and architectures for cooperative manipulation with aerial and ground robots: Modèles, algorithmes et architectures pour la manipulation coopérative entre robots au sol et aériens*. Doctoral thesis, Université Toulouse III–Paul Sabatier, Toulouse.
- [Suarez et al., 2015] Suarez, A., Heredia, G., and Ollero, A. (2015). Lightweight compliant arm for aerial manipulation. In *Proceedings of IEEE International Conference on Intelligent Robots and Systems (IROS)*, pages 1627–1632.
- [Suarez et al., 2016] Suarez, A., Heredia, G., and Ollero, A. (2016). Lightweight compliant arm with compliant finger for aerial manipulation and inspection. In *Proceedings of IEEE International Conference on Intelligent Robots and Systems (IROS)*, pages 4449–4454.
- [Suarez et al., 2017a] Suarez, A., Jimenez-Cano, A., Vega, V., Heredia, G., Rodriguez-Castaño, A., and Ollero, A. (2017). Lightweight and human-size dual arm aerial ma-

-
- nipulator. In *Proceedings of IEEE International Conference on Unmanned Aircraft Systems (ICUAS)*, pages 1778–1784.
- [Suarez et al., 2019] Suarez, A., Perez, M., Heredia, G., and Ollero, A. (2019). Small-scale compliant dual arm with tail for winged aerial robots. In *Proceedings of IEEE International Conference on Intelligent Robots and Systems (IROS)*, pages 208–214.
- [Suarez et al., 2017b] Suarez, A., Soria, P. R., Heredia, G., Arrue, B. C., and Ollero, A. (2017). Anthropomorphic, compliant and lightweight dual arm system for aerial manipulation. In *Proceedings of IEEE International Conference on Intelligent Robots and Systems (IROS)*, pages 992–997.
- [Thomas et al., 2013] Thomas, J., Polin, J., Sreenath, K., and Kumar, V. (August, 2013). Avian-inspired grasping for quadrotor micro uavs. In *Proceedings of ASME International Design Engineering Technical Conferences and Computers and Information in Engineering Conference*, volume 6A.
- [Tiwary, 2007] Tiwary, H. R. (2007). On the hardness of minkowski addition and related operations. In *Proceedings of the Twenty-Third Annual Symposium on Computational Geometry*, pages 306–309.
- [Tiwary, 2008] Tiwary, H. R. (2008). On the hardness of computing intersection, union and minkowski sum of polytopes. *Discrete & Computational Geometry*, 40(3):469–479.
- [Tiwary, 2009] Tiwary, H. R. (2009). *Complexity of some polyhedral enumeration problems*. Doctoral thesis, Universität des Saarlandes, Saarbrücken, Germany.
- [Tognon et al., 2017] Tognon, M., Yüksel, B., Buondonno, G., and Franchi, A. (2017). Dynamic decentralized control for protocentric aerial manipulators. In *Proceedings of IEEE International Conference on Robotics and Automation (ICRA)*, pages 6375–6380.
- [Townsend, 2000] Townsend, W. (2000). The barretthand grasper—programmably flexible part handling and assembly. *Industrial Robot: an international journal*, 27(3):181–188.
- [Wall et al., 2017] Wall, V., Zöller, G., and Brock, O. (2017). A method for sensorizing soft actuators and its application to the RBO hand 2. In *Proceedings of IEEE International Conference on Robotics and Automation (ICRA)*, pages 4965–4970.
- [Wikipedia contributors, 2020a] Wikipedia contributors (2020). Freewheel — Wikipedia, the free encyclopedia. [Online; accessed 16-January-2021].
- [Wikipedia contributors, 2020b] Wikipedia contributors (2020). Helicopter — Wikipedia, the free encyclopedia. [Online; accessed 3-January-2021].

-
- [Yoshikawa, 1985] Yoshikawa, T. (1985). Manipulability of robotic mechanisms. *The international journal of Robotics Research*, 4(2):3–9.
- [Yu et al., 2019] Yu, P., Wang, Z., and Wong, K. (2019). Exploring aerial perching and grasping with dual symmetric manipulators and compliant end-effectors. *International Journal of Micro Air Vehicles*, 11. <https://doi.org/10.1177/1756829319877416>.
- [Zhang et al., 2019] Zhang, H., Sun, J., and Zhao, J. (2019). Compliant bistable gripper for aerial perching and grasping. In *Proceedings of IEEE International Conference on Robotics and Automation (ICRA)*, pages 1248–1253.
- [Zhao et al., 2018] Zhao, M., Kawasaki, K., Anzai, T., Chen, X., Noda, S., Shi, F., Okada, K., and Inaba, M. (2018). Transformable multirotor with two-dimensional multilinks: Modeling, control, and whole-body aerial manipulation. *The International Journal of Robotics Research*, 37(9):1085–1112.
- [Zhao et al., 2017] Zhao, M., Kawasaki, K., Chen, X., Noda, S., Okada, K., and Inaba, M. (2017). Whole-body aerial manipulation by transformable multirotor with two-dimensional multilinks. In *Proceedings of IEEE International Conference on Robotics and Automation (ICRA)*, pages 5175–5182.
- [Zhao et al., 2016] Zhao, M., Kawasaki, K., Okada, K., and Inaba, M. (2016). Transformable multirotor with two-dimensional multilinks: modeling, control, and motion planning for aerial transformation. *Advanced Robotics*, 30(13):825–845.

Titre : Développements théoriques et évaluation expérimentale d'un nouveau système collaboratif multi-drones de saisie et de manipulation de grands objets

Mot clés : Systèmes aériens, Mécanique et contrôle, Saisie, Modèle dynamique, Commande prédictive, Allocation de contrôle dynamique

Résumé : Cette thèse propose un nouveau concept de robot de manipulation aérienne appelé Flying Gripper. Ce robot est un manipulateur aérien, destiné à la saisie, la manipulation et le transport de grands objets de manière autonome. Le robot Flying Gripper est composé de quatre quadrotors, de quatre doigts auto-adaptatifs et d'un châssis.

Les principaux apports de ces travaux sont : (1) un concept mécanique original reposant sur l'utilisation de plusieurs quadrotors et tirant parti de la rotation en lacet des quadrotors pour actionner un mécanisme de préhension auto-adaptatif et intrinsèquement sûr (2) une méthode pour analy-

ser des torseurs disponibles en tenant compte des contraintes d'égalité et d'inégalité imposées par les limites d'actionnement, les butées mécaniques et les relations d'équilibre ; (3) une commande prédictive permettant de manipuler l'objet saisi avec une masse, des inerties et un centre de masse inconnus ; (4) un algorithme d'allocation de contrôle dynamique pour la distribution de l'effort de contrôle, de manière à optimiser l'efficacité énergétique et à assurer la continuité de la commande, en considérant les limites mécaniques du robot.

Des simulations numériques et des tests expérimentaux ont été effectués pour valider les performances du contrôleur.

Title: Theoretical developments and experimental evaluation of a novel collaborative multi-drones grasping and manipulation system of large objects

Keywords: Aerial Systems, Mechanics and Control, Grasping, Dynamic model, Model Predictive Control, Dynamic Control Allocation

Abstract: This thesis proposes a new concept of aerial manipulation robot named Flying Gripper that is intended to perform grasping, manipulating, and transporting of large objects autonomously. The Flying Gripper robot is composed of four quadrotors, four self-adaptive fingers and a body structure.

The main contributions of these works are: (1) an original mechanical concept using multiple quadrotors to obtain full manipulability in $SE(3)$ and taking advantage of their yaw rotations to actuate a self-adaptive and intrinsically safe grasping mechanism; (2) a wrench capability analysis method taking into account the

equality and inequality constraints imposed by actuation limits, mechanical stops and equilibrium relations; (3) a model predictive controller to deal with unknown mass, inertia and center of mass due to the grasped object; (4) a Dynamic Control Allocation algorithm to distribute the control output in a way that guarantees the continuity of actuator's velocity, improves the energy efficiency and satisfies the robot mechanical limits.

Numerical simulations and experimental tests have been carried out to validate the controller performances.